

# **Unoccupied Electronic Structure and Ultrafast Dynamics in Quasi Low-Dimensional Systems**

---

Der Fakultät für Physik  
der Universität Duisburg-Essen vorgelegte

## **Doktorarbeit**

zur Erlangung des akademischen Grades eines Doktors der Naturwissenschaft  
(Dr. rer. nat.)

von

**Abdul Samad Syed**

aus Karachi, Pakistan

Referent: Prof. Dr. Uwe Bovensiepen

Korreferent 1: Prof. Dr. Christoph Tegenkamp

Prüfer: Prof. Dr. Michael Horn-von Hoegen

Vorsitzende des Prüfungsausschusses: Prof. Dr. Rossitza Pentcheva

Tag der mündlichen Prüfung: 12.11.2018



*Dedicated to Ammi, Tariq, and Soheera*



# Abstract

In the field of low dimensional materials, metal-semiconductor structures are exceptionally appealing due to their intriguing fundamental and extensive technological aspects. Two-dimensional metal-semiconductor systems are known to exhibit various exciting physics including the charge density wave formation, superconducting properties, and strong spin-orbit coupling. Metallic nanowires on semiconductor surfaces are prototypical quasi one-dimensional systems that undergo a phase transition at low temperatures due to various instabilities in the system. A profound insight into these interesting physics unravels with the knowledge of the electronic structure. The electron scattering dynamics that plays a crucial role in device functionality is largely unexplored for the quasi low-dimensional systems. In this study, we aim at understanding the electronic structure and the electron scattering dynamics in such systems by means of femtosecond time-resolved linear and non-linear photoemission.

In the quasi two-dimensional Pb/Si(111), three electronic states were identified whose unoccupied nature was verified from the temporal evolution of their population dynamics. These unoccupied states exhibited asymmetric photoemission intensity distribution and electronic dispersion across  $\Gamma$  ( $k_{\parallel}=0$ ). These asymmetries have been found to be a consequence of various processes including the off-normal light incidence, involvement of bulk states, final states effects, and spin-effects.

Investigation of the unoccupied electronic structure of quasi-one-dimensional reconstructions of Pb atoms on a Si(557) surface identified two states. Density functional theory calculations revealed their presence in an energy region degenerate with a reduced electronic density of states of the Si substrate resulting in rather high momentum-averaged lifetimes. It was further identified that the photoemission yield and the population dynamics depend on the electron momentum component perpendicular to the steps of the Si substrate. We conclude that momentum- and direction-dependent dephasing caused by elastic scattering at the step edges, modifies the excited-state population dynamics in this system. In addition, the electron dynamics found to exhibit no signature of the phase transition reported earlier for this system.

For the In/Si(111) system, the structural phase transition results in modification of the occupied electronic structure at the BZ center ( $k_{\parallel}=0$ ) and boundary  $k_F$  along the wire direction. Optically excited carriers revealed a lifetime of  $\sim 500$  fs. This confirms that the excited carriers survive on a timescale at which a structural transition occurs.



# Deutsche Kurzfassung

Im Bereich niedrig-dimensionaler Materialien sind insbesondere Metall-Halbleiter-Strukturen aufgrund ihrer faszinierenden fundamentalen und umfassenden technologischen Aspekt interessant. Zwei-dimensionale Metall-Halbleiter Systeme zeichnen sich durch verschiedenartige physikalische Phänomene wie bspw. die Ausbildung von Ladungsdichtewellen, supraleitende Eigenschaften und starke Spin-Bahn-Wechselwirkung aus. Metallische Nanodrähte auf Halbleiteroberflächen sind prototypische quasi-eindimensionale Systeme die aufgrund von verschiedenen Instabilitäten Phasenübergänge bei niedrigen Temperaturen zeigen. Ein tiefgreifendes Verständnis dieser interessanten Physik ergibt sich aus der Kenntnis der entsprechenden elektronischen Struktur. Die elektronische Streudynamik, welche eine wesentliche Rolle in der Funktionalität von nanoskaligen Bauteilen spielt, ist zu weiten Teilen für quasi-niedrigdimensionale Systeme nicht untersucht. In dieser Arbeit zielen wir mit Hilfe von femtosekunden zeitaufgelöster linearer und nicht-linearer Photoemission auf ein Verständnis der elektronischen Struktur und Streudynamik in solchen Systemen. In dem 2D Pb/Si(111)-System wurden drei elektronische Zustände identifiziert, deren unbesetzte Natur durch ihre Populationsdynamik nachgewiesen wurde. Diese unbesetzten Zustände zeigen eine asymmetrische Photoemissionsausbeute und elektronische Dispersion entlang  $\Gamma$  ( $k_{\parallel} = 0$ ). Diese Asymmetrie wurde als Konsequenz verschiedener Prozessen wie dem nicht-normalen Lichteinfall, der Beteiligung von Festkörperzuständen, Endzustandeffekten und Spineffekten identifiziert. Untersuchungen der unbesetzten Bandstruktur der quasi-eindimensionalen Pb/Si(557)-Rekonstruktion zeigten zwei elektronische Zustände. Dichtefunktionaltheorie-Rechnungen identifizierten deren energetische Entartung mit Bereichen reduzierter Zustandsdichte des unterliegenden Si-Substrates, was zu einer hohen, impulsgemittelten Lebensdauer führt. Weiterhin zeigte sich, dass die Photoemissionsausbeute und die Populationsdynamik von dem Elektronenimpuls, insbesondere in Bezug auf die Stufenkanten, abhängt. Wir schlussfolgern, dass die impuls- und richtungsabhängige Dephasierung durch elastische Streuung an den Stufenkanten die Populationsdynamik angeregter Zustände in diesem System modifiziert. Weiterhin wurde keine Signatur eines zuvor berichteten Phasenüberganges in der Elektronendynamik gefunden. In In/Si(111) führt ein struktureller Phasenübergang zu einer Veränderung der besetzten elektronischen Struktur im Zentrum und Rand der Brillouin-Zone entlang der Drahrichtung. Der optisch induzierte Phasenübergang zeigt für angeregte Ladungsträger eine Lebensdauer von  $\sim 500$  fs. Dieser Befund bestätigt, dass die elektronische Anregung auf der Zeitskala des strukturellen Übergangs bestehen bleibt.



# Acknowledgments

I would like to take this opportunity to express my gratitude to all the people who have been supportive throughout my journey to reach this important goal of my life. First of all, I would like to thank my supervisor Prof. Uwe Bovensiepen who gave me the opportunity to work in his group. I am particularly grateful to you for the continuous support, guidance at every stage, and constant availability to discuss my results despite your busy schedule. I am also grateful to the principal investigator of this project Manuel Ligges. Throughout my research work you have provided technical and non-technical support for me with a kind and understanding way which is the trademark of your nature.

Our collaborators made some important contributions to propel this project. The Group of Prof. Herbert Pfnür and Prof. Christoph Tegenkamp from Leibniz Universität Hannover was the main support for Pb/Si(557) project and Daniel Lükermann from their group came over to Duisburg for helping us with the sample preparation. The work group of Prof. Horn-von Hoegen collaborated with us for the In/Si(111) project. From their group, I would like to particularly thank Boris Krenzer, Tim Frigge, Bernd Hafke, and Tobias Witte for helping us with In/Si(111) sample preparation. I would also like to thank Prof. Peter Kratzer for providing us with the theoretical calculations and for various useful discussions we had to interpret our results. Prof. Eugene Krasovskii (Universidad del Pais Vasco ,Spain) provided us with some latest calculations related to Pb/Si(111) system and also deserve our especial thanks.

I would also like to appreciate my colleagues within the group for their technical and non-technical support. This includes Vesna Trontl who worked as a postdoc on this project and made valuable contributions. My very especial thanks goes to Ishita Agarwal for all her help and support in and outside work environment and for being a great friend. Mathias Sandhofer also helped me to understand the fundamentals of our experimental setup besides being a great

---

mate. I would also like to convey my appreciation to Ping Zhou, Isabella Avigo and other current and former member of photoemission team. I am also in general thankful to all of my current and former colleagues including Andre Seyen, Mehdi Afshari, and Yasin Beyazit for memorable times. I am also very grateful to Christina Boese, Michael Bieske, and Roland Kohn for all their help and support during my stay at the group.

My deepest gratitude goes to my siblings and my whole family who were a great source of motivation throughout. I cannot thank you guys enough for all you have done for me. Your happiness and pride on all my achievement was always a great source of strength and a driving force for me. The space does not allow me to write every single name but you all are here. A very very especial thanks goes to my mother who faced so much of hardship for all of us and there is no way I can pay you back for what you have given us. Another very especial thanks goes to my brother Tariq for being the best person I have ever known. The affection and strong bonds that you have created nobody else could have done that. You are definitely a blessing for all of us, stay the same and stay strong forever :-) I am also grateful to my wife Soheera. I would like to appreciate you for being very supportive, understanding, for making tasty meals, and for the excellent job of proofreading my thesis. Now if anything goes wrong in my thesis, blame will lay on you :-)

Memories that I will cherish throughout my life are made by my childhood friends including Kimistin, Shahab, Qurban, Jawed, Waseem, Safdar, and Nabeel. Few years ago, Nabeel passed away and we lost a very dear friend full of life and ambitions. Nabeel, you were a great person and you will stay alive in our memories forever. Away from home, I met Asifa Iqbal and Asim Aijaz in Sweden during my masters studies. Asifa, no words are enough to describe the support that you provided me during that particular phase. Thank you for being so kind and amazing. Asim Aijaz, in you I found a wonderful friend and a mentor whom I can always approach without hesitation. There are many

---

other friends, and acquaintances I got to know during different phases of my life who inspired to become a touch better person than what I used to be. To all these people, I convey my heartfelt gratitude.



# Abbreviations

<b>ARPES</b>	Angle-resolved photemission spectroscopy
<b>BBO</b>	$\beta$ - barium-borate
<b>XC</b>	Cross correlation
<b>DFT</b>	Density functional theory
<b>DS</b>	Devil's staircase
<b>EDC</b>	Energy distribution curves
<i>e-e</i>	Electron-electron
<i>e-ph</i>	Electron-phonon
<b>FWHM</b>	Full width at half maximum
<b>LEED</b>	Low-energy electron diffraction
<b>MCP</b>	Micro channel plate
<b>ML</b>	Monolayer
<b>NOPA</b>	Non-collinear optical parametric amplifier

---

<b>1D</b>	One-dimensional
<b>OPA</b>	Optical parametric amplifier
<b>pTOF</b>	Position-sensitive time of flight
<b>RegA</b>	Regenerative amplifier
<b>SHG</b>	Second harmonic generation
<b>TOF</b>	Time of flight
<b>tr2PPE</b>	Time-resolved two-photon photoemission
<b>trARPES</b>	Time- and angle-resolved photoemission spectroscopy
<b>3D</b>	Three-dimensional
<b>2PPE</b>	Two-photon photoemission
<b>2D</b>	Two-dimensional
<b>UV</b>	Ultraviolet
<b>UHV</b>	Ultrahigh vacuum
<b>VIS</b>	Visible

---



---

---

# Contents

Abstract . . . . .	V
Deutsche Kurzfassung . . . . .	VII
Acknowledgments . . . . .	IX
Abbreviations . . . . .	XV
Table of Contents . . . . .	XVII
<b>1 Introduction and Motivation</b>	<b>1</b>
1.1 Low-Dimensional Systems . . . . .	1
1.2 Experimental Techniques . . . . .	3
1.3 Systems Under Investigation . . . . .	5
1.3.1 Pb/Si(111) . . . . .	5
1.3.2 Pb/Si(557) . . . . .	6
1.3.3 In/Si(111) . . . . .	7
<b>2 Theoretical Background</b>	<b>9</b>
2.1 Photoemission Spectroscopy . . . . .	9
2.1.1 3-Step Model of Photoemission . . . . .	15
2.1.2 1-Step Model of Photoemission . . . . .	16
2.1.3 Angle-Resolved Photoemission Spectroscopy . . . . .	17
2.1.4 Polarization Dependent ARPES . . . . .	20
2.1.5 Two-Photon Photoemission Spectroscopy . . . . .	22
2.1.6 Time-Resolved 2PPE . . . . .	27

---

2.1.7	Time- and Angle-Resolved Photoemission Spectroscopy . . . . .	28
2.2	Electron Dynamics at Surfaces . . . . .	30
2.2.1	Inter-band and Intra-band Scattering . . . . .	33
2.2.2	Coherent Excitation . . . . .	34
<b>3</b>	<b>Experimental Methods</b>	<b>39</b>
3.1	Laser Setup . . . . .	39
3.1.1	Pulse Incoupling . . . . .	42
3.1.2	Pulse Characterization . . . . .	45
3.1.3	Beam Path . . . . .	49
3.2	Ultra High Vacuum Chamber . . . . .	50
3.2.1	Time of Flight Spectrometer . . . . .	53
3.2.2	Position-Sensitive Time of Flight Spectrometer . . . . .	56
3.3	Spectrometer Data . . . . .	60
3.3.1	Acquisition . . . . .	60
3.3.2	Analysis . . . . .	61
3.4	Sample Preparation . . . . .	62
3.4.1	Si Surface Structure . . . . .	62
3.4.2	Si Surface Preparation . . . . .	63
3.4.3	Structure of Pb Overlayers on Si Surface . . . . .	67
3.4.4	Preparation of Pb Overlayer Structure on Si Surface . . . . .	72
<b>4</b>	<b>Strong Linear Dichroism in the Non-Linear Photoemission of 4/3-ML Pb/Si(111)</b>	<b>77</b>
4.1	Introduction . . . . .	77
4.2	Experimental Method . . . . .	80
4.3	Results . . . . .	83
4.3.1	Unoccupied Electronic Structure . . . . .	83
4.3.2	Ultrafast Dynamics . . . . .	85

---

4.3.3	Theoretical Calculations . . . . .	89
4.3.4	Polarization Dependence . . . . .	92
4.3.5	Spin-Orbit Splitting . . . . .	96
4.4	Discussions . . . . .	100
4.4.1	Off-normal Light Incidence . . . . .	102
4.4.2	Bulk State Effects . . . . .	104
4.4.3	Effect of Final States . . . . .	107
4.4.4	Spin Effect . . . . .	109
4.4.5	Summary . . . . .	110
4.5	Conclusion . . . . .	112
<b>5</b>	<b>Electron Scattering Dynamics in</b>	
	<b>Pb/Si(557)</b>	<b>115</b>
5.1	Introduction . . . . .	115
5.2	Experimental Method . . . . .	120
5.3	Results . . . . .	122
5.3.1	Angle- and Time-Resolved 2PPE of Pb/Si(557) . . . . .	122
5.3.2	Discussion . . . . .	133
5.3.3	Temperature-Dependent Electron Dynamics . . . . .	140
5.3.4	Discussion . . . . .	144
5.4	Summary . . . . .	146
<b>6</b>	<b>Phase Transition in In/Si(111) System</b>	<b>149</b>
6.1	Introduction . . . . .	149
6.2	Experimental Method . . . . .	153
6.2.1	In Nanowires: Preparation and Characterization . . . . .	154
6.3	Temperature Driven Phase Transition . . . . .	156
6.3.1	Phase Transition at Brillouin Zone Boundary . . . . .	156
6.3.2	Electronic Band Structure of $8\times 2$ and $4\times 1$ Phases . . . . .	158
6.3.3	DFT Calculations . . . . .	162

---

6.3.4	Discussions . . . . .	164
6.4	Optically Induced Phase Transition . . . . .	166
6.4.1	Pump-Probe Spectroscopy . . . . .	166
6.4.2	Discussions . . . . .	168
6.5	Summary . . . . .	170
<b>7</b>	<b>Conclusion</b>	<b>173</b>
<b>A</b>	<b>Polarization Dependent Linear and Non-Linear Photoemission of Pb/Si(557)</b>	<b>177</b>
A.1	Introduction . . . . .	177
A.2	Experimental Setup . . . . .	178
A.3	Occupied Electronic Structure . . . . .	179
A.3.1	Polarization Dependent Linear Photoemission . . . . .	181
A.3.2	Discussions . . . . .	186
A.4	Unoccupied Electronic Structure . . . . .	187
A.4.1	Pump Polarization Dependence . . . . .	187
A.4.2	Probe Polarization Dependence . . . . .	190
A.4.3	Discussions . . . . .	192
	Bibliography . . . . .	195
	List of Publications . . . . .	217

---

# Introduction and Motivation

## 1.1 Low-Dimensional Systems

The fascinating idea of the multi-dimensional universe has been proposed in order to understand the mysteries of our three-dimensional world. The concept of the existence of more than ten dimensions in the universe has been suggested so far [1]. Human minds can perceive three-dimensions of space and another dimension of time is added in the Einstein theory of relativity. Amid all the discussions of these higher dimensions, the concepts of the reduced two- or one-dimensions are no less intriguing.

In lower dimensional systems, the electronic wavefunction is confined in one- or two-dimensions. The spatial confinement gives rise to quantum size effects that can result in a strong modification in the electronic properties of the lower dimensional system compared to their bulk counterparts. Modification of electronic properties results in numerous intriguing physical phenomena [2–9] that alter the electronic, optical, mechanical, chemical, and thermal properties of these systems and make them attractive for their potential application in the

field of nanotechnology. Indeed, these lower dimensional systems are already a major part of the modern electronics industry.

The aspiration of reaching low dimensions began from the increasing demands of shrinking device sizes governed by Moore's law which in 1965 predicted a doubling of components every year in integrated circuits [10]. In the year 1975, he revised the prediction and indicated a doubling every two years [11]. His predictions have been proven successful for several decades. The transistor size which was  $10\ \mu\text{m}$  in 1970 is expected to reach  $5\ \text{nm}$  by the end of 2021. Electronic confinement generally appears in the range from  $1\ \text{nm}$  to  $100\ \text{nm}$  that demands the understanding of physical phenomenon at the quantum mechanical level.

In the regime of low dimensional materials, metal-semiconductor interfaces are exceptionally appealing due to their far-reaching fundamental and technological aspects. In particular, these interfaces play a crucial role in the semiconductor devices functionality as the charge transfer process requires their coupling with the metallic interconnects. In this regard, the Si substrate being the most widely used material in the semiconductor device fabrication draws major interest and is subject of various studies [12–16].

An interesting case of the metal-semiconductor interfaces is the two dimensional system, which is formed by adsorbing monoatomic and subatomic coverage of metal on the semiconductor surfaces. These two-dimensional metal-semiconductor systems are known to exhibit various exciting physics, e.g. the charge-density wave formation in Pb/Ge (111) [2], Mott phase on Sn/Si(111) [3], and superconducting properties in Pb/Si (111) system [4]. In addition, these systems can be considered as prototypical systems with very strong spin-orbit coupling. A large number of systems with such structural configuration are shown to possess spin-orbit splitting in their surface electronic structure known as Rashba splitting, e.g. Pb/Ge(111) [5, 6], Bi/Si(111) [17–20], Bi/Ge(111) [21, 22], Ti/Si(111) [18, 23–26], and Ti/Ge(111) [21, 27].

More interesting physics unveils when the dimension is reduced further to a regime of quasi-1D structures. Metallic nanowires on semiconductor surfaces are prototypical one-dimensional electronic systems, that exhibit exotic electronic properties, e.g. quantization of conductance and possible spin-charge separation, Peierls instability [7], charge-density waves (CDW), spin density wave [8], and Luttinger-liquid behavior [9]. These varieties of instabilities result in the phase transition in metallic nanowires systems at lower temperatures. However, at the higher temperature, the 1D properties of the systems are strongly modified or completely destroyed.

## 1.2 Experimental Techniques

A profound insight into the fascinating world of physics of low-dimensional material is realized with the investigation of their electronic structure. The immense interest in the knowledge of electronic structure emanates from the fact that it reveals bulk of information regarding the macroscopic properties, such as the electronic, magnetic, and chemical properties of a material.

The well-established technique of angle-resolved photoemission spectroscopy (ARPES) has been in use and contributed significantly in determining the electronic band structure of surfaces, interfaces, and bulk. It allows the mapping of the binding energy  $E$  of electrons as a function of their in-plane momentum  $k$  in the crystal. The limitation of ARPES associated with its capability to probe only the occupied electronic band structure is lifted with the advent of two-photon photoemission (2PPE) that permits the characterization of the unoccupied electronic band structure also. Furthermore, the implication of the two photons in a pump-probe scheme provides an additional advantage of studying the excited carriers energy and momentum relaxation dynamics in the time-domain.

Relaxation dynamics of the excited carriers are governed by various ele-

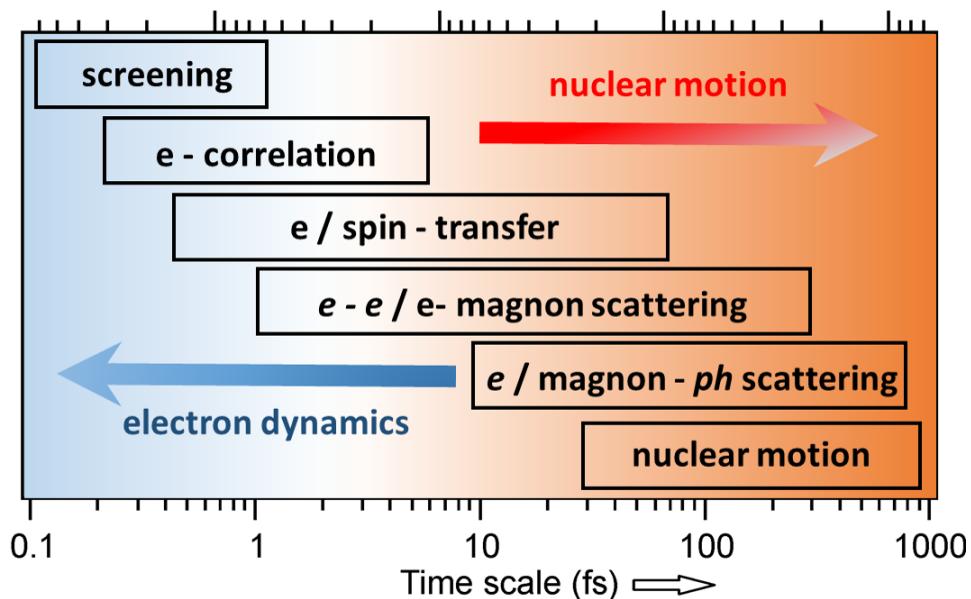


Figure 1.1: A scheme of various ultrafast elementary interaction processes occurring at solid surfaces and interfaces as a function of time. Our femtosecond laser based photoemission technique allows us to access the elementary excitations occurring at femtosecond or the larger time-scales. The figure is taken from [28].

mentary excitation processes. These processes occur at ultrafast time scales and are listed in Fig. 1.1, as a function of time, which is in the range of pico-, femto-, and attoseconds. In order to probe such processes, scientific tools with ultrahigh time-resolutions are required. The femtosecond laser based time-resolved photoemission spectroscopy with a time-resolution in the range of tens of femtoseconds enables to explore various listed interaction processes occurring at timescales of femtoseconds and longer. Out of these various processes, electron-electron ( $e-e$ ) and electron-phonon ( $e-ph$ ) interactions are particularly interesting owing to their major role in the device functionality. These scatterings are responsible for the heat build-up in the small-scale devices [29] and conversion efficiency limits in the photovoltaics [30]. Therefore, understanding of such phenomena at the surfaces and interfaces draws a huge interest from the technological prospects. On a more fundamental level, hot

electron relaxation which is governed by the  $e-e$  and  $e-ph$  scattering depend largely on the screening process and energy phase space availability. A deeper understanding of these phenomena of fundamental nature is attained with the investigation of the scattering processes, in particular in the low dimensional 2D and 1D systems for which they are still largely unexplored.

In order to investigate these intriguing physical phenomenon, that are of paramount nature both from fundamental and applied prospects, we employed time- and angle-resolved two-photoemission technique in various scientifically appealing low-dimensional systems discussed below.

## 1.3 Systems Under Investigation

### 1.3.1 Pb/Si(111)

A small  $4/3$ - monolayer (ML) coverage of Pb on Si (111) substrate (also known as the dense  $\alpha$ -phase) is an example of a quasi two-dimensional (2D) system. The 2D systems are known to exhibit exotic physical phenomena including the charge density wave formation [2], Mott phase [3], superconducting properties [4], and Rashba type spin-orbit splitting [5, 6, 17–27]. These exciting aspects of the 2D systems make them attractive from the prospect of fundamental and applied research.

This also lays a foundation for our motivation towards understanding the electronic band structure in the  $4/3$ -ML Pb/Si(111). Pb adsorbates on Si(111) substrate exhibit various stable structural phases between a coverage of  $1/6$  to  $4/3$  ML [31], thus acting as a prototypical system to study the coverage dependent change in the electronic structure and other fields of interest. Various experimental and theoretical studies have been performed to understand the structure of these phases [16, 31–34]. For the  $4/3$ -ML coverage, theoretical [35] and photoemission studies [36] revealed about the Rashba type spin-orbit

splitting in the *occupied* electronic bands. However, in our knowledge, no experimental work has been done so far to explore the *unoccupied* electronic structure of this coverage.

Therefore, this study aims at understanding the *unoccupied* electronic band structure of the  $\alpha$ -phase Pb/Si(111) using femtosecond angle- and time-resolved two-photon photoemission (tr2PPE), in the vicinity of the  $\Gamma$  ( $k_{\parallel}=0$ ). The non-linearity of the 2PPE process can result in a discrepancy in the determination of the origin of the photoemission signal. This particular issue is addressed and resolved in this study by analyzing the temporal evolution of population dynamics curve obtained using time-resolved 2PPE measurements. An insight into the symmetry character of electronic states is obtained by changing the polarization of incident light and exploiting the dipole selection rules [37–39]. This specific characteristic of photoemission technique is employed to study the unoccupied electronic structure of 4/3-ML Pb/Si(111) in detail.

A peculiar phenomenon of pronounced asymmetry in the photoemission signal across the  $\Gamma$  point, also known as linear dichroism in the angular distribution (LDAD), has been reported in various studies. Numerous effects, such as the off-normal light incidence of the  $p$  polarized light [40, 41], involvement of the bulk state [42–44], final states effect [45], and large spin-orbit coupling [3, 19, 40, 41, 46–65] are investigated to be the underlying reason of this asymmetry. The origin of pronounced asymmetry specific to our system and experimental geometry is investigated and a qualitative understanding of the underlying reasons is developed. These results are part of **chapter 4** of this thesis work.

#### 1.3.2 Pb/Si(557)

The reason of interest in quasi one-dimensional Pb/Si(557) system is two-fold. Si(557) being a vicinal surface of Si(111) contains steps or terraces which upon adsorption of 1.31 ML of Pb becomes equally stepped. Consequently, a structural geometry with an anisotropy perpendicular to the wire or step

direction is formed. Presence of steps or terraces is already known to have its influence on the scattering and relaxation dynamics in the image potential states of vicinal Cu(100) surfaces [66–71].

In addition to step-induced effects, the dimensionality of the electronic system can also greatly influence the relaxation dynamics of the excited carriers. Scattering dynamics mainly depend on two factors of the strength of the screened Coulomb interaction and energy and momentum phase space. Both of the factors act in an opposite manner upon the change of dimensionality of a system. The Pb/Si(557) has been shown to exhibit one-dimensional electrical conductivity below a phase transition temperature of  $T = 78$  K [72, 73].

In this study, we investigated the unoccupied electronic band structure of Pb/Si(557) using 2PPE. In addition, tr2PPE is employed for obtaining the momentum-integrated lifetime of the excited carriers in the unoccupied electronic states. The obtained lifetimes are compared with the lifetime obtained for 2D epitaxially grown Pb thin films on Si(111) substrate [74]. Furthermore,  $k$ -resolved electron scattering dynamics are analyzed to understand the influence of steps on the scattering process. Phase transition induced changes on the momentum-averaged electron relaxation dynamics are studied using temperature dependent tr2PPE investigations. All of these results are discussed in **chapter 5** and a major part has been published in [75].

### 1.3.3 In/Si(111)

Metal to insulator phase transition of  $4\times 1$ -In/Si(111) system driven by a charge density wave formation was discovered almost two decades ago [76] and since then this system has become a subject of vast investigation. Following that discovery, considerable efforts have been made to understand the geometrical [77–79] and the electronic structure [80–84] of this system. These studies revealed that the metallic  $4\times 1$ -In/Si(111) structure undergoes a reversible structural phase transition to an insulating  $8\times 2$ -In/Si(111) structure, below

a temperature of  $T_c \approx 124$  K [80]. Investigation of the electronic structure of  $4 \times 1$ -In/Si(111) revealed the presence of three metallic bands (m1, m2, and m3 bands) of 1-D nature [76, 80–84]. Formation of  $8 \times 2$ -In/Si(111) phase comes along with a bandgap opening of  $\Delta E \approx 100 - 200$  meV [76, 85].

In **chapter 6** of this thesis work, photoemission studies of phase transition in the electronic structure achieved by thermal heating is presented. The effect of thermally driven phase transition on the occupied electronic structure from the Brillouin zone (BZ) center  $\Gamma$  to the BZ boundary  $k_F$  (along the wire direction) is investigated using angle-resolved photoemission (ARPES). Time-resolved ARPES study conducted at BZ center  $\Gamma$  and the BZ boundary  $k_F$  (along the chain direction) is also presented in this chapter. In order to drive the phase transition, a large number of electrons are excited from the valence band to above the Fermi level  $E_F$ , that brings the material in the non-equilibrium state. This can bring the instabilities which are inherent to the 1D systems. Time-resolved electron diffraction combined with the *ab initio* molecular dynamics simulations study on this system revealed that upon laser excitation, the phase transition occurs at a time-scale of 350 fs [86]. Our complementary trARPES study addressed this specific question, i.e. whether the electrons remain long enough in the excited state to derive this transition? These findings have been published in [86].

---

## Theoretical Background

### 2.1 Photoemission Spectroscopy

Photoemission spectroscopy has become a major scientific tool for investigation of the electronic band structure and has made significant contributions towards the advancement of solid state and surface physics since the early sixties. This experimental technique is based on the phenomenon of the photoelectric effect. The physics of photoelectric effects spans over more than a century. It started in 1887 when Heinrich Hertz detected electrons from a secondary arc as a result of irradiation with ultraviolet (UV) light [87]. This primitive observation developed into a mature subject with the advancement in the field of electromagnetic radiation. In the year 1905, Albert Einstein in his famous paper [88] described the concept of the photoelectric effect that won him the Nobel Prize later in 1921. This phenomenon explains that when the light of sufficient energy is shone onto a material, it absorbs the light and emits electrons as a result, that are termed photoelectrons. The maximum kinetic energy of the photoelectrons depends on the workfunction  $\phi$  of the material

## 2.1. PHOTOEMISSION SPECTROSCOPY

---

which is the measure of a potential barrier that prevents the valence electron from escaping the material. Maximum kinetic energy  $E_{max}$  of photoelectrons is related to the energy of the incident photons of light with the expression given below,

$$E_{max} = h\nu - \phi \quad (2.1)$$

where,  $\nu$  is the frequency of light.

Metals have workfunction in the range of 4 – 5 eV. Therefore, ultrashort laser pulses of  $\sim 6$  eV photon energies are sufficient to generate the photoelectrons. In a microscopic picture, photoemission process is actually a transition of an electron from an initial state  $\psi_i$  to a final state  $\psi_f$  of a system upon absorption of light. Measurement of the binding energy of photoelectron gives insight into the electronic band structure of the material under investigation.

### Universal Curve

Due to the finite escape depth of photoelectrons, the photoemission spectroscopy is considered as a surface sensitive technique. The universal curve which depicts the mean free path of photoelectrons is shown in Fig. 2.1 [89, 90]. As can be seen, the inelastic mean free path is independent of the (monoatomic-) materials and shows a minimum of only a few Å at 10-50 eV. Around this energy, the photoemission technique is extremely surface sensitive. At lower energies of 4.5 – 6 eV, it becomes bulk sensitive also, with an escape depth reaching  $> 30\text{Å}$ . The added advantage of working at the lower excitation energies is improved energy and the momentum resolution.

### Sudden Approximation

The removal of an electron as a result of a photon absorption from an initial state causes an unperturbed electron system with N electron to become a system with the final energy of N-1 electrons. In PES theory, an assumption termed as the *sudden approximation* is used in which photoemission process

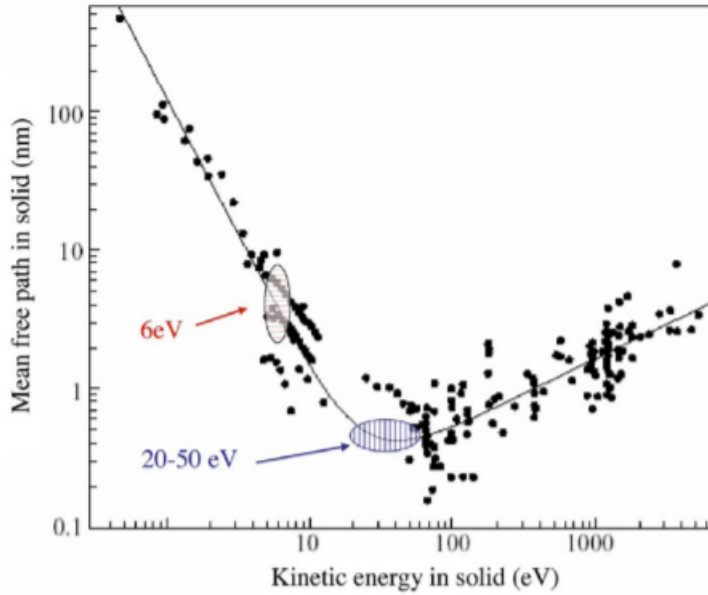


Figure 2.1: Universal Curve (taken from [89, 90]) shows the value of the mean free path of electrons in the solid as a function of the kinetic energy. Mean free path of the electrons in the solid is material independent and exhibits a minimum around  $E_{kin} = 30$  eV. For the energies used in our experiment  $\leq 6$  eV, mean free path is  $> 30\text{\AA}$ .

is assumed to occur at a much faster timescale compared to the time needed for the electronic system to relax the excited electronic state. In reality, the relaxation of electronic states of the  $N-1$  electron system can cause incoherent background and satellite peaks in the photoemission spectra. However, these effects are usually small and for this reason, the sudden approximation is widely used.

### Fermi's Golden Rule

Absorption of light in a material causes the transition of electrons from an initial state  $\psi_i$  to a final state  $\psi_f$ . In the independent electron picture, the transition probability is given by Fermi's golden rule

$$w_{if} = \frac{2\pi}{\hbar} |\langle \psi_f | H_{int} | \psi_i \rangle|^2 \delta(E_f - E_i - \hbar\omega) \quad (2.2)$$

## 2.1. PHOTOEMISSION SPECTROSCOPY

---

where,  $|\langle \psi_f | H_{int} | \psi_i \rangle| = M_{if}$  is the transition matrix element term in which  $H_{int}$  refers to the Hamiltonian term taking into account the perturbation from the incident light and  $\delta(E_f - E_i - \hbar\omega)$  accounts for the energy conservation during the photoemission process.

The total Hamiltonian of the electron inside solid in the presence of light field can be described as

$$H = \frac{1}{2m} \left( p + \frac{e}{c} A \right)^2 + V(r) \quad (2.3)$$

where,  $A$  is the vector potential of the electromagnetic field and  $p$  is the momentum operator of electrons. After a few simplification steps and ignoring the non-linear photoemission processes, the transition matrix element term can be expressed as

$$M_{if} = \langle \psi_f | H_{int} | \psi_i \rangle = -\frac{e}{m} \langle \psi_f | e^{iq \cdot r} A_o \cdot p | \psi_i \rangle \quad (2.4)$$

in the above equation, the term  $A_o \cdot e^{i(q \cdot r - \omega t)} = A$  is the vector potential.

### Dipole Approximation

Upon expansion of plane wave function one gains

$$e^{iq \cdot r} = 1 + iq \cdot r + \dots \approx 1 \quad (2.5)$$

The above approximation comes from the fact, that for the energies in UV (5 – 100 eV) range, the wavelength is very large and the expression  $q \cdot r = 2\pi \frac{a_0}{\lambda} \ll 1$  holds. This is called the dipole approximation. Finally, the matrix element in the dipole approximation can be written as

$$M_{if} = \langle \psi_f | H_{int} | \psi_f \rangle = -\frac{e}{m} \int \psi_f^*(A \cdot p) \psi_i dV \quad (2.6)$$

### Dipole Selection Rules

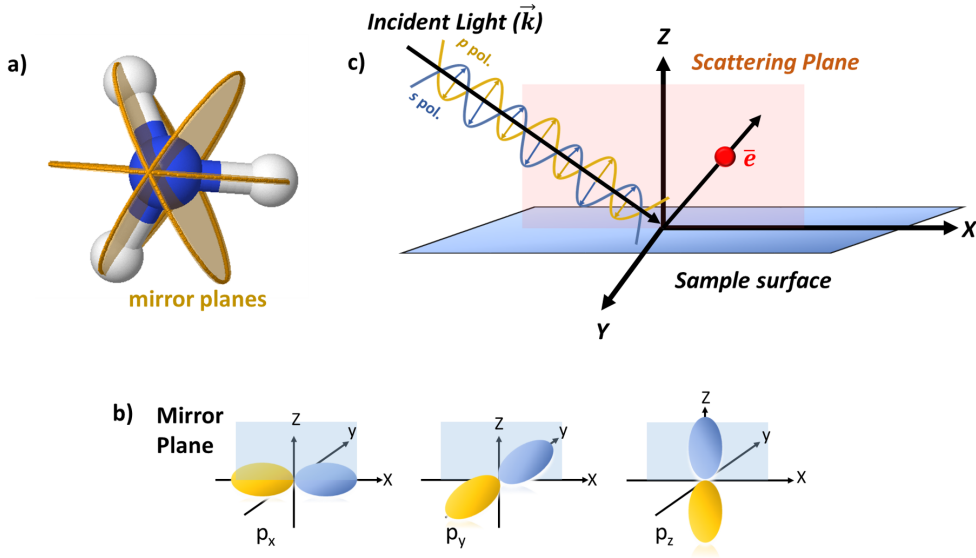


Figure 2.2: (a) Illustration of the mirror planes in an imaginary molecule with 3-fold rotational symmetry. (b) Sketch of the XZ mirror plane and  $p$  orbital components in which  $p_x$  and  $p_z$  have even but  $p_y$  has odd symmetry character. (c) Illustration of scattering plane, incident light, and outgoing photoelectron light in a photoemission experimental geometry.

Based on the transition matrix element in the dipole approximation, the dipole selection rules are formed. These dipole selection rules infer whether a transition from an initial electronic state  $\psi_i$  to a final electronic state  $\psi_f$  is allowed or forbidden based on the polarization of the incident light. These selection rules are only strictly valid when the scattering plane in the photoemission geometry overlaps with the mirror plane of the investigated material. The concept of scattering and mirror planes is illustrated in Fig. 2.2.

As can be seen in the top left panel, a molecule with a 3-fold rotation symmetry is divided by a plane in such a way that the two parts of the molecules are the mirror reflection of each other. There are three such planes for this molecule and are termed mirror planes. The molecule is said to possess *even* symmetry character across these mirror planes. With respect to the mirror planes, the orbitals or wavefunctions of electronic states in a crystal can have

either even or odd symmetry. This extended concept for the  $p$  orbitals is illustrated in Fig. 2.2b. As can be seen with respect to the XZ mirror plane,  $p_x$  and  $p_z$  orbital possess even symmetry but  $p_y$  orbital has an odd symmetry.

The scattering plane of a photoemission experimental geometry is illustrated in Fig. 2.2c. It is defined as a plane containing the momentum of photon and photoelectron that are co-planar with the surface normal. The incident light vector can have either  $p$  or  $s$  polarization that carries even and odd symmetry character, respectively, with respect to the scattering plane. In the theoretical model of photoemission, the final states  $\psi_f$  are considered to have plane wave character and thus even symmetry with respect to the scattering plane.

For an incoming  $p$  polarized (even symmetry) light, the transition matrix elements  $M_{if} = \langle \psi_f | A_o.p | \psi_i \rangle$  will be

$$\begin{aligned} \langle even | even | odd \rangle &= 0 \\ \langle even | even | even \rangle &= 1 \end{aligned} \tag{2.7}$$

while for incoming  $s$  polarized (odd symmetry) light, transitional matrix element will be

$$\begin{aligned} \langle even | odd | odd \rangle &= 1 \\ \langle even | odd | even \rangle &= 0 \end{aligned} \tag{2.8}$$

From the above equations, the symmetry character of initial electronic states can be determined. However, these dipole selection rules are strictly valid for the experimental geometry where the scattering and the mirror plane overlap because at a generic  $k$ -point away from mirror plane the wavefunctions will be a linear combination of even and odd character. These selection rules are also called non-relativistic selection rules as they take into account only the spatial symmetry character [91].

### 2.1.1 3-Step Model of Photoemission

The three-step model was the first phenomenological model proposed to treat the process of photoemission in which the whole process is described in three steps [92] that are following.

1. Absorption of the light and excitation of the electron from a bulk initial Bloch eigenstate to the final bulk Bloch eigenstate.
2. Travel of the excited electron to the surface.
3. Overcoming the surface potential barrier and escape into the vacuum.

This is schematically illustrated in Fig. 2.3b. The first step discusses the probability according to Fermi's golden rule derived in Eq. 2.6 that an electron initially residing in the initial state  $\psi_i$  will be excited to the final state  $\psi_f$  upon absorption of a photon of energy  $h\nu$ . It contains the information about the intrinsic electronic structure of the system.

The second step considers the probability that the flux of photoexcited electrons could reach the surface and be transmitted into the vacuum. As a result of photoemission process, electrons with the original energy and momentum information of their initial states  $\psi_i$  are emitted. Additionally, the secondary electrons that are inelastically scattered or lost their energy and/or momentum in the process also come out. The third step is the transmission probability that the excited electrons that reached to the surface will be transmitted to the vacuum and later are propagated to the detector. The parallel component of the momentum  $k_{\parallel}$  is conserved due to the small momentum of the photons, while the perpendicular momentum component  $k_{\perp}$  does not conserve because of the symmetry break caused by the termination of crystal.

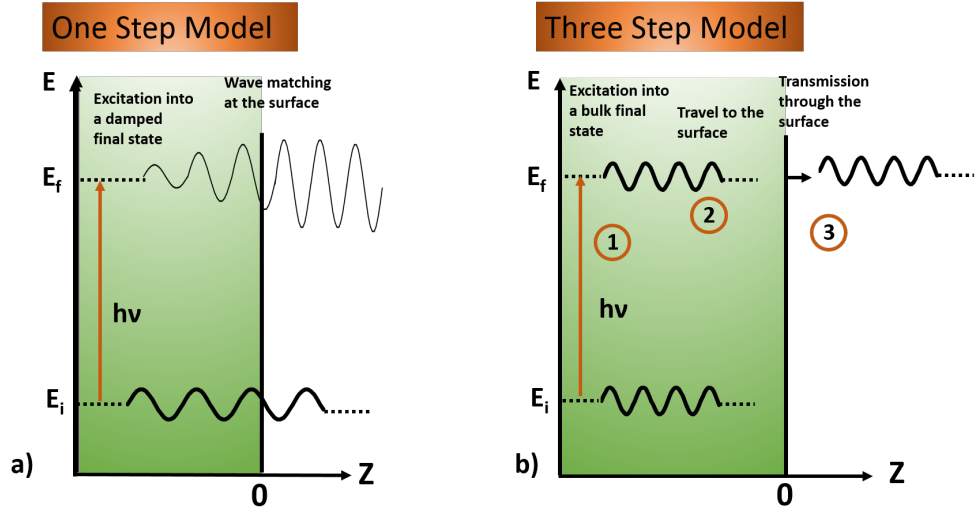


Figure 2.3: (a) Sketch of the 3-step model of photoemission in which the total photoemission process is divided into three steps of (1) the optical excitation of a wavepacket, (2) that propagates to the surface, and (3) the emission out of the crystal. (b) Sketch of the 1-step model of photoemission: a quantum mechanical description in which initial state is a Bloch state which is optically coupled to an inverse LEED final state with damped wavefunction inside the crystal but a plane wave character outside. The image is taken from [93].

### 2.1.2 1-Step Model of Photoemission

Another model that is often used to describe the photoemission process is called the 1-step model [94] and is schematically illustrated in Fig. 2.3a. This model is considered more accurate compared to the 3-step model because it takes into account the quantum mechanical description, which describes the PE process to be consist of one step rather than three. The model implies that the initial state is one of the eigenstate from many-body system of  $N$  electrons. For the final state, so-called inverse LEED wavefunction formalism is used. In LEED, the incoming monochromatic beam of electrons scatters from the ions at the surface and forms a diffraction pattern in return. So in inverse LEED formalism, monochromatized electrons are supposed to be generated

from the ions and propagate freely in the vacuum. Thus the final state can be thought of as a plane wave in the vacuum with a finite amplitude that decays exponentially inside the solid.

### 2.1.3 Angle-Resolved Photoemission Spectroscopy

Angle-resolved photoemission spectroscopy is a widely used technique to study the electronic band structure of solids. In the photoemission process, the energy and the parallel momentum of the photoelectron is conserved which allows the mapping of the band structure of solids. In Fig. 2.4, the transmission process of photoexcited electrons from the solid into the vacuum, is sketched. The conservation of energy implies

$$E_f - E_i = h\nu \quad (2.9)$$

where  $E_f$  and  $E_i$  are the energies of the final and initial state, respectively. The conserved momentum during a photoemission process can be written as,

$$\vec{k}_{\parallel} = \vec{K}_{\parallel} + \vec{k}_{ph} \quad (2.10)$$

where,  $\vec{k}_{\parallel}$  and  $\vec{K}_{\parallel}$  represent the parallel component of electron momentum in the vacuum and in the solid, respectively, and  $\vec{k}_{ph}$  is the momentum of incident photon.

Since the typical energies used in the photoemission spectroscopy are  $< 100$  eV, the photon momentum in the above equation can be neglected because it is much smaller compared to the typical dimension of a Brillouin zone given by  $\frac{2\pi}{a}$  (where  $a$  is the lattice constant). Eq. 2.10 then simply reduces to

$$\vec{k}_{\parallel} = \vec{K}_{\parallel} \quad (2.11)$$

i.e the parallel momentum component inside the crystal is equals to the

## 2.1. PHOTOEMISSION SPECTROSCOPY

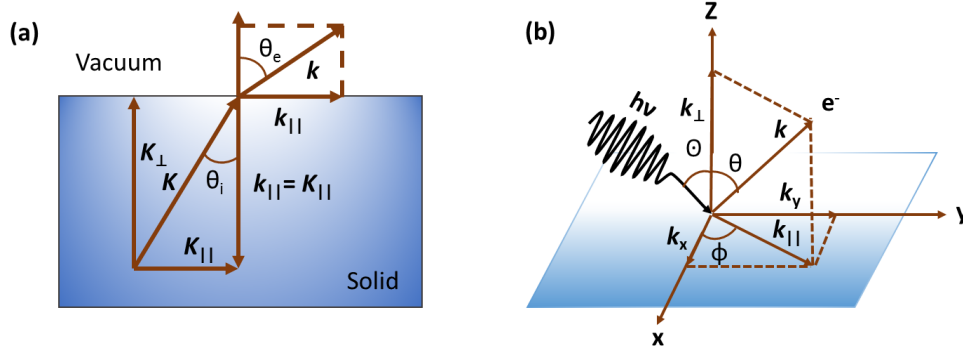


Figure 2.4: (a) Sketch of the photoemission process at the solid-vacuum interface, explaining the conservation of parallel component of momentum  $k_{\parallel} = K_{\parallel}$  due to in-plane translation symmetry. Symmetry break due to the crystal termination, causes an altered  $k_{\perp}$  component. (b) Sketch of the top of the surface depicting the experimental geometry and kinematic parameters of the photoelectrons.

parallel momentum component of electrons in the vacuum. When the photoelectron is detected by the analyzer, momentum in the vacuum is completely determined,

$$|\vec{k}| = \frac{1}{\hbar} \sqrt{2mE_{kin}} \quad (2.12)$$

Parallel and perpendicular components of momentum in the vacuum are determined by,

$$\vec{k}_{\parallel} = \vec{k}_x + \vec{k}_y \quad (2.13)$$

$$\vec{k}_{\perp} = \vec{k}_z \quad (2.14)$$

where  $x, y$ , and  $z$  component of momentum are determined by polar ( $\theta$ ) and azimuthal ( $\phi$ ) angles defined in the experimental geometry (Fig. 2.4)

$$\vec{k}_x = |\vec{k}| \sin \theta \cos \phi \quad (2.15)$$

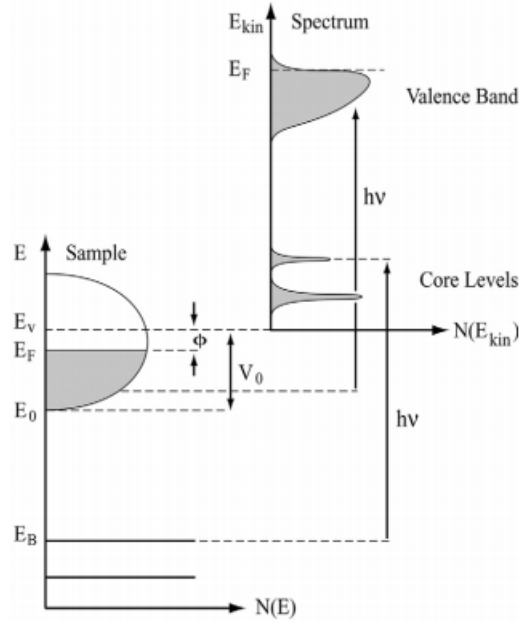


Figure 2.5: Sketch of the energetics of a photoemission process (taken from [93]). A photon of energy sufficiently more than the workfunction of the material takes out the electron outside of the material where its kinetic energy is measured (right). The kinetic energy is more conveniently represented in the binding energy picture as depicted on the left side.

$$\vec{k}_y = |\vec{k}| \sin \theta \sin \phi \quad (2.16)$$

$$\vec{k}_z = |\vec{k}| \cos \theta \quad (2.17)$$

As a final step, it is required to obtain the dispersion relation i.e the binding energy  $E_B$  as a function of crystal momentum  $K$  by using the measured  $E_{kin}$  and the momentum  $k$  of the photoelectrons in the vacuum. The energetics of a photoemission process is sketched in Fig. 2.5. With the help of the energy diagram and law of conservation of energy (eq. 2.9), binding energies can be determined using the equation,

$$E_{kin} = \hbar\omega - |E_B| - \phi \quad (2.18)$$

### 2.1.4 Polarization Dependent ARPES

With the conventional ARPES measurements, the electronic structure is determined. This technique becomes more effective when a different polarization of incident light is used. For example, the different polarization of incident light is used to characterize the symmetry of the initial electronic state  $\psi_i$  with respect to the scattering plane. The technique is termed as the polarization-dependent ARPES.

The dipole selection rules (eq. 2.7 and 2.8) are exploited to understand the symmetry of the initial electronic state  $\psi_i$  with respect to the scattering plane at the  $\Gamma$  point and also at a generic  $k$  point. However, correct symmetry determination requires an experimental geometry in which the scattering plane matches with the mirror plane of the system under investigation. At a generic  $k$  point away from the mirror plane, the symmetry mixing of the final state occurs implying the assumption of even final symmetry is no more valid leading to no strict application of dipole selection rules [93].

Linear polarization of the laser light can be tuned with the help of an  $\lambda/2$  plate and  $p$  (parallel to the optical table) or  $s$  polarization (perpendicular to the optical table) of light can be achieved. As it has been discussed in the context of the dipole selection rules, the final state is assumed to be free electron like and thus have an even symmetry. If the incident light is  $p$  polarized, the transitional matrix element  $M_{if} = \langle \psi_f | H_{int} | \psi_i \rangle$  outcome will be one only for those orbitals which have even symmetry, such as  $p_x$  and  $p_z$  orbitals. For the orbitals with odd symmetry with respect to the scattering plane, such as  $p_y$  orbital, transition matrix element will be zero for the  $p$  polarized laser light. The situation will be completely reversed for the  $s$  polarized light where transition matrix element will be one for the odd symmetry orbitals and zero for even symmetry orbitals.

In Fig. 2.6, polarization dependent ARPES measurements performed on Cu(111) surface with a laser beam of energy  $h\nu = 18$  eV and  $p$  and  $s$  polarization

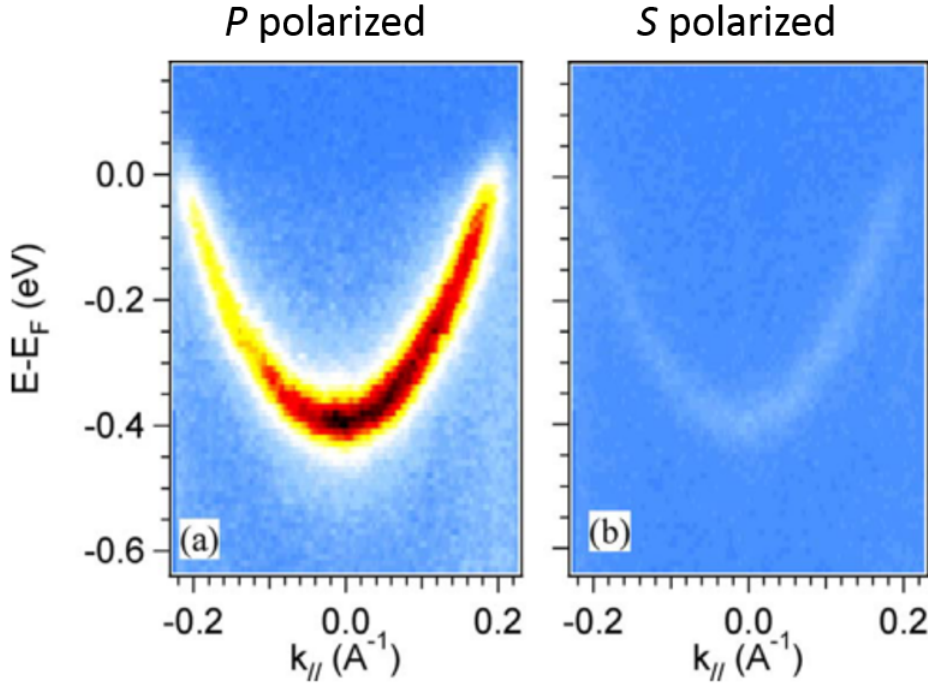


Figure 2.6: False color representation of linear photoemission measurement performed on Cu(111) surface with  $h\nu = 18$  eV (a)  $p$  polarized (b)  $s$  polarized light. Blue to black is the lowest to the highest intensity. A drastic change in the angular dependent PE intensity upon the change of light polarization is evident. The figure is taken from [45].

is shown [45]. As can be seen, with the  $p$  polarized light the surface state of Cu(111) shows a very strong photoemission intensity which almost vanishes for  $s$  polarized light. This response indicates that the Cu(111) surface states are of even symmetry with respect to the scattering plane.

Polarization dependent measurements can also be performed in two-photon photoemission (2PPE) spectroscopy by changing the polarization of two photons independently. It, therefore, allows to determine the symmetry character of the initial  $\psi_i$  and the states lying in between the Fermi and vacuum level called the intermediate states  $\psi_{im}$  [37–39].

### 2.1.5 Two-Photon Photoemission Spectroscopy

With the conventional ARPES, only the occupied electronic states can be studied. In order to investigate the unoccupied electronic states lying in the energetic region between Fermi level  $E_F$  and vacuum level  $E_{vac}$ , other techniques are used. Inverse photoemission spectroscopy was one earlier widely used technique to study the unoccupied electronic states of a material [95]. This technique is simply the time-reversal photoemission in which the impinging beam is of electrons with specifically chosen kinetic energy and angle and the output are the photons whose energies are measured. The disadvantage of this technique is its considerably lower energy resolution. The incident electron beam has an energy distribution of several hundred meV causing the resolution to significantly reduced compared to a typical photoemission technique [96].

Two-photon photoemission (2PPE) technique, combines the advantage of both direct photoemission and inverse photoemission processes and thus allows the investigation of occupied as well as the unoccupied electronic structure with higher energy resolution. The 2PPE process is schematically illustrated in Fig. 2.7.

As can be seen, two photons that together excite the electron above the vacuum level has their individual energies less than the workfunction  $\phi$  of the material. Mathematically, the following conditions should be fulfilled for the 2PPE spectroscopy,

$$h\nu_{pump} + h\nu_{probe} > \phi \quad (2.19)$$

and

$$h\nu_{pump} < \phi, h\nu_{probe} < \phi \quad (2.20)$$

where,  $h\nu_{pump}$  and  $h\nu_{probe}$  refer to the energies of two photons that are used in the electron excitation process. The details of the different electronic state

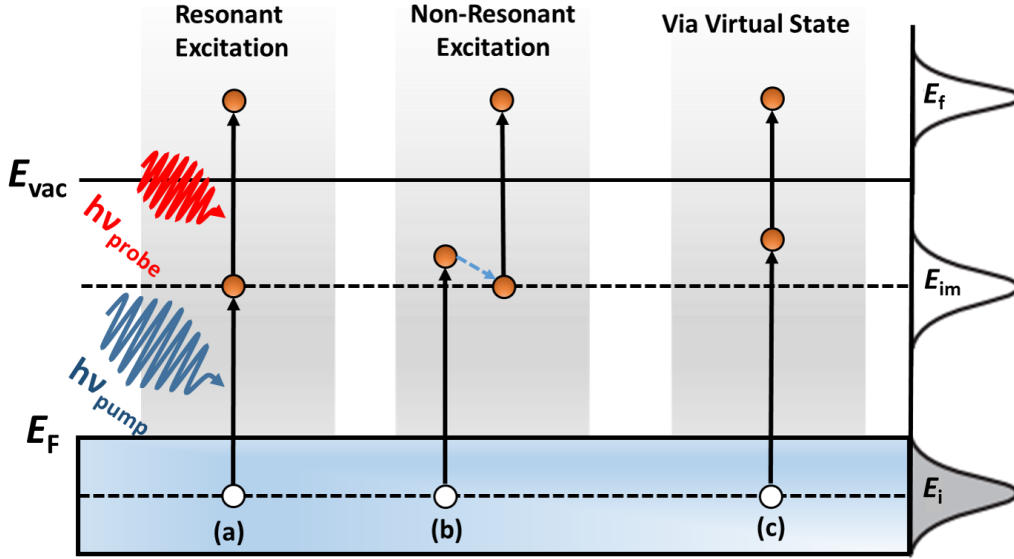


Figure 2.7: Sketch of different excitation mechanism possible in a 2PPE process that involve two photons of different energies  $h\nu_{pump}$  and  $h\nu_{probe}$  and three different electronic states  $E_i$ ,  $E_{im}$ , and  $E_f$ . (a) Resonant excitation (b) non-resonant excitation, and (c) excitation via virtual intermediate state.

involved in the 2PPE process, is given below.

**Initial State**  $E_i$  is the occupied electronic state that lies below the Fermi level  $E_F$  and also called the occupied state  $E_{occ}$ . In the first step of a 2PPE process, electrons are excited by the pump pulse  $h\nu_{pump}$  above the Fermi level  $E_F$ . Depending on the material under investigation, the continuum of electronic states could also be present instead of a well defined electronic state.

**Intermediate State**  $E_{im}$  is the unoccupied electronic state that energetically located in between the Fermi  $E_F$  and the vacuum  $E_{vac}$  levels. In the second step of 2PPE, the excited electrons localized in the unoccupied states are excited further above the vacuum level  $E_{vac}$  by probe pulse  $h\nu_{probe}$ .

**Final State**  $E_f$  lies above the vacuum level. Absorption of the probe

## 2.1. PHOTOEMISSION SPECTROSCOPY

---

photon  $h\nu_{probe}$  causes the excited electron to overcome the workfunction  $\phi$  of the material and reach to the final state  $E_f$ . Electrons that reach to the final state are propagated through the surface and analyzed by the spectrometer.

In order to perform 2PPE spectroscopy, both  $h\nu_{pump}$  and  $h\nu_{probe}$  laser pulses are made to overlap spatially and temporally to achieve a zero time delay ( $\Delta t = 0$ ) between the two pulses.

**Excitation mechanism** in a 2PPE process could proceed through various pathways and are illustrated in Fig. 2.7.

1. **Resonant Excitation:** If the energy difference between the initial state  $E_i$  and the intermediate state  $E_{im}$  matches with the pump photon energy  $h\nu_{pump}$ , then a resonant excitation is achieved. The energy peaks which are the result of a resonant process are stronger in a 2PPE spectrum.
2. **Non-resonant Excitation:** This is also called the indirect process in which an intermediate state  $E_{im}$  is populated by another intermediate electronic state via inelastic scattering. This kind of excitation is mostly observed for a continuum of the initial state and dispersing state. This actually allows the excitation in large momentum range and cause the inter- and intra-band scattering to occur.
3. **Excitation Via the Virtual Intermediate State:** In the absence of any intermediate state  $E_{im}$ , this excitation mechanism dominates. It can also be visualized as the simultaneous absorption of  $h\nu_{pump}$  and  $h\nu_{probe}$  photons [97].

The peaks present in a 2PPE spectrum could in principle originate from the initial, intermediate, or the final state and it is not possible to directly designate their origin. To do so, **photon energy dependent** experiments are performed in which incident  $h\nu_{pump}$  and  $h\nu_{probe}$  energies are tuned independently. A peak

in the 2PPE spectrum which is originated from an initial electronic state  $E_i$  via a virtual intermediate state will linearly change its kinetic energy with the energy sum of the pump and probe beams. Mathematically, their relationship will follow the expression:  $E_{peak} = h\nu_{pump} + h\nu_{probe} + E_i$ , where  $E_{peak}$  is the peak position in the kinetic energy scale. Peak in the 2PPE spectrum originated from the intermediate state will scale linearly with the energy of  $h\nu_{probe}$ . In this case, the mathematical relation will be  $E_{peak} = h\nu_{probe} + E_{im}$ . A peak originating from the final state will show no change upon energy tuning of either  $h\nu_{pump}$  or  $h\nu_{probe}$ .

**The intensity** of 2PPE signal  $S$  in a bichromatic 2PPE is directly proportional to the product of intensities of the pump and the probe beams, i.e.  $S \propto I(h\nu_{pump}) \times I(h\nu_{probe})$  [96].

### Binding Energy Determination

It has been discussed in the previous section in details, that a typical 2PPE spectrum may contain the peaks which are originated as a result of different excitation mechanisms. Therefore, assigning the correct binding energies to the observed peaks requires important considerations. A 2PPE spectrum obtained for 8 ML Pb film on Si(111) substrate is shown in Fig. 2.8 (taken from ref. [98]).

The spectrum shows two unoccupied states, and the low- and high-energy cutoffs at the vacuum and Fermi edge, respectively. The low-energy cutoff  $E_{slow}$  is termed secondary edge (position (a) on the spectrum). It belongs to the electrons which suffer energy losses due to inelastic scattering and barely made to the surface. The high-energy cutoff  $E_{fast}$  (d) represents the electron emitting from the density of states located near the Fermi level  $E_F$ . Transition of electrons, in this case takes place via virtual intermediate states. From these low and high energy cutoffs, the workfunction  $\phi$  of the material can be

## 2.1. PHOTOEMISSION SPECTROSCOPY

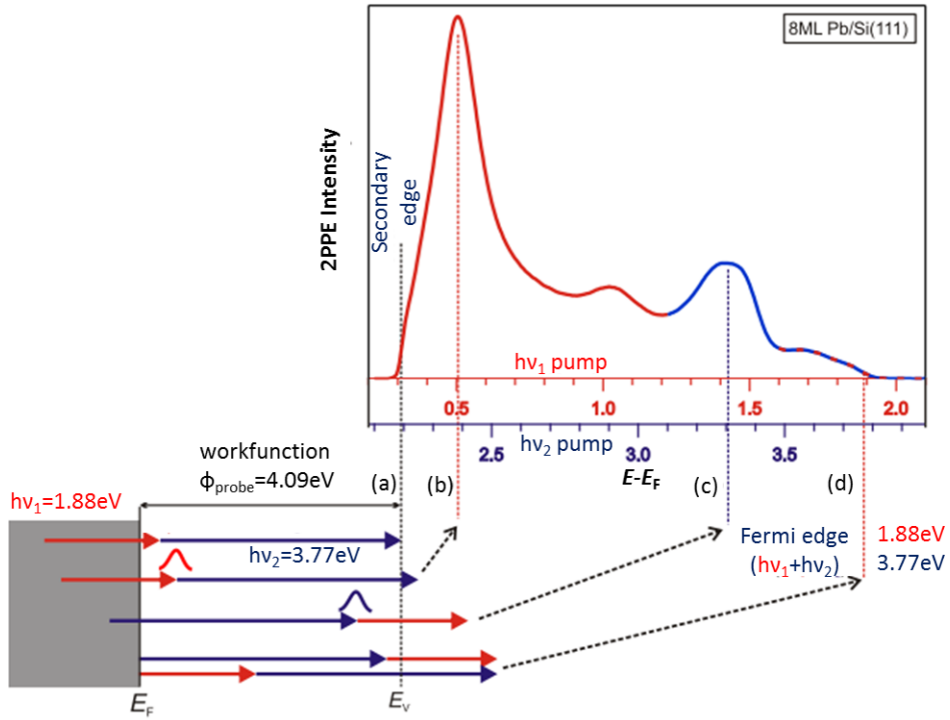


Figure 2.8: A sketch of the energy scales and the excitation mechanism together with the obtained 2PPE spectrum for 8 ML Pb/Si(111). The two horizontal scales describe binding energies that depend upon the sequence of the population to the intermediate state and photoemission. Important features of the 2PPE spectra are highlighted. (a) Low-energy cutoff at the so-called secondary edge. (b) and (c) Two different intermediate states that became accessible by pumping with the visible (VIS) and ultraviolet (UV) lights, respectively (d) High-energy cutoff at the Fermi-edge. The figure is taken from [98].

extracted.

$$\phi = h\nu_{\text{pump}} + h\nu_{\text{probe}} - [E_{\text{fast}} - E_{\text{slow}}] \quad (2.21)$$

The two horizontal scales describe binding energies that depend upon the sequence of pumping and probing of the laser pulses. This information is obtained by the photon energy dependent 2PPE or alternatively through time-resolved 2PPE measurements, that will be discussed in the next section. In the 2PPE spectrum, two intermediate energy peaks (b) and (c) are also

highlighted. The intermediate peak at low kinetic energy (b) is pumped by VIS ( $h\nu_1$ ) and probed by UV ( $h\nu_2$ ) laser pulses and thus have a binding energy  $E - E_F = 0.5$  eV given by the horizontal axis in red. In the inverted sequence, the intermediate state at the higher kinetic energy (c) is pumped and probed by UV and VIS pulses, respectively. In this sequence, the binding energy of the involved intermediate state is  $E - E_F = 3.5$  eV as given by the horizontal axis in blue. The appropriate binding energies for an intermediate state at a kinetic energy  $E_{peak}$  can be calculated using the following expressions:

$$E_{im} - E_F = h\nu_{pump} + E_{peak} - E_{fast} \quad (2.22)$$

$$E_{im} - E_{vac} = E_{peak} - E_{slow} - h\nu_{probe} \quad (2.23)$$

### 2.1.6 Time-Resolved 2PPE

The advantage of 2PPE over the conventional ARPES is not only limited to the probing of the unoccupied electronic states but also the information concerning the carrier scattering mechanism inside these states can be obtained. The experimental method to study carrier dynamics is the time-resolved two-photon photoemission (tr2PPE). In this method, a time delay  $\Delta t$  between the pump and the probe pulses is introduced by changing the optical path length. This is schematically sketched in Fig. 2.9.

As can be seen, there are two different pump and probe sequences that can generate the photoelectrons. In one case, the VIS pulse populates the intermediate state and the subsequently UV pulse probes the excited electrons. Only those intermediate states can be populated by the VIS pulses, which are energetically located near the Fermi level  $E_F$ . In the other scenario, the sequence of pump and probe pulses are inverted. The UV pulse excite electrons to the intermediate states, which are energetically located near the vacuum level

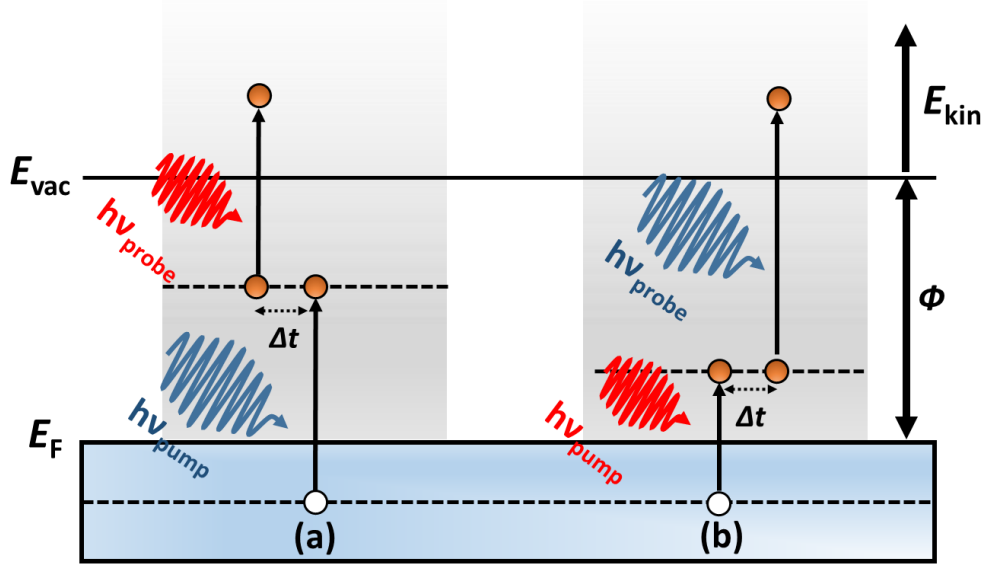


Figure 2.9: A different sequence of the pump and the probe pulses, allows to probe intermediate states lying close to the Fermi level  $E_F$  and the vacuum level  $E_{vac}$ . For positive time delay  $\Delta t$ , the VIS pulse precedes the UV pulse and the sequence is inverted for the negative time delay  $\Delta t$ .

$E_{vac}$  and they are subsequently probed by the VIS pulse. A typical tr2PPE measurement provides the so-called population dynamics curve. The temporal evolution of population dynamics curve helps to unambiguously assign the pump and probe sequence and consequently the assignment of the binding energies of the probed intermediate states.

### 2.1.7 Time- and Angle-Resolved Photoemission Spectroscopy

In a tr2PPE experiment, pump and probe pulses have their individual energies less than the workfunction  $\phi$  of the material but their combined energies are sufficient to photoexcite electrons into the vacuum. In addition, fluences of both pulses are kept low in order to suppress the signals originating from multiple UV and VIS photons.

Similar to tr2PPE, time- and angle-resolved photoemission (trARPES)

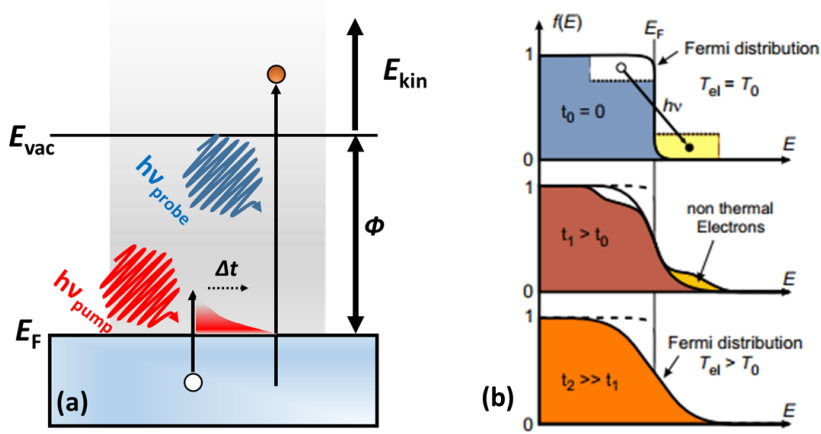


Figure 2.10: (a) A sketch of time-resolved photoemission process. A high fluence pump pulse generates a large number of hot carrier above the Fermi level  $E_F$ . The time-delayed UV pulse with  $h\nu_{probe} > \phi$  probes the transient change in the occupied band, as well as the short-lived population of excited carriers above  $E_F$ . (b) A sketch of the time-dependent distribution function and thermalization process [98]. A system with a population which can be described by the Fermi Dirac distribution function of temperature  $T_0$  initially undergoes a population redistribution at time zero. Inelastic scattering of the excited carriers reestablishes a Fermi-Dirac distribution at a higher temperature  $T_{el} > T_0$ .

technique also utilizes two photons, but the energy of the probe pulse is more than the workfunction of the material  $h\nu_{probe} > \phi$ . Furthermore, the pump pulse has much higher fluence, which drives the system out of the equilibrium by modifying the electron distribution close to the Fermi level  $E_F$ . Using this method, both the occupied and the unoccupied electronics states lying close to the Fermi level  $E_F$  can be probed. Typical fluences of the pump pulses are in the range of  $F = 40 \mu\text{J}/\text{cm}^2 - 2 \text{mJ}/\text{cm}^2$ , that are able to produce a strong perturbation in the material and create a significant number of excited carriers. The fluence of probe pulses is just sufficient to probe the transient evolution of excited carriers produced by the pump pulse. In Fig. 2.10, trARPES scheme is illustrated together with the electronic distribution close to the Fermi level  $E_F$

Before the arrival of the pump pulse, the electronic population can be

described by the Fermi Dirac distribution with the temperature of the macroscopic sample system  $T_0$  equals to the temperature of electron  $T_{el}$ . Strong pump induced changes drive the system to non-equilibrium condition at time zero. Due to redistribution of electrons, their population cannot be described with a Fermi-Dirac distribution anymore. The inelastic electron-electron ( $e-e$ ) scattering causes again a redistribution of this non-thermal population within 10 – 100 fs [99–101] and the system can again be described by the Fermi-Dirac distribution with a higher electronic temperature  $T_{el} > T_0$ . The whole process is termed as thermalization. The equilibrium between the electronic and the phononic system takes place at the timescale of  $> 1$  ps due to electron-phonon ( $e-ph$ ) scattering. Equilibrium time depends strongly upon the excited carrier density and the  $e-ph$  coupling strength. The strong change in the carrier density near the Fermi level creates a drastic impact on the occupied energy levels in a trARPES experiment. Reduction of electron density changes the Coulomb's interaction and the associated screening [98, 102].

## 2.2 Electron Dynamics at Surfaces

As soon as an electron excited from an initial state to an intermediate state during a 2PPE process, several physical processes begin to act on the excited electron and govern phenomenon of so-called electron dynamics. Consequently, the excited electron decays into a lower state by losing its energy and momentum with a certain decay rate  $\Gamma$ . The main processes that contribute to the decay rate are (i) electron-electron ( $e-e$ ) scattering  $\Gamma_{e-e}$  (ii) electron-phonon ( $e-ph$ ) scattering  $\Gamma_{e-ph}$ , and (iii) electron-defect scattering  $\Gamma_{e-def}$  [103, 104]. In the following sections, we will briefly discuss the above scattering processes.

### (i) Electron-Electron Scattering

Electron-electron scattering is the main process that governs the loss of

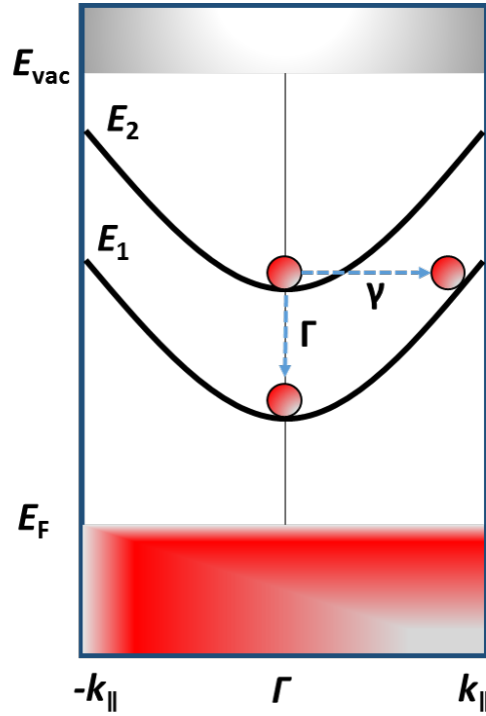


Figure 2.11: Schematic of the energy diagram showing two intermediate states  $E_1$  and  $E_2$  with parabolic dispersion and the different scattering processes occurring within. The excited electron (red circle) suffers an energy loss during inelastic scattering  $\Gamma$ . An elastic or quasi-elastic scattering event  $\gamma$  bring no or very small energy change but a large change of momentum.

energy and the momentum of the excited electrons. During this scattering process, the excited electrons decay into the bulk or the surface state which is at lower energy, on a short timescale. For the excited electron with larger binding energies  $E - E_F \gg k_B T$ , this scattering process dominates. The e-e scattering can be subdivided into two more categories, namely (i) elastic scattering ( $\gamma$ ) and (ii) inelastic scattering ( $\Gamma$ ). They are schematically illustrated in Fig. 2.11.

### Elastic Scattering $\gamma$

This scattering is also called *quasi-elastic* and represents a case when the energy loss as a result of scattering is either null or small compared to the experimental

resolution. However, it can cause considerable momentum change that can lead to the decay in the other states or even in the substrate. In Fig. 2.11, the elastic scattering event  $\gamma$  is indicated by a dashed arrow which shows that the excited electron after scattering ends up from the unoccupied level  $E_2$  into the level  $E_1$ . From the energy  $E$  and momentum  $k$  axes, it can be followed that scattering causes a negligible energy but a large momentum change.

### Inelastic Scattering $\Gamma_{e-e}$

These type of scattering events lead to a large energy loss (or gain). The dynamics of electrons investigated in this study e.g. for Pb/Si (557) nanowires arrays, was for the excited electrons with binding energies  $E - E_F < 3.3$  eV which is way larger than  $k_B T$  (temperature  $T = 100$  K corresponds to  $k_B T = 9$  meV). Therefore, inelastic  $e - e$  scattering will be the dominant scattering process in this system.

The inelastic scattering between the electrons is described under the framework of Fermi liquid theory, a model that explains the behavior of interacting Fermions in metals at low temperature [105, 106]. From this theory, the decay rate due to the e-e scattering  $\Gamma_{e-e}$  is proportional to the transition probability  $w$  together with conservation factors of momentum, energy, spin, and particle number of the involved scattered particle [98]. The transition probability itself is directly proportional to the energy phase space  $\Omega$  and the square of the screened Coulomb's interaction  $W$ . Phase space  $\Omega$  is the total energy space available for an electron to scatter and increases with increasing the dimensionality of the electronic system. Likewise, the interaction strength  $W$  is also dimensionality dependent but expected to decrease with an increase in dimension. With reducing dimension, screening reduces and therefore, electrons interact more intensely with each other. Therefore, both of these effects will counteract each other.

Phase space in 3D electronic system is a sphere in which electrons are filled

to  $k_F$ . The scattering rate  $\Gamma_{e-e}$  in 3D scales with the square of the excess energy  $\xi$  and is given by [105],

$$\Gamma_{e-e} = \frac{1}{\tau_{e-e}} = an^{-5/6}(E - E_F)^2 \quad (2.24)$$

where,  $\tau_{e-e}$  is the *lifetime* of the excited electrons,  $a$  is a dimensionality dependent constant, and  $n$  is the electron density that influences both the phase space  $\Omega$  and the screening.

### (ii) Electron-Phonon Scattering

Since phonon energies at metal surfaces are small [93],  $e - ph$  scattering events are quasi-elastic. Amount of transferred energy is usually in the range of few meV but a large change of momentum can occur. The influence of phonons can be increased on the total scattering events by an increase of temperature.

### (iii) Electron Defect Scattering

It describes the case in which scattering occurs due to interaction with the imperfections in the crystal, such as adatoms and steps. This kind of scattering is also classified in the category of the quasi-elastic scattering because of the manifestation of small energy and large momentum change. A large part of this study is dedicated to the investigation of *stepped Si(557)* surface that has been used to grow Pb nanowires and therefore provides an interesting case to study the influence of steps on scattering processes.

## 2.2.1 Inter-band and Intra-band Scattering

Scattering processes are further classified into two types called (i) inter-band scattering and (ii) intra-band scattering. This classification is based on where the electron ends up as a result of going through any of the scattering events

described in the previous sections. Inter- and intra-band scattering types are schematically illustrated in Fig. 2.12. The figure illustrates an energy diagram with two unoccupied electronic states designated as  $E_1$  and  $E_2$ . The events marked 3 and 4, refer to the intra-band scattering, which is simply a redistribution of the electrons within the same band after the scattering event. In contrast, in the inter-band scattering events, electrons are depopulated from a band and scatter to any other electronic band (event 1 and 2) or into the bulk.

Clearly, both of these processes could take place through inelastic or quasi-elastic scattering events, although intra-band scattering is mostly quasi-elastic. In any band with an effective mass  $m^* > 0$ , such as  $E_1$  and  $E_2$  plotted in Fig. 2.12, the binding energy increases with the momentum. This leads to a condition where a larger phase space  $\Omega$  is available for the electron at the higher momenta. Therefore, in the intra-band scattering analysis, the scattering rate will rise with the increase of momentum.

### 2.2.2 Coherent Excitation

As described in the section 2.1.5, a 2PPE process can evolve through several excitation mechanism and coherent excitation are one among them. For this type of excitation in the 2PPE experiments, the rate of excitation no longer obeys the Fermi's golden rule and cannot be described by the simple rate equation, [107] which is given by

$$\frac{dN_{\bar{k}}}{dt} = A \cdot \exp \left\{ - \left( \frac{t}{\sigma} \right)^2 \right\} - \frac{\Gamma_{\bar{k}}}{\hbar} N_{\bar{k}} \quad (2.25)$$

where,  $N_{\bar{k}}$  denotes the transient population of the bands. The first term on the right-hand side accounts for the population build-up due to the pump laser pulse and the finite temporal resolution of the experiment, estimated by a Gaussian of width  $\sigma$ . The second term describes the relaxation with a

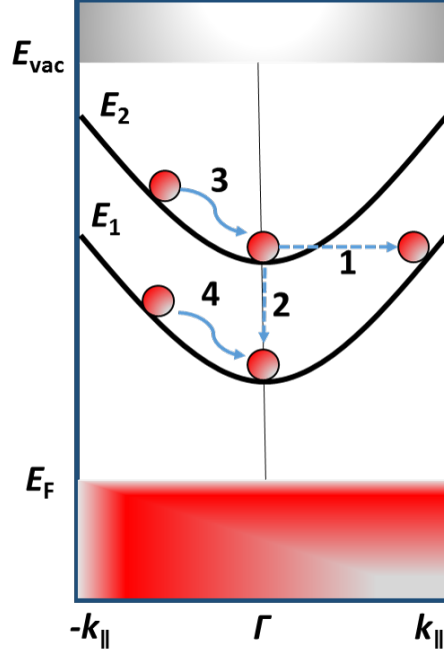


Figure 2.12: Schematic of the energy diagram showing two intermediate states  $E_1$  and  $E_2$  with parabolic dispersion and different scattering processes occurring within. Relaxation of the excited electron (red circle) could be inter-band (events 1 and 2) in which scattered electron ends up on different band or intra-band (events 3 and 4) in which scattered electron remains in the same band.

transition rate  $\Gamma_{\vec{k}}$ .

In order to describe the dynamics of the near-resonant excitation conditions, Liouville-von Neumann (LVN) equation is used. In the limiting case of resonant excitation ( $\Delta E(k_y)=0$ ) and laser pulse long compare to the dephasing time, the population inversion  $\Delta N = N_A - N_i$  between the initial state  $N_i$  and the intermediate state  $N_A$ , LVN equation is given by [97],

$$\frac{d(\Delta N)}{dt} = [4T_2^{iA} |\mu_{iA}|^2 E(t)^2 + \frac{1}{T_1}] \Delta N + \frac{1}{T_1} \quad (2.26)$$

where,  $\mu_{iA}$  is the transitional matrix element for the transition  $|i\rangle \rightarrow |A\rangle$  and  $E(t)$  denotes the transient electric field of populating laser pulse.

It should be noted from the above equation, that along with the lifetime  $T_1$  of the involved state (inelastic scattering rate), the pure dephasing time

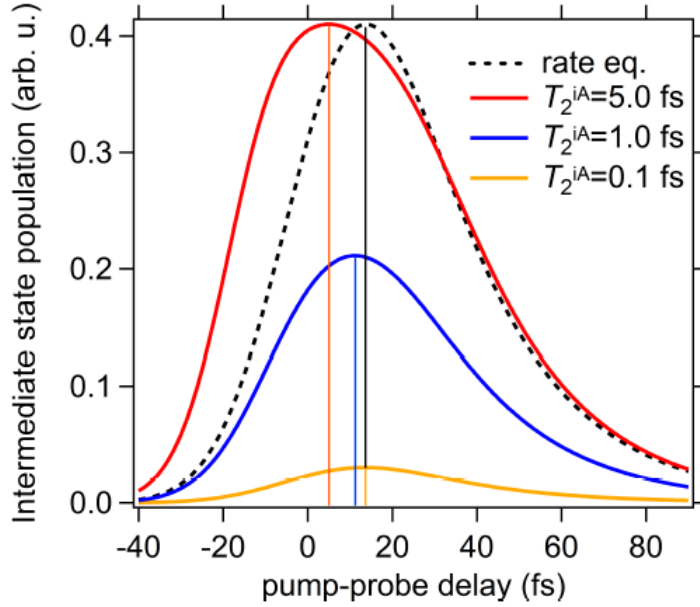


Figure 2.13: Numerical solutions of the LVN equations for different dephasing times  $T_2^{iA}$  using the parameters from the experiment ( $XC = 70$  fs,  $T_1 = 24$  fs) and resonant excitation conditions ( $\Delta E(k_y)=0$ ). The solution of the rate equation approach (Equation 2.25) is also shown and was scaled to the result for  $T_2^{iA} = 5$  fs for direct comparison. Both, the time of maximum population (indicated by the vertical lines) as well as the absolute maximum of intermediate state population change with dephasing time  $T_2^{iA}$ . In the limiting case of rapid dephasing ( $T_2^{iA} \rightarrow 0$ ), the solution of the LVN equation converges towards the solution of the rate equation approach.

$T_2^{iA}$  (quasi-elastic scattering rate) plays an important role in determining the population built-up behavior. The dephasing times  $T_2^{iA}$ , refers to the scattering with phonons and defects such as *steps* which leads to a decay of the coherence between the involved states [108].

The numerical solutions of Equation 2.26 for different dephasing time  $T_2^{iA}$  are plotted in Fig. 2.13 for the  $XC = 70$  fs and  $T_1 = 24$  fs. The horizontal axis represents the time delay between the pump and the probe pulses and the vertical axis is the 2PPE intensity yield. For the same parameters, the solution of the simple rate equation from Equation 2.25 is also plotted together for the

sake of comparison (dotted line). It is evident that different dephasing times  $T_2^{iA}$  influence both, the maximum population of the intermediate state as well as the time of maximum population. In particular, 2PPE yield is reduced by an increase of dephasing rate. Also, a population maximum occurring before as compared to the rate equation approach can be observed. In conclusion, steps can play a major role in determining the 2PPE yield as well as the scattering rate in case of a coherent excitation 2PPE process.



---

## Experimental Methods

### 3.1 Laser Setup

A tunable femtosecond laser system is one of the main building blocks of the whole experimental setup. This laser system is commercially available (Coherent) and a basic scheme is sketched in Fig. 3.1. The laser system has been discussed in detail in the previous thesis works [98, 102, 109] and therefore, will be discussed here, very briefly. More detailed information is provided in the technical documents [110–113]. A brief description of the important parts of the laser system is given below.

#### Continuous Wave Laser

It is a solid state laser (Coherent *Verdi* V-18) [110] with an output power of 18 Watts which is used as a pumping source for the femtosecond oscillator (Coherent *Micra* 900-B) [113] and the regenerative amplifier (Coherent *RegA*) [111]. The 18 Watts output is split into 5 Watts and 13 Watts to drive the *Micra* oscillator and *RegA*, respectively.

### 3.1. LASER SETUP

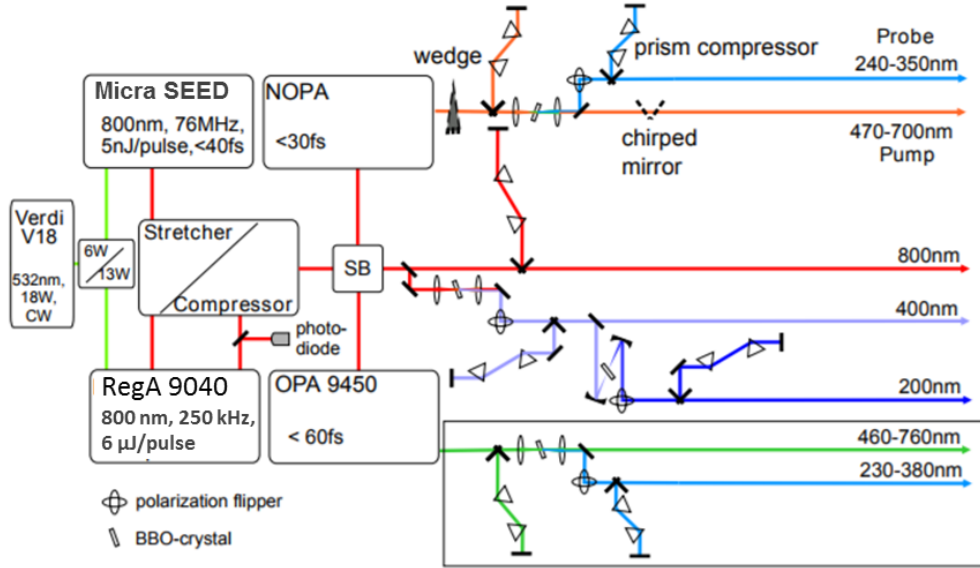


Figure 3.1: A schematic view of the femtosecond laser setup. The output of the solid state *Verdi* laser pumps the *Micra* oscillator and the *RegA*. Output pulses from *RegA* are recompressed and drive the optical parametric amplifier (OPA) and non-collinear OPA (NOPA) or used for the fourth harmonic generation. Thus, the laser system provides femtosecond laser pulses in a wide wavelength range. The figure is taken from [114].

#### Oscillator

Of utmost importance is the generation of ultrashort femtosecond laser pulses which takes place in the *Micra* oscillator (Micra-900B)[113] containing a titanium-doped sapphire (Ti:Sa) crystal as a lasing medium. According to the Heisenberg's uncertainty principle, generation of ultrashort laser pulses in the time domain requires a large bandwidth in the energy domain. This condition is fulfilled reasonably well in Ti:Sa, which owing to its broad emission spectrum of 670 – 1070 nm, allows the generation of femtosecond laser pulses at a central wavelength of  $\lambda \approx 800$  nm. Furthermore, Ti:Sa crystal has an absorption band in the wavelength range of 500 – 600 nm, which allows efficient pumping of the gain medium from the frequency doubled solid state laser (Nd:YAG, Nd:YVO<sub>2</sub>, 532 nm). Pumping produces various cavity modes and phase coherence among

these modes is required for the ultrashort pulse generation. The process of achieving the phase coherence is termed as mode locking. In the Ti:Sa based laser system, mode locking is achieved by the optical Kerr effect and termed passive mode locking [115].

The oscillator delivers femtosecond laser pulses centered at  $\lambda \approx 800$  nm with a pulse duration of  $\approx 40$  fs and pulse energies of  $\approx 3$  nJ. However, the pulse energies produced by the oscillator is not sufficient to drive the non-linear processes in the optical parametric amplifiers (OPAs) setup. In order to drive the OPAs, a minimum pulse energy of a few  $\mu\text{J}$  are required and this is achieved using the regenerative amplifier (*RegA*).

### **Stretcher**

Before feeding the seed pulse from the oscillator to the *RegA*, these pulses are stretched in time in order to avoid damage to the amplifier crystal that can be caused by the powerful laser pulses. Stretching is achieved with a grating which enables the temporal components of the beam to be separated in space.

### **Regenerative Amplifier**

It receives a major portion of  $\sim 13$  Watts from the solid state continuous wave (CW) (*Verdi V-18*) laser. It also utilizes the Ti:Sa crystal in which a large population inversion is build up due to the suppression of lasing by an opto-acoustic modulator (Q-switch). With the help of the population inversion in the crystal, a stretched seed pulse of the *Micra* oscillator is amplified in the cavity after making 20-30 round trips and is coupled out via another opto-acoustic modulator (cavity dumper). The output of the *RegA* is an amplified pulse of  $\approx 6$   $\mu\text{J}$  energy at a repetition rate of 250 kHz, pulse duration of 40 fs and  $p$  polarization (E-field vector parallel to the plane of the optical table).

### **OPA and NOPA**

### 3.1. LASER SETUP

---

The possibility of independent energy tunability in OPA and NOPA allows probing the unoccupied electronic structure existing in the different energetic range between the Fermi level  $E_F$  and the vacuum level  $E_{vac}$ . OPA (Coherent OPA-9450) [112] produces visible (VIS) pulses ranging between 460 – 760 nm with pulse duration of  $< 60$  fs and spectral bandwidth of 50 nm. NOPA on the other hand, provides a better time resolution of  $< 30$  fs but with a reduced energy tuning range of 480 – 650 nm and a spectral bandwidth of 80 nm [114]. NOPA is therefore preferable where the time resolution is of importance such as in the analysis of carrier dynamics during a time-resolved 2PPE measurements. However, for the static photoemission measurements, better energy resolution is required which is fulfilled by the use of OPA. For the major part of this study, the output of the OPA is used for the measurement purposes. Frequency doubling or the second harmonic generation (SHG) of the OPA/NOPA pulses is achieved in  $\beta$ -barium borate (BBO) crystals to produce pulses in the near UV range. VIS pulses from OPA/NOPA output, together with its frequency doubled UV pulses are overlapped spatially and temporally on the sample to perform 2PPE experiments.

#### **Frequency Quadrupling of Fundamental RegA Output**

Linear photoemission and trARPES measurements require photon energies higher than the workfunction  $\phi$  of the material. To achieve this, the RegA output pulses at  $\sim 820$  nm are frequency quadrupled by the subsequent doubling of the SHG with the use of two BBO crystals. The generated pulses of  $\hbar\omega \approx 6.2$  eV have the pulse duration of  $\sim 80$  fs. A fraction of the RegA fundamental ( $\hbar\omega \approx 1.55$  eV) together with  $\hbar\omega \approx 6.2$  eV is utilized in trARPES experiments as pump and probe source, respectively.

### 3.1.1 Pulse Incoupling

After the generation of the desired frequencies from the fundamental output of the *RegA*, the next step is incoupling of the generated pulses into the UHV chamber. For the 2PPE experiments fundamental output of OPA/NOPA and its second harmonics laser pulses and for trARPES fundamental of the *RegA* and its fourth harmonics must be spatially and temporally overlapped at the sample surface placed in front of acceptance cone of time-of-flight (TOF) or position-sensitive time-of-flight (pTOF) spectrometer. A schematic view of pulse incoupling paths with necessary components is sketched in Fig. 3.2. Both incoming beams are independently focused on the sample by using dedicated lenses ( $f = 500$  mm) mounted on a detachable breadboard closed to the incoupling window of the UHV chamber. Use of separate lenses for the two beams allows the independent control of their focal diameter on the sample. A CCD camera enables to focus the position of the VIS beam within the acceptance cone of the spectrometer, which usually serves as a *reference* beam. The count rate of the photoelectrons further helps to optimize the position of the VIS beam correctly on the sample. Visualization of the UV beam is only possible on a white paper card which is enhanced by the use of optical brightener on the paper.

Time-resolved measurements are conducted by introducing a time-delay between the pump and the probe laser beams which is achieved by a delay stage in the path of the VIS beam. The computer controlled delay stage (Physik Instrumente) provides a precision and repeatability of  $< 0.5$  fs between the two pulses. The polarization of both beams can be controlled independently by placing  $\lambda/2$  wave plates in their respective beam paths to carry out the polarization dependent measurements that are required in the investigation of the orbital character of the electronic states.

In order to achieve the **spatial overlap** between the two pulses, a flipping

### 3.1. LASER SETUP

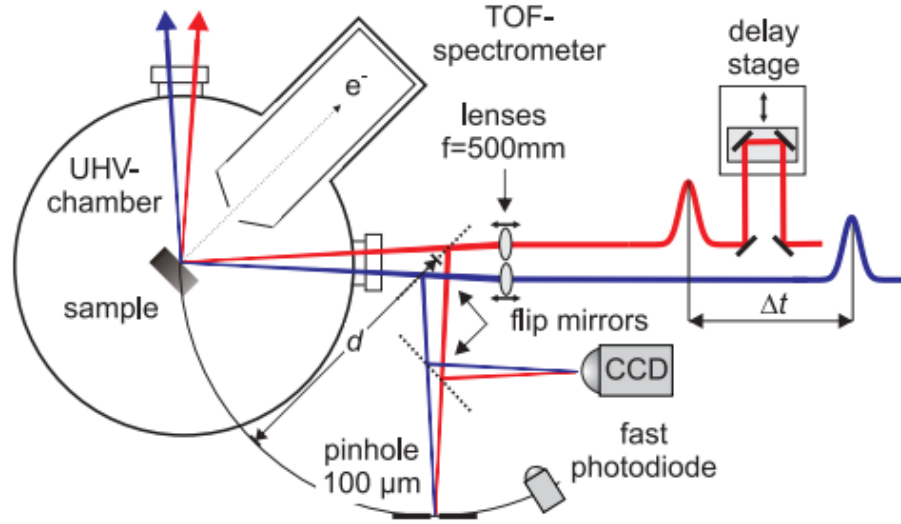


Figure 3.2: A sketch of incoupling of the pump and probe beams to the UHV chamber. Sample faces the opening of either time-of-flight (TOF) or the position-sensitive time-of-flight (pTOF) spectrometer. Incoming beams are independently focused using two different lenses on to the sample where the spatial and temporal overlap is required. Spatial overlap is achieved using a pinhole. With the help of a flipping mirror and a UV sensitive CCD camera, beam profiles of VIS and UV are obtained. A coarse and fine temporal overlap is established using a fast photodiode and scanning of the delay stage, respectively. The image is taken from [98].

mirror placed close to the beam entrance window of the UHV chamber is utilized. Outside the chamber, a  $100 \mu\text{m}$  pinhole is mounted in such a way that the distance between the flipping mirror and the sample is equal to the distance between the flipping mirror and the pinhole. Presence of both beams at the pinhole corroborates their spatial overlap at the sample surface.

Beam profile of both beams is obtained by addition of another flipping mirror mounted before the pinhole to guide the beam to a CCD camera (The Imaging source). It is desirable in a 2PPE experiment to have equal VIS and UV beam sizes to ensure suppression of the uncorrelated background signal. For trARPES experiments, the probe beam is kept smaller compared to the

pump beam to ensure a homogeneously excited sample surface.

**Temporal overlap** of the two beams is ensured first within a time of 100 ps by the use of a fast photodiode and a broadband oscilloscope. Fine temporal overlap is achieved by scanning the delay stage while monitoring the correlated signal. In a 2PPE experiment, the correlated signal is easily detectable as it increases up to three orders of magnitude for a complete VIS-UV overlap. In the trARPES experiments, however, the correlated signal is very weak and therefore, its detection requires several scans. By fine tuning of the incoupling mirrors, spatial overlap can be maximized which gives an enhanced correlated signal output.

### 3.1.2 Pulse Characterization

The desired information of the various frequencies of the laser pulses generated as a result of non-linear processes are acquired using three main types of pulse characterization, namely (i) spectral profile, (ii) spatial beam profile, and (iii) temporal profile. OPA and NOPA are able to produce the laser pulses in a large VIS wavelength range (460 – 760 nm) that together with its second harmonic laser pulses are used in the bichromatic experiments. Characterization of such a large wavelength range is achieved by *Ocean Optics* (HR4000CG-UV-NIR) spectrometer. This spectrometer, with a measuring wavelength range of 200 – 1200 nm, is placed anywhere in the beam path to perform the spectral characterization. A typical measurement for OPA fundamental and its frequency doubled UV pulse obtained from this spectrometer is shown in Fig. 3.3. Obtained spectra were fitted with Gaussian functions and provide full width at half maximum (FWHM) values of 61.7 meV and 47.4 meV for the VIS and UV pulses, respectively. By assuming it to be a Fourier limited pulse and using the equation  $\Delta\omega\Delta t = 0.4413$  (Gaussian), an FWHM value of 29.6 fs and 38.4 fs in the time domain is found for VIS and UV pulses, respectively.

In the second part of the beam characterization, the beam profiles of the

### 3.1. LASER SETUP

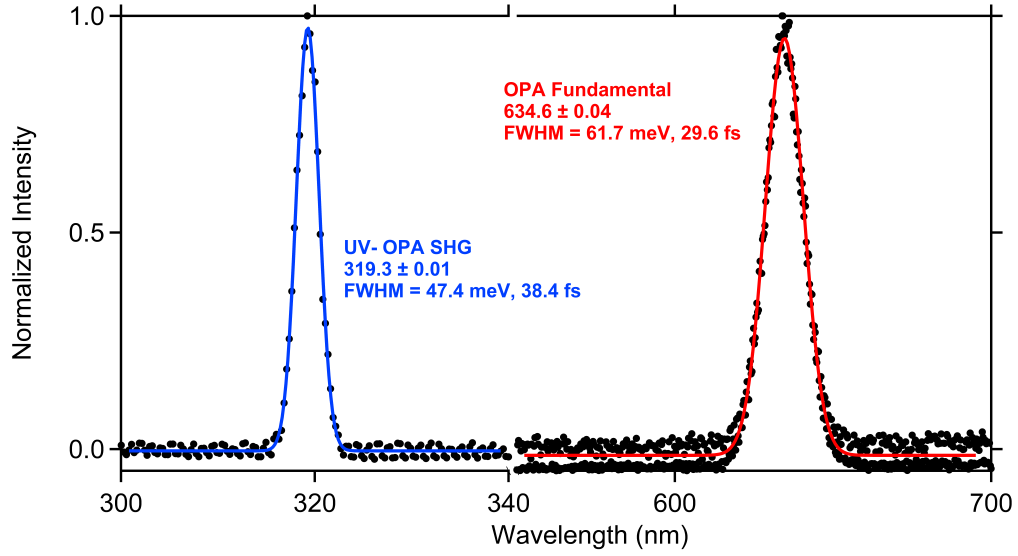


Figure 3.3: A typical spectra of the OPA fundamental output (VIS) and its second harmonic laser pulse (UV). FWHM is calculated for the energy and in the time domain using Fourier limited equation. The dotted points represent the recorded spectra and solid lines are the Gaussian fits.

laser pulses are obtained. This is achieved by using a CCD camera which is mounted near the entrance window of the chamber. The intensity of the beams is lowered by using neutral density filters in the beam paths to avoid potential power driven damages to the CCD camera. A typical beam profile of the second harmonic of the OPA fundamental beam is shown in Fig. 3.4. FWHM of the captured beam in horizontal (a) and vertical (b) directions are obtained by fitting with the Gaussian function. Power  $P$  of the beam is measured using a power meter by placing it at the closest possible distance from the chamber entrance window. Finally, from the beam profile, the laser fluence reaching to the sample surface can be calculated using the following equation.

$$F = \frac{TP \cos\alpha \cos\beta}{R \pi ab}$$

where,  $T = 95\%$  is the transmission from the  $CaF_2$  window of the UHV chamber,  $R = 250$  kHz is the repetition rate, and  $\alpha = 0^\circ$ ,  $\beta = 45^\circ$  are the polar

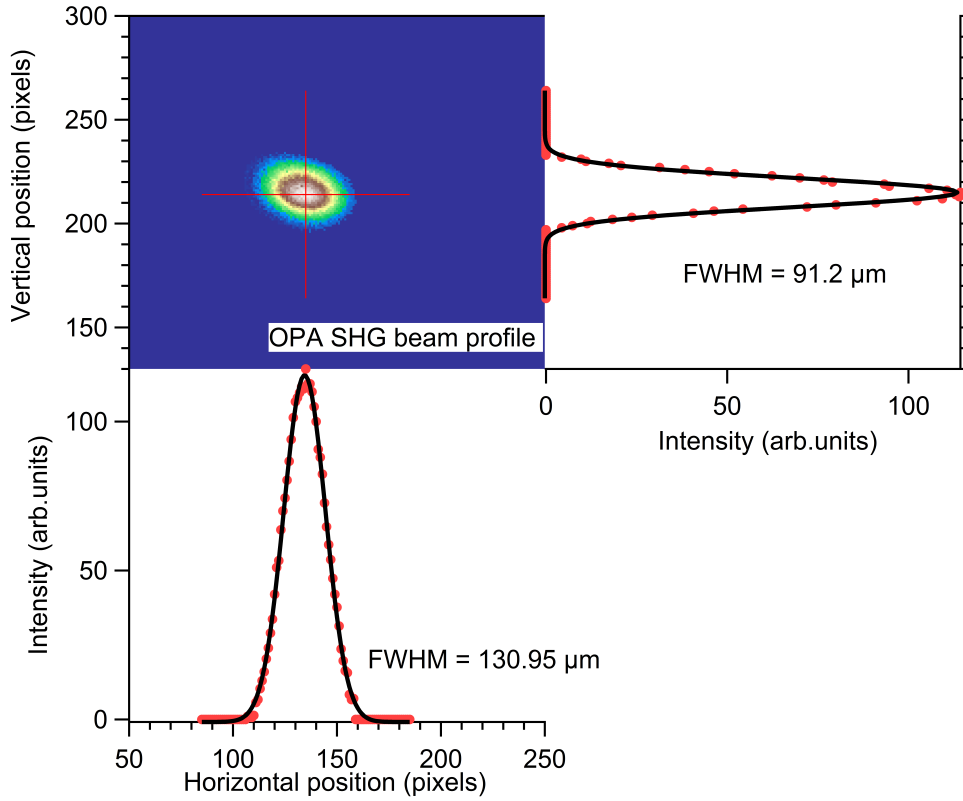


Figure 3.4: A typical beam profile of the second harmonic of the OPA VIS output. Profile recorded near the entrance window of the UHV chamber through a UV sensitized CCD camera. A Gaussian fit is used to determine the horizontal and the vertical beam diameter. A uniform beam size is desirable in the experiments.

and azimuthal angle of the incident light with respect to the surface normal, respectively. Typical fluences in 2PPE experiments are  $<2 \mu\text{J}/\text{cm}^2$  for UV and in the range of  $20\text{-}60 \mu\text{J}/\text{cm}^2$  for VIS pulse. In trARPES experiments, pumping fluence of up to  $3 \text{ mJ}/\text{cm}^2$  can be used.

In the third part of the pulse characterization, the **temporal profile** of the pump and probe pulses are measured. Determination of temporal profile is crucial for a correct measurement of the electrons relaxation dynamics in the unoccupied states. A direct and reliable way of obtaining the temporal resolution is from the tr2PPE intensity plots from which the cross-correlation

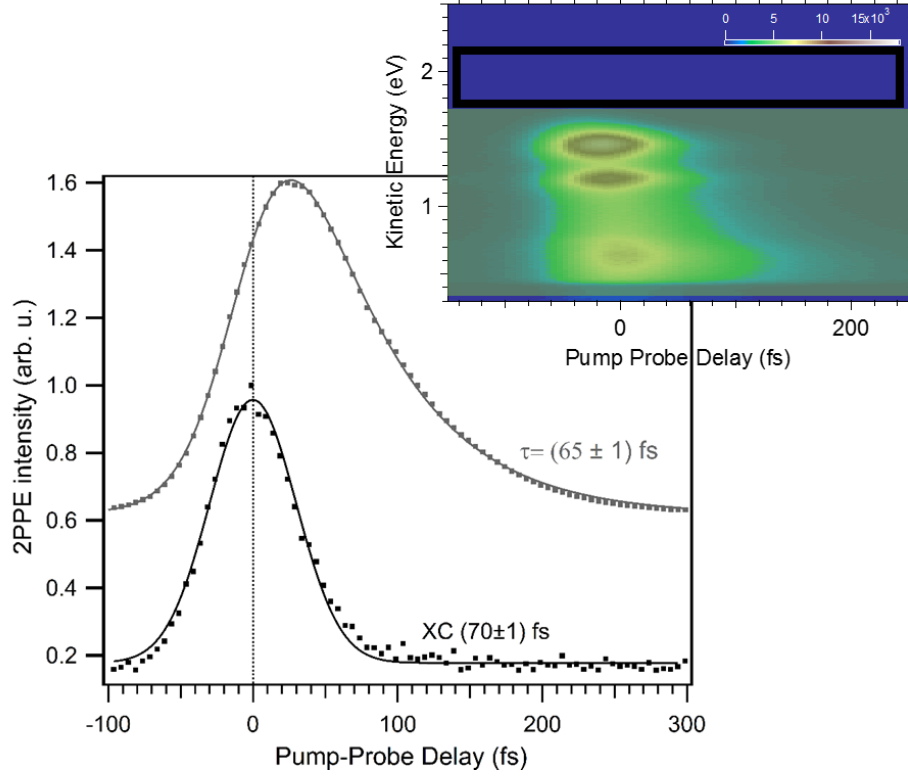


Figure 3.5: A cross-correlation curve (black boxes) along with a Gaussian function fit (black solid line) obtained by extracting the time evolution of the highest kinetic electron energy is shown by the black box in the tr2PPE intensity plot, given in the false color representation. A cross-correlation (XC) curve which is a result of the maximum overlap of pump and probe pulses give the temporal resolution of 70 fs as a result of the fitting of the Gaussian function. A population dynamics curve (grey boxes) extracted at a lower kinetic energy shows a delayed population maximum build-up. A fit function consists of a convolution of Gaussian and exponential decay function (grey solid line) gives a lifetime of 65 fs. This is the data obtained for Pb/Si(557) sample and will be discussed in detail in chapter-4.

(XC) of the pump and probe pulses can be extracted. Electrons from the highest occupied bands, photoemit via a virtual intermediate state if they are non-resonant with any unoccupied state. These photoelectrons in the 2PPE spectrum represents the convolution of pulse and probe beam temporal profile without a lifetime effect. A cross-correlation curve obtained from a tr2PPE measurement on the Pb/Si(557) system by integrating the energy window where the electrons have the maximum kinetic energy is shown in Fig. 3.5 . The absence of any relaxation dynamics can clearly be seen in the symmetry of the XC curve with a temporal width of 70(1) fs. On the other hand, the grey curve obtained at a lower kinetic energy shows the effect of carrier relaxation by shifting its peak maxima and an exponential decay at the trailing edge. For this population dynamics curve, a lifetime of 65(1) fs is obtained as a result of a fit function consisting of the convolution of Gaussian and exponential decay function. These results will be discussed in detail in chapter-4 of this thesis work.

### 3.1.3 Beam Path

Group velocity dispersion (GVD) is induced in the laser pulses as a result of traversing through various optical elements such as the beam splitters, lenses, and mirrors. GVD is required to be compressed at the optical table to carry out the experiments with time-bandwidth limited laser pulses. In the 2PPE experiments, fundamental output of the OPA (VIS) and its frequency doubled UV pulses are used. GVD in the VIS pulse is compensated using a prism compressor in the path before it enters the BBO crystal for UV pulse generation. As a result of frequency doubling in the BBO, the generated UV pulses become *s* polarized and they are made *p* polarized again with the help of a periscope. GVD in the UV beam is also compensated using another independent prism compressor. For trARPES experiment, two BBO crystals are subsequently placed to generate the fourth harmonic of the *RegA* fundamental. After the first

frequency doubling process, the fundamental is separated using the dichroic mirror and the polarization is flipped back to  $p$  with the use of a periscope. GVD in the second harmonic pulse is also reduced using prism compressor. The fourth harmonic is generated by passing the frequency doubled beam to the BBO crystal and its polarization is flipped back from  $s$  to  $p$ . The fundamental pulse from the *RegA* ( $\sim 820$  nm) along with the fourth harmonic ( $\sim 205$  nm) is guided to the ultra-high vacuum (UHV) chamber for measurements. The paths of the beams with the optical components, to be used for 2PPE and trARPES experiments are sketched in Fig. 3.1.

## 3.2 Ultra High Vacuum Chamber

A prerequisite for performing surface science experiments is the presence of an ultra-high vacuum which corresponds to a pressure of  $p < 10^{-10}$  mbar inside the chamber. Strict ultra-high vacuum (UHV) conditions are required for two reasons. First, during the preparation and characterization of the surfaces, the residual gas atom level in the chamber should be lowest in order to keep the prepared surface free of undesirable adsorbates. At a pressure  $p \approx 10^{-6}$  mbar, it takes a few seconds for the residual gas atoms to form 1 monolayer (ML) on the sample surface, whereas, under UHV conditions this time increases to  $\sim 10$  hours [116]. Secondly, the mean free path of photoelectrons has to be larger than the drift distance in the TOF spectrometer. The UHV chamber is placed on an air damped laser table to ensure a vibration free, stable position of the sample during preparation and measurements.

The UHV chamber is split into upper and lower parts where sample preparation and photoemission is performed, respectively. Both parts of the chamber are sketched in Fig. 3.6.

In the **upper chamber**, preparation and characterization of the samples is carried out and it operates at a UHV pressure  $p < 2 \times 10^{-10}$  mbar. The

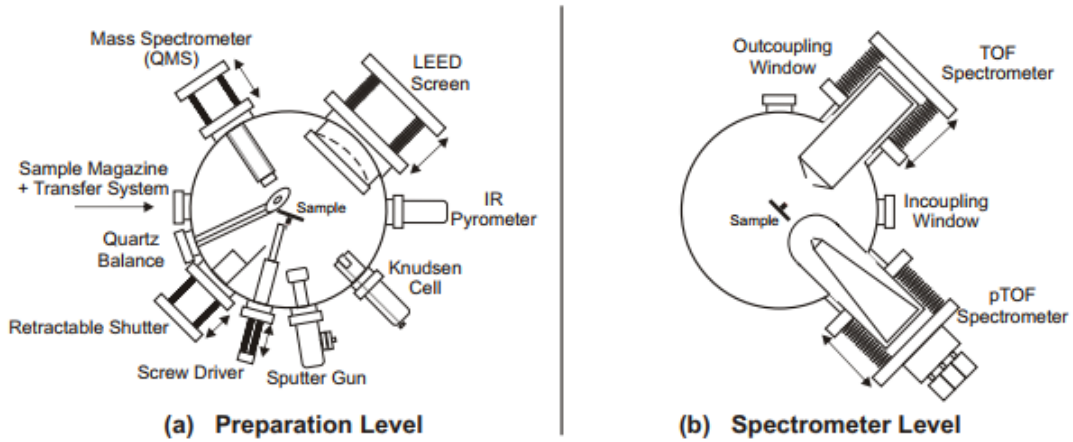


Figure 3.6: A sketch of the UHV chamber which is divided by a gate valve into the upper and the lower parts (a) The upper chamber is dedicated for sample preparation and characterization and equipped with the relevant tools. One side is connected to the magazine through a valve where samples are stored. (b) The lower chamber is dedicated for the photoemission investigation and equipped with TOF and pTOF spectrometers. The image is taken from [102].

vacuum is created by a turbo-molecular pump (*Pfeiffer*) connected to a pre-turbo pump and a four-stage membrane pump which create the pre-vacuum condition ( $p < 10^{-6}$  mbar) in the chamber. Various tools related to the surface preparation and characterization are mounted at the upper chamber. To grow Pb nanowires system on Si (557) and the two-dimensional structure of 4/3 ML Pb/Si (111), the chamber is equipped with a self-built water-cooled Knudsen cell. A homemade e-beam evaporator also attached to the chamber to prepare the Indium nanowires on Si (111). A Quartz microbalance (*Inficon*) is used to calibrate the evaporation rate and the surface quality is verified using low energy electron diffraction (LEED) optics (*Specs*). For the analysis of the residual gases, a quadrupole mass spectrometer (*MKS instruments*) is used.

The chamber is also equipped with other preparation tools such as a gas dosing system and a sputter gun. In addition, the upper chamber is connected to a sample storage (magazine) containing six slots to store the samples in vacuum. Transfer of the new samples to the magazine takes place through a

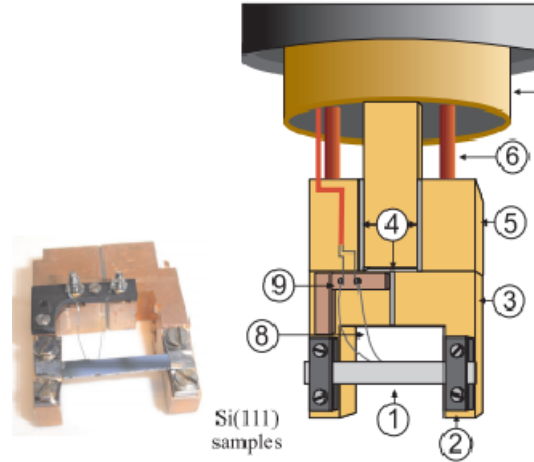


Figure 3.7: A photograph of exchangeable sample boat on the left and the drawing of the sample holder on the right. The photograph shows a rectangular shaped Si wafer of size  $26 \text{ mm} \times 4 \text{ mm}$  mounted with the help of tantalum sheets and titanium screws on the sample boat. They are schematically shown in (1) and (2). Other parts in the sample holder scheme include (3) transferable sample boat (4) sapphire plates (5) gold-plated Cu-blocks (fixed to the cryostat) (6) current leads (7) cryostat. The image is taken from [98].

transfer line. Presence of the valves between the transfer line and the magazine, and the magazine to the upper chamber ensure the sample transfer to the main chamber without breaking the UHV conditions.

**The lower chamber** is pumped down using a Titanium sublimation pump (*Riber*) and an ion getter pump (*Riber*). The chamber is equipped with time-of-flight (TOF) and position-sensitive time-of-flight (pTOF) spectrometers to perform the photoemission measurements. The working principle of both of the spectrometer will be discussed in detail in sections 3.2.1 and 3.2.2.

**The manipulator** is equipped with a 400 mm long Helium-flow cryostat (*CryoVac*), a heating coil, and a silicon diode for measurement of temperature which is controlled by a proportional-integral-differential (PID) controller (*Lakeshore 330*). The manipulator can be cooled using liquid-*He* or liquid-*N<sub>2</sub>* which allows sample cooling down to  $\sim 30 \text{ K}$  and  $\sim 85 \text{ K}$ , respectively. Vertical

movement of 400 mm and lateral movement of  $\pm 12$  mm for manipulator is made possible by electric stepper motors. An independent  $360^\circ$  rotation around the vertical axis is achieved by a differentially pumped feedthrough. These 4 degrees of movements allow the sample to move to different parts of the chambers for preparation, characterization, and measurements.

The **sample holder** is shown in Fig. 3.7 along with an exchangeable **sample boat** on which the rectangular shaped Si wafer is mounted. The sample holder is constructed using non-magnetic materials like Titanium (Ti), Tantalum (Ta), Aluminum (Al), Copper (Cu), and ceramics. Use of non-magnetic materials ensures a region around the sample which is free of magnetic fields that can severely distort the photoemission signals on the detector. Sample boat is made of two symmetrically shaped parts that are electrically insulated through 0.5 mm thick sapphire plate. Both parts are thermally connected to the cryostat. The Si wafer in a rectangular shape of size  $26 \text{ mm} \times 4 \text{ mm}$ , is mounted on the sample boat with the help of Ta sheet and Ti screws. During the preparation process, the Si wafers are heated using the direct current heating method.

### 3.2.1 Time of Flight Spectrometer

The lower chamber contains the TOF and the pTOF spectrometers which are the key elements of photoemission experimental setup. A very small part of the experimental work in this study was conducted using the TOF spectrometer, and therefore it will be discussed very briefly. However, a basic understanding of the working principle of this spectrometer is necessary and will be helpful for understanding the functioning of the pTOF spectrometer to be discussed in the next section.

A schematic of the TOF spectrometer is sketched in the Fig. 3.8 taken from [98]. The photoelectron emitted from the sample travels through a field-free Al drift tube with an opening aperture of 1.5 mm and length  $L = 300$  mm. Nearly

### 3.2. ULTRA HIGH VACUUM CHAMBER

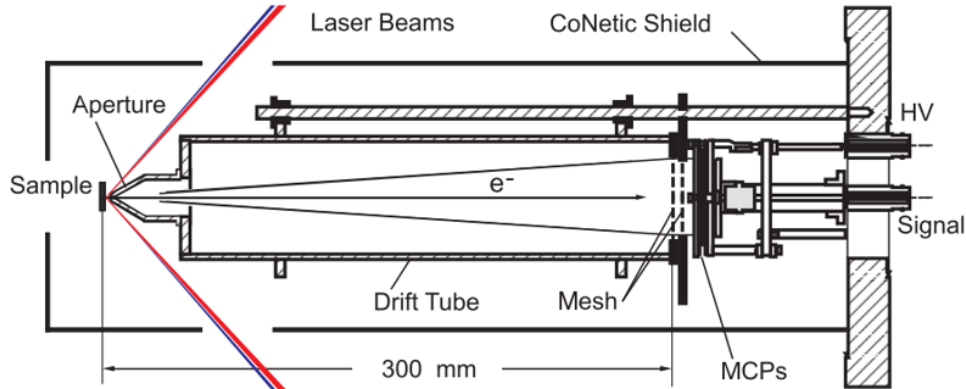


Figure 3.8: A schematic view of the TOF spectrometer indicating the main components. A tube of 300 mm length, which photoelectrons traverse to be detected by the MCPs. Signal generated as a result of electron impact on the MCPs is outcoupled and then amplified. The schematic is taken from [98].

at the end of the drift tube, two grids are placed in front of 40 mm diameter multi-channel plates (MCPs). Photoelectrons are accelerated by the first grid towards the second grid which provides the energy needed for the electrons to induce an avalanche in the channels of the MCPs which are biased at +2.3 kV. A hit of a single electron on the MCP results in the generation of an electron cloud containing  $10^6 - 10^7$  electrons. The signal resulting from the charge cloud is amplified in a broadband amplifier (*Ortec*) directly after the outcoupling.

Homogeneous workfunction throughout the spectrometer is ensured by coating it with graphite that gives the workfunction of  $\phi_{spec} \approx 4.3$  eV. Trajectories of electrons, especially those with lower kinetic energy are distorted if there is any surrounding magnetic fields. In order to eliminate such possibilities, the whole spectrometer is housed in a  $\mu$ -metal shield which ensures a field free region. The electrons have to overcome a potential energy barrier  $eU$  caused by the difference between the workfunction of the spectrometer  $\phi_{spec}$  and the sample  $\phi_{sample}$ , as well as a bias voltage  $e_o U_{bias}$  which is applied so that the electrons finds an unperturbed trajectory while traveling between the sample and the spectrometer.

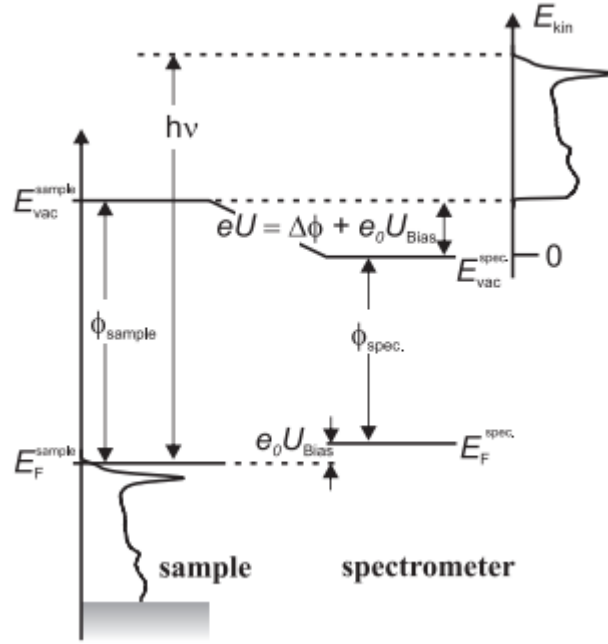


Figure 3.9: A schematic view of the potential gradient between the sample and the spectrometer. The spectrometer is permanently grounded, whereas a bias voltage  $U_{bias}$  can be applied to the sample which adjusts the difference of vacuum for angle-resolved measurements. Kinetic energies of photoelectrons are measured with respect to the vacuum level of the spectrometer, whereas the vacuum level of the sample defines the secondary edge of the spectrum. The schematic is taken from [98].

$$e_o U = \phi_{sample} - \phi_{spec} + e_o U_{bias} \quad (3.1)$$

The potential energy diagram of a TOF spectrometer is shown in Fig. 3.9. The TOF signal is calculated by guiding a very small portion of the incident laser beam to a photodiode which serves as a start signal. Stop pulses come from the MCP of the spectrometer. From the time of flight  $t$  of the photoelectrons the kinetic energy is calculated using the following relation

$$E_{kin} = \frac{1}{2} m_e v^2 = \frac{m_e L^2}{2t^2} \quad (3.2)$$

## 3.2. ULTRA HIGH VACUUM CHAMBER

---

where  $m_e$  is the mass of an electron. However, a wrong time of flight can be measured if the difference in the electrical and optical propagation  $t_o$  is not taken in to account. The  $t_o$  is measured by performing so-called bias series where  $t_o$  is adjusted as a free parameter in various spectra collected at different bias voltages. Time of flight is then modified and a new relation can be written by using eq. 3.1 and 3.2 as

$$E_{kin} = \frac{m_e}{2} \left( \frac{L}{t - t_o} \right)^2 - (\phi_{sample} - \phi_{spec}) - e_o U_{bias} \quad (3.3)$$

The energy and momentum resolution is dependent on the kinetic energy of photoelectrons and estimated to be  $\Delta E_{kin} \approx 20$  meV and  $\Delta k_{||} \approx 0.1 \text{ \AA}^{-1}$ , respectively at  $E_{kin} = 2$  eV [98, 102]. However, the effective energy resolution of the experiment requires the spectral width of the pump and probe pulses ( $< 50$  meV) to be taken into account. Overall energy resolution in the experiment is approximately 50 meV.

### 3.2.2 Position-Sensitive Time of Flight Spectrometer

In order to perform conventional ARPES measurements with the TOF spectrometer, the sample is rotated with respect to the spectrometer axis as the typical TOF measurements provide only one spectrum per emission angle or at one particular momentum of the electron. To overcome this limitation a position-sensitive time-of-flight (pTOF) spectrometer was built [117], which allows the measurement of the kinetic energy of electrons in two mutually perpendicular momentum directions  $k_x$  and  $k_y$  in a 'single shot'. A schematic sketch and photograph of pTOF geometry are shown in Fig. 3.10. As can be seen, pTOF geometry also utilizes a field-free drift tube with the length  $Z = 200$  mm and a large acceptance angle of  $\pm 11^\circ$  with a chevron-mounted MCP stack of 80 mm active diameter at the end of the tube. The drift tube is made of vacuum compatible aluminum to provide a magnetic field free drift region. Similar to

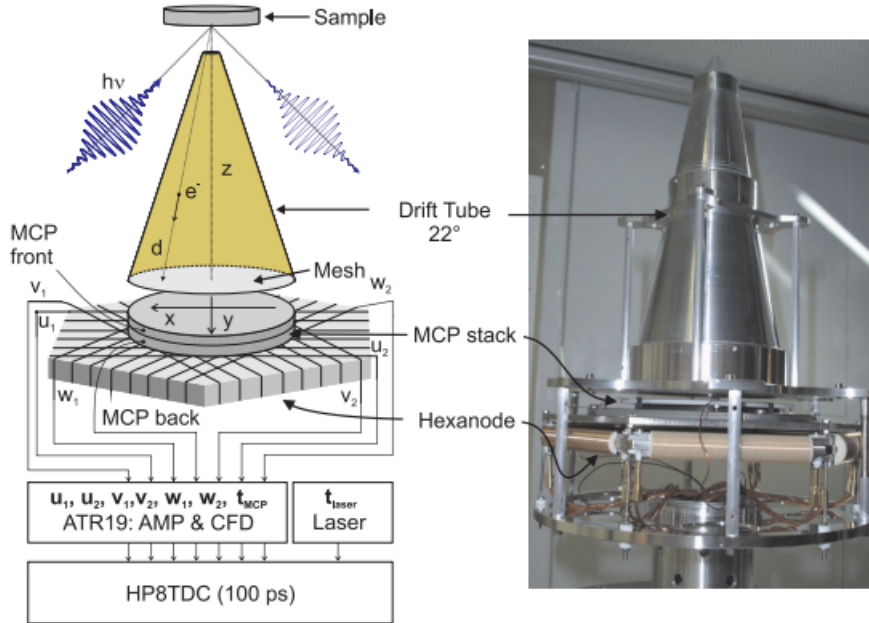


Figure 3.10: A schematic drawing (left) and a photograph (right) of the pTOF electron spectrometer. Photoelectrons traverse through the field-free drift tube and are detected by a two-dimensional position-sensitive detector based on a microchannel plate (MCP) stack and a delay line anode. A total of six signals from three wire layers along with  $t_{MCP}$  are amplified and digitized in constant-fraction-discriminator (CFD) and later with  $t_{laser}$  recorded by a time-to-digital-converter (TDC). The image is taken from [117].

TOF, the aperture and the inside of the drift tube is also coated with graphite to ensure a homogeneous work function of the pTOF. Most important part of the pTOF spectrometer is a 2D detector based on a commercially available delay-line readout concept (*RoentDeck* [118]). A voltage of +150 V is applied to the MCP front to attract the electrons traversing through the field free drift tube. Each electron hit on the MCP results in a charge cloud which is received by three meandering anode wires wrapped at  $60^\circ$  with respect to each other. The anode wires are biased with the highest potential of +2850 V, whereas back of the MCP with +2450 V for charge amplification process. Due to the highest potential, the emitted charges clouds are attracted towards the anode

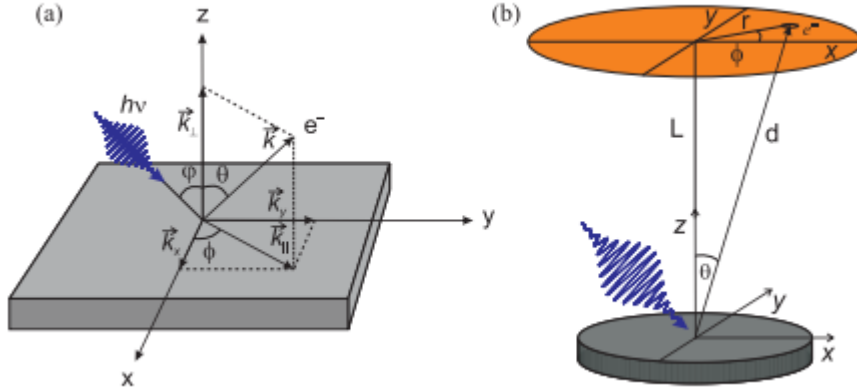


Figure 3.11: Sketch of a typical experimental geometry of electron emission at solid state surfaces. (a) The incoming laser pulse of energy  $h\nu$  makes an angle  $\varphi$  with respect to the surface normal  $z$ , the photoelectrons make an angle of  $\theta$  (out of plane) and  $\phi$  (in-plane), while  $k_{\parallel}$  and  $k_{\perp}$  are their in-plane and perpendicular momentum components, respectively. (b) A sketch of position resolve detector of photoelectrons after their flight through the drift tube of length  $L$ . The sketch is taken from [98].

wires. The holder floats at +2700 V to expand the charge cloud in between the MCP and the anode wires.

Six voltage pulses generated in the hexanode along with the timing signal from the MCP are coupled out. These seven signals along with the laser reference signal  $t_{laser}$  are fed to broad-band amplifier which is coupled with a constant-fraction-discriminator (CFD) (*ATR19, RoentDek*) to digitize the signals to obtain reliable pulse signals. Signals from CFD then sent to the time-to-digital converter (TDC) (*TDC8HP PCI card, RoentDek*) and are processed in real time by customized C++ based routine. LabView and Igor Pro are used as front end software and raw data can be saved for the later post processing and analysis [98].

A sketch of a typical photoemission geometry at a solid surface is shown in Fig. 3.11. The laser beam hits the sample surface at an angle  $\varphi$  with respect to the surface normal  $z$ . In-plane surface components are defined as  $x$  and

$y$  and corresponding momentum of the electron as  $k_x$  and  $k_y$ . Out of plane and in-plane angle of photoelectrons is denoted by  $\theta$  and  $\phi$ , respectively. The pTOF spectrometer measures the kinetic energy of electrons, using time of flight measurement similar to the principle described in the TOF spectrometer section. However, the drift distance is modified in this new configuration as it also takes into account the off-normal electron emission and can be expressed as  $d = \sqrt{x^2 + y^2 + z^2}$ . Kinetic energy can then be mathematically expressed as,

$$E_{kin} = \frac{m_e d^2}{2(t - t_o)^2} = \frac{m_e(r^2 + L^2)}{2(t - t_o)^2} \quad (3.4)$$

where,  $z = L$  is the length of drift tube and  $r^2 = \sqrt{x^2 + y^2}$  denotes the electron position on the detector and is determined using polar ( $\theta$ ) and azimuthal ( $\phi$ ) angles using the relation,

$$\tan\theta = \frac{\sqrt{x^2 + y^2}}{z} \quad (3.5)$$

and

$$\tan\phi = \frac{y}{x} \quad (3.6)$$

In-plane momentum component  $k_x$  and  $k_y$  of the photoelectrons are calculated using x- and y-component of electron velocity, respectively,

$$\begin{pmatrix} k_x \\ k_y \end{pmatrix} = k_{\parallel} \begin{pmatrix} \cos\phi \\ \sin\phi \end{pmatrix} = \frac{m_e}{\hbar(t - t_o)} \begin{pmatrix} x \\ y \end{pmatrix} \quad (3.7)$$

The energy resolution of the spectrometer depends on the accurate determination of the time of flight (TOF) and the length of the drift tube. Drift length is fixed by the geometrical consideration, then the resolution is defined by the precise determination of the TOF. An overall energy resolution of  $<10$  meV is achieved with the pTOF. However, overall energy resolution depends upon the spectral bandwidth of the femtosecond laser pulses (10 – 50 meV) used. Mo-

momentum resolution depends upon the accuracy with which the position on the spectrometer is determined and the temporal resolution of TOF measurements, which provides a typical momentum resolution of  $\Delta k_{\parallel} \approx 0.002\text{\AA}$  [117].

## 3.3 Spectrometer Data

### 3.3.1 Acquisition

Typical data rate during a pTOF measurement exceeds 10 megabytes per seconds and therefore requires a computer with a large data storage and bandwidth. The system is also equipped with LabView program which allows the real-time observation and analysis of the measured pTOF spectra. A total of 8 generated signals have to be processed by the electronic system out of which 6 are the timing signals generated in the Hexanode resulting from the impact of an electron on the MCP which also gives a timing stop signal  $t_{MCP}$  indicating the time when an electron hit the MCP. The last signal is the timing signal from a photo diode  $t_{laser}$  which receives a very tiny part of the incoming laser beam. The time of flight of electrons is calculated using  $t_{MCP}$  and  $t_{laser}$ . Digital processing of these 8 timing signals is performed using various electronic instruments. First, with the use of constant frequency discriminator (CFD), signals are converted to digitally processable nuclear instrumentation module (NIM) pulses. These 8 signals are then fed into the time to digital converter (TDC) (RoentDek HP8TDC). TDC ensures the detection of multiple electrons per laser pulse. These raw timing signals are separately stored in the form of a data file available for later analysis and post-processing. Acquisition of 4D data  $I(E_{kin}, k_x, k_y, t)$  is performed by varying the time delay between the pump and the probe pulses by feeding VIS pulse to a computer controlled delay stage. Good statistics which allow resolving the tiny details in the spectra are obtained by accumulation of data for 500 – 2000 ms at each delay point with

the number of scans  $> 100$ , which provides a signal to noise ration  $> 104 : 1$  [102]. The main contribution for a better signal to noise ratio comes from the counting statistics. Therefore, a high number of counting electron is required but a count rate more than 150 kHz leads to outgassing of the MCP in the pTOF.

### 3.3.2 Analysis

With the determination of the time of flight of photoelectrons and their position on the detector, kinetic energy  $E_{kin}$  and the in-plane momentum components  $k_x$  and  $k_y$  are calculated using equation 3.4 and 3.7, respectively. This provides a data set of photoemission intensity as a function of kinetic energy and in-plane momentum:  $I(E_{kin}, k_x, k_y)$ . Scans along the different polar angle  $\theta$  are merged together to give a single data volume. Through this integrated data volume, energy distribution curves (EDCs) can be obtained by a vertical cut in the momentum axes, for a particular momentum direction. For a fixed  $k_x$  value  $I(E_{kin}, k_y)$  or for a fixed  $k_y$  value  $I(E_{kin}, k_x)$  curves can be extracted. Momentum distribution curves (MDCs) on the other hand, obtained by perpendicular cut through the kinetic energy axis, thus giving intensity as a function of in-plane momentum components  $I(k_x, k_y)$ .

Time-resolved measurements provide a 4-dimensional data set where intensity is recorded and combined for each time-delay yielding  $I(E_{kin}, k_x, k_y, t)$ . Through cuts in the respective directions, 3D data sets can be obtained such as  $I(E_{kin}, k_x, t)$ ,  $I(E_{kin}, k_y, t)$ , and  $I(k_x, k_y, t)$  which can be visualized as transient energy and momentum distribution curves. Further cuts can be made to extract EDCs  $I(E_{kin}, k)$  and MDCs  $I(k_x, k_y)$  for a particular time delay. Through the fitting of the model function, information regarding the peak heights, FWHM, and their transient response can be figured out.

## 3.4 Sample Preparation

### 3.4.1 Si Surface Structure

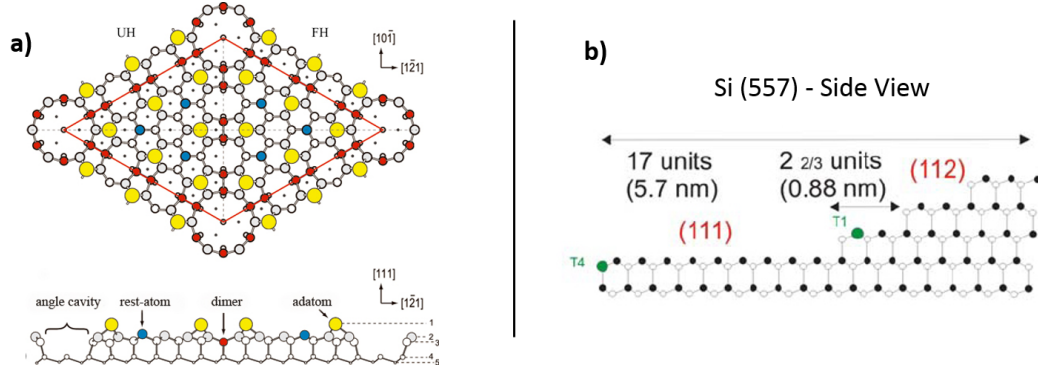


Figure 3.12: (a) Atomically clean surface of Si(111)-7 $\times$ 7 reconstruction with top view on the upper panel and the side view in the lower panel. Yellow, red, and blue circles represent Si atoms, dimerized Si atoms, and the second layer Si rest-atoms, respectively. Taken from [119]. (b) Sketch of the side view of a clean Si (557) structure. The clean Si (557) surface consists of large faces of (111) orientation and small facets of (112) orientation. The image is taken from [120].

Fig. 3.12a and 3.12b show the structural model of atomically cleaned Si(111)-7 $\times$ 7 reconstructed surface and side view of Si(557) surface, respectively. The Si(111)-7 $\times$ 7 surface reconstruction model was proposed by Kunio Takayanagi in 1985 [119]. The unit cell consists of two triangular sub-cells divided by dimer Si atoms (red circles) chains and an angle cavity. Each sub-cell contains 6 atoms (adatoms) to be adsorbed on the crystal surface.

After cutting Si (111) with a miscut angle of 9.45 $^\circ$  along  $[\bar{1}\bar{1}2]$  direction, the vicinal surface of Si (557) is obtained. All vicinal surfaces have steps or terraces which are a few atomic distances wide and run along  $[1\bar{1}0]$  direction. In Si (557), steps are not of uniform size and the surface is non-homogenous [121]. The surface consists of large facets of (111) orientation and smaller facets of (112) orientation, together forming a unit cell of length  $17a_o$  (atomic distance

of Si:  $a_o = 3.32\text{\AA}$ ) along  $[\bar{1}\bar{1}2]$  or perpendicular to the steps direction. The Si atom on the steps have two unsaturated dangling bonds which dimerize at the step edge [120].

### 3.4.2 Si Surface Preparation

#### Outside the UHV Chamber

Cleaning of the sample surface using a specific heating procedure and obtaining the famous Si(111)- $7\times 7$  reconstruction (Fig. 3.12) is the most important part of the surface preparation which is required for the flat Si(111) as well as for the vicinal Si(111) surfaces with a miscut angle. The heating procedure remains mostly the same for the different Si surfaces.

Samples of length 26 mm and width 4 mm are cut from Boron-doped single sided polished, four inch Si(111) wafers with a thickness of  $525\ \mu\text{m}$ . Commercial vicinal Si(557) surface (MaTeck Germany) with  $9.5^\circ$  miscut along  $[\bar{1}\bar{1}2]$  direction, are also  $p$ -doped with a specific resistance of  $1 - 20\ \Omega\text{cm}$ . For the preparation of Indium nanowires, Si wafer with a smaller miscut angle of  $2^\circ$  along  $[\bar{1}\bar{1}2]$  direction were used.

The wafers are precisely cut to the desired size with the use of a diamond cutter in a customized Polyethylene box, where the orientation is determined by the primary flat surface, as shown in Fig. 3.13. The Si sample put in a sample boat between a 2 mm Ta block and a 0.1 mm Ta sheet. However, due to frequent heating during sample preparation, the Ta sheets become bumpy and result in a non-uniform contact with the sample surface. Alternatively, Ta blocks can also be used as a replacement for thin sheets that provide a more uniform electrical contact. The downside of the thicker block is, that it leads to stress in the sample and often results in cracks in the sample during the annealing cycle. Therefore, a Ta sheet is a better choice but needed to be replaced frequently.

The Si surface reacts very quickly with the contamination metals like Chro-

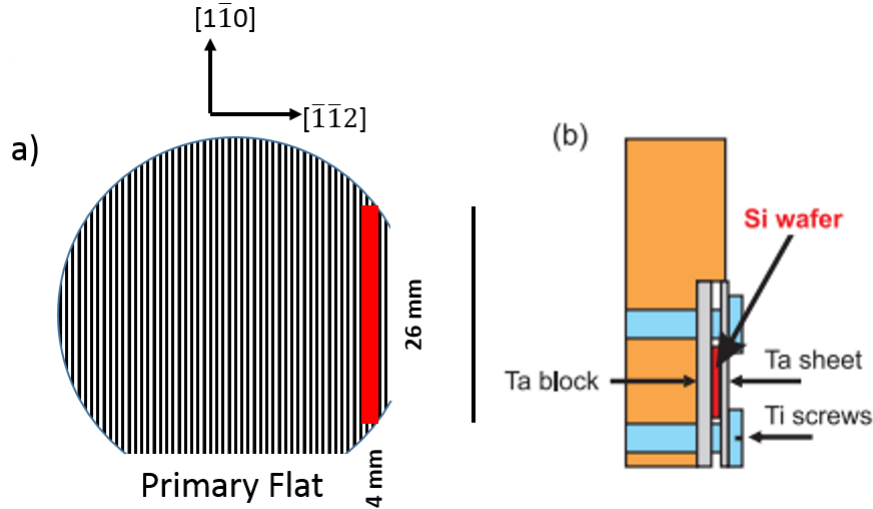


Figure 3.13: (a) Si samples of size 26 mm  $\times$  4 mm are cut from 4 inch Si wafers. For the vicinal Si surfaces, the cutting direction should always be along the step to avoid the step bunching that can be produced as a result of direct current heating. (b) Side view of the sample boat showing the mounted Si wafer.

mium, Nickel, and Cobalt by forming undesired reconstructions on the surface. Therefore, contacts of such metals with the Si wafer must be avoided during cutting process. In addition, the sample holder itself does not contain parts made of these metals. Dirt produced during cutting is removed by the dust blower. Organic contaminants attached to the surface are removed in an ultrasonic bath using ethanol and acetone. Finally, the clean samples are put on the sample boat and transferred to the magazine via a transfer line. In the magazine, they are baked out at 105° C for 8 – 10 hours to ensure removal of water vapor and to make it ready for the UHV conditions.

### Inside the UHV Chamber

Prior to the growth of Pb overlayer structure, an atomically clean Si substrate is necessary to be produced which requires a specific heating procedure achieved by direct current heating. This also demands a precise temperature monitoring throughout the preparation cycles which is obtained using an infrared pyrometer

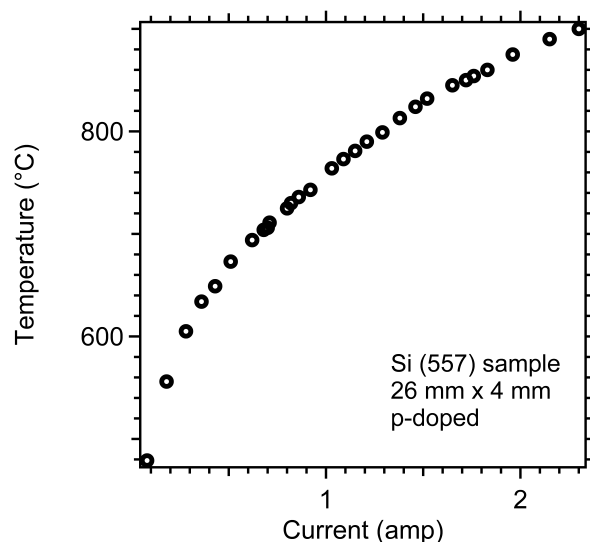


Figure 3.14: A graph of Si (557) sample temperature against the applied current. In the lower applied current regime, the sample temperature increases rapidly against current and saturates for larger applied current values.

(IMPAC IGA 140, LumaSense) able to measure in the temperature range between 300 – 2000° C. During the whole process of sample preparation, the sample is constantly cooled with the running Liquid  $N_2$  through the cryostat. The heating process starts with sample ignition inside the UHV chamber which is achieved by slowly increasing the voltage applied to the sample kept in the current limited mode ( $I \approx 0.1$  Amp).

The temperature of the Si substrate increases with increasing voltage which produces more free carriers and a sudden drop of resistivity at a certain applied voltage ( $< 150$  V). This action switches the Si substrate from a voltage controlled to a current controlled mode and allows a smooth change of the sample temperature by changing the current. Dependence of the temperature on the applied current for a Si (557) sample is shown in Fig. 3.14. As can be seen, for the lower values of applied current, the sample temperature increases rapidly and starts to saturate at larger applied current values. Degassing of the Si substrates is performed by heating the sample at 600°C for 10-12 hours.

### 3.4. SAMPLE PREPARATION

---

Samples are then trained to maintain good pressure conditions ( $p < 7 \times 10^{-10}$  mbar) under a higher temperature of  $700 - 800^\circ\text{C}$  for a relatively shorter time of  $\sim 5$  minutes in order to obtain a better pressure ( $p < 2 \times 10^{-9}$  mbar) during flashing at higher temperature of  $1100 - 1200^\circ\text{C}$ . This training procedure is required especially for the vicinal Si(557) surface. During this step, several  $\mu\text{m}$  thick  $\text{SiO}_2$  layer which protects the commercial Si wafers is also desorbed.

Final state of flashing is done 2-3 times for  $\sim 5$  seconds that sublimates the uppermost Si layers and removes SiC contamination. High temperature flashing ( $> 1100^\circ\text{C}$ ) for Si (557) is avoided as it leads to step bunching. In the last cycle of flashing, the temperature is ramped down slowly ( $\sim 2 - 5$  minutes) from  $900 - 700^\circ\text{C}$  to obtain a large defect free surface.

#### Characterization of Si Surfaces

Morphology of the Si (111) and Si (557) surfaces after preparation is verified by the low energy electron diffraction (LEED) technique and shown in Fig. 3.15. Long range order of the clean Si(111)- $7 \times 7$  reconstruction is evident in the LEED picture taken with primary electron energy of 130 eV and at a temperature of 90 K. The six intermediate spots between two main integer spots along the three high symmetry directions indicate the seven-fold reconstructed structure. A good surface quality is evident by the sharp spots and low inelastic background.

LEED image of the clean Si (557) surface, taken at a primary electron energy of 129 eV and at a temperature of 90 K, is shown in Fig. 3.15b. A visibly different diffraction pattern compared to the Si(111)- $7 \times 7$  reconstruction is evident.

In between the integer spots, 16 diffraction spots appear along  $[\bar{1}\bar{1}2]$  direction which are not distinctly identified in our case possibly due to the low resolution of conventional LEED. The appearance of these spots reflects the fact that terraces consist of different width with large (111) and small (112) facets (Fig.

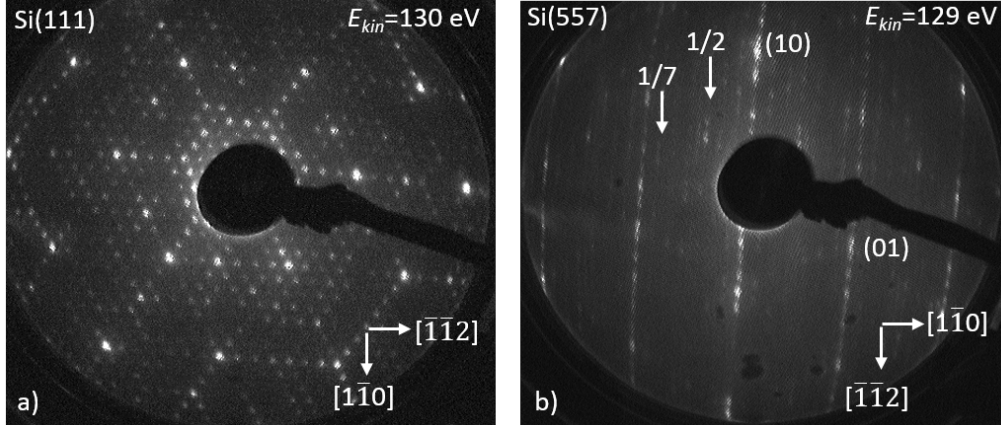


Figure 3.15: LEED image of the (a) Si(111)- $7\times 7$  reconstruction taken with a primary electron energy of 130 eV. Sharp diffraction spots are clearly visible indicating the long range order of the surface. (b) atomically cleaned Si(557) surface taken with a primary electron energy of 129 eV. For this vicinal surface, a different diffraction pattern is evident. These surfaces are characterized by the appearance of  $1/2$  order streak, elongated  $7\times 7$  spots, and 16 spots in between two integer spots along  $[\bar{1}\bar{1}2]$  direction.

3.12b) that together give a unit cell of length  $17a_o$  ( $a_o$  =Si lattice constant) perpendicular to the step direction. Furthermore, strongly elongated ( $7\times 7$ ) spots along  $[\bar{1}\bar{1}2]$  indicate the presence of strongly anisotropic Si (111) terraces in between. A streak formation at half the distance between the step train of integer order spots is also observed. This is formed because at the step edge two dangling bonds exist that dimerize to minimize the energy and explain the periodic doubling along the step edges [120].

### 3.4.3 Structure of Pb Overlayers on Si Surface

Pb adsorbates on the Si (111) surfaces in the low coverage regime, exhibit formation of various stable phases that leads to a complex phase diagram [31]. In particular, the Pb coverage region between  $\theta = 1/6$  ML -  $4/3$  ML on Si (111) is important. A stable phase termed as mosaic phase found at a coverage of  $\theta = 1/6$  ML. Another well known stable phase is  $\beta$ -phase with a coverage of

### 3.4. SAMPLE PREPARATION

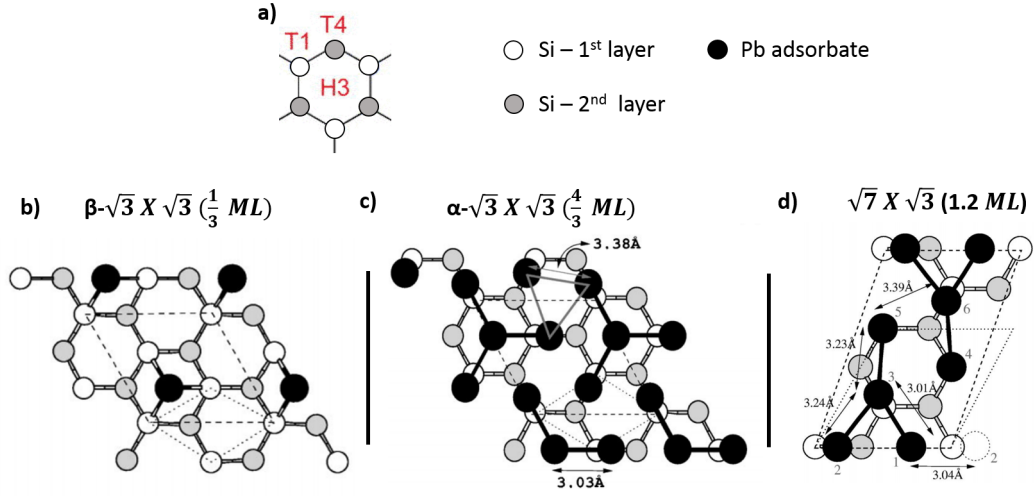


Figure 3.16: A top view of the structural model of selected Pb adsorbate phases formed on the Si (111) substrate a) showing the available adsorption sites T1, T4, and H3, representing the top of the first Si layer, second Si layer, and centered position, respectively. Pb adsorbate atoms are shown by black circles, and the Si first and second layer atoms are shown by white and grey circles, respectively. b)  $\beta$ -phase with coverage  $\theta = 1/3$  ML in which the dotted and dashed lines show the  $1 \times 1$  and  $\sqrt{3} \times \sqrt{3}$  unit cells, respectively. c)  $\alpha$ -phase with coverage  $\theta = 4/3$  ML with the similar unit cell description as in (b) and a formation of trimer is indicated by solid lines triangle d)  $\theta = 1.2$  ML: dotted and dashed lines show the unit cell of  $\sqrt{3} \times \sqrt{3}$  and  $\sqrt{7} \times \sqrt{3}$ , respectively. Schematics are only depicting the H3 model but the T4 model is also energetically favorable and coexists in the system. Image taken from [31].

$\theta = 1/3$  ML. Structures of these two mentioned phases are well understood [33]. Upon going to higher coverage  $> 1.2$  ML, one enters to a more complicated "Devil's Staircase" (DS) phase regime implying a region where a large number of stable phases are formed with a very little change in the coverage [33].

Fig. 3.16 depicts the schematic view of a few selected phases out of various stable Pb overlayer phases that form on the Si (111) substrate. As can be seen in the top panel, Pb adatoms could be attached to three different atomic sites termed as T1 (top of first Si layer), T4 (top of second Si layer), and H3 (centered) site.

The lowest coverage mosaic phase (not shown in the Fig. 3.16), contains the Pb adsorbate atoms sitting on half of the all available T4 sites whereas the other half of T4 sites are occupied by the Si adsorbate atoms.

For an increased coverage of  $\theta = 1/3$  ML, the  $\beta$ -phase takes over, where the Si adsorbate atoms present in the mosaic phase are replaced by the Pb atoms. This phase possesses a  $\sqrt{3} \times \sqrt{3}$  symmetry. Pb adsorbate atoms can sit either at the T4 site or the other T1 or the H3 site. However, it was found out that the T4 site is most energetically favorable site among the three [31].

The densely covered  $\alpha$ -phase at a coverage of  $\theta = 4/3$  ML contains 4 Pb atoms in the unit cell. Out of these four Pb atoms, three sit in off-centered T1 sites and form a trimer like structure. The remaining one atom sits either at the H3 or the T4 site. Since both the sites are energetically favorable, both H3 and T4 structures can coexist in a given system.

The last structure depicted in Fig. 3.16 is  $\theta = 1.2$  ML coverage with  $\sqrt{7} \times \sqrt{3}$  symmetry. The unit cell contains a total of six Pb atoms with one placed at the central H3 site and others placed at T1 or off-centered T1 site. Also for this phase, only the H3 model is shown in the schematic but T4 structure could also exist with both being the energetically favorable site.

### Devil Staircase Phases

Dense Pb coverage of Pb on Si (111) at sufficiently low temperature undergoes an interesting phase evolution indicating the formation of Devil's Staircase (DS) phases. A DS phase is the realization of a large number of linear phases in a very small coverage range as a result of competing interaction of two structure of different densities. In the Pb/Si (111) structure, the competing orders are  $1.2 \text{ ML} - \sqrt{7} \times \sqrt{3}$  (n) and  $4/3 \text{ ML} - \sqrt{3} \times \sqrt{3}$  (m) structures. As much as 16 DS phases have been reported in a coverage range of  $1.2 - 1.33$  ML as a result of a different combination of  $(n, m)$  phases [33, 34, 122]. A phase diagram of the

### 3.4. SAMPLE PREPARATION

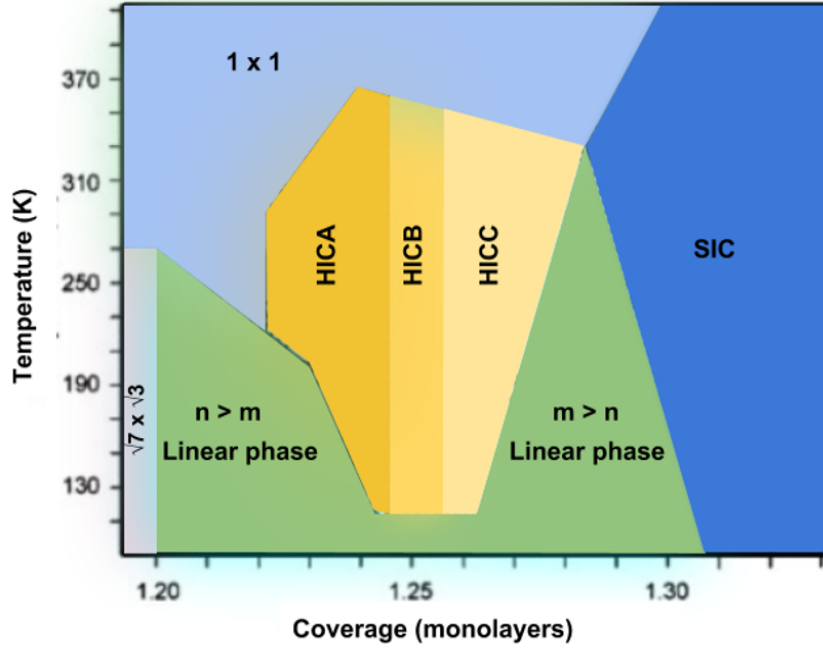


Figure 3.17: A phase diagram for Pb/Si(111) in the coverage range  $6/5 \text{ ML} < \theta < 4/3 \text{ ML}$  showing the linear DS phases at low temperatures. At intermediate temperature, DS phases convert to HIC phases and at a higher temperature, they transform into disordered  $1 \times 1$  phase. Diagram taken from [33] and modified.

DS phases is shown in Fig. 3.17. As can be seen, along with the linear DS phases at lower temperature, other commensurate phases such as hexagonal incommensurate (HIC) and striped incommensurate (SIC) are also formed. The HIC phase is suggested to be composed of  $\sqrt{3} \times \sqrt{3}$  structure separated by hexagonal domain walls made of  $\sqrt{7} \times \sqrt{3}$  like phases. The SIC phase, on the other hand, has a little higher Pb coverage compared to the HIC phase and large domains of  $\sqrt{3} \times \sqrt{3}$  are separated by a meandering  $\sqrt{7} \times \sqrt{3}$  domain walls [32, 33]. At a higher temperature of 250-350 K, all domain walls, and superstructure disappear and a  $1 \times 1$  disordered phase is formed.

It has also been observed that depending on the preparation method (i.e. it is prepared by low temperature deposition or deposition followed by subsequent annealing), one might not observe the presence of HIC and SIC at all. In the

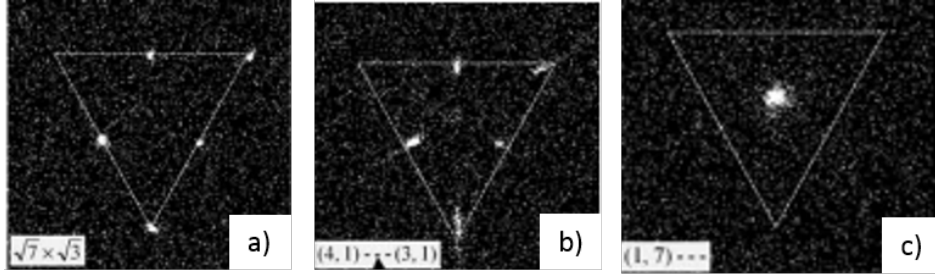


Figure 3.18: Evolution of a specific part of the BZ showing Pb diffraction spots as a function of various DS phases. (a) 1.2 ML- $\sqrt{7} \times \sqrt{3}$  phase (b) a mixture of  $(n, m) = (4, 1) + (3, 1)$  phase, where  $(n, m) = (\sqrt{7} \times \sqrt{3}, \sqrt{3} \times \sqrt{3})$ , and (c)  $(n, m) = (1, 7)$  phase, indicating large domains of  $\sqrt{3}, \sqrt{3} \times \sqrt{3}$  structure. It can be followed that a large contribution from  $\sqrt{3} \times \sqrt{3}$  phase leads to convergence of diffraction spots. Taken from [34].

SPA-LEED study performed on DS phases of Pb/Si (111), it was reported that the diffraction spots from Pb are arranged around the high symmetry points in the shape of a triangle indicating the three-fold symmetry of the surface [32–34, 122].

Such a case is depicted in SPA-LEED images for three different DS phases shown in Fig. 3.18 (taken from [34]). As can be seen in the right panel, that shows the  $\sqrt{7} \times \sqrt{3}$  (n) LEED structure, the diffraction spots are arranged at the lines of the triangle. With the growing contribution of  $\sqrt{3} \times \sqrt{3}$  (m) structure, the spots start to converge, as shown in the middle panel for (4,1)...(3,1) phase. For a very large domain of  $m$  structure, all diffraction spots converge completely and show a single spot as shown in the left panel with a (1, 7) phase combination.

### 3.4.4 Preparation of Pb Overlayer Structure on Si Surface

#### Preparation of Pb on Si(111)

### 3.4. SAMPLE PREPARATION

---

Due to the formation of a very large number of phases brought about by slight changes of coverage in Pb/Si (111) system, the preparation and precise determination of the required coverage becomes difficult. Therefore, a systematic way was followed in which phases with well-known structure e.g. mosaic and  $\beta$  phases were prepared first and later the required dense-  $\alpha$  phase with the required coverage of  $\sim 4/3$  ML was prepared.

In the UHV chamber, under base pressure  $p < 2 \times 10^{-10}$  mbar, Pb deposition from a Knudsen cell with an evaporation rate of  $\sim 0.5$  ML/min was performed to the cleaned Si(111)- $7 \times 7$  reconstructed surface. The evaporation rate was monitored by a Quartz microbalance. In total, 5 ML of Pb was deposited on to the clean Si surface sustained at a sample temperature of 85 K which was monitored by a temperature diode mounted adjacent to the sample holder. Subsequent annealing for 3-4 minutes was performed at various temperature that result in the formation of different stable phases.

As a result of annealing performed at the temperatures of  $\sim 450^\circ$  C,  $\sim 410^\circ$  C, and  $\sim 385^\circ$ , three different stable phases were obtained and their morphology were verified using LEED.

#### **Characterization of Pb/Si(111) Structures**

Characterization of the obtained structure using LEED is shown in Fig. 3.19. As can be seen for the three different LEED images, a general feature is the newly formed Pb overlayer diffraction pattern that shows a rotation of  $30^\circ$  compared to the hexagon formed by the diffraction spots from the Si atoms.

The diffraction patterns in Fig. 3.19a and 3.19b, are similar to the mosaic ( $1/6$  ML) and  $\beta$ ( $1/3$  ML) phases, respectively, which is consistent also with the diffraction pattern reported earlier [16, 123]. Determination of the third phase achieved at a lower annealed temperature of  $\sim 380^\circ$  C is not straightforward. First of all, it is understood that this must have a higher coverage than the  $\beta$  phase due to the lower annealing temperature. However, the diffraction spots

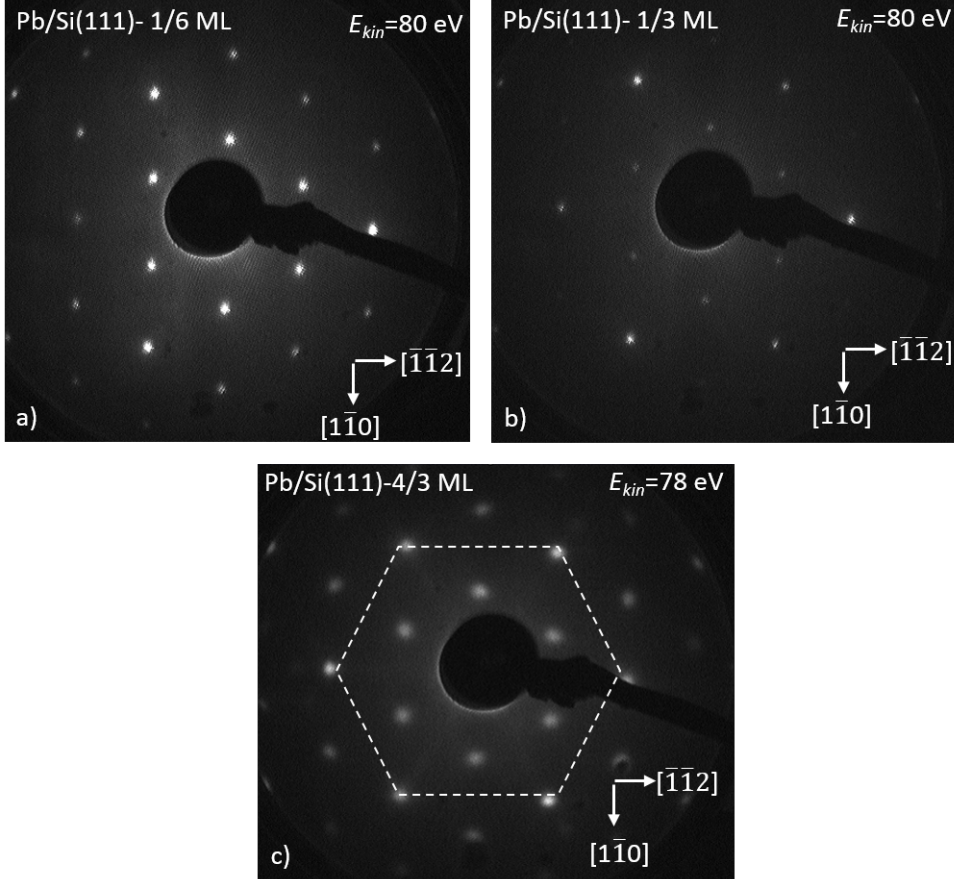


Figure 3.19: LEED images obtained at  $\sim 85$  K for various phases formed as a result of annealing the deposited  $\sim 3$ ML of Pb at different temperatures. The hexagon formed by the Pb diffraction spots show a rotation of  $30^\circ$  due to the formation of  $\sqrt{3} \times \sqrt{3}$  symmetry (a) Mosaic phase with 1/6 ML coverage (b)  $\beta$  phase with 1/3 ML coverage (c)  $\alpha$ -dense phase with  $\sim 4/3$  ML coverage.

are not similar to the reported diffraction pattern for phases between 0.6-0.8 ML coverage [16, 123]. Furthermore, trimer structures are already formed at 1 ML [16, 31, 124] This proves that the last diffraction pattern represents none of these coverage. Therefore, this must belong to an even higher  $\alpha$  coverage regime. As we have seen in Fig. 3.18 that a large domain of  $\sqrt{3} \times \sqrt{3}$  symmetry grows, leading to a convergence of the diffraction spots. Based on that, we conclude that the coverage of the last phase is close to the  $(n,m) = (1,7)$  phase. This phase implies a total of 34 Pb atoms per 26 Si atoms which gives a coverage

### 3.4. SAMPLE PREPARATION

---

$\theta = 1.304$  ML. Therefore, the structure is the dense  $\alpha$  phase with a coverage close to  $4/3$  ML.

#### **Preparation of Pb Nanowires on Si(557)**

After obtaining the clean Si (557) substrate, Pb is deposited onto the surface using Knudsen cell in a two step process. During the first step,  $\sim 5$ ML of Pb is deposited at a temperature of  $330^\circ\text{C}$ . Temperature is then quickly reduced to  $300^\circ\text{C}$  and  $\sim 3$  ML of Pb is deposited in the second step. Deposition of Pb at elevated temperature creates a fine balance between adsorption and desorption and results in a coverage of 1.31 ML. Presence of steps set a predefined direction for the growth of Pb nanowire arrays. A precise monitoring of the temperature is mandatory to obtain a good quality of prepared nanowires. Due to strong fluctuations in the sample temperature during the deposition process, the heating current needs to be consistently controlled to maintain the required temperature. A tolerance level of  $\pm 5^\circ\text{C}$  during both steps of deposition is acceptable and provide better structural quality.

#### **Characterization of Pb/Si(557) Structure**

Morphology of the Pb nanowires arrays is again verified using LEED and is shown in Fig. 3.20. As can be recognized quickly, diffraction spots are strongly modified upon the Pb nanowires formation compared to the bare cleaned Si (557). Along the  $[\bar{1}\bar{1}2]$  direction, in between two main integer spots, 4 sharp diffraction spots with a split of  $\Delta k_y = 21.3\%$  of BZ appear replacing the previous 16 spots observed for Si (557) surface. This indicates a change in the structure along this direction.

This is indeed the case, as depicted in the side view of the structure model formed upon the adsorption of 1.31 ML of Pb concentration (Fig. 3.20c).

As can be seen, non-uniform terraces of Si (557) grow into equally sized terraces of 1.55 nm ( $4\frac{2}{3}a_o$ ) explaining the origin of four diffraction spots along

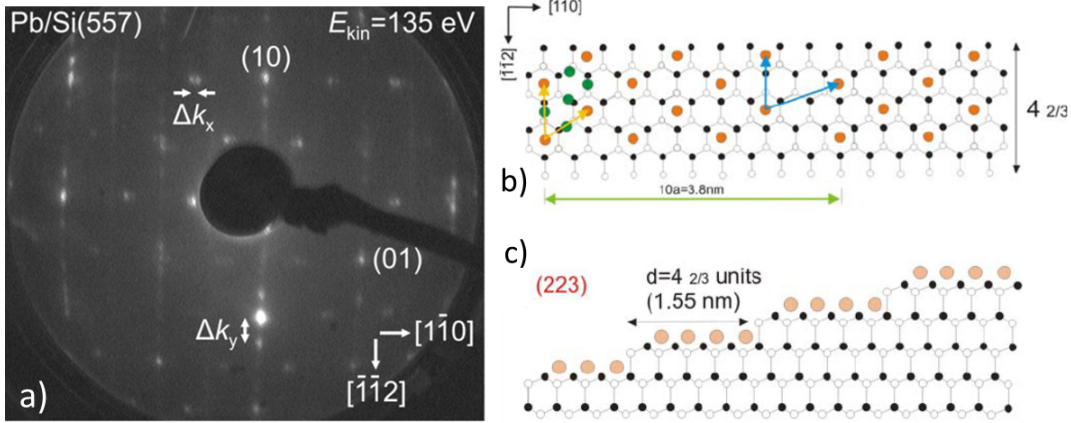


Figure 3.20: (a) LEED image obtained at  $\sim 85$  K for 1.31 ML Pb/Si (557) structure. In between the two main integer spots along the  $[\bar{1}\bar{1}2]$  direction, four diffraction spots appear. A splitting of 10 % indicates the formation of linear phase which is the combination of 5 unit cell of  $\sqrt{3} \times \sqrt{3}$  separated by single domain of  $\sqrt{7} \times \sqrt{3}$  structure. (b) Structure model of the (1,5) phase of 1.31ML Pb on Si(557). The closed and open small circles denote Si atoms of the first and second substrate layer, respectively. Orange and green filled circles represent Pb atoms on H3 positions and on off-centered T1 positions, respectively. This linear phase can be seen as a 10-fold periodicity within a single Pb-chain. (c) Side view of the 1.31 ML Pb/Si (557) structure, showing the modified equally spaced terrace width replacing the non-uniform terrace width of Si (557) structure, explaining the observed four diffraction spots in the LEED pattern. Structure models are taken from [120].

this direction. The absence of Si(111)- $7 \times 7$  reconstruction spots indicates that adsorption of this coverage results in the modification of the surface energy and leads to the destabilization of even the most stable (111) facet and destruction of ( $7 \times 7$ ) reconstruction. Furthermore, the  $7 \times 7$  reconstruction is replaced by superstructure appearing at the  $\sqrt{3}$  position showing a spot splitting of 10% along the terraces or the  $[1\bar{1}0]$  direction [120].

The spot splitting can be explained by a phase arrangement in which 5 unit cells of  $\sqrt{3} \times \sqrt{3}$  are separated by a single domain wall of  $\sqrt{7} \times \sqrt{3}$  structure, along the terrace thus giving a coverage of 1.31 ML. This is also sketched in the

### 3.4. SAMPLE PREPARATION

---

structure model shown in Fig. 3.20b. This structure was also verified by STM results [120]. Streak from the dimerized Si atom present in the Si (557) LEED converts into a sharp diffraction spot indicating a strong correlation between atoms at steps. An excess coverage of Pb leads to the decoration of step edges and reduction in the small splitting size of  $\Delta k_x = 8\%$  of BZ (for coverage 1.42 ML to 1.62 ML). A Pb concentration of  $< 1.31$  ML results in the modification of steps size as well as the combination of  $\sqrt{3} \times \sqrt{3}$  and  $\sqrt{7} \times \sqrt{3}$  structure. These set of information help to get the desired structure and a precise coverage of 1.31 ML of Pb on Si (557) that exhibits a quasi-1D structure.

---

# Strong Linear Dichroism in the Non-Linear Photoemission of 4/3-ML Pb/Si(111)

## 4.1 Introduction

Monolayer and submonolayer coverage of metal-induced reconstruction on the semiconductor surfaces are the examples of two-dimensional systems and have drawn considerable interest due to various exciting physics that they manifest. They have been shown to exhibit charge density waves formation on Pb/Ge(111) [2], Mott phase on Sn/Si(111) [3], and superconducting properties in Pb/Si(111) [4]. They are particularly interesting in view of their potential application in semiconductor based spintronics. The specific structural configuration of an atom of heavy nuclei and a semiconductor surface across which the crystal potential changes rapidly, gives rise to strong spin-orbit coupling (SOC). Surface inversion asymmetry is further known to lift the spin degeneracy and producing a spin-orbit splitting in the two-dimensional electronic state, so called the Rashba effect [125]. This strong SOC effect has been reported in a large

number of systems with metal-semiconductor structural configuration, such as in Pb/Ge(111) [5, 6], Bi/Si(111) [17–20], Bi/Ge(111) [21, 22], Ti/Si(111) [18, 23–26], and Ti/Ge(111) [27, 126].

A 4/3- monolayer (ML) coverage of Pb on Si (111) substrate (also known as  $\alpha$ -phase, and the term will be used interchangeably hereafter) can, therefore, be a potential candidate for such SOC system and a fundamental study towards understanding its electronic band structure is much desirable. On an experimental level, Rashba type of spin-orbit splitting has been reported for very similar systems of 4/3-ML Pb/Ge (111) [6], Pb/Si(557) [127], and quantum well states of ultrathin Pb films on Si(111) [128]. For the  $\alpha$ -phase Pb/Si(111), density functional theory (DFT) calculations predicted a large Rashba spin-splitting in the occupied and unoccupied electronic band structure near the Fermi level  $E_F$  [35]. This was experimentally verified in the spin- and angle-resolved photoemission study performed for the occupied electronic bands lying below the Fermi level  $E_F$  [36].

We aim here at understanding the *unoccupied* electronic band structure of the  $\alpha$ -phase Pb/Si(111) using femtosecond angle- and time-resolved two-photon photoemission (tr2PPE), in the vicinity of the  $\Gamma$  ( $k_{\parallel} = 0$ ) point. An added advantage of this non-linear technique over the conventional ARPES is the possibility to probe carrier lifetimes by changing the time-delay between the two photon pulses. Similar to conventional ARPES, the symmetry character of the unoccupied electronic bands can also be investigated by modifying the polarization of pump and probe beam and exploiting the dipole selection rules [37–39]. However, a careful approach is required for analyzing the electronic structure obtained by 2PPE. Since it is a non-linear process, the photoemission signal can arise either from the occupied, unoccupied or even from the final electronic state which must be distinguished. Furthermore, due to lower photon energies used in the 2PPE measurements, the technique becomes more bulk sensitive due to a longer mean free path of the photoelectrons in the solid,

as predicted by the universal curve [90]. This implies that the photoemission process can also probe the electronic structure of Si in addition to the Pb overlayer. Involvement of the bulk electronic state in the photoemission process results in asymmetries in the photoemission intensities of the electronic band structure [42–44]. The free electron like final state assumption may also not be fully valid at such low energies which can also result in asymmetric photoemission intensities across the  $\Gamma$  ( $k_{\parallel} = 0$ ) point [45]. In addition, the systems with strong SOC, such as Rashba and topological insulators, are known to produce various peculiar asymmetric effects such as  $k$ -dependent orbital switching and photoemission intensity [3, 19, 40, 41, 46–65, 126].

These experimental and system dependent complexities make the analysis a rather complicated task that requires careful analysis. In order to make the task comprehensive, capabilities of our experimental system were exploited to its maximum. First, using the static 2PPE, three different electronic states were identified in the vicinity of the  $\Gamma$  point along two high symmetry directions  $k_x \parallel [\bar{1}\bar{1}2]$  and  $k_y \parallel [1\bar{1}0]$  (will be denoted as  $k_x$  and  $k_y$  from hereafter). The identified electronic states showed a strong asymmetry in the photoemission intensity distribution and electronic structure across the  $\Gamma$  point. Time-resolved 2PPE measurements performed to understand the origin of identified electronic states revealed their unoccupied nature. The peculiarities of the unoccupied electronic states were finally investigated by pump polarization dependent measurements, which further revealed a type of symmetry break in which the orbital character switched at the opposite momentum  $\pm k_x$ . We argue that the asymmetric intensity distribution or the linear dichroism in the angular distribution (LDAD) [40, 125] is the underlying cause of the observed asymmetries. A qualitative understanding of the occurrence of LDAD is developed in the end.

## 4.2 Experimental Method

The experimental methods have been discussed in the third chapter of this thesis work. In addition, the chapter also covers the details concerning the Pb/Si(111) sample preparation and their coverage determination. Therefore, only the relevant details of the experimental technique will be briefly discussed here.

Two-photon photoemission experiments require the generation of two different laser pulses of energies  $\hbar\omega_1$  and  $\hbar\omega_2$ , that are less than the workfunction  $\phi$  of the material under investigation. To obtain them, the optical parametric amplifier (OPA, Coherent 9450) is utilized, which is pumped by femtosecond laser pulses generated by a commercial mode-locked Ti:Sa laser system (Coherent RegA 9040) operating at a repetition rate of 250 kHz, central wavelength of  $\lambda = 818$  nm ( $\hbar\omega = 1.52$  eV). The OPA output was tuned to obtain the fundamental energy of  $\hbar\omega_1 = 1.9$  eV (visible, VIS), which was subsequently frequency doubled using  $\beta$ -Barium Borate (BBO) crystal to obtain  $\hbar\omega_2 = 3.8$  eV (ultraviolet, UV) pulse. The obtained laser beams were focused to have a diameter of 100  $\mu\text{m}$  and fluences  $< 2\mu\text{J}/\text{cm}^2$ . The spatial and temporal overlap between the two laser pulses is established at the sample surface in the UHV chamber. Typically all the laser pulses reaching to sample are  $p$  polarized.

To obtain the polarization dependent measurements, the E-field vector of pump (UV) laser pulses was modified from  $p$  to  $s$  using  $\lambda/2$  wave plate. In a typical 2PPE analysis, the intermediate state energy with respect to the Fermi level  $E_F$  is determined by using the relation  $E_{int} - E_F = \hbar\omega_{pump} - (K.E_{fast} - K.E_{int})$ , where  $K.E_{fast}$  is the kinetic energy of the fastest photoelectrons and  $K.E_{int}$  is the kinetic energy of electrons coming from intermediate or unoccupied states. It can clearly be seen from the equation, that the binding energy determination requires assigning the sequence of the populating (pump) and photoemitting (probe) beams. This is achieved by analyzing the population

and scattering dynamics of the excited carriers obtained in the time-resolved 2PPE measurements. Time-resolved measurements are performed by controlling the time delay  $\Delta t$  between pump and probe pulses. Self-built position sensitive time-of-flight spectrometer (pTOF) was used to analyze the photoelectrons. The output of the pTOF is the intensity of photoelectrons as a function of their energy and momentum in two mutually perpendicular directions  $k_y \parallel [1\bar{1}0]$  and  $k_x \parallel [\bar{1}\bar{1}2]$ . The overall spectral, temporal, and momentum resolution was 60 meV, 85 fs, and  $2 \text{ m\AA}^{-1}$ , respectively. An accelerating bias voltage of -400 meV was applied to align the vacuum level of the sample with the electrically grounded pTOF spectrometer. During the measurements, samples were continuously cooled with liquid nitrogen and the temperature of the samples stayed below 90 K.

The experimental geometry is shown in Fig. 4.1a. The incident pump and probe pulses make an angle of  $45^\circ$  with respect to normal to the surface. Electric field vector of  $p$  polarized light is parallel to the  $[\bar{1}\bar{1}2]$  direction implying the match of the scattering and the mirror plane of this system. Position-sensitive TOF spectrometer is also positioned normal to the surface and accepts photoelectrons emitted normal as well as in off-normal to the surface owing to its large acceptance angle of  $\pm 11^\circ$ . A sketch of the 2PPE process is also shown in Fig. 4.1a, in which a pump (blue) laser pulse takes the electron from an occupied continuum of state to an intermediate state from where a probe (red) laser pulse photoemits the electron out of the surface where it can be detected by the pTOF.

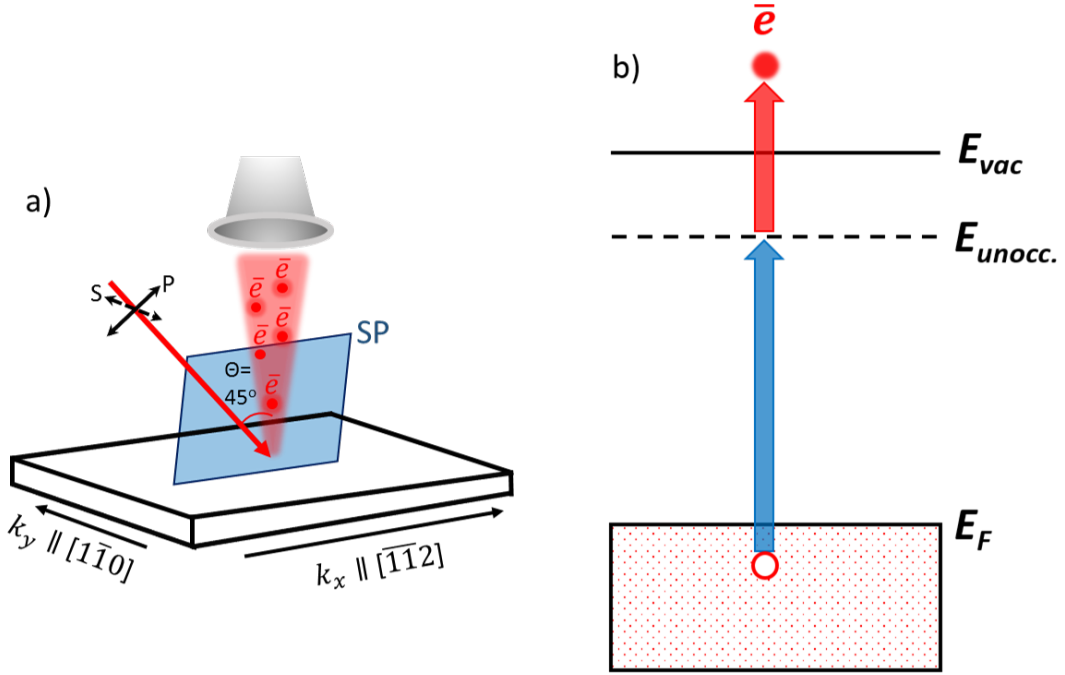


Figure 4.1: (a) Sketch of the 2PPE experimental geometry. Both pump and probe beams incident at an angle of  $45^\circ$  with respect to the surface normal. Position-sensitive time of flight spectrometer (pTOF) also placed normal to the surface which detects the photoelectrons in two mutually perpendicular momentum directions ( $k_y \parallel [1\bar{1}0]$  and  $k_x \parallel [\bar{1}\bar{1}2]$  of Si(111)) as a function of their energy and intensity. Both pump and probe beams are *p* polarized (E-field vector parallel to  $[\bar{1}\bar{1}2]$ , unless otherwise specified). Scattering plane (SP) of the experimental geometry is also indicated. In this experimental configuration, the mirror plane of the system overlaps with the scattering plane. (b) A simplified scheme of a two-photon photoemission process in which pump laser pulse takes the electron lying below the Fermi level to an unoccupied electronic state, probe laser beam excites the electron further above the vacuum level where it is detected by the pTOF.

## 4.3 Results

### 4.3.1 Unoccupied Electronic Structure

Fig. 4.2a and 4.2b show a false color representation of the 2PPE signal obtained at maximum temporal overlap ( $\Delta t = 0$ ) and  $p$ - $p$  polarization combination of the pump and probe laser pulses along two mutually perpendicular high symmetric momentum directions  $k_x$  and  $k_y$ , respectively. The energy distribution curves (EDCs) extracted from the 2PPE intensity plots at various momenta obtained in an integrated momentum window of size  $\Delta k = 0.02 \text{ \AA}^{-1}$ , are shown by the blue dots in panel (c) and (d), along the  $k_x$  and  $k_y$  directions, respectively. The extracted EDCs are fitted using a fit function comprising of Lorentzian and exponential background functions, as shown by the red solid lines. The energy peak positions obtained by the fit functions are plotted on top of the 2PPE intensity plots in Fig. 4.2a and 4.2b, as shown by the white '+' symbols. They denote the dispersion of the various electronic features in the vicinity of the  $\Gamma$  point. At the  $\Gamma$  point, three distinct electronic features are identified. Energies of the identified unoccupied electronic states, with respect to the Fermi level are found to be  $E - E_F = 3.6 \text{ eV}$  ( $A_{upper}$ ),  $3.5 \text{ eV}$  (A), and  $3.3 \text{ eV}$  (B), respectively, as determined at  $k_y = 0$ . Correct determination of the binding energies of the observed 2PPE peaks, require a prior assignment of the sequence of populating (pump) and photoemitting (probe) pulses which were found to be UV and VIS, respectively. This assignment was performed using time-resolved 2PPE results, which will be discussed in detail in the next section.

A remarkable observation along  $k_x$  direction is the apparent symmetry break in the electronic dispersion relation across  $k_x = 0$ , as  $E(+k_x) = E(-k_x)$  does not hold particularly for states  $A_{upper}$  and B. At the momentum regions  $k_x > 0$  and  $k_x < 0$ , the electron state  $A_{upper}$  exhibits no spectral weight and a finite spectral weight, respectively. For the electronic state B, only one lower branch

### 4.3. RESULTS

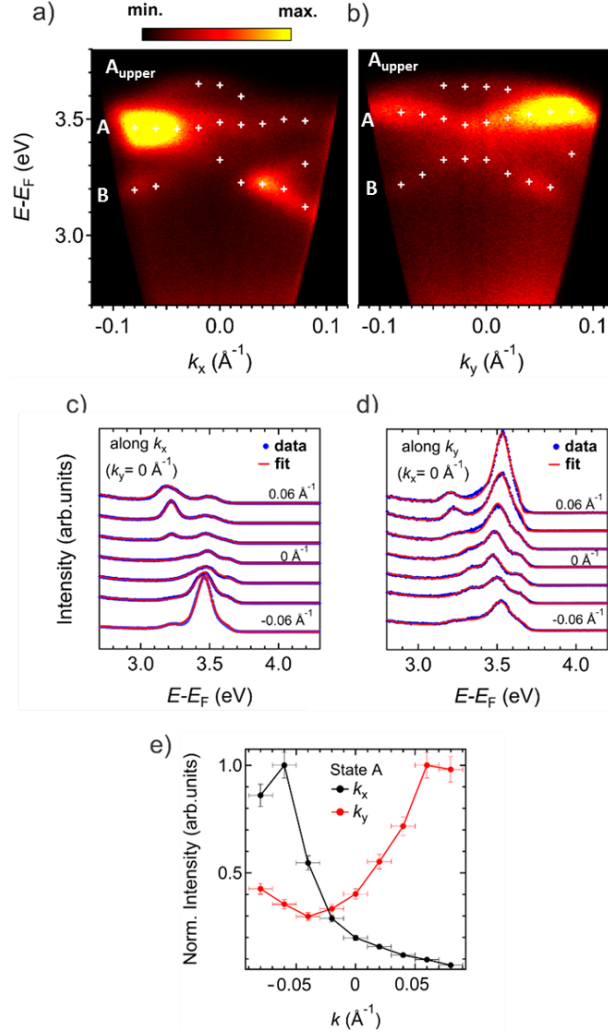


Figure 4.2: (a) and (b) False color representation of 2PPE intensity plots along  $k_x \parallel [\bar{1}\bar{1}2]$  and  $k_y \parallel [1\bar{1}0]$ , obtained at a maximum temporal overlap ( $\Delta t = 0$ ) of the  $p$  polarized UV ( $\hbar\omega_2 = 3.8$  eV) and VIS ( $\hbar\omega_1 = 1.9$  eV) laser pulses. From the color legend on top of the panel (a), minimum and maximum 2PPE signal can be identified. The white '+' marks show the dispersion of electronic states. The energy distribution curves (EDCs) extracted for momentum window  $\Delta k = 0.02 \text{\AA}^{-1}$  at various momenta are shown by the blue filled dots, as shown along  $k_x$  (c) and  $k_y$  (d) directions. For clear visibility, an offset is artificially introduced among the EDCs. A fit function comprising of multiple Lorentzian peaks and exponential function for the secondary electrons background describes the data well (solid red lines). (e) Peak intensities obtained as a result of fit are plotted against the momentum  $k_x$  (black) and  $k_y$  (red), shown only for state A ( $E - E_F = 3.55$  eV).

can be identified at the momentum region  $k_x < 0$  out of the two observed branches at the momentum region  $k_x > 0$ . In contrast, the electronic state A exhibits a nearly flat and symmetric dispersion relation but a strong asymmetry in the photoemission intensity. A visibly large spectral weight is present at  $k_x < 0$  as compared to  $k_x > 0$ .

A strong asymmetric intensity distribution was observed also across  $k_y = 0$  for the upward dispersing electronic state A. However, in contrast to  $k_x$  direction, a larger spectral weight is present at  $k_y > 0$  as compared to  $k_y < 0$ . Asymmetric intensity is also observed for state B, but the effect is weaker compared to state A. Prominent asymmetric intensity effects of state A are quantitatively analyzed by plotting the intensities obtained as a result of fitting from Fig. 4.2c and 4.2d in Fig. 4.2e as a function of momentum  $k_x$  and  $k_y$ . Both curves are individually normalized with their respective maximum in order to clearly visualize their respective momentum dependent change in the intensity. As can be seen, photoemission intensities decrease with changing momentum from their respective maximum and a drop of 90% and 65% is observed along  $k_x$  and  $k_y$  directions, respectively.

One can observe a small shift in  $k_y$  due to which the spectrum does not seem to be symmetric around  $k_y=0$ . This is potentially a result of sample misalignment which can be caused by extra tightening of the screws that results in the slight bending of the sample holder in the  $y$  direction. A bending of 1-2° can result in the offset of  $0.01\text{\AA}^{-1}$ . Also along  $k_x$  direction, the spectrum seems to be shifted by  $0.02\text{\AA}^{-1}$ . This is a result of sample misalignment along  $x$  direction.

### 4.3.2 Ultrafast Dynamics

Ultrafast dynamics within the unoccupied electronic states of the Pb/Si(111) system is investigated by time-resolved 2PPE measurement and achieved by inducing a time delay  $\Delta t$  between the UV and the VIS laser pulses. The

### 4.3. RESULTS

---

outcome of the tr2PPE measurements is a 4-dimensional data set in which the photoemission intensity is obtained as a function of the kinetic energy, momentum in two mutually perpendicular directions, and the time delay,  $I(E, k_x, k_y, \Delta t)$ . Such a data set obtained for the 4/3-ML Pb/Si(111) system is shown in Fig. 4.3a, for integrated accessible momentum space ( $|k_x| \leq 0.11 \text{ \AA}^{-1}$ ,  $|k_y| \leq 0.11 \text{ \AA}^{-1}$ ). For this  $k$ -integrated time-dependent measurement, not all the electronic states are distinctly observed as was the case for static 2PPE measurements along the momentum directions  $k_x$  and  $k_y$  at  $\Delta t = 0$  (Fig. 4.2). However, two clear signatures lying at the energetic region of observed state A ( $E - E_F \approx 3.5$  eV) and B ( $E - E_F \approx 3.3$  eV) are present.

In order to quantify the time evolution of the two identified electronic states, population dynamics curves are extracted from Fig. 4.3a by a horizontal cut along the pump-probe delay axis in the energetic range indicated by white dashed line boxes. In addition, the cross-correlation curve (XC) of pump and probe laser pulses is also extracted from an energy region that contains the signal from the carriers having the highest kinetic energy as their transition is assumed to take place via virtual state that contains no lifetime effect.

All three extracted curves are shown in Fig. 4.3b with an artificial offset induced between them along the vertical intensity scale for clear visibility. As can be seen, the XC does not show any asymmetry in time indicating a signal originating purely from the overlap of pump and probe laser pulses. A Gaussian function fit to the XC gives a full width half maximum (FWHM) value of 88(2) fs. For the signatures A and B, a population build-up occurs at negative time delays which subsequently decays at positive time delays. From the temporal evolution of the curves, the sequence of pump and probe pulses is deduced. A curve showing a finite decay at the positive pump-probe delay refers to states which are pumped by UV and probed by VIS pulses and an opposite sequence holds for the decays at the negative pump-probe delay. Therefore, in this case the pump and probe sequence is UV ( $\hbar\omega_2 = 3.8$  eV) and VIS ( $\hbar\omega_1 = 1.9$  eV),

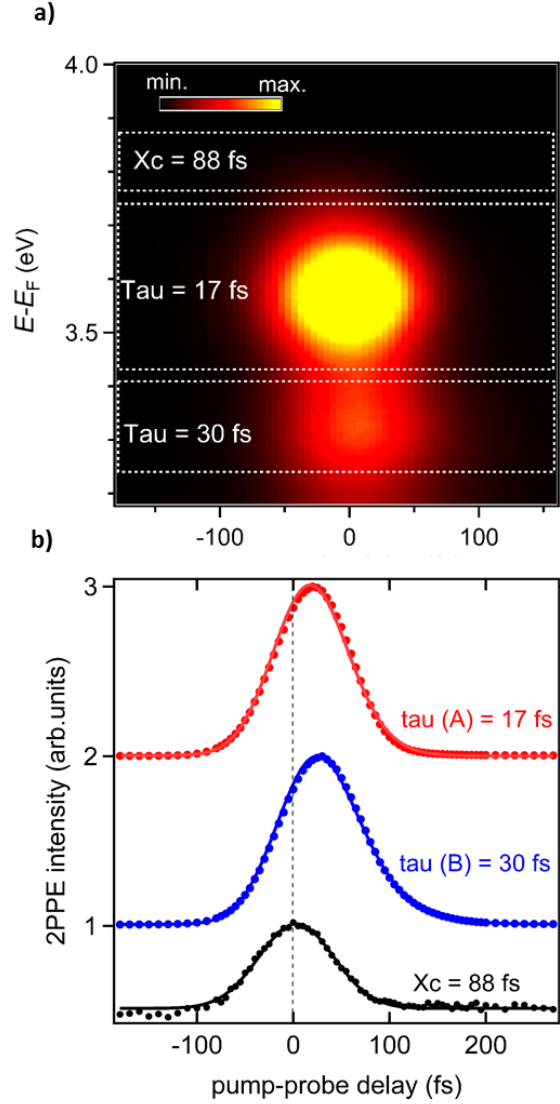


Figure 4.3: (a) False color representation of the time-resolved 2PPE intensity plot obtained in accessible  $k$ -integrated window ( $|k_x| \leq 0.11 \text{ \AA}^{-1}$ ,  $|k_y| \leq 0.11 \text{ \AA}^{-1}$ ) as a function of pump-probe delay. White dashed boxes indicate the energy window at which the population dynamics curve of state A and B and cross-correlation curve of the pump and probe beams are extracted. All extracted curves are plotted in (b) shown by the colored dots. Their decay towards positive delays indicates the UV ( $\hbar\omega_2 = 3.8 \text{ eV}$ ) pump and VIS ( $\hbar\omega_1 = 1.9 \text{ eV}$ ) probe sequence. Fitting based on simple rate equation for states A and B, as well as a Gaussian function fit for the cross-correlation curves is shown by solid lines. The obtained lifetime values for states A and B is found to be  $\tau = 17(4) \text{ fs}$  and  $\tau = 30(4) \text{ fs}$ , respectively.

### 4.3. RESULTS

---

respectively. This also confirms the unoccupied nature of the electronic states. Fitting of the population dynamics curves for states A and B is shown by the solid lines in Fig. 4.3b. The following rate equation was used to describe the transient behavior of the unoccupied electronic states.

$$\frac{dN_{\bar{k}}}{dt} = A \cdot \exp\left\{-\left(\frac{t}{\sigma}\right)^2\right\} - \frac{\Gamma_{\bar{k}}}{\hbar} N_{\bar{k}} \quad (4.1)$$

where,  $\bar{k}$  index used in subscripts refers to momentum-averaging and  $N_{\bar{k}}$  denotes the transient population. The first term on the right hand side of equation refers to the population build-up due to the pump beam and the finite temporal resolution of the experiment, estimated by a Gaussian of width  $\sigma$ . The second term describes the relaxation with a transition rate  $\Gamma_{\bar{k}}$ . In this simple rate equation, the intra-band scattering processes are not considered as the data is already momentum averaged. Therefore, if any redistribution of the population occurs within the band, it is already taken into account. Thus the  $\Gamma_{\bar{k}}$  indicates inelastic inter-band scattering rate that leads to the depopulation of the corresponding band. The analytical solution of Eq. 4.1,  $N_{\bar{k}}(t) \propto \exp\{-\Gamma_{\bar{k}}t/\hbar\}[1 + \text{erf}(t/\sigma - \sigma\Gamma_{\bar{k}}/2\hbar)]$ , was fitted to the experimental data under the constraint of the extracted pulse XC width  $\sigma$ . The model describes the experimental data well, as shown by the solid lines in Fig. 4.3b. Extracted momentum averaged lifetime values are found to be 17(4) fs and 30(4) fs for states A and B, respectively. The most important information obtained from the analysis of tr2PPE data is the confirmation of the unoccupied nature of the electronic states A and B. With this information in hand, we will look in the theoretical DFT calculations to gain further insight into the character of these unoccupied electronic states.

### 4.3.3 Theoretical Calculations

The relativistic density functional theory (DFT) calculations performed by Prof. Peter Kratzer (University of Duisburg-Essen) for the 4/3-ML coverage of Pb on Si(111) is shown in Fig. 4.4a and 4.4b, along two high symmetry directions  $\Gamma K$  ( $k_y \parallel [1\bar{1}0]$ ) and  $\Gamma M$  ( $k_x \parallel [\bar{1}\bar{1}2]$ ), respectively.

The calculations are performed for a much larger  $k$  window compared to our experimentally accessible momentum range. Only about 1/4 of the total momentum is relevant in our result as indicated by the red boxes in Fig. 4.4a and 4.4b. The red boxes further indicate the electronic states present at the binding energies 3.5, 3.4, and 3.2 eV above the Fermi level  $E_F$ , at the  $\Gamma$  point, that are similar to the experimentally observed  $A_{upper}$ , A, and B states, in terms of their dispersion and energy separation. In order to visualize this clearly, the red box regions in the calculations are enlarged and put together with experimentally obtained results as shown in Fig. 4.4c and 4.4d for  $k_x$  and  $k_y$  directions, respectively.

Absolute energies of observed electronic states do not match with the theory, however, the density function used in the DFT calculations could result in non precise estimation of the energy as it is not designed for the unoccupied state calculations. Note also that the dominant orbital contribution indicated the DFT calculations is  $p_z$  (red circles) for state A and  $p_y$  (blue box) for state B and  $A_{upper}$ . This is also consistent with the experiment as the intensity for both  $A_{upper}$  and B is small for  $p$ - $p$  polarization combination and large for state A. This refers to the validity of the dipole selection rules that predicts with this polarization combination a maximum photoemission signal for the even symmetry wavefunctions such as  $p_x$  and  $p_z$  orbitals and a minimum intensity for the odd symmetry wavefunction such as  $p_y$  orbitals.

The above relativistic DFT calculations indicate a reasonable reproduction of experimental results. All three experimentally observed states with similar

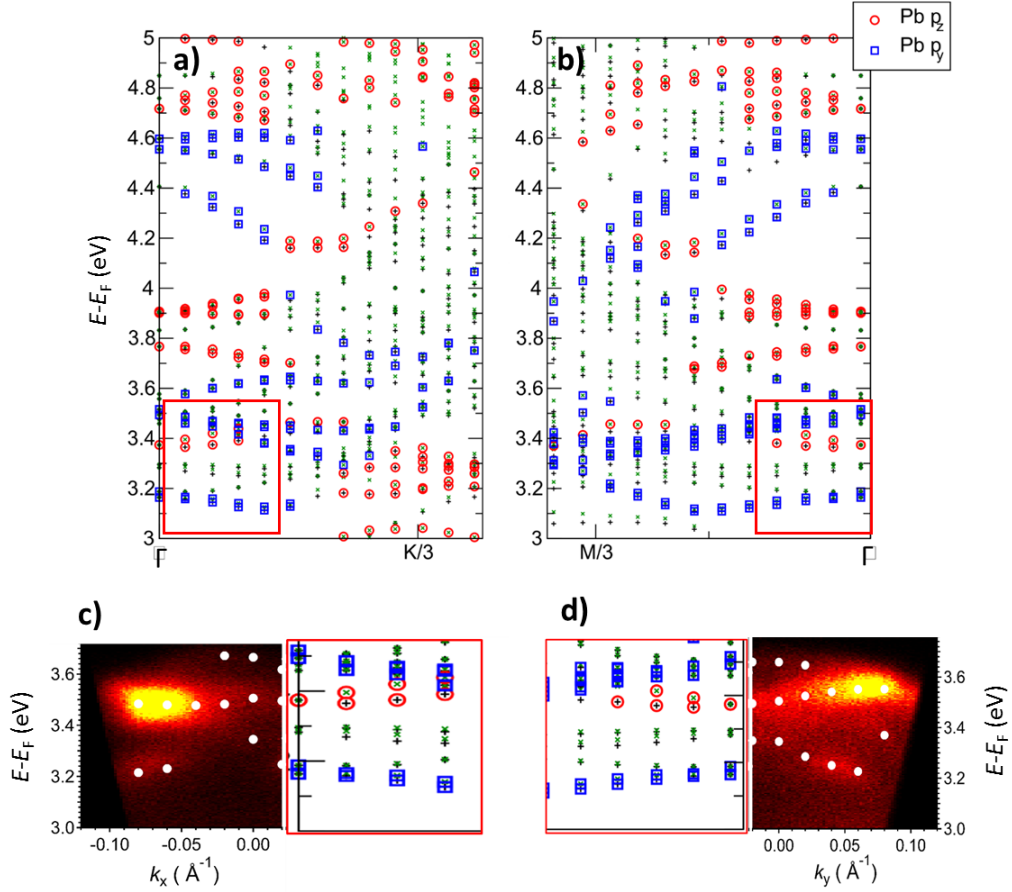


Figure 4.4: DFT calculations including the spin-orbit coupling effect performed for 4/3-ML Pb/ Si(111) along the directions  $\Gamma K$  ( $k_y$ ) (a) and  $\Gamma M$  ( $k_x$ ) (b). Red circles and blue boxes indicate dominant  $p_z$  and  $p_y$  orbital character, respectively. The '+' and 'x' signs within the box refer to spin-up and down directions. Red boxes along encompassing the electronic bands indicate the relevant momentum and energy region in which experimentally observed and theoretically calculated states are comparable. These boxes are enlarged and placed with the experimental findings for the momentum directions  $k_x$  (c) and  $k_y$  (d). Figure courtesy of Prof. Peter Kratzer (Faculty of Physics, University of Duisburg-Essen).

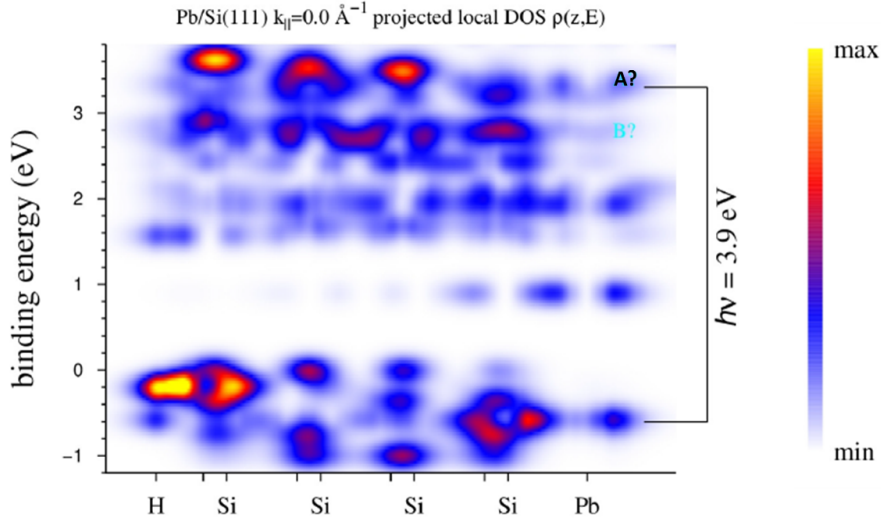


Figure 4.5:  $k_{\parallel}$ -projected local depth-resolved DOS for  $k_{\parallel} = 0$ . The color maps are obtained with the  $\delta$ -function replaced by a Gaussian of 0.25 eV FWHM. The feature marked  $A?$  (at  $E = 3.4$  eV) shows a dominant density from Si substrate layers. Figure courtesy of Prof. Eugene Krasovskii (University of the Basque Country, Spain).

dispersion are identified in the binding energy region  $E - E_F = 3.2 - 3.5$  eV. From these findings the unoccupied electronic nature of the observed states is further confirmed.

In addition to the DFT calculation of the electronic band structure of this system, the local depth resolved density of states  $\rho$  are also calculated. A preliminary result of calculations performed by Prof. Eugene Krasovskii (University of the Basque Country, Spain) for a model system of 4-layer Si(111) slab covered by a monolayer of Pb is shown in Fig. 4.5. A hydrogen monolayer is deposited on the opposite surface. Interestingly, the final state of the first step of photoexcitation, located around the energetic region of  $E - E_F = 3.4$  eV (potentially representing our state A), shows dominant density originating from Si atomic layers. This is in contrast to the DFT calculations that indicate the presence of Pb dominated surface state in this energy region.

### 4.3.4 Polarization Dependence

Polarization dependent change occurring in the photoemission intensity of electronic states is recorded by modifying the pump laser pulses ( $\hbar\omega_2 = 3.8$  eV) polarization from  $p$  to  $s$  using  $\lambda/2$  wave plate while keeping the polarization of probe laser pulses ( $\hbar\omega_1 = 1.9$  eV) fixed at  $p$ . For every  $10^\circ$  change in the E-field vector of the pump beam, a 2PPE intensity plot was recorded at maximum pump-probe overlap ( $\Delta t = 0$ ) and the complete set along  $k_x$  direction is presented in Fig. 4.6. First 2PPE plot, obtained with  $p$  polarized pump laser using  $\lambda/2$  wave plate shows a nice reproduction of the data obtained without using any polarizer (Fig. 4.2b). Keeping in view the fact that the experimental data contains rich amount of information, following discussion is divided in order to address particular state and momentum region in a step wise manner.

Analyzing the momentum region  $k_x > 0$  for state A, a weak intensity was observed initially for  $p$  polarized light, which enhances as the light vector moves towards  $s$  polarization. An interesting observation is the appearance of a split feature, already clearly observable when the light vector is at  $30^\circ$ . The intensity of this feature further enhances until the light vector reaches  $s$  polarization. This feature will be discussed in detail in the later part of this section. Contrary to positive momentum region, the intensity of state A in momentum region  $k_x < 0$  is stronger for  $p$  polarized light. However, it demonstrates a strong reduction in the photoemission intensity with respect to the change in the polarization and almost completely vanishes for  $s$  polarized light.

For state B, a symmetry break in the dispersion relation is already observed for  $p$  polarized light where the dispersion relation does not hold, i.e.  $E(+k_x) \neq E(-k_x)$ . In the momentum region  $k_x > 0$ , two branches of state B appear for  $p$  polarized light. As the light field vector rotates towards  $s$  polarization, the intensities of both electronic branches fade and finally vanish. Once again, an opposite behavior in the momentum range  $k_x < 0$  is observed, where initially

a weak feature at  $p$  polarized light, enhances along with the rotation of light polarization and becomes very strong for  $s$  polarized light.

Quantification of these complex evolution of polarization dependent photoemission intensity for states A and B is necessary for a comprehensive visualization. In addition, an insight into the symmetry character of the electronic states can be gained. In order to achieve this, the energy distribution curves (EDCs) are extracted by cutting along the binding energy axes from the polarization dependent 2PPE intensity plots, at the opposite momentum  $\pm k_x = 0.08 \text{ \AA}^{-1}$  (indicated by the white dashed lines in the bottom right panel of Fig. 4.6) integrated in a window of  $\Delta k_x = 0.02 \text{ \AA}^{-1}$ . The extracted EDCs are normalized with respect to the secondary edge and fitted with Lorentzian peak function while the exponential background related to the secondary electron is carefully subtracted. The fit function (red solid lines) describes the data (blue dots) well as can be seen in Fig. 4.7a and 4.7b in which vertical offset in the intensity scale is induced among the curves for clear visibility.

The peak intensities obtained as a result of fit function are plotted as a function of the polarization angle of the E-field vector of pump laser beam, at the opposite momentum  $\pm k_x$  for the electronic state A and B, as shown in Fig. 4.7c and 4.7d, respectively. 0 and  $90^\circ$  on polarization axes correspond to  $p$  and  $s$  polarized pump light, respectively. The electronic state  $A_{upper}$  and the upper branch of B (at  $+k_x$ ) are omitted from this analysis because owing to their weaker intensity, no meaningful dependence on the light polarization could be extracted. Nevertheless, for the upper branch of state B, polarization dependent evolution follows the similar trend as that of the lower branch, as can be seen in Fig. 4.6. For both states A and B, an opposite pump polarization dependent photoemission intensity at the opposite momentum  $+k_x$  and  $-k_x$ , is observed. This finding indicates opposite orbital characters present at the opposite momentum and contradicts the time-reversal symmetry in the electronic band structures of solid. The opposite orbital character can be

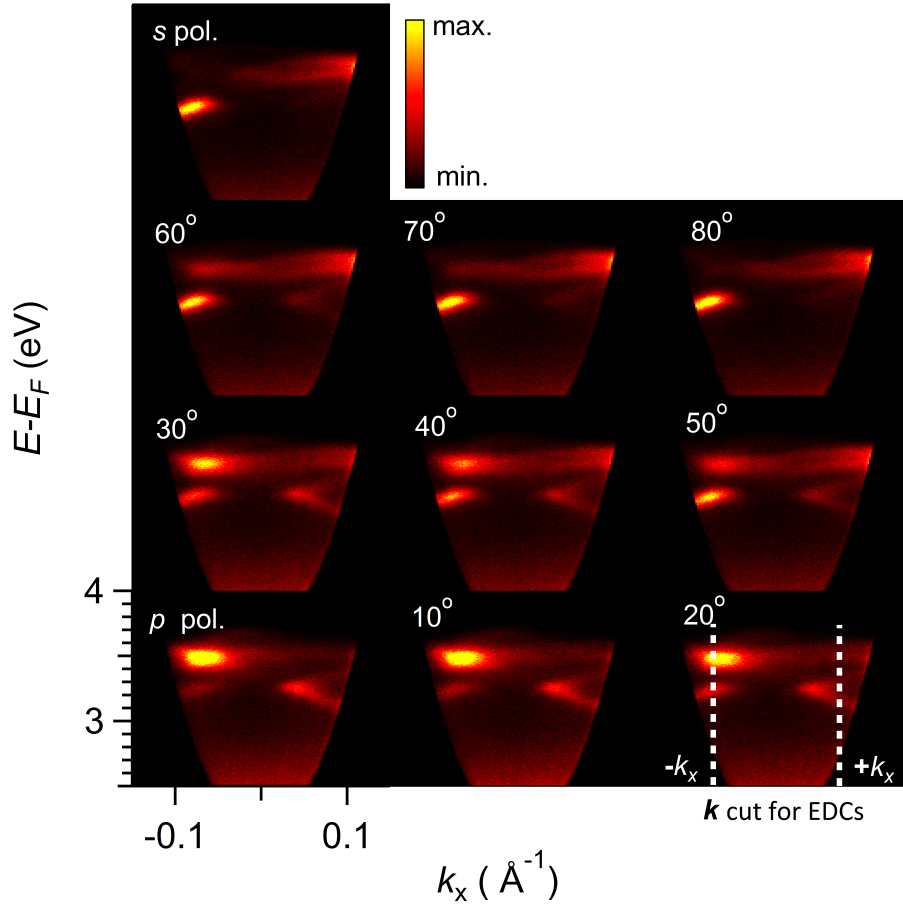


Figure 4.6: False color representation of the pump (UV:  $\hbar\omega_2 = 3.8$  eV) polarization dependent 2PPE spectra recorded along  $k_x$  for each  $10^\circ$  change in the E-field vector until it reaches  $s$  polarization. The color legend shows the intensity scale which remains same for each spectrum so that a change in the intensity as per polarization could be visualized. Horizontal and vertical axes range is the same as the bottom left panel for all the other panels. Probe beam (VIS:  $\hbar\omega_1 = 1.9$  eV) polarization remains fixed at  $p$  during the whole measurements. Dashed lines in the bottom right panel indicate the opposite momentum at which the energy distribution curves shown in Fig. 4.7 are extracted.

understood with the concept of dipole selection rules that have been explained in detail in the second chapter of this thesis work. Here, they are briefly described to make the content self-supporting.

The dipole selection rules, based upon the polarization of the incident light predict whether a specific transition between the free electron like final state  $\psi_f$  of even symmetry and an initial state  $\psi_i$  will be allowed or forbidden. They are strictly valid only when the mirror plane of a system coincides with the scattering plane that is spanned by the incident light vector, and photoelectrons that are coplanar with the surface normal. These selection rules can also be generalized for the 2PPE spectroscopy in which the final state in the first step of excitation will be an intermediate state. Following will be the results of the transition matrix element for various combinations of incident light and the initial state. Middle term  $H_{int}$  in the above equation refers to the Hamiltonian of system perturbed by the light field.

For an incoming  $p$  polarized (even symmetry with respect to the scattering plane) light, transition matrix element  $M_{if} = \langle \psi_f | H_{int} | \psi_i \rangle$  will be,

$$\begin{aligned} \langle even | even | odd \rangle &= 0 \\ \langle even | even | even \rangle &= 1 \end{aligned} \tag{4.2}$$

while for incoming  $s$  polarized (odd symmetry with respect to the scattering plane) light, transition matrix element will be

$$\begin{aligned} \langle even | odd | odd \rangle &= 1 \\ \langle even | odd | even \rangle &= 0 \end{aligned} \tag{4.3}$$

Although, the above set of equations is valid for the direct photoemission process, a general understanding can be drawn, that the same orbital symmetry character should exhibit the same evolution of polarization dependent intensity at the opposite momentum based upon the time-reversal symmetry relation

$E(+k_{\parallel}) = E(-k_{\parallel})$ . Based on the observations in Fig. 4.7, state A at  $-k_x$  and B at  $+k_x$  exhibit a similar trend by showing maximum and minimum intensity at  $p$  and  $s$  polarized light, respectively, indicating their even symmetry character ( $p_x$  or  $p_z$  orbital) with respect to the scattering plane. The presence of a  $p_z$  orbital is also indicated by the DFT calculations (Fig.4.4, state present at  $E - E_F = 3.4$  eV). The  $+k_x$  side of state A and  $-k_x$  side of state B exhibit maximum and minimum intensity for  $s$  and  $p$  polarized light, respectively, indicating an odd symmetry character ( $p_y$  orbital) with respect to the scattering plane. For state B at  $-k_x$ , again the similar state showing  $p_y$  orbital character is identified with the binding energy  $E - E_F = 3.2$  eV in the DFT calculation (Fig.4.4).

Along the high symmetry momentum direction  $k_y$ , the polarization dependent change is very small and no orbital switching at the opposite momentum of  $\pm k_y$  is observed. Therefore, the discussion of polarization dependent data along  $k_y$  direction is omitted.

### 4.3.5 Spin-Orbit Splitting

Following discussions will focus on the energy splitting of state A, observed along  $k_x$  direction for the polarization dependent 2PPE plots from the pump beam polarization angle of  $20^\circ$  and above (Fig. 4.6). Fig. 4.8a shows the EDCs extracted by cutting along the energy axis at various momentum values in the positive momentum region  $k_x \geq 0$ , from the 2PPE plot obtained for  $s$ - $p$  right panel in Fig. 4.6). An artificial offset on the vertical scale is introduced among the EDCs for clear visibility. Due to very low intensity, no clear energy splitting is observed at the momentum region  $k_x < 0$ . As can be seen, no energy splitting is present at the  $\Gamma$  point but it appears at a slightly higher momentum of  $k_x > 0.03\text{\AA}^{-1}$ . By fitting of the split energy feature with two Lorentzian type peak functions, the energetic position of peaks is extracted and plotted as a function of the momentum  $k_x$  in Fig. 4.8b. As can be seen,

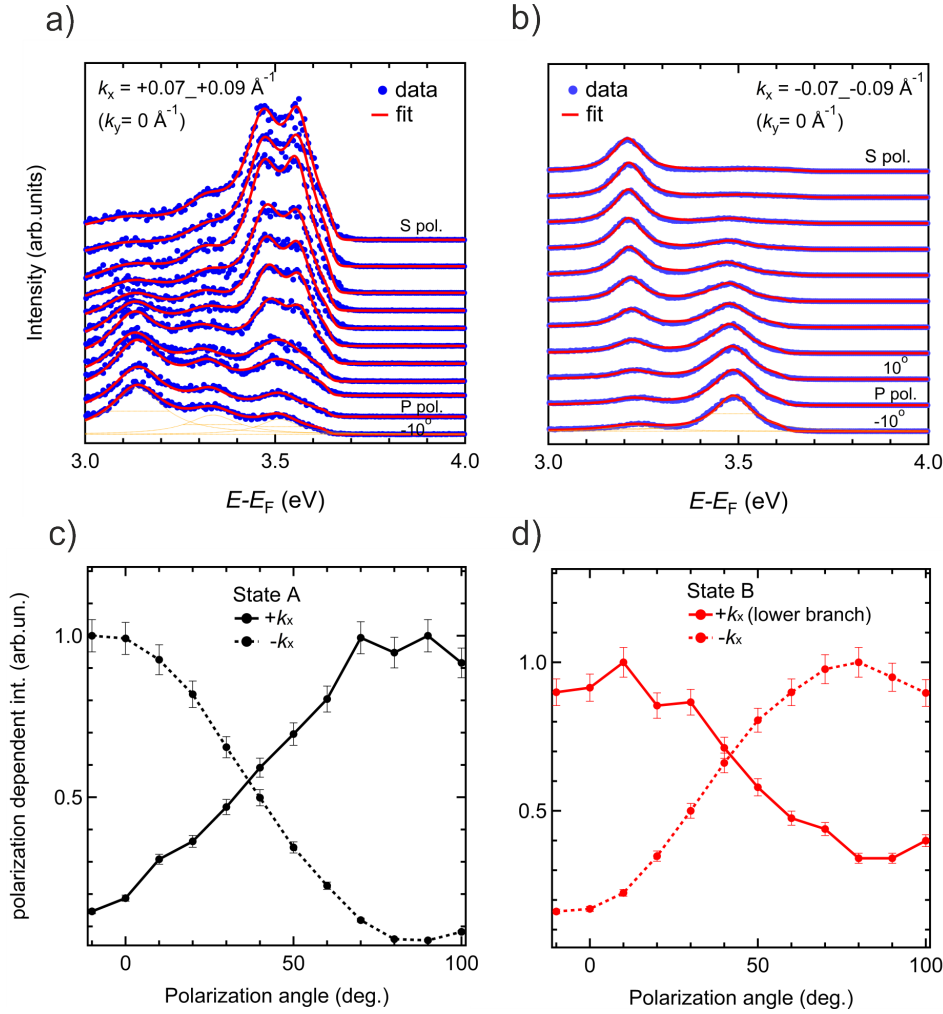


Figure 4.7: The energy distribution curves obtained from polarization dependent 2PPE intensity plots (Fig. 4.6) in a  $k$ -window range  $0.07 - 0.09 \text{ \AA}^{-1}$  (dashed lines in the bottom right panel of Fig. 4.6) are shown (blue dots) with fit function comprising of Lorentzian peaks and secondary electron background (red curves) for (a)  $+k_x$  and (b)  $-k_x$  directions. An offset along the intensity direction is introduced among the extracted curves for clear visibility. The obtained 2PPE intensity obtained from the fit function is plotted as a function of the pump polarization for state A in (c) state B (lower branch) in (d).  $0^\circ$  on x-axis corresponds to  $p$  and  $90^\circ$  to  $s$  polarized pump beam. An opposite evolution of polarization dependent 2PPE intensity indicates the opposite symmetry character of the orbitals present at the opposite momentum  $\pm k_x$  for both A and B states.

the size of the energy splitting  $\Delta E$  does not change significantly throughout the measured momentum space.

Is this splitting a manifestation of Rashba type of splitting, which is known for lifting the spin-degeneracy in the surface states due to break of space-inversion symmetry [129, 130]? To answer this question, we need to closely look at the main observations of the energy split state A and compare them to the general properties of a Rashba system.

- The presence of the peak splitting of state A at the higher momenta and the absence at the  $\Gamma$  point is a Rashba character [131] which related the absence of splitting at the  $\Gamma$  to its time-reversal in-variance.
- No significant change in the energy splitting magnitude  $\Delta E$  occurs in the accessible momentum range and maximum split value of  $\Delta E = 115$  meV is observed. This lie in an intermediate range compared to the other Rashba systems, such as the quantum well Pb states on Si (111) with  $\Delta E = 12$  meV [128] and a rather large  $\Delta E = 200$  meV for the Pb/Ge(111) [6]. The relativistic calculations for 4/3-ML Pb/Si(111) (Fig. 4.4) also indicated Rashba type splitting but with a rather small size of  $\Delta E < 20$  meV.
- The wavefunctions of the split peaks are identical as can be seen from the almost same intensity magnitude and a similar symmetry character revealed by the polarization dependent measurement (Fig. 4.6) in which both peaks exhibit similar polarization dependent intensity evolution. A peak split due to Rashba effect implies both peaks should have identical wave functions [131].

Furthermore, for the 4/3-ML Pb/Si(111) system, DFT calculations [35] and spin- and angle-resolved photoemission study [36] also indicated the Rashba splitting in the occupied electronic states.

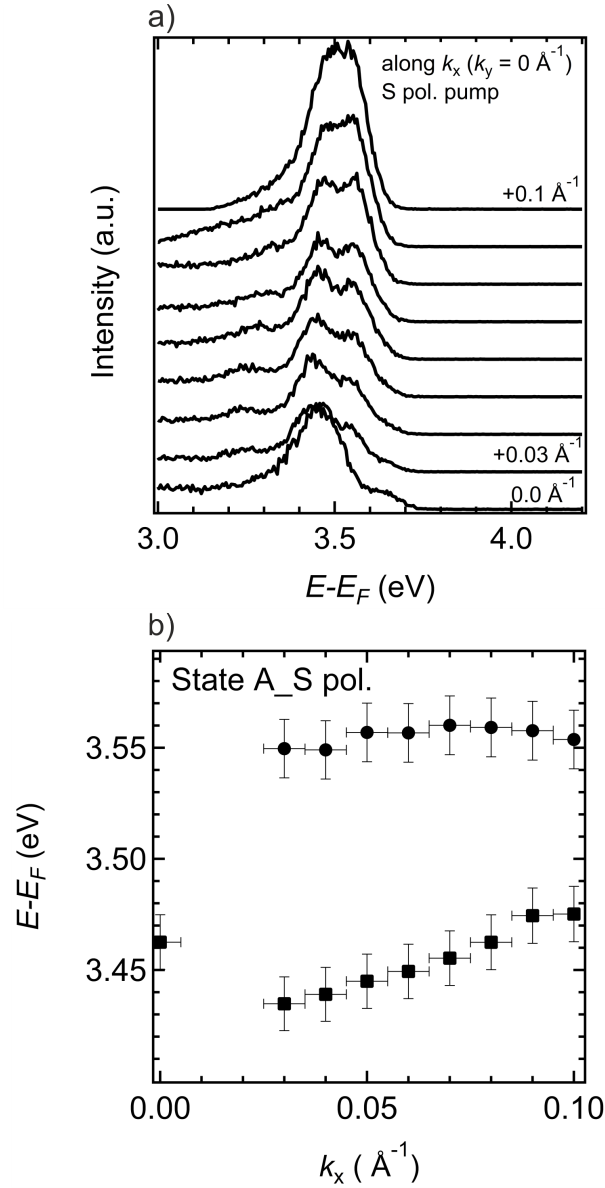


Figure 4.8: (a) Extracted energy distribution curves (EDCs) from various momentum points at the region  $k_x \geq 0$  from the 2PPE plot obtained for  $s$ - $p$  polarization combination of the pump and probe beams (top right panel in Fig. 4.6) are shown with an introduced offset along the intensity scale for clear visibility. Energy splitting in state A can be seen for the EDCs obtained at the momentum  $k_x > 0$ . (b) Energetic position of the split peak obtained in (a) is plotted as a function of momentum  $k_x$ . A maximum energy split of  $\Delta E = 115$  meV and a minimum of  $\Delta E = 80$  meV are observed. At the  $\Gamma$  point, the separate peaks merge and no splitting is observed.

Although the above discussions made a strong case of the presence of Rashba effect in our Pb/Si(111) system, it is understood that its confirmation requires further investigations using spin-resolved photoemission with large momentum accessibility. Nevertheless, our findings provide interesting points and motivation for the further study of this system, which can be important for the field of spin-based electronics.

## 4.4 Discussions

The observed symmetry breaking in the experimental data can be divided into three different categories. (i) The asymmetric intensity distribution across the  $\Gamma$  point, i.e.  $I(+k_x) \neq I(-k_x)$  and  $I(+k_y) \neq I(-k_y)$ . (ii) An apparent symmetry break in the electronic dispersion relation. (iii) Opposite orbital character at  $+k_x$  and  $-k_x$  momentum. The first symmetry breaking observation i.e. the asymmetric intensity distribution across  $\Gamma$  is not a new phenomenon and has been observed in various photoemission studies before and most often quoted as the linear dichroism in the angular distribution (LDAD) of ARPES in the literature [40, 126] and will be quoted the same hereafter. We argue that the last two symmetry breaking categories i.e. an apparently different electronic band structure across the  $\Gamma$  point and a switching of the orbital character at the opposite momentum  $\pm k_x$  are also a manifestation of the LDAD.

This can be understood as following. Presence of LDAD can fully suppress the photoemission intensity at a particular momentum region, which can result in an apparently different electronic state across the  $\Gamma$  point. This has been our observation in the angular resolved 2PPE intensity plot (Fig. 4.2a) along  $k_x$  direction where state  $A_{upper}$  exhibits a finite photoemission intensity at the momentum region  $k_x < 0$  but no intensity at  $k_x > 0$ . The upper branch of state B shows a finite intensity at  $k_x > 0$  but no intensity at  $k_x < 0$ .

An apparent reversal of the orbital character, that we observed in Fig.

4.7 at  $\pm k_x$ , can also occur due to the presence of the LDAD. It is assumed here, that the investigated electronic states A and B have mixed symmetry character i.e. they are composed of both the even ( $p_x$  and  $p_z$ ) and odd ( $p_y$ ) orbitals with respect to the scattering plane. Mixing of orbitals with different symmetry character occur in the system with strong spin-orbit coupling effects [54, 132] and should also be expected in our Pb/Si (111) system. Taking into account the presence of the LDAD, the even part of the wavefunction of state A, which is probed by  $p$  polarized light (bottom left panel of Fig. 4.6) shows a stronger spectral weight only at the momentum region  $k_x < 0$  and switches side to  $k_x > 0$  with  $s$  polarized light (top right panel of Fig. 4.6) which probes the odd character of the wavefunction. For the energetically lower lying state B, the whole process completely reverses (Fig. 4.7d). It should be noted that no complete suppression of intensity was observed which might be caused by the incomplete  $s$  or  $p$  polarization. This selective excitation at a particular momentum with a particular polarization gives an evolution of the polarization dependent 2PPE intensity in which the orbital characters appear to switch between even and odd symmetry at the opposite momenta. With the established argument, that the LDAD is the underlying cause of the different symmetry breaking phenomenon observed in our system, the discussion boils down to a single point, i.e. what is causing the LDAD in the photoemission process? It should be noted here that the LDAD has been reported in a large number of studies before [3, 19, 40–65, 125, 133–135] and in particular for the systems that have strong spin-orbit coupling such as the Rashba system [3, 19, 40, 41, 46–55, 126] and topological insulators [56–65]. However, the interpretations of the underlying causes are diverse and have not been discussed in detail in every literature. In the following discussion, we will review the main reasons of the LDAD that have been discussed in the literature and develop a qualitative understanding of the LDAD based on their interpretations.

### 4.4.1 Off-normal Light Incidence

One of the most widely used interpretations concerning the LDAD is the off-normal light incidence of  $p$  polarized light which breaks the mirror symmetry of the experimental geometry [40, 41, 133]. No asymmetry was seen or predicted for  $s$  polarized light.

In his paper on Bi-Ag surface alloy that exhibits electronic states with Rashba type splitting, Bentmann et. al. [40] explained that with  $p$  polarized light, the transition matrix element towards the  $x$  (in-plane) direction  $T_x$  and towards the  $z$  (normal) direction  $T_z$  add up differently at the opposite momentum region to induce the asymmetry. At the momentum  $+k_x$  the total intensity could be represented by  $|T_z + T_x|^2$  and at  $-k_x$  by  $|T_z - T_x|^2$ . It was further noted that the individual  $T_x$  and  $T_z$  components strongly modulate depending on the photon energies that causes the spectral asymmetry to shift and even to disappear for certain energies. Their findings are shown in Fig. 4.9. A strong asymmetry is evident from the angle-resolved photoemission intensity plots (darker color indicates higher intensity) obtained with  $p$  polarized light of energy 22 eV and 26 eV as shown in Fig. 4.9a and 4.9b. The shifting of the spectral weight and upon the change of energy is also evident. Contrary to that, the angle-resolved measurement obtained with 30 eV light energy exhibits a symmetric photoemission intensity distribution, as can be seen in Fig. 4.9c. In Fig. 4.9d, the calculated results of modulation in the individual component of intensity along the  $x$  or  $z$  direction as a function of the photon energies are shown. This gives a clear evidence of the major role played by this modulation in the photon energy dependent LDAD.

The above interpretation provides a satisfactory explanation of our results also, in particular for the results obtained with  $p$  polarized light that exhibit a strong LDAD (Fig. 4.3a). Nevertheless, a strong LDAD was also observed even with the data obtained with  $s$  polarized light (top right panel in Fig. 4.6),

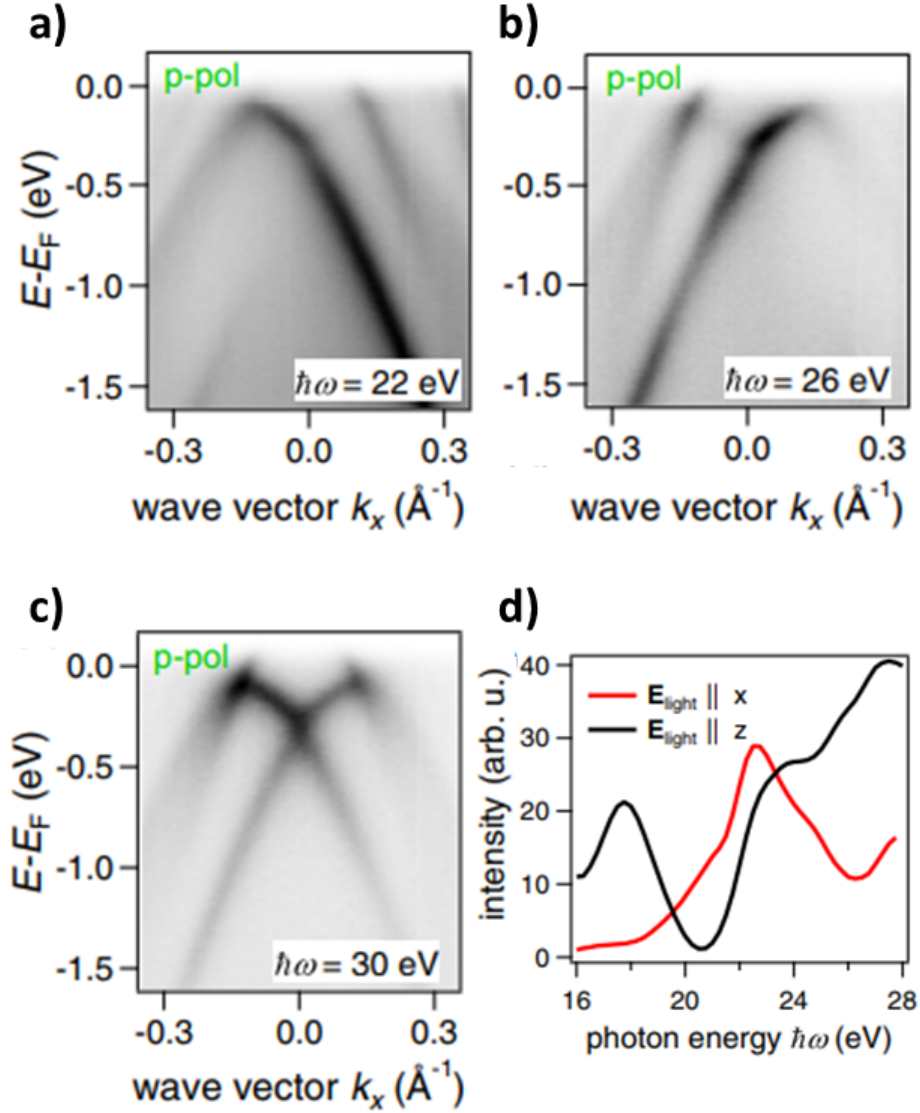


Figure 4.9: Angle-resolved photoemission intensity maps along  $k_x$  direction for BiAg<sub>2</sub>/Ag(111) taken with  $p$  polarized light for photon energy of 22 eV, (a) 28 eV, (b) and 30 eV (c). (d) shows the results of the calculation for the photon energy dependent intensities  $I_x$  and  $I_z$  contributions at the momentum  $-k_x$ . Taken from [40].

contrary to their finding. However, this should be noted here, that out of the two laser pulses, only the pump laser pulse was tuned to  $s$  polarization where  $p$  polarized probe laser pulses can still break the symmetry of the experimental geometry.

#### 4.4.2 Bulk State Effects

One of the widely discussed reasons of the asymmetry in the electronic structure and the photoemission intensity is the involvement of the bulk state in the photoemission process. The asymmetric electronic dispersion was observed in various photoemission studies performed on different systems such as H-terminated Si surface [43], As-Si(111)[44], Au/Si(553) [42], and Si (111)- $7\times 7$  [136]. The asymmetry was particularly evident along the  $\Gamma M$  direction which is also the asymmetric direction in the real space for (111) diamond like unit cell structures, due to their atomic arrangement.

This fact is depicted in Fig. 4.10a, in which the schematic of top four atomic layers is shown for the H-terminated Si(111) reconstructed surface. Taking into account the atomic layer of the bulk, the directions  $\Gamma K$  and  $\overline{\Gamma K}$  are equivalent but the  $\Gamma M$  and  $\overline{\Gamma M}$  are nonequivalent. Photoemission in the bulk state proceeds via the bulk final states. Depending on the perpendicular momentum component direction, electron can either emit out of the surface or disappear in the bulk. This perpendicular momentum component may change sign while going from  $k_{\parallel}$  to  $-k_{\parallel}$  and cause some electronic states to completely disappear at a given momentum direction and electronic structure to look different across the  $\Gamma$  point. This causes the break of the time-reversal symmetry for the bulk state that typically holds for the surface states [42–44].

The equivalent  $\Gamma K$  and the nonequivalent  $\Gamma M$  directions are also evident from the cross-sectional view of the bulk BZ projected onto the (111) surface as given in Fig. 4.10b. Results of angle-resolved photoemission investigation of the Si(111)- $7\times 7$  reconstructed surface (ref. [136]) are shown in Fig. 4.10c and

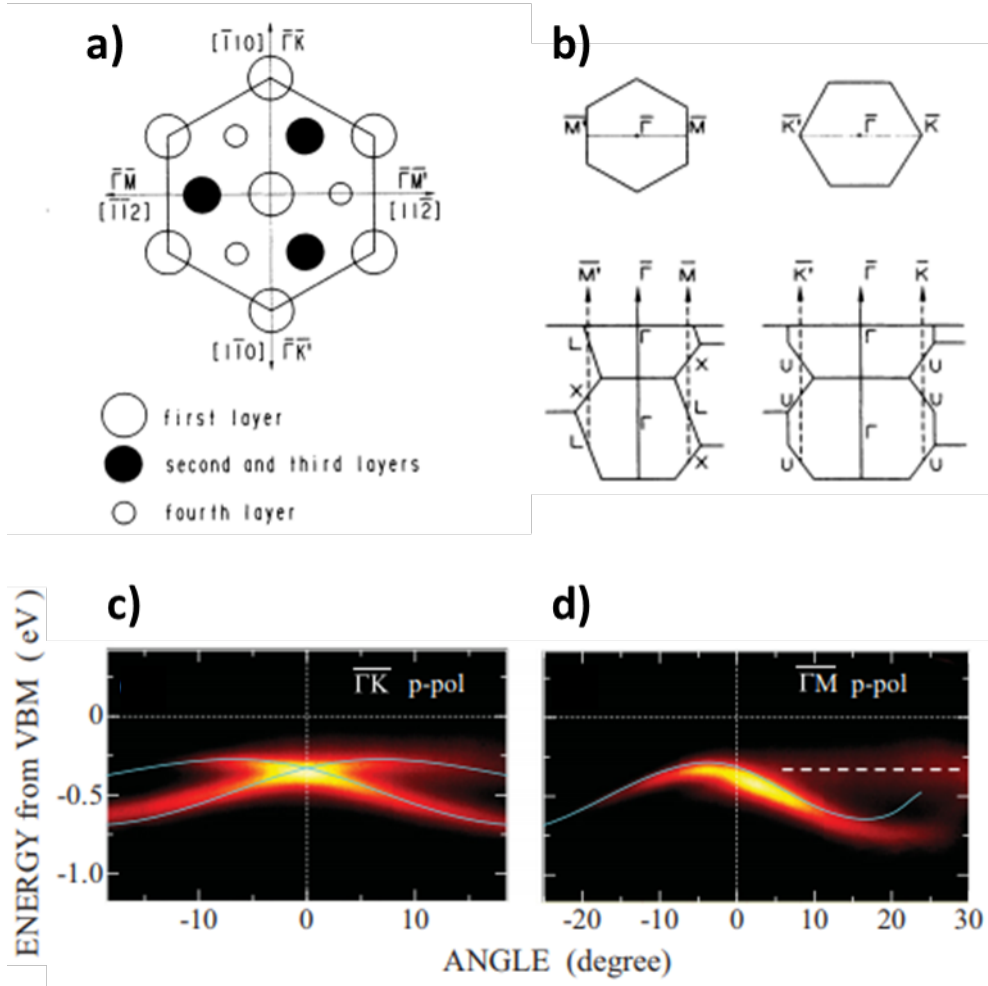


Figure 4.10: (a) Schematic view of the atomic arrangement below the (111) surface in Si(111)-(1 $\times$ 1) reconstruction. The corresponding reciprocal space directions are also marked. (b) Top and bottom sketches show the surface Brillouin zone and cross-section view of the bulk Brillouin zone, respectively. Both (a) and (b) are taken from [43]. Angle-resolved photoemission maps in false color representation for the Si(111)-(7 $\times$ 7) surface along the  $\Gamma\bar{K}$   $\parallel$   $[\bar{1}\bar{1}0]$  (c), and  $\Gamma\bar{M}$   $\parallel$   $[\bar{1}\bar{1}2]$  direction (d) taken with  $p$  polarized probe light. Results of theoretical calculations are shown with the light blue curves. Both ARPES plots are taken from [136].

#### 4.4. DISCUSSIONS

---

4.10d, for the  $\Gamma K$  and  $\Gamma M$  directions, respectively. A single electronic feature presenting asymmetric electronic dispersion across  $\Gamma$  in the  $\Gamma M$  direction can be observed. However, along the  $\Gamma K$  direction, the split energy states exhibit symmetric dispersion and intensity.

Bulk induced asymmetry is not only limited to the bulk electronic states but has been also observed in the pure topological surface state (TSS) of  $\text{Bi}_2\text{Se}_3$  [64]. It has been argued that the TSS has finite depth in the bulk due to its layer by layer structure. The photoemission signal is then the interference of the photoelectrons from all the layers but the photoelectron phase is defined by perpendicular  $k_z$  and parallel  $k_{\parallel}$  momentum components contributions. Change of sign from any of the momentum component leads to the asymmetric intensity.

Based on the bulk feature induced asymmetry interpretation, reasonable understanding of the asymmetric electronic structure observed along  $k_x$  ( $\Gamma M$ ) direction (Fig.4.2a) in our Pb/Si(111) system can be obtained.

Asymmetry in the electronic structure was observed in the electronic state  $A_{upper}$  and the upper branch of state B. The electronic state  $A_{upper}$  manifests presence and absence of the spectral weight at the momentum regions  $k_x < 0$  and  $k_x > 0$ , respectively. In contrast, the electronic state B exhibits a finite spectral weight only in the momentum region  $k_x > 0$  and is completely absent in the momentum region  $k_x < 0$ . It can be noticed, that this apparent asymmetry of the electronic structure was completely absent along  $k_y$  ( $\Gamma K$ ) direction (Fig. 4.2b) which is consistent with the description of symmetric  $\Gamma K$  direction indicated in Fig.4.10a and 4.10b. The presence of a dominant density of states from Si atomic layers around the energy region  $E = 3.4$  eV above the Fermi level was also indicated in the calculations (Fig. 4.5). Therefore, it is concluded that the  $A_{upper}$  and B states along  $k_x$  direction are the bulk Si features.

### 4.4.3 Effect of Final States

Another aspect of the LDAD has been associated with the structure of the final electronic state that is involved in the photoemission process. In his polarization and energy dependent photoemission investigations performed on Cu (111), Mulazzi et. al., reported a strong asymmetry in the photoemission intensity distribution from the Shockley surface state [45].

It was observed that the asymmetry remains for different excitation energies, polarization, and even by changing light incidence from off-normal to the normal angle. It was further claimed that Shockley state in Cu(111) is of pure surface nature and the bulk contributions that could potentially lead to asymmetries [42–44] do not play a role. The DFT calculations provided a reasonable reproduction of the experimentally observed photoemission intensity distribution, except when a channel of transition from an initial  $p$  orbitals of the surface state to  $d$  orbital of the final state is suppressed, which caused the asymmetry in the photoemission intensity to disappear. This results of these DFT calculations are shown in Fig. 4.11. The ARPES plots in the right and left columns were obtained with the right and the left circularly polarized light, respectively. The second, third, and fourth rows represent the photon energies of 50, 55, and 65 eV, respectively, at which the calculations were performed. All of these DFT results exhibited a strong asymmetry, which was only quenched when  $p$  to  $d$  channel of transition was suppressed that resulted in a symmetric photoemission intensity distribution for both right and left circularly polarized light, as shown in the top row. It was concluded that an assumption of free electron like final state in a photoemission process may not be always accurate. Even with much higher photon energies at which plane wave character of final states are expected, the asymmetry did not vanish.

From the above results, the important connection of the final states in determining the symmetric spectra in a photoemission experiment becomes

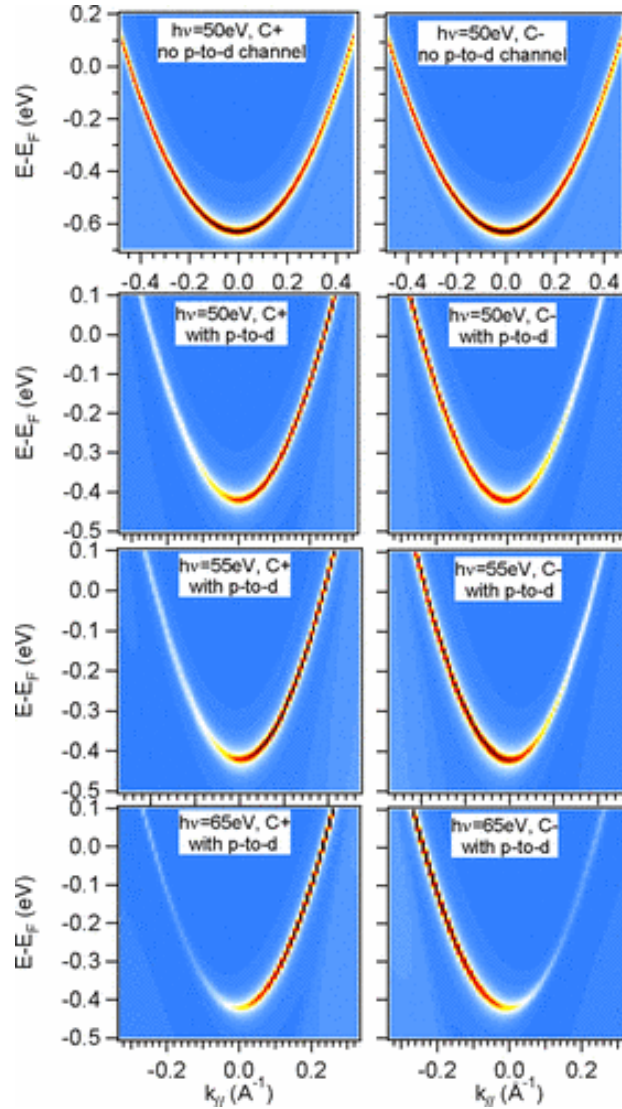


Figure 4.11: Calculated angle-resolved photoemission intensity plots of Cu(111) surface shown in false color representation. The right and left column shows the calculation obtained with the right and left circularly polarized light, respectively. The second, third, and fourth rows present the results obtained with the photon energies ( $\hbar\omega$ ) of 50, 55, and 65 eV. All the calculations, except the top row, are performed considering the transition from an initial  $p$  to  $d$  state, which gives the asymmetric intensity distribution. The symmetric photoemission intensity distribution shown in the top row presents the calculations obtained with the suppressed  $p$  to  $d$  channel. Taken from [45].

apparent. This can play a major role in the 2PPE experiments where the excitation energies are small and occurrence of the free electron like final states are less probable. Therefore, the presence of the LDAD can normally be expected in 2PPE experiments. Although a complete verification of this argument in our case requires proper calculations but cannot be totally omitted in our attempt to develop a qualitative understanding.

#### 4.4.4 Spin Effect

In a study of Bi/Ag(111) [47] system in which surface state exhibits Rashba type spin-orbit splitting, a strong asymmetry in the ARPES map along the  $\Gamma$ M direction was observed experimentally for the measurements obtained with the 22 eV linearly polarized light. The experimentally observed asymmetry was fully reproduced in the photoemission calculations taken into account the SOC effect. The calculations assuming no spin-orbit coupling removed the imbalance of the spectral weight across the  $\Gamma$  and produced a symmetric photoemission spectra. It was concluded that the spectral imbalance across the  $\Gamma$  is a spin-effect.

In several other Rashba systems [46, 137] and topological insulators [60, 62, 63], it was argued that the strong spin-orbit coupling effect produces a  $k$ -dependent orbital composition change. In  $k_x$ - $k_y$  momentum plot, this leads to a picture where the orbital character can switch between *even* and *odd* depending upon the momentum. This is schematically depicted for a Rashba system in Fig. 4.12 in which the inner and outer bands are shown. As can be followed from the in-plane orbital texture, the orbital character switches between *even* and *odd* symmetry upon a  $90^\circ$  rotation. Consequently,  $k$ -dependent asymmetries in the photoemission intensity also appear. Although this generic picture indicates an orbital switch by a rotation of  $90^\circ$  instead of  $180^\circ$ , it reflects the importance of symmetry mixing of the orbitals that occur in strong SOC systems [132] and that can lead to such asymmetries.

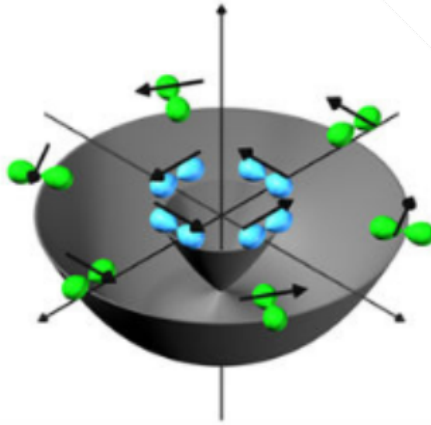


Figure 4.12: Schematic view of the in-plane orbital texture of inner and outer Rashba bands. Taken from [60]

The SOC in our Pb/Si(111) system is presumably strong because of the heavy nuclei of Pb and its monoatomic coverage on the Si surface. The DFT theory [35] and photoemission experiments [36] have indicated the presence of Rashba type splitting in this system. In fact, our DFT calculations (Fig. 4.4) and experimental results (Fig. 4.8) indicate the presence of Rashba type splitting in the unoccupied electronic band structure. Therefore, the asymmetries observed in our system can also be a consequence of spin-dependent effects in the photoemission process, despite the fact that the picture of  $k$ -dependent orbital switching does not fully fit to our findings.

#### 4.4.5 Summary

The above overview elaborates the various effects that lead to the LDAD in photoemission process. The observed LDAD in our Pb/Si(111) system cannot be sufficiently described by a single underlying reason. In fact, multiple effects have been contributed to induce these asymmetries.

The symmetry breaking resulting from the off-normal light incidence do explain the LDAD in the 2PPE spectra obtained with  $p$  polarized pump light. However, the LDAD observed with  $s$  polarized pump light may not be fully

explained under this phenomena because the symmetry of the photoemission geometry does not break with the  $s$  polarized light. Furthermore, this phenomenon does not describe the apparent asymmetry in the electronic structure observed in state  $A_{upper}$  and upper branch of state B along the momentum direction  $k_x$  ( $\Gamma M$ ). Nevertheless, this asymmetry can be explained under the phenomenon of bulk states effects which are known to exhibit asymmetry along  $k_x$  ( $\Gamma M$ ) due to asymmetry in the atomic arrangement. Lower energies used in the 2PPE experiments implies a longer mean free path which makes the photoemission from the bulk Si atomic layers possible in addition to the surface. Also, calculations (Fig. 4.5) indicated a dominant density of states belonging to Si layer in the energy region  $E = 3.4$  eV above the Fermi level. This confirms the bulk Si character of the two states and clarifies the origin of their symmetry.

Final states also play a major role in producing the LDAD in case they are not completely free electron like and possess a symmetry character which is not completely even with respect to the scattering plane. This is in general important in linear photoemission but could potentially have a significant impact in 2PPE measurements because of the low photon excitation energies used in these experiments. The final states in 2PPE are not far apart from the vacuum level and may not be completely free electron like. However, the investigation of the influence of final state effects requires the use of photon energy dependent photoemission measurements with excitation energies reaching upto 100 eV or even more. This is not possible to achieve in a 2PPE experiments in which both pump and probe beam energies are kept below the workfunction of materials which typically are in the range of 4-6 eV. A detailed theoretical calculation of the photoemission intensity distribution taking into account the original final states of Pb/Si(111) system is a possible way to investigate the correlation of final states and the LDAD.

Presence of the LDAD in systems with strong spin-orbit coupling is also discussed, and is important for Pb/Si(111) which exhibited Rashba type of

spin-orbit splitting in its electronic structure indicating strong SOC in this system. However, further understanding for verification of SOC being the underlying reason of the LDAD, spin-resolved photoemission measurements and relevant theory calculations are required, which could identify the effect of electrons spin on photoemission intensity distribution.

In summary, the phenomenon of off-normal light incidence explains the LDAD observed in the 2PPE spectra obtained with the  $p$  polarized light. Bulk states contribution explains the apparent asymmetry in the electronic band structure. However, none of them explain completely the LDAD observed with the  $s$  polarized pump light. The other two significant effects are the final states in 2PPE and strong SOC in Pb/Si(111), which can bring strong asymmetries in the photoemission intensity distribution irrespective of the polarization of light. However, their contribution and influence in producing the observed LDAD demand further experimental investigations and theoretical calculations.

## 4.5 Conclusion

In conclusion, we have investigated the unoccupied electronic band structure of the 4/3-ML of Pb/Si(111) in the vicinity of the  $\Gamma$  point, using femtosecond angle-resolved two-photon photoemission. The unoccupied nature of the identified electronics states are verified by the temporal evolution of their population dynamics obtained by employing the time-resolved two-photon photoemission. The electronic structure across  $\Gamma$  manifests several peculiar symmetry breaking characters including the presence of asymmetric photoemission intensity distribution ( $I(+k) \neq I(-k)$ ), apparently asymmetric electronic band structure, and an apparent switching of the orbital character at the opposite momentum  $\pm k_x$ . Our investigations reveal, that all of the observed symmetry breaking phenomenon is caused by the presence of the LDAD. It is further established, that the LDAD can arise due to various reasons including the symmetry breaking

of experimental geometry caused by off-normal incidence of  $p$  polarized light, involvement of bulk states, final state effects, and spin-dependent asymmetries present in the strong SOC system. While the parts of the observed LDAD such as an apparently asymmetric electronic band structure and photoemission intensity distributions are reasonably described by the phenomenon of bulk states effects and off-normal light incidence, the asymmetry observed with the  $s$  polarized pump light may not. Here, the phenomenon of final state effect and strong SOC might play a role which can induce LDAD irrespective of the polarization of the incident light. However, investigation of the real magnitude of their contribution in resulting LDAD requires further experimental and theoretical studies that are beyond the scope of this thesis work.



---

# Electron Scattering Dynamics in Pb/Si(557)

## 5.1 Introduction

In the previous chapter, we presented the results related to the 2D Pb/Si(111) system. More interesting physics unravel with further reduction in the dimensionality. On the structural level, preparation of a quasi-1D Pb/Si system is achieved using vicinal Si(111) surfaces that owing to their finite miscut angle give rise to the formation of steps. With this geometry, the direction of growth for the Pb nanowires arrays is predefined and continuity of structure in perpendicular to steps direction is disrupted. This chapter deals with the quasi-1D Pb/Si(557) system which is investigated by means of femtosecond laser based non-linear time-resolved photoemission spectroscopy. The results concerning the polarization-dependent direct photoemission and static non-linear photoemission of this system are presented in the Appendix.

Due to the opportunities offered by non-linear photoemission spectroscopy,

the experimental analysis of the unoccupied electronic states at surfaces has made immense development during the last two decades. Early experiments utilized the peak intensity increase of short pulse dye lasers over continuous wave sources to generate photoelectrons by absorption of two photons simultaneously in two-photon photoemission (2PPE) [138]. The application of femtosecond Ti:sapphire lasers continued this evolution and permitted a widespread investigation of ultrafast electron dynamics at surfaces by performing time-resolved experiments using pump-probe techniques [138–141] jointly with theoretical developments [142, 143]. Recently, the time-resolution has been pushed further to few femto-[144] and well into the attosecond regime [145] offering exciting future opportunities to analyze collective electron dynamics directly in the time domain.

Extensive investigations of the image potential states [140, 141, 146, 147] and the electronic surface resonances induced by alkali adsorption on metal surfaces [148–150] established that the lifetime of excited electrons is typically several ten to hundred femtoseconds if the respective unoccupied surface state occurs within an orientational band gap. The absence of such an orientational band gap and degeneracy with the electronic bulk state leads to ultrafast wave packet propagation into the bulk [150] which is inherently linked to a broadening of the photoemission line width limiting its detection by the surface sensitive 2PPE technique. Moreover, hot electron dynamics in quantum well states in metallic overlayers have been investigated [28]. Relaxation times of few femtoseconds have been reported for layers on metallic substrates [151, 152], which increased to above 100 fs for states in a layer degenerate with a band gap of a semiconducting substrate [74]. These differences suggest elastic scattering into bulk states on the metallic substrates to play a major role in the relaxation times in metallic overlayers on metallic substrates. All these studies show that hot electron dynamics in two dimensional metallic systems have been investigated in detail and the essential elementary processes relevant

in ultrafast electron dynamics are known and understood.

On single crystal surfaces, one dimensional structures like steps, terrace step decoration, and reconstructions can be prepared using established surface science methods under ultrahigh vacuum (UHV) conditions [153]. The influence of steps regarding the scattering and relaxation dynamics of image potential states were investigated on vicinal Cu(100) surfaces [66–71].

Fig. 5.1 shows the result of an investigation of Cu(119) surface by means of two-photon photoemission (taken from [71]). On top panel of Fig. 5.1a, a hard-sphere model of Cu(119) surface is drawn indicating the presence of steps. In the energy  $E$  versus parallel momentum  $k_{\parallel}$  graph, three image potential states  $n=1, 2$ , and  $3$  can be seen with their mapped band dispersion (filled circles). The bottom panel shows the momentum dependent decay rate of image potential state  $n=1$  and  $2$ . As can be seen for  $n=2$ , the decay rate  $\Gamma_n$  is symmetric and roughly parabolic. With the increase of binding energy the energy phase space grows, that leads to an increase of the decay rate across  $k_{\parallel}=0$ . On the other hand, the decay rate for image potential state  $n=1$ , shows momentum dependence indicating longer lifetimes for electrons running upstairs compared to those running downstairs.

In addition to step induced scattering, these 1D surface systems provide an interesting field of study for one dimensional physics including spin-charge separation and charge density wave (CDW) formation leading to metal-insulator transitions. While pump-induced melting of CDW in layered crystals has been investigated in the time domain using femtosecond optical [154], time- and angle-resolved direct photoemission [155, 156], and transmission electron diffraction [157, 158] pump-probe methods, the investigation of photoinduced melting of CDW on 1D surface reconstructions is so far limited to surface sensitive electron diffraction [159]. Rügheimer et al. have published a first time-resolved 2PPE study of the one dimensional Si(557)-Au atomic chain system [38]. This work reported three electronic states, which were absent in electronic structure

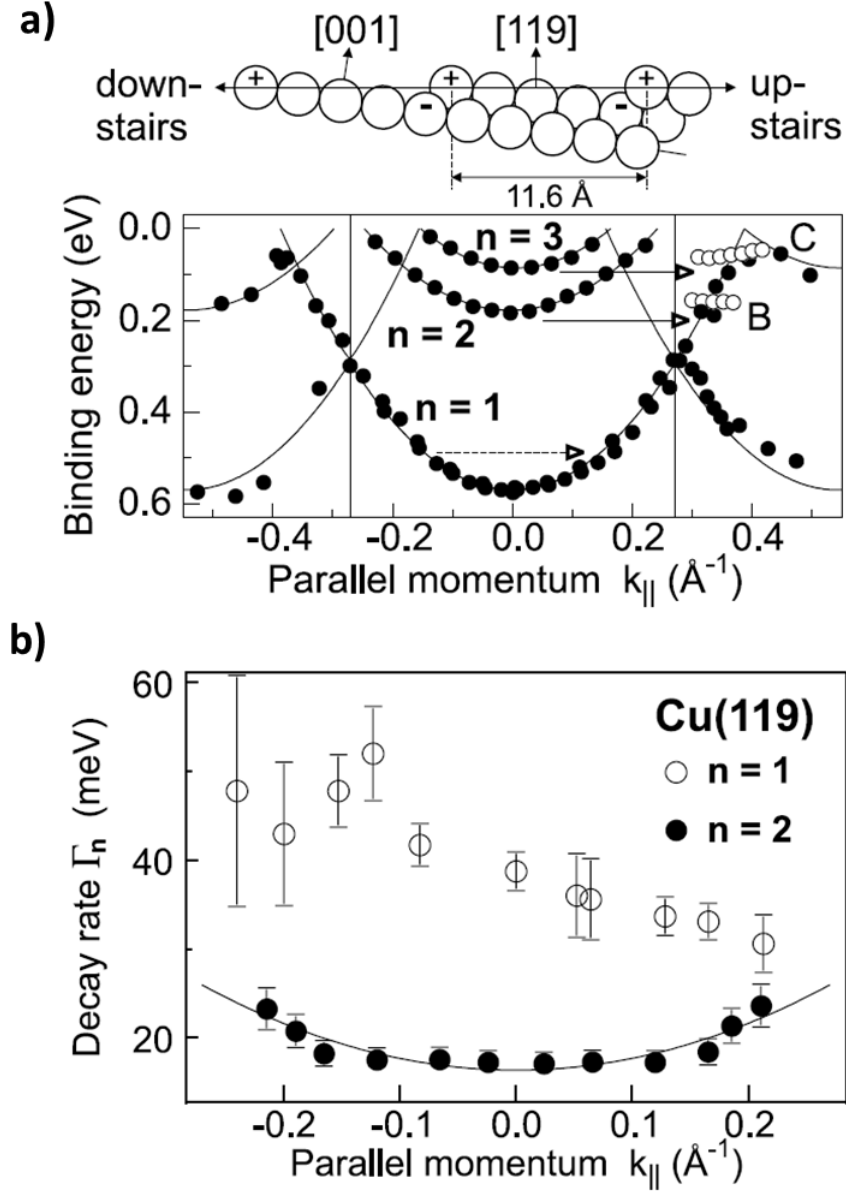


Figure 5.1: (a) On top, a hard-sphere model of bulk truncated Cu(119) surface is presented. The graph plot in the bottom shows the dispersion curves  $E(k_{\parallel})$  for the three image potential states  $n=1,2$ , and 3. Positive and negative  $k_{\parallel}$  values correspond to the direction running upstairs and downstairs, respectively. The boundary of the surface Brillouin zone is indicated by vertical lines. (b) The decay rate as a function of parallel momentum for image potential states  $n=1$  and 2. The figure is taken from [71].

calculations. Biedermann et al. studied the occupied and unoccupied electronic structure of the quasi one-dimensional Si(553)-Au reconstruction and identified an unoccupied spin-split silicon step-edge state [42].

Our focus here is the study of quasi- one dimensional surface system Si(557)-Pb which was previously shown to exhibit one dimensional electric conductivity below a transition temperature of  $T_c = 78$  K [72, 73], while high-resolution angle-resolved photoemission measurements did not show any noticeable temperature dependence of core- and valence-band photoemission spectra [160, 161].

In Fig. 5.2, the temperature-dependent conductivity measurements performed parallel ( $[1\bar{1}0]$ ) and perpendicular ( $[\bar{1}\bar{1}2]$ ) to the wire direction is shown (taken from [162]). Above the phase transition temperature of  $T_c = 78$  K, the system is conducting in both directions. Below  $T_c$ , the conductivity ceases in perpendicular to wire direction. No indication of further instabilities for this system was observed until a temperate reaching down to 4 K.

The experimental investigations performed on Pb/Si(557) in this chapter is divided into two parts. In the major part of the study, angle- and time-resolved 2PPE is employed to analyze the unoccupied electronic structure and understand the influence of step edges on electron scattering dynamics. Most of the results from this part have been published in [75]. The investigations revealed two electronic bands whose dispersion and binding energies are in reasonable agreement with results obtained by density functional theory (DFT) calculations. We observe momentum averaged lifetimes of 24 fs and 35 fs at energies 3.55 eV and 3.30 eV above the Fermi level that are explained by a position of these states within an energetic region with a strongly reduced electronic density of states of the Si substrate. Furthermore, varying relaxation rates as a function of electron momentum perpendicular to the step edges have been identified that cannot be described by simple rate equation models. We rather have to take anisotropic, momentum-dependent dephasing processes, caused by (quasi-)elastic scattering, into account.

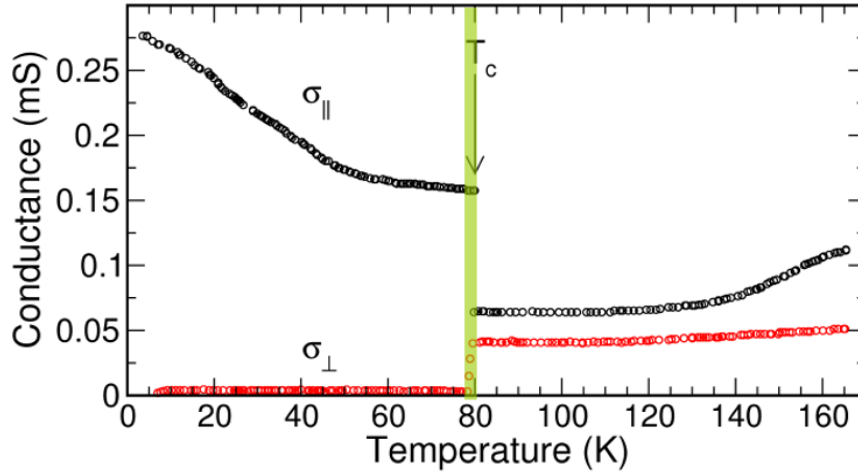


Figure 5.2: Conductance curve obtained for Pb nanowires on Si(557) as a function of temperature along parallel ( $[1\bar{1}0]$ ) and perpendicular ( $[\bar{1}\bar{1}2]$ ) to the wire direction. A vertical line is drawn to indicate the occurrence of phase transition. The figure is taken from [162].

In the second part, temperature-dependent angle- and time-resolved 2PPE is used to study the effect of the phase transition on the electron scattering dynamics. While the small differences among the population dynamics obtained for integrated-momentum and at various temperature were observed, no clear evidence of the phase transition was found on the electrons scattering process.

## 5.2 Experimental Method

The experimental methods have been discussed in the third chapter of this thesis work. In addition, the chapter also covers the details concerning the Pb/Si(557) sample preparation. Therefore, only the relevant details of the experimental technique will be briefly discussed here.

Femtosecond laser pulses were generated by a commercial mode-locked Ti:Sapphire based pulsed laser system (Coherent RegA 9040) operating at a repetition rate of 250 kHz and a central wavelength  $\lambda = 818$  nm ( $\hbar\omega = 1.52$  eV). We employed frequency conversion of the fundamental laser output through

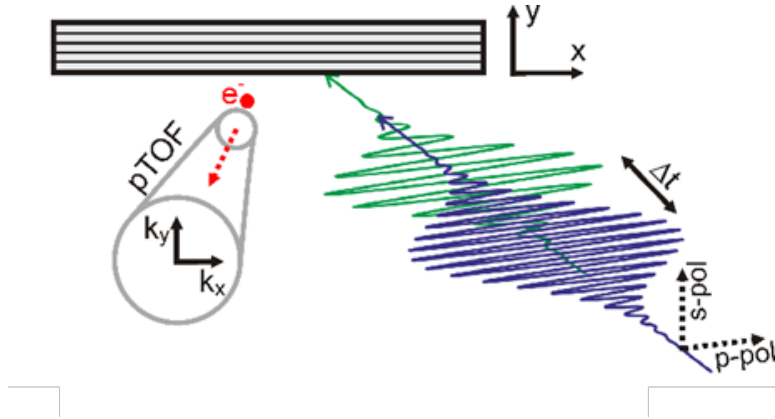


Figure 5.3: (a) Sketch of the experimental geometry. Unless otherwise specified, both pulses  $\hbar\omega_1$  and  $\hbar\omega_2$  used for the 2PPE process were p-polarized (parallel to the step edges). Photoemission spectra were recorded by a position-sensitive time-of-flight spectrometer that records photoemission events with momentum components along ( $k_x$ ) and perpendicular ( $k_y$ ) to the wire array simultaneously. Taken from [75].

nonlinear optical processes in a commercial optical parametric amplifier system (OPA, Coherent 9450) for bi-chromatic 2PPE. The fundamental OPA photon energy was tuned to  $\hbar\omega_2 = 1.9$  eV (visible, VIS) and part of the beam was subsequently frequency-doubled in a  $\beta$ -barium borate crystal to  $\hbar\omega_1 = 3.8$  eV (ultra-violet, UV). Temperature-dependent measurements were performed using slightly higher energies of  $\hbar\omega_2 = 2.08$  eV and frequency doubled  $\hbar\omega_1 = 4.13$  eV. Both pulses were  $p$  polarized. Femtosecond temporal resolution was obtained by controlling the time delay  $\Delta t$  between both pulses. Photoelectrons were analyzed with a self-built position sensitive time-of-flight spectrometer (pTOF) which employs a commercial position sensitive delay line anode (RoentDek Handels GmbH, Germany)[117]. This instrument acquires four-dimensional data sets, i.e. photoemission intensity as a function of photoelectron kinetic energy and two mutually independent momentum directions  $k_x$  and  $k_y$  (Figure 5.3). The overall spectral, temporal, and momentum resolution was 60 meV, 70 fs and  $2 \text{ m\AA}^{-1}$ , respectively. To avoid electric field induced acceleration of the laser excited photoelectrons with few eV kinetic energy, the vacuum levels

of the sample and the electrically grounded pTOF spectrometer were aligned by applying an accelerating bias voltage of -400 meV.

A major part of these measurements was performed at a temperature of 85 K by cooling with liquid nitrogen. This temperature is above the phase transition temperature of 78 K which was earlier reported for this system [72, 73]. Temperature-dependent measurements were carried out with the aid of liquid helium that allows reaching the lowest temperature of 35 K at the sample, and thereby, enables a study of the effect of the phase transition on the sample properties. During measurements, the temperature at the sample was measured by a diode temperature probe mounted adjacent to the Si wafer on the sample holder.

## 5.3 Results

### 5.3.1 Angle- and Time-Resolved 2PPE of Pb/Si(557)

#### Unoccupied Electronic Structure

Figure 5.4 shows the 2PPE data extracted at the temporal pump-probe overlap ( $\Delta t = 0$ ) and for the  $p$ - $p$  polarization combination of UV and VIS laser pulses obtained along two high symmetry, parallel ( $k_x \parallel [1\bar{1}0]$ ) and perpendicular ( $k_y \parallel [\bar{1}\bar{1}2]$ ) to the step directions. Zero in-plane electron momentum  $\Gamma$  refers to normal photoemission from the macroscopic Si(557)-surface, which is 9.45 degree tilted with respect to the microscopic Si(111) terraces. At normal photoemission, two distinct unoccupied electronic signatures A and B could be identified at the binding energies 3.55(5) eV and 3.30(5) eV above the Fermi level  $E_F$ , respectively. Note that the binding energy determination requires the assignment of the populating (pump) and photoemitting (probe) laser pulses, which was found to be UV and VIS, respectively based on the result of our time-resolved experiments discussed in Section 5.3.1. In a separate direct

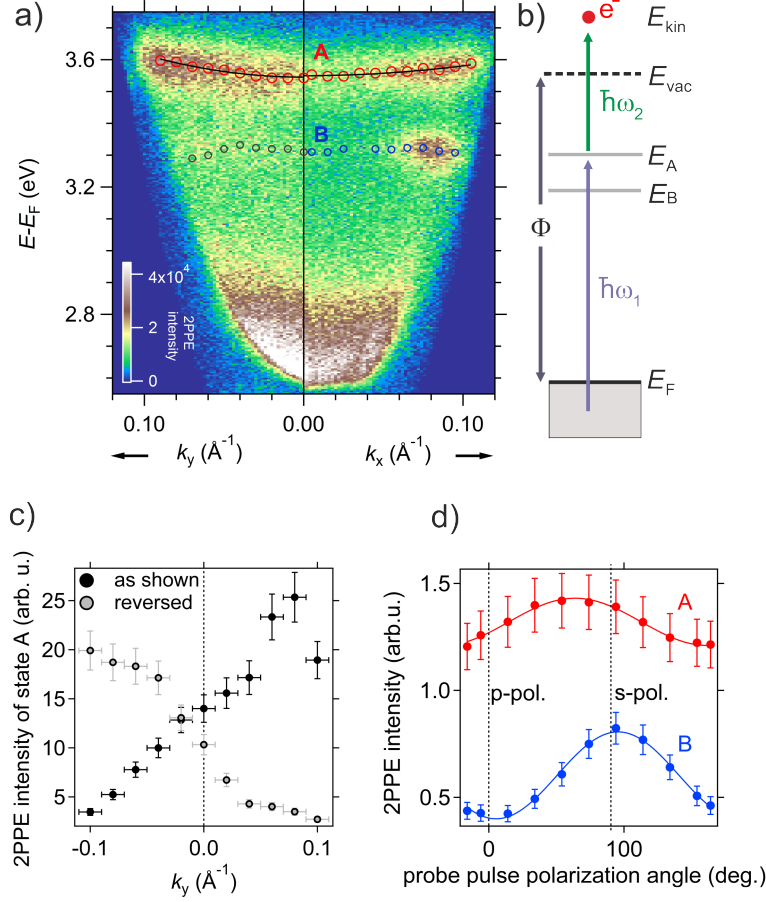


Figure 5.4: (a) 2PPE spectra recorded parallel ( $k_x$ ) and perpendicular ( $k_y$ ) to the wire directions at  $\Delta t=0$  for  $\hbar\omega_1 = 3.8$  eV and  $\hbar\omega_2 = 1.9$  eV. The energy axis shows the intermediate state energy, referenced to the Fermi level  $E_F$ . Open circles indicate the peak maxima. (b) Schematic energy level diagram for the pump-probe process. Intermediate states with energy  $E_A$  and  $E_B$  are first populated by the UV pulse ( $\hbar\omega_1$ ). Subsequently, the electrons are promoted above the vacuum level  $E_{\text{vac}}$  by the VIS pulse ( $\hbar\omega_2$ ), where they are detected with respect to their kinetic energy  $E_{\text{kin}}$ . (c) Total 2PPE yield (including background) in the energy window dominated by state A as a function of step-perpendicular momentum direction  $k_y$  for the dataset discussed throughout the manuscript (black markers) and for the reversed sample (grey markers). (d) The momentum-averaged 2PPE intensity in the energy window dominated by states A (red markers) and B (blue markers) as a function of probe pulse ( $\hbar\omega_2$ ) polarization. Taken from [75].

### 5.3. RESULTS

---

photoemission measurement performed with frequency-quadrupled pulses of the fundamental laser wavelength ( $4\hbar\omega = 6.06$  eV), workfunction of the system was determined to be  $\Phi = 4.35(5)$  eV. This obtained  $\Phi$  is then used to finally determine the binding energies of the observed electronic signatures with respect to the Fermi level  $E_F$  can be calculated as  $E - E_F = E_{\text{kin}} + \Phi - \hbar\omega_2$ . The whole 2PPE process with the respective level of different energies is described in the schematic of Fig. 5.4b. From the 2PPE intensity plots, energy distribution curves (EDCs) at various  $k$  values are extracted by making a cut along the energy axis and the intensity maxima of both electronic signatures representing  $E(k_x, k_y)$ , are plotted by the open circles in Fig. 5.4. Effective electron masses of  $m_{x,A}^* = 1.4(2)$  and  $m_{y,A}^* = 0.6(1)$  were extracted for the uppermost state A along the high symmetry directions  $k_x$  and  $k_y$ , respectively. Determination of effective electron masses for state B is omitted as it shows no simple parabolic dispersion.

The spread of corresponding electronic wave function across the steps is evident by the low effective mass of electron in this direction, contrary to the case of occupied electronic band structure from earlier direct photoemission measurements on this system [73]. It was shown in this study that anisotropic contours replicated with  $\Delta k_y = 2\pi/d_{\text{step}}$  forms the Fermi surface of the system. Furthermore, it was indicated that electronic excitations far above the electronic band gap of  $\Delta E \approx 20$  meV can propagate almost freely above the step edges [73].

State A also exhibits an interesting behavior of the photoemission intensity change perpendicular to the step ( $k_y$ ) direction. As can be seen in Fig. 5.4c, the state can be well observed for  $k_y > 0$ , while for  $k_y < 0$  the photoemission signal is reduced. A clearly opposite trend of intensity dependence was observed for a  $180^\circ$  azimuthal rotated sample. At large negative momentum values ( $k_y \leq -0.06 \text{ \AA}^{-1}$ ) for the non-rotated sample, the photoemission signal of A gets broadened and an incoherent background that possibly originates from

excitation in the Si substrate, starts to contribute in the total signal in a non-negligible way. However, total 2PPE signal, including the background will be referred as the intensity of electronic signatures everywhere in the text. The inversion of 2PPE intensity observed for azimuthal rotation of the sample indicates that the contrast in the photoemission yield is the intrinsic property of the Pb-Si(557) reconstruction. We conclude that such behavior is the result of the presence of steps where the opposite momenta  $k_y$  correspond to "step-up" and "step-down" situations, respectively.

Figure 5.4 also shows the dependence of the momentum-averaged 2PPE yield for states A and B on the change of probe (VIS) pulse polarization angle. The maximum and minimum photoemission yield corresponding to  $s$  and  $p$  polarized light was only found for state B. State A shows a non-trivial dependence on the polarization angle. This aspect of polarization dependence on the probe beam will be discussed further in the discussion Section 5.3.2, related to the origin of states A and B.

### Analysis of Relaxation Dynamics

Ultrafast dynamics in the Pb/Si(557) system was measured by changing the pump-probe delay time  $\Delta t$  between the laser pulses at  $\hbar\omega_1$  and  $\hbar\omega_2$ .

Fig. 5.5 shows the 2PPE intensity as a function of  $\Delta t$  after averaging over the accessible momentum space ( $|k_x| \leq 0.11\text{\AA}^{-1}$ ,  $|k_y| \leq 0.11\text{\AA}^{-1}$ ). A delay dependent 2PPE intensity can be observed for both intermediate states A and B, as well as for the third, continuum-like signature C which we did not discuss above. This feature is centered around  $E - E_F = 2.7$  eV but spans in the whole energy range between the secondary edge and the region where electronic signatures A and B are found (3.55(5) eV and 3.30(5) eV above  $E_F$ , respectively). It is also evident from Fig. 5.4, where C is spectrally incoherent and does not show any clear  $\mathbf{k}$ -dependence indicating its secondary electronic excitation nature. In general, an energy-dependent relaxation time can be

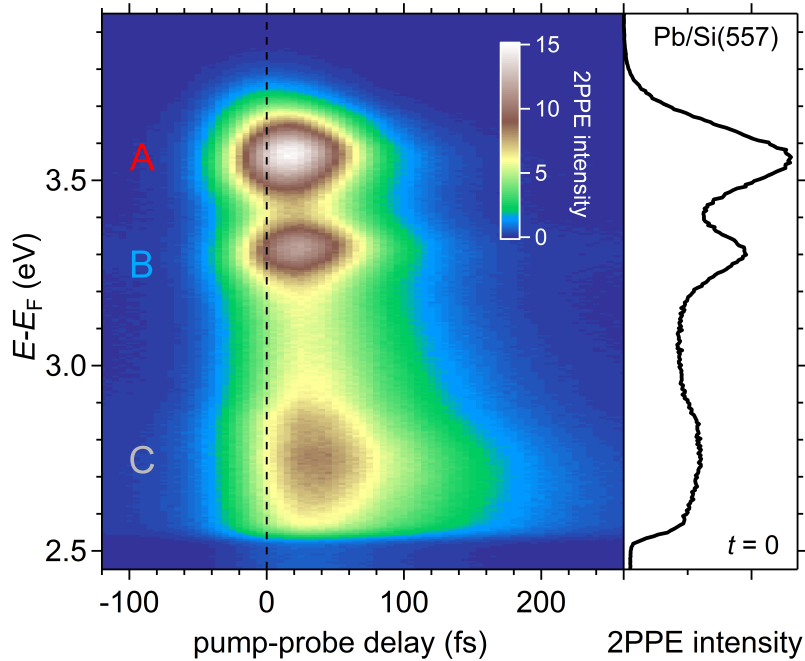


Figure 5.5: The momentum-averaged 2PPE intensity as a function of pump-probe delay  $\Delta t$  in a false-color representation. Positive delay times refer to the situation where the intermediate states are populated by the UV pulse ( $\hbar\omega_1 = 3.8$  eV) and probed by the VIS pulse ( $\hbar\omega_2 = 1.9$  eV). The right panel shows the momentum-averaged 2PPE spectrum recorded at  $\Delta t = 0$ . Taken from [75].

observed that increases with decreasing the energetic distance to the Fermi level.

In order to quantify the ultrafast dynamics of electronic signatures, the population dynamics curves were extracted by a horizontal cut along the pump-probe delay axis in the respective energy windows where the 2PPE signal from the electronic signatures is visible (Fig.5.5). The cross-correlation (XC) curve of the pump and probe laser pulses was extracted from the high energy carriers (corresponding to intermediate state energies of  $E - E_F = 3.73$ - $3.80$  eV. The XC curve shows no clear asymmetry in time domain indicating that no lifetime is involved and a simple Gaussian function fitting gives the full width half maximum value of  $70(1)$  fs. Extracted population dynamics curves along with

the cross-correlation curve are shown in Fig.5.6.

For all three signatures, population first build-up at negative time delays and subsequently decays towards positive time delays. From the temporal evolution it is confirmed that these states are of unoccupied electronic nature which are populated by UV pulse and subsequently photo-emitted by the VIS pulse.

For determination of the lifetimes of observed unoccupied states, following rate equation was used:

$$\frac{dN_{\bar{k}}}{dt} = A \cdot \exp\left\{-\left(\frac{t}{\sigma}\right)^2\right\} - \frac{\Gamma_{\bar{k}}}{\hbar} N_{\bar{k}} \quad (5.1)$$

where,  $\bar{k}$  index used in subscripts refers to momentum-averaging and  $N_{\bar{k}}$  denotes the transient population. The first term on the right hand side accounts for the population build-up due to the pump laser pulse and the finite temporal resolution of the experiment, estimated by a Gaussian of width  $\sigma$ . The second term describes the relaxation with a transition rate  $\Gamma_{\bar{k}}$ . Such analysis discards intra-band scattering processes, as a redistribution of population within the band does not change the momentum averaged population  $N_{\bar{k}}$ . Thus, the scattering rate  $\Gamma_{\bar{k}}$  can be understood as the inelastic inter-band scattering rate that leads to the depopulation of the corresponding band. The analytical solution of Equation 5.1,  $N_{\bar{k}}(t) \propto \exp\{-\Gamma_{\bar{k}}t/\hbar\}[1 + \text{erf}(t/\sigma - \sigma\Gamma_{\bar{k}}/2\hbar)]$ , was fitted to the experimental data under the constraint of the extracted pulse XC width  $\sigma$ . The fit results describe the experimental data very well and are shown in Fig. 5.6 as solid lines. For the momentum-averaged lifetimes  $\tau_{\bar{k}} = \hbar\Gamma_{\bar{k}}^{-1}$  of states A and B, values of  $\tau_A=24(3)$  fs and  $\tau_B=35(3)$  fs were found.

In order to access the intra-band scattering processes, momentum dependent analysis is performed in the time-resolved data. This aspect was discarded in the momentum-averaged dynamics analysis discussed above. Momentum dependent dynamics are especially interesting for this system as they provide

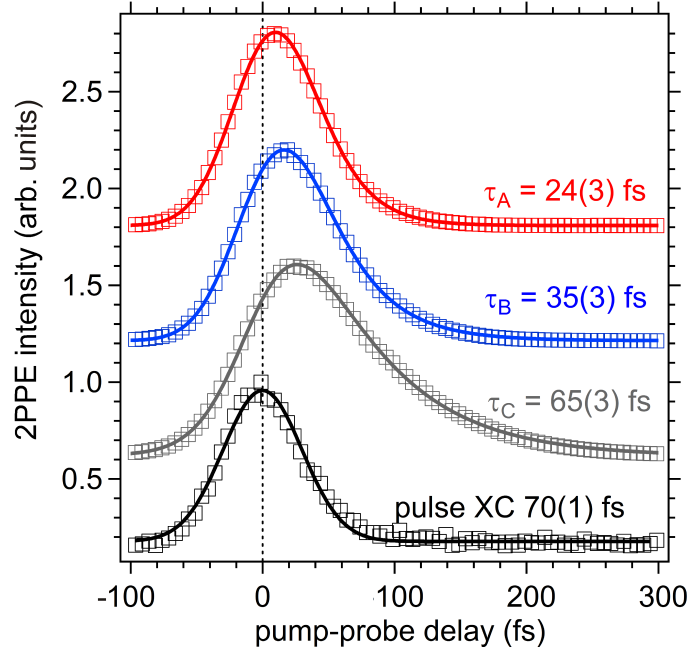


Figure 5.6: The momentum-averaged population dynamics for the spectral signatures A and B, as well as for the spectrally incoherent continuum signature C. The individual curves are offset for better visibility. The solid lines represent fits based on a rate equation approach (Equation 5.1). The cross-correlation (XC) curve of the pump and probe pulses was extracted from high energy carriers in the intermediate state energy region  $E - E_F = 3.73\text{--}3.80$  eV. Taken from [75].

a way to study the step-induced effect on the scattering process. Presence of steps should manifest in the symmetry breaking along the in-plane momentum direction perpendicular to the steps only and therefore this momentum direction  $k_y$  for  $k_x=0$  is chosen for the dynamics investigation in state A. Fig. 5.7 shows the population dynamics on a logarithmic intensity scale for the uppermost state A for three different momenta  $k_y$ , where  $k_x$  was integrated within a window of  $\Delta k_x = \pm 0.01 \text{ \AA}^{-1}$  around  $k_x=0$  and windows of width  $\Delta k_y = 0.02 \text{ \AA}^{-1}$  were chosen for the analysis. In these population dynamics curves, at positive delay times ( $\Delta t > 80$  fs) the signature of momentum dependent change becomes clear where the population decay becomes faster for increasing electron momentum  $k_y$ .

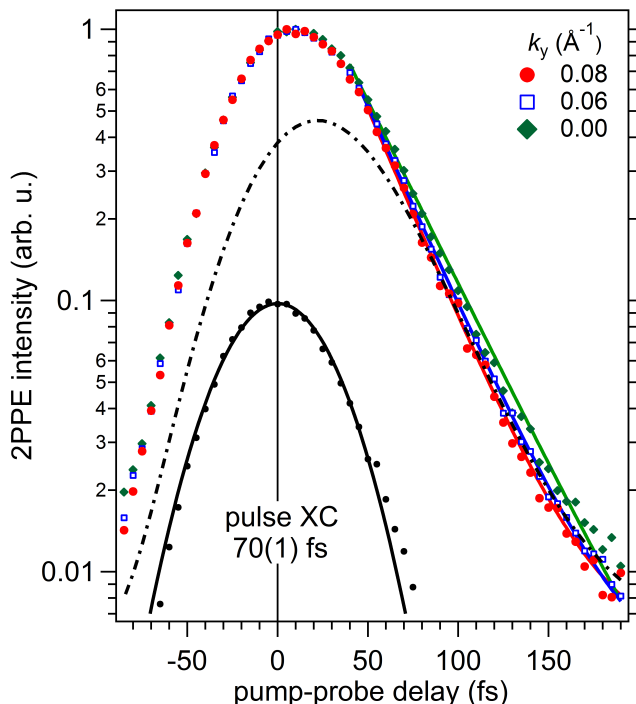


Figure 5.7: The time-dependent population dynamics for the uppermost state A for selected momentum windows  $k_y$ . The dash-dotted line represents a fit based on the rate equation approach (Equation 5.1) which is insufficiently describing the data. Solid lines represent exponential fits to the trailing edges of the population dynamic traces ( $\Delta t \geq 45$  fs). Taken from [75].

Contrary to the case of momentum-averaged analysis, the population dynamics curves obtained from the momentum-resolved analysis cannot be completely described by a simple rate equation model under the constraint of a fixed pulsed cross-correlation. The time delay of the population maxima is known to be an effective measure of the lifetime [97, 107], cannot be reproduced. This situation is depicted in Fig. 5.7 where the dash-dotted line which is a least mean square fit to the population decay observed at positive delay times ( $\Delta t \geq 80$  fs) using a fixed pulse XC, is not able to sufficiently describe the data.

Relaxation dynamics are then extracted from these curves by analyzing the population decay at positive delay times. Exponential fits to the trailing edges ( $\Delta t \geq 45$  fs) of the population curves, taking into account the temporal resolution

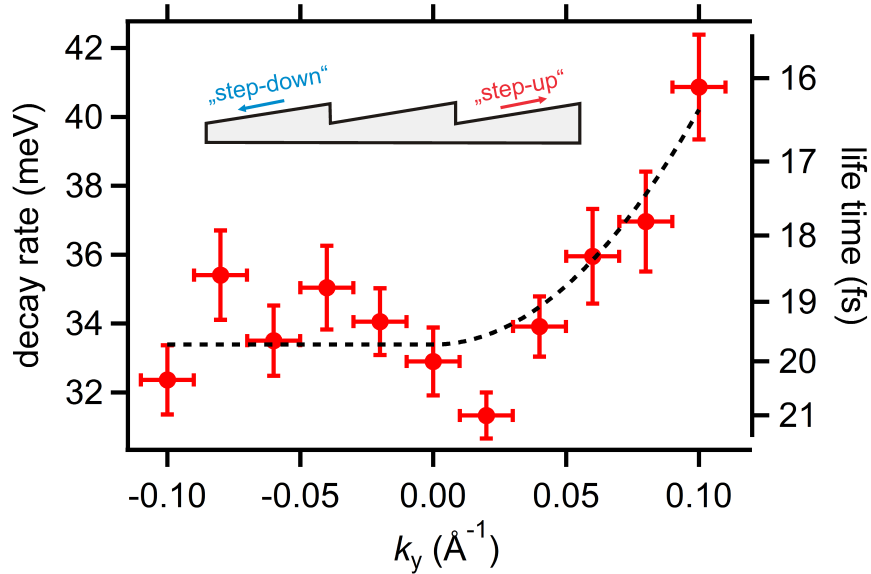


Figure 5.8: Population decay rates for state A as a function of step-perpendicular in-plane momentum  $k_y$ . Error bars along the momentum axis indicate the integration windows used for data analysis. The dashed line is a guide to the eye. The inset sketches "step-down" and "step-up" processes with respect to the macroscopic sample surface. Taken from [75].

of the experiment by convolution with a Gaussian of width  $\sigma$ , are shown as solid lines in Fig. 5.7. As a result of fitting, changes of the population decay rates  $\Gamma(k_y)$  are obtained for perpendicular to the step momentum direction  $k_y$  and are summarized in Fig. 5.8. The origin of the complex build-up of the population at different  $k_y$  will follow later in Section 5.3.2.

In a typical electronic band structure with effective mass  $m^* > 0$ , the excited electrons tend to relax towards the band bottom by inelastic scattering, consequently increasing the relaxation rate with the energy and thus the in-plane momentum. Such a behavior in the carrier dynamics was previously observed on isotropic 2D surfaces, e.g. Pb thin films grown on Cu(111) [152], image potential states on a Cu(100) surface [146], and at the Ar/Cu(100) interface [163]. As shown in Fig. 5.8 a similar trend is observed in our system where, for  $k_y > 0$ , the scattering rates gradually increase for larger parallel momentum components  $k_y$ . Interestingly, in the momentum range  $k_y < 0$ , an almost con-

stant decay rate is observed within the experimental accuracy. It presents a similar behavior of symmetry breaking observed in the photoemission intensity for  $k_y$  larger or smaller than zero, e.g. situations where electrons have a finite momentum component towards ("step-down") or away ("step-up") from the steps. The possible origins of these effects will be discussed in detail in Section 5.3.2. First, however, the experimentally obtained results of electronic band structure will be compared to the DFT calculations in the next section.

### Density Functional Theory Calculations

The Pb nanowires on Si(557) locally resemble the structure of a close-packed 2D layer of Pb atoms. This local arrangement is equivalent to the  $\sqrt{3} \times \sqrt{3}R30^\circ$  reconstruction with a Pb coverage of  $4/3$  ML. In order to support the interpretation of the 2PPE spectra, Prof. Kratzer group performed DFT calculations for a Si(111) slab covered with  $4/3$  ML Pb in the above reconstruction. The details of the calculation were similar to their previous work [164]. The starting geometry corresponded to the T4 structural model in Ref. [31], and was re-optimized using the forces calculated from our DFT calculations performed with the VASP code [165].

The electronic exchange and correlation effects were described using the generalized gradient approximation (GGA-PBE) functional [166] and a plane-wave expansion of the wavefunctions up to a 300 eV cut-off. The Si(111) slab consisted of five bilayers and a hydrogen-passivated backside, and for the lateral supercell dimensions the Si lattice constant of 5.46 Å obtained in PBE was used. The results for the unoccupied Kohn-Sham band structure along the high-symmetry line  $\bar{\Gamma} - \bar{K}$  ( $\parallel [\bar{1}\bar{1}2]$  or  $k_y$ ) of the  $\sqrt{3} \times \sqrt{3}$  surface Brillouin zone are shown in Fig. 5.9. In the energy regions  $E - E_F = 3.7 - 3.9$  eV and  $4.2 - 4.4$  eV above the Fermi energy in the vicinity of the  $\bar{\Gamma}$  point, Pb dominated states are observed. Grey shaded area represents the density of states from the Si substrate. As it can be clearly seen, Pb-dominated states are degenerate with

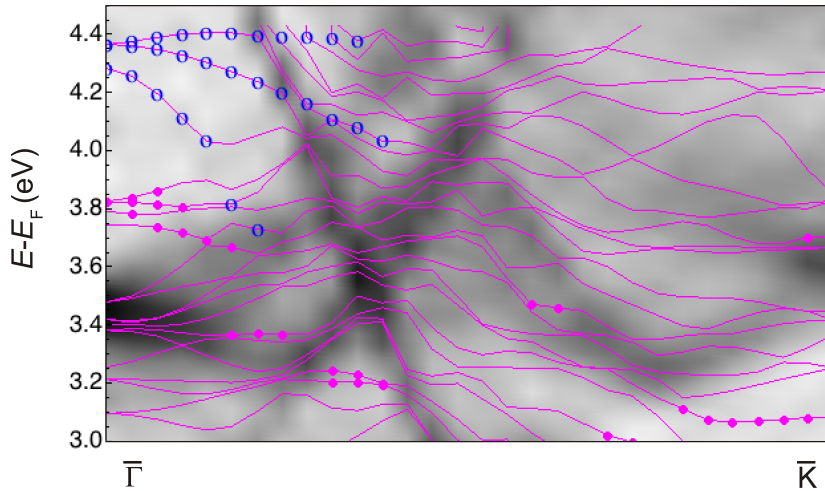


Figure 5.9: Unoccupied band structure of the  $\sqrt{3} \times \sqrt{3}R30^\circ$  Pb/Si(111) reconstruction at  $4/3$  ML Pb coverage obtained from GGA-PBE calculations. Regions where the projected density of states indicates significant overlap of the Bloch states with Pb  $6p_{x,y}$  or  $6p_z$  orbitals are highlighted by the open and filled circles, respectively. The gray-scale plot in the background indicates the electronic density of states of bulk Si, black color indicating high density, as obtained from a separate calculation after projection onto the (111) surface normal. Taken from [75].

the spectral region from a strongly reduced density of states from Si substrate. These states then essentially lie in the orientation band gap of Si substrate where they are decoupled from the substrate, which suggests that these states may be long-lived.

Our experimentally observed states A and B can be explained by Pb-dominated states lying in the 3.7– 3.9 eV region. The upper band in this energy region shows a similar dispersion as that of experimentally observed state A. The difference between the calculated and measured energy position could be caused by the small differences in the Fermi energy in the p-doped sample and/or due to the slab used for the calculation. In the DFT calculations the surface morphology of steps are disregarded and only the local Pb atom environment was considered.

### 5.3.2 Discussion

In this section, the origin of experimentally observed electronic states in light of DFT calculations will be discussed. Experimentally, the binding energies of the states with respect to the vacuum level  $E_{\text{vac}}$  were found to be  $E_A - E_{\text{vac}} = -0.80(5)$  eV (for state A at  $E - E_{\text{F}}=3.55$  eV) and  $E_B - E_{\text{vac}} = -1.05(5)$  eV (for state B at  $E - E_{\text{F}}=3.30$  eV). Also, the DFT calculations indicate the presence of two Pb-dominated unoccupied electronic states in the binding energy region close to the experimentally observed energy region of electronic states A and B. For the lower lying electronic state B, the calculations show a downward dispersion, while the higher lying state A appears to be consist of several branches where one branch exhibits positive dispersion near  $k = \bar{\Gamma}$ .

The binding energy of state A with respect to the vacuum level is close to the first ( $n=1$ ) image potential state (IPS) located in front of the Pb/Si(557) surface [167, 168]. This similarity in the binding energy indicates that state A could be an image potential state which is further supported by the fact that the effective mass of electrons in this state is similar to free-electron like state. However, the marked asymmetry in the 2PPE intensity for  $\pm k_y$  shown in Fig. 5.4 is a distinct observation which is not reported in the IPS residing on vicinal surfaces [66–70].

Furthermore, an IPS exhibits an orbital character of even symmetry with respect to the scattering plane, which is also clearly not the case for state A as shown in the measured probe pulse polarization dependence shown in Fig. 5.4. Based on the above discussions, we conclude that the signature A does not originate from an IPS. However, an image potential may influence and modify the binding energies and the dispersion of states and therefore induce a change in the electronic band structure calculated by the conventional DFT shown in Fig. 5.9.

This discussion, however, does not altogether rejects the existence of IPS

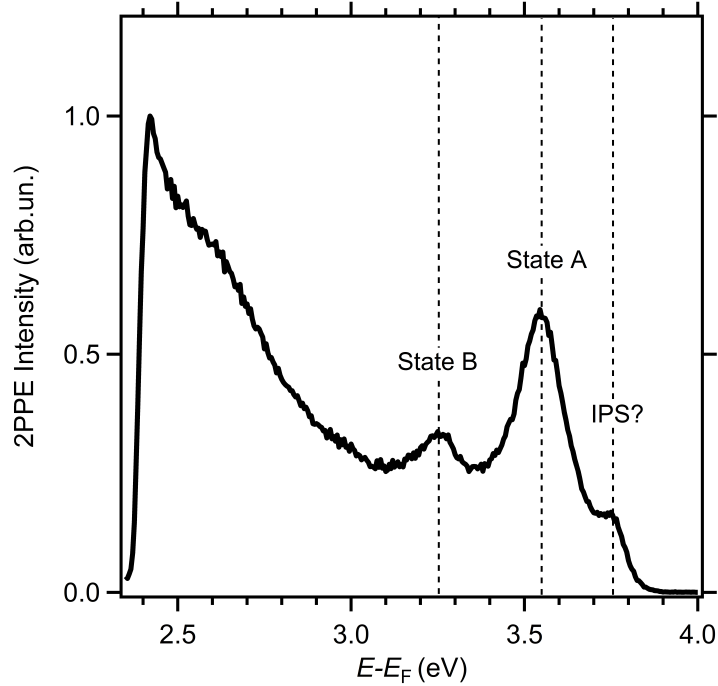


Figure 5.10: A 2PPE energy distribution curve obtained with the photon energies  $\hbar\omega_1 = 1.95$  eV  $\hbar\omega_2 = 3.9$  eV. In addition to states A and B, a higher energy peak is evident with a possible image state origin.

present at the Pb/Si(557) interface. Biedermann et al. [42] suggest that the binding energy of IPS is governed by the dielectric properties of the Si substrate since the Pb adlayer will only exhibit reduced polarizability due to the saturation of Si surface dangling bonds. Taking these conditions into account, a binding energy of  $E_{\text{IPS}} - E_{\text{vac}} = -0.59$  eV for the  $n=1$  IPS should be expected. Upon tuning the excitation energy to higher value ( $\hbar\omega_2 = 3.9$  eV), we indeed observe an additional electronic signature. This new signature that can be seen in the energy distribution curve in Fig. 5.10 is found at the binding energy  $E - E_{\text{vac}} = -0.59$  eV and therefore we suggest that it is originated from an IPS. No further analysis of this state was done as we are particularly interested in the investigation of purely Pb derived surface states in this system.

From the momentum-averaged analysis of the time-dependent 2PPE measu-

rements, lifetimes of  $\tau_A=24(3)$  fs and  $\tau_B=35(3)$  fs are obtained for states A and B, respectively (Fig. 5.6). The obtained lifetimes are rather long compared to the measured lifetimes in other metallic systems excluding the case of IPS or alkali metals on noble metal surfaces [150]. Comparatively smaller lifetimes were obtained also for other nanoscale systems on different substrates, such as atomic Au wires on Si(557) [38], Bi films on Cu(111) [53], epitaxial Ag films on MgO(100) [169], and Pb quantum well states on Cu(111) [152].

Kirchmann et al. [74] investigated a system of epitaxially grown Pb thin films on Si(111) substrate. Their studies showed that the carrier lifetime in the system (although exhibits a quasi-2D electronic structure) can be described by the electron-electron scattering and follow the 3D Fermi liquid theory behavior,  $\tau_{FLT} \propto n^{5/6}(E - E_F)^{-2}$ , where the power-law dependence on free carrier density  $n$  represents screening of the effective Coulomb interaction and the number of possible scattering partners and the dependence on energy  $E$  accounts for the possible scattering phase space. The lifetime results from [74] together with the extracted lifetime from states A and B are illustrated in Fig. 5.11. This figure also shows a schematic describing the scattering process within the film and across the interface. This schematic suggests that an additional decay channel of the substrate becomes available for the electrons in the Pb film if their electronic states become degenerate with the conduction bands of the Si substrate. This is the reason that the states in the energetic region  $>1$  eV manifest deviation from FLT and exhibit shorter lifetimes.

Based on the above description, electronic states that are located 3 eV above  $E_F$ , as being under discussion here, should possess lifetime value shorter than 5 fs. A rather long time that was observed for state A and B in our system is then explained with reference to the DFT calculations which indicated that the identified electronic states lie within the orientation band gap of Si substrate where the density of states from Si is strongly reduced. In addition, in the Pb thin film on Si(111), the scatterings occur within the metal film also which is

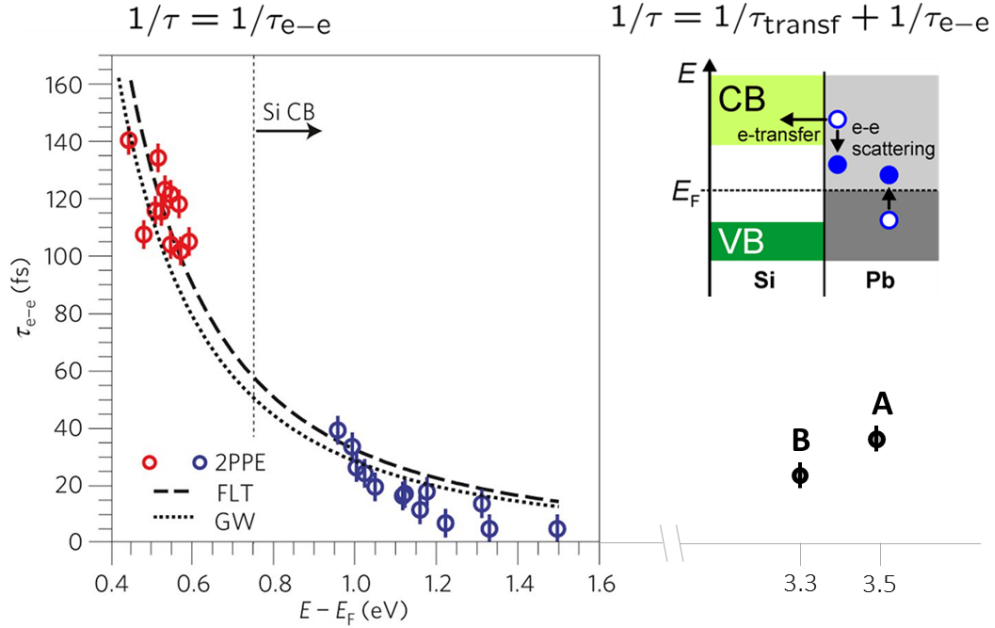


Figure 5.11: (a) Graph is taken from [74] and combined with observed lifetime value of state A and B. Their experimental as well as theoretical results from FLT and GW approximation would yield lifetime value of  $< 5$  fs for state A and B. (b) Simple scheme representing the situation in which electrons in the Pb film could either be degenerate with the conduction band or with the band gap of Si substrate. In the earlier case, electrons will decay faster due to availability of an additional decay channel.

minimized in the Pb/Si(557) that has merely a coverage of 1.31 ML of Pb.

In the momentum-resolved analysis of time-dependent 2PPE measurements, the scattering rates for state A (Fig. 5.8) show an interesting dependence on step-perpendicular momentum  $k_y$ . The gradual increase in the scattering rate for  $k_y > 0$  can easily be explained by means of intra-band scattering contribution within a band of effective mass  $m^* > 0$ , where the phase space available for intra-band scattering increases with the states binding energy and, thus, in-plane electron momentum.

In the next step, we compare the scattering rates obtained for momentum-averaged value (inter-band scattering) with the rates obtained for momentum-resolved value using Matthiessen's rule. The inter-band scattering rate value

from momentum-averaged dynamics using the relation  $\tau_{\bar{k}} = \hbar\Gamma_{\bar{k}}^{-1}$ , was found to be  $\Gamma_{\bar{k}} \approx 27$  meV, while the intra-band scattering rate, for the data collected at  $k_y = 0.1 \text{ \AA}^{-1}$ , we obtain  $\Gamma_{\text{intra}} = 41 \text{ meV} - \Gamma_{\bar{k}} \approx 14 \text{ meV}$ . Even at this most extreme case, the scattering rate is approximately half of inter-band scattering rate of  $\Gamma_{\bar{k}} \approx 27$  meV, which indicates that the population dynamics are dominated by inter-band scattering events. For the momentum range  $k_y < 0$ , no clear change on the scattering rate was observed and the overall scattering rate was found to be smaller than for  $k_y > 0$ . A simplified understanding of presence of an additional (quasi-)elastic intra-band scattering channel induced by steps causing an increase in the scattering probability for electrons with finite momentum towards the step edges, contradicts the findings. Furthermore, reduced 2PPE intensity at the negative  $k_y$  indicates the presence of additional processes which destroys the spectral coherence in this momentum range.

Nearly a constant decay rate observed from the band bottom to the measured range of negative momentum  $k_y$  for state A indicates a similar inelastic decay channels available for  $k_y < 0$  and  $k_y > 0$ . For these momenta, the observed population dynamics could reflect excitations in the Si substrate. However, earlier studies found that excitation to Si and subsequent transport to the surface takes place on a timescale of 100-1000 fs [168], which is much larger than the observed lifetimes here and therefore can simply be excluded from the discussion. This is further supported by the fact, that even at small negative momentum value, uniform decay rate was observed where the signal at such momentum values were mainly governed by the spectral signature of state A. Therefore, it is safely concluded that the excitations leading to the spectral incoherent background only play minor role in the observed population dynamics.

We discussed earlier, in reference to Fig. 5.7 that the population dynamics curves cannot be described completely by the simple rate equation model. However, such a complex build-up of the population could be due to the coherent

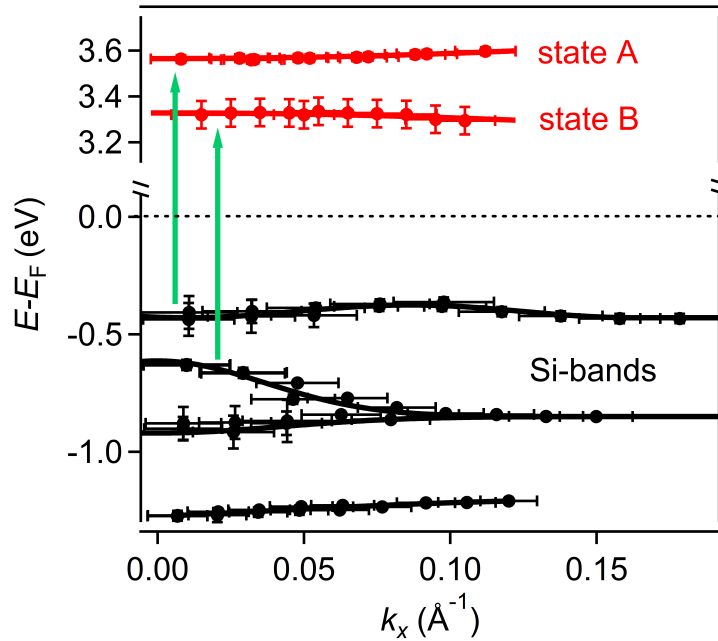


Figure 5.12: Experimentally determined band structure of the occupied (black) and unoccupied (red) states in the Pb/Si(557) system as a function of in-plane momentum  $k_x$ . Error bars along  $k_x$  indicate the momentum windows used for the analysis of the binding energy. The near-resonant excitation pathways for state A and B are indicated by the green arrows. Taken from [75].

excitation process, that occurs when the laser fields and electronic excitation have a well-defined phase relation. To investigate the potential existence of a resonant excitation case in the system, the occupied electronic states were probed. From the direct photoemission measurements, an occupied electronic state at the binding energy  $E - E_F = -0.43(5)$  eV, was identified. This state would allow a near-resonant excitation with the uppermost spectral signature A. Our experimental findings of occupied and the unoccupied electronic band structure obtained with the direct and 2PPE photoemission measurements, respectively, are summarized in Fig. 5.12. This explains the near-resonant excitation pathways for state A and B with the energy of the laser pulse used for the excitation process. The relevant initial state at  $E - E_F = -0.43$  eV is the Si valence band maximum and was also observed in DFT calculations on

the Pb/Si(111) system [164] as well as in experimental studies on Au/Si(557) [38] and Au/Si(553) [42].

In order to describe the dynamics in the near-resonant excitation conditions, Liouville-von Neumann (LVN) equation is used. For a more detailed discussion of this topic, readers are referred to the section *Coherent Excitation* in chapter-2. The solution of the LVN equation is governed by the pure dephasing times  $T_2^*$  (elastic scattering), the lifetimes  $T_1$  of the involved states (inelastic scattering), which is equal to our experimentally determined values  $\tau(k_y)$ , and the momentum-dependent energy detuning  $\Delta E(k_y) = (E_A(k_y) - E_i(k_y)) - \hbar\omega_1$  between the energy difference of the initial and intermediate state  $E_A - E_i$  and the populating photon energy  $\hbar\omega_1$  [39, 97, 108, 170]. This equation along with its numerical solutions for various different values of dephasing time has been discussed in chapter-2. This suggests the importance of the elastic scattering rate or the dephasing time in describing the momentum-dependent population dynamics, such as shown in Fig. 5.8. A strongly anisotropic dephasing time can be caused by the elastic scattering at the step edges, that ultimately influences the population dynamics within the individual momentum windows and additionally modulates the total 2PPE yield as a function of  $k_y$  [39, 171].

Different dephasing time  $T_2^{iA}$  modifies the 2PPE yield as well as the build-up time of the population maxima. A high dephasing rate reduces the 2PPE yield which is consistent with the expected increase in the scattering processes due to step-edges. Furthermore, an earlier build-up of the population maximum compared to rate equation also goes hand in hand with the experimentally observed results in Fig. 5.7. It should be noted here, that the discussed approach only qualitatively describes the experimental observation and the full description of the 2PPE process will require the addition of photoemission probe process, where the electrons are further excited from the intermediate to the final state lying above the vacuum level. Furthermore, for a full description of the rich amount of data  $I(k_x, k_y, E, t)$  collected in our experiment, intra-band

scattering has to be explicitly taken into account by coupling the LVN equations for different momentum windows, a task clearly beyond the scope of this thesis work.

The simple distinction of "step-up" and "step-down" carriers might be oversimplified, but the influence of real-space anisotropy on the experimentally observed different 2PPE yield and the scattering rate for positive and negative  $k_y$  on excited electronic state is evident. The step induced scattering rate associated with the loss of 2PPE intensity for  $k_y < 0$  is considerably larger than those observed in the time domain for image potential states on vicinal Cu(001) [71]. Considering that the scattering at the steps is mediated by the dipolar scattering potential located at step edges [69], such an increase in scattering rate is reasonable due to the larger step-induced dipole at metal-semiconductor hybrid interfaces.

### 5.3.3 Temperature-Dependent Electron Dynamics

Fig. 5.13 shows the false color representation of the time-resolved 2PPE intensity plots obtained at four different temperatures of  $T = 35$  K, 65 K, 90 K, and 125 K and the  $k$ -integrated window of range  $k_{x,y} = 0.24 \text{ \AA}^{-1}$  across the  $\Gamma$  point. The vertical axes are the kinetic energies of photoelectrons and the horizontal axes represent the time-delay in femtoseconds between the VIS ( $h\nu_1 = 2.08$  eV) and the UV ( $h\nu_2 = 4.13$  eV) laser pulses. These time-resolved measurements with higher photon energies show two distinct electronic features with their maximum spectral weight at  $E - E_F = 3.78$  eV and  $E - E_F = 3.38$  eV. Also, a continuum like feature exists which represents the secondary electron suffering heavy energy losses due to inelastic scattering and thus losing the original information of the electronic states they are excited from. Therefore, we will focus only on the well-defined states present at higher kinetic energies and name them A\* ( $E - E_F = 3.78$  eV) and B\* ( $E - E_F = 3.38$  eV) for convenience. It should be noted here that these newly identified states have different binding

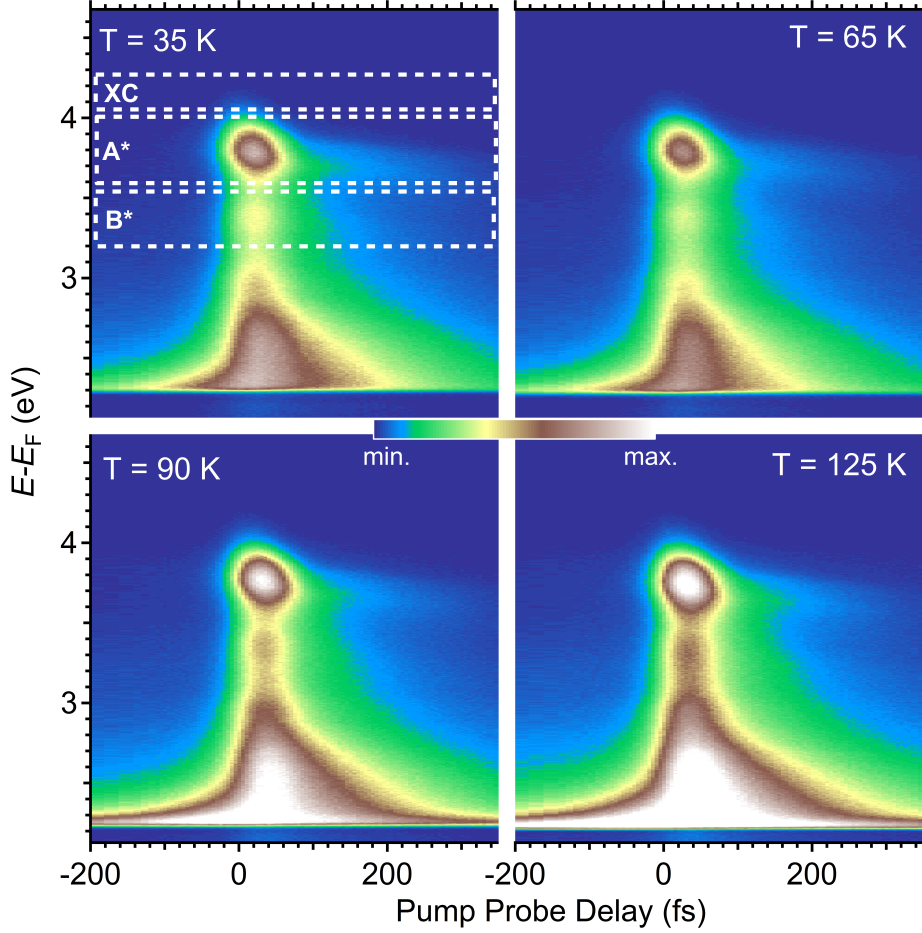


Figure 5.13: Temperature-dependent time-resolved two-photon photoemission intensity plots shown in the false color representation for four different temperatures of  $T = 35\text{K}$  (top left),  $65\text{ K}$  (top right),  $90\text{ K}$  (bottom left), and  $125\text{ K}$  (bottom right). All the plots obtained for a  $k$ -integrated window of range  $k_{x,y} = 0.24\text{\AA}^{-1}$  across the  $\Gamma$  point. Two distinct electronic signatures with their spectral weights centered around  $E - E_F = 3.78\text{ eV}$  ( $A^*$ ) and  $E - E_F = 3.38\text{ eV}$  ( $B^*$ ) can be identified for all four intensity plots. A continuum like feature with lower kinetic energy indicates the secondary electrons. The dashed boxes indicate the energy integrated window for which the population dynamics curves are extracted (see Fig. 5.14).

### 5.3. RESULTS

---

energies compared to states A and B probed previously. Furthermore, the presence of states A\* and B\* are not fully verified in the DFT calculations (Fig. 5.3.1). However, the primary concern of this study is to investigate potential temperature-dependent change in the scattering processes and any possible effects that are the result of the phase transition from a 2D to quasi-1D structure reported in Pb/Si(557) nanowires at a temperature of  $T_c = 78$  K [72, 172].

From the temperature-dependent tr2PPE intensity plots, it can also be observed that both states A\* and B\* show a large spectral weight at time zero  $t = 0$  which exhibits a temporal evolution in which states decay or their intensity fade along the positive pump-probe delay axes. In order to visualize the relaxation dynamics of the observed electronic states clearly, population dynamics curves are extracted, in an integrated energy window indicated by dashed boxes in the top left panel of Fig. 5.13, and shown in Fig. 5.14a and 5.14b for state A\* and B\*, respectively.

The horizontal axes of the graphs represent the pump-probe delay in femtoseconds and refer to the temporal evolution of the excited carrier in the unoccupied states whereas the vertical axes represent the intensity of the obtained cross-correlation (XC) and population dynamics curves (PDCs). The XC curves (black filled boxes) are shown in both graph plots with an artificial offset introduced along the intensity axes to distinguish them from the PDCs shown by the solid colored lines. The XC curves represent the dynamics of photoelectrons in the virtual intermediate states assumed to be containing no temporal asymmetry caused by the finite lifetime effects and are obtained by a cut made along the pump-probe delay axis for electrons with the highest kinetic energies. A Gaussian function fit shown by the grey solid line gives the XC width of 68 fs. In both panels, the PDCs obtained for the specific electronic state at four different temperatures are put together to directly visualize the temporal evolution of relaxation dynamics.

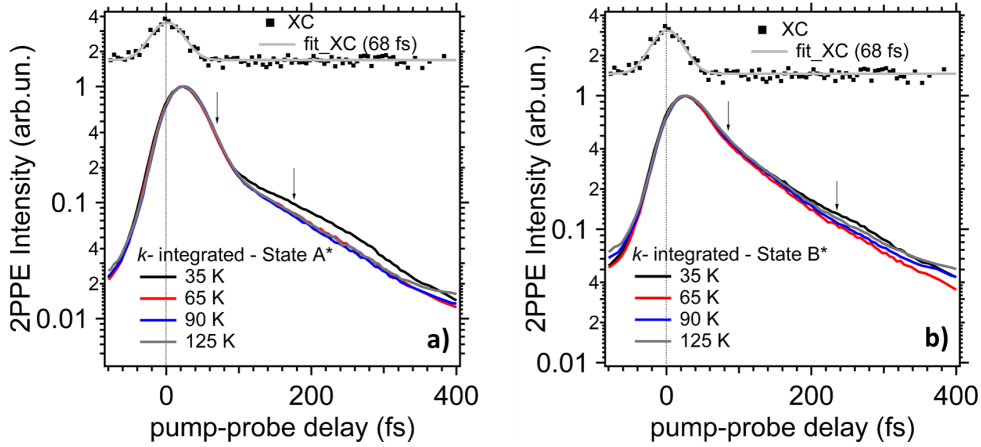


Figure 5.14: Momentum-averaged temperature-dependent normalized population dynamics curves for the spectral signatures A in (a) and B in (b) given in the solid colored lines. The curves are put together for better visualization of any temperature-dependent change in the dynamics. The XC correlation curve (black square symbol) with a Gaussian function fit (grey line) is also shown with an artificially introduced offset in the intensity scale for better visualization. Cross-correlation and population dynamics curves are extracted in the integrated energy windows mentioned in Fig. 5.13.

The transient response of state  $A^*$  shows that the depopulation of the excited carriers begin right after the peak maximum is passed as evident from the asymmetric shape. This is indicated by an arrow and denotes the first decay component of the PDCs. A second decay component marked by another arrow starts at  $\sim 100$  fs and accounts for  $\sim 20\%$  of the maximum population. The identical slopes of first decay components indicate the similar relaxation dynamics at various temperatures. The second decay component contains different relaxation dynamics only for the lowest temperature of  $T = 35$  K. The transient response of state  $B^*$  also shows two different decay components that do not exhibit identical slopes at different temperatures. This indicates a different but non-systematic response in which the relaxation dynamics do not vary according to the temperature.

In the next step, we attempted to quantify the relaxation dynamics of

the PDCs using the simple rate equation model involving the convolution of Gaussian function and double exponential decay. It turned out that this simple model does not describe the experimental data. Only a bi-exponential fit to the population decay part of the curve is also unable to describe all the curves. This indicates the population and depopulation evolve through more complex processes which cannot be defined under the simple rate equation approach. Therefore, we restrain ourselves from extracting lifetime and focus on the main intent of this study, i.e. to look for signatures of the phase transition.

The observation from the temperature-dependent PDCs can be summarized as follows.

1. For state A\*, PDCs at various temperature exhibit a very similar relaxation dynamics except for the lowest temperature ( $T = 35$  K) that shows a slower second decay component.
2. For state B\*, PDCs obtained at different temperature show a relaxation dynamics which are slightly at variance from each other. However, their dependence on temperature does not follow a simple systematic.
3. Most importantly, no drastic change in the dynamics is observed above and below the phase transition temperature of  $T_c = 78$ K [72, 73, 172].

#### 5.3.4 Discussion

Macroscopic conductance measurements performed on Pb/Si(557) revealed a phase transition occurring in the system at a temperature of  $T_c = 78$  K. Above and below the  $T_c$ , the system perpendicular to wire direction is described being metallic and insulating, while along the wire direction, is characterized as metallic and semiconducting, respectively. In summary, the 2D Pb/Si(557) undergoes a phase transition to a quasi-1D system below  $T_c$  [72, 172].

Phase transition can greatly influence the excited carrier lifetime in a system. The change of dimensionality associated with the phase transition modifies the

energy phase space and Coulomb's interaction between electrons. Both the factors play opposite role in determining the carrier lifetimes with the change in the dimensionality of electronic structure. A transition from 2D to 1D leads to the reduction in the energy phase space and ultimately the electron scattering rate as per the relation  $\Gamma_{e-e} \propto (E - E_F)^2$ . In contrast, the interaction strength increases between the electrons that lead to increased scattering.

Temperature-dependent tr2PPE results indicate the absence of any strong modification in carrier scattering rate associated with the phase transition (Fig. 5.14). The small differences observed in the depopulation processes for state B\* are not systematic. For state A\*, the curve at  $T = 35$  K manifests small difference in the second decay component only. This difference cannot be a signature of phase transition either because it would have manifested in T=65 K curve also, which is below the  $T_c$ . This indicates that the phase transition in Pb/Si(557) bears no implication on the scattering rate of the excited carriers as suggested by our experimental findings.

The observation of this indifference might be linked to several factors. The competing factors of energy phase space reduction and enhanced interaction between carriers associated with the phase transition could completely balance out each other if their impact is similar in magnitude. In this case, the net result will be no change in the scattering rate. Furthermore, the bandgap opening size leading to the phase transition is rather small, i.e.  $\Delta E = 20$  meV [73] for this system. This may not greatly influence the energy phase space for the excited carriers residing in the electronic states lying much above ( $>3$  eV) the Fermi level  $E_F$ . Therefore, it may lead to the changes in the scattering rate which are very small and below the time-resolution of our experimental setup.

## 5.4 Summary

Our 2PPE measurements on Pb nanowire arrays grown on a stepped Si(557) surface, identified two unoccupied electronic states. DFT calculations performed on the  $\sqrt{3} \times \sqrt{3} - R30^\circ/\text{Si}(111)$  reconstruction found the Pb- dominated state lying in a similar energetic region and showing the similar dispersion. From the time-resolved measurements, extracted momentum-averaged lifetimes for the identified states suggest that these states are energetically located within a window of a reduced electronic density of states of the underlying silicon substrate. Furthermore, obtained momentum-resolved population dynamics cannot be described within the framework of the simple rate equation model. In fact, a pronounced momentum dependence  $\Gamma(k_y)$  was found and it is suggested that a momentum-dependent dephasing rate, possibly caused by elastic scattering from the step edges is responsible for the non-trivial population dynamics and a difference in 2PPE yield for positive and negative  $k_y$ . Our experimental findings are significantly different from those obtained for image potential states on single crystal vicinal metallic surfaces, indicating that the Pb/Si reconstruction exhibits a stronger dipolar character than metallic surfaces which finally leads to a strongly anisotropic scattering potential for carriers with finite momentum towards or away from the step edges. Further studies on a possible influence of such anisotropy on scattering dynamics requires a strong theoretical basis to clearly separate intra-band scattering processes resulting from energetic relaxation and quasi-elastic scattering or dephasing processes induced by the presence of the steps.

In our temperature-dependent time- and angle-resolved 2PPE measurements, we identified two unoccupied electronic states A\* and B\* at the binding energies  $E - E_F = 3.78$  eV and  $E - E_F = 3.38$  eV, respectively. The momentum integrated scattering dynamics analysis revealed that the depopulation of the scattering dynamics evolved through pathways that are different compared

to the previous results obtained at  $T = 85$  K as discussed in the first part. Their population dynamics curves indicate the presence of two different decay components that could not be quantified under the model of simple rate equation. This difference is possibly originated due to higher photon energies used in our temperature-dependent measurements that led to a probe of different unoccupied electronic states.

In addition, both electronic states demonstrated different temperature-dependent excited carrier decay dynamics and none manifested any notable dependence on the phase transition. This indifference of the dynamics on the phase transition is potentially linked to an equal impact of the energy phase reduction and enhanced scattering that balances out any expected modification in the carriers lifetimes. Another underlying reason is associated with the large binding energies ( $E - E_F > 3$  eV) of the investigated unoccupied electronic states in which the residing carrier may not be affected strongly by a small bandgap opening of  $\Delta E = 20$  meV at the Fermi level  $E_F$  caused by the phase transition and, therefore, result in a modification in the scattering dynamics which is very small.



---

## Phase Transition in In/Si(111) System

### 6.1 Introduction

In the previous two chapters of this thesis works, photoemission investigations of quasi-2D Pb/Si(111) and quasi-1D Pb/Si(557) systems have been presented. In this chapter, we extend our focus to another prototypical quasi-1D system of Indium nanowires on Si(111) substrate.

Due to the formation of various ordered phases in the low coverage regime (1-2 ML), the Indium adsorbate on Si (111) surfaces has drawn considerable interest in the past few decades [173, 174]. Of particular interest is the  $4\times 1$ -In/Si(111) ordered phase which became a subject of vast investigations after the first time discovery of its temperature-dependent metallic to insulator transition driven by the charge density wave (CDW) formation [76]. Over the course, considerable efforts are made to understand the geometrical [77–79] as well as the electronic structure [80–84] of this system.

These studies reveal that the  $4\times 1$ -In/Si(111) system exhibits metallic behavior at room temperature and undergoes a phase transition by changing its

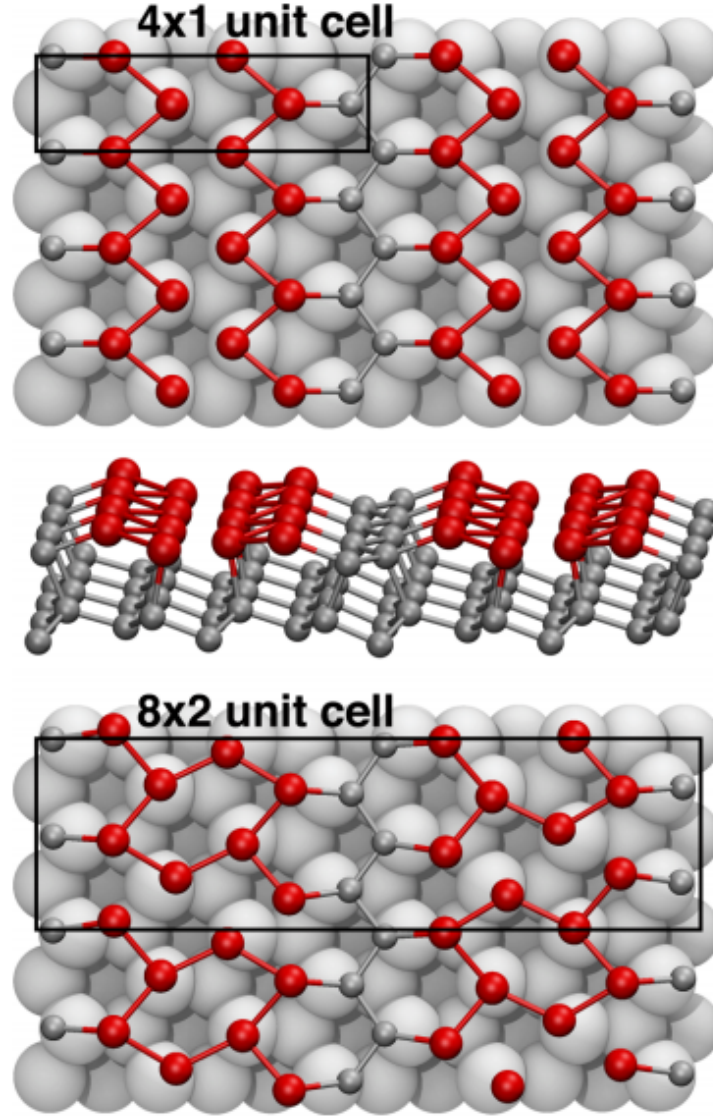


Figure 6.1: Schematic views of the In reconstructions on Si(111) surface. Indium and Si atoms are represented by red and grey color balls, respectively. Top and middle view belongs to metallic- $4 \times 1$ -In/Si(111) phase in which two zigzag-shaped In chains are separated by a zigzag-shaped Si atom chain. Transition to insulating-  $8 \times 2$ -In/Si(111) phase comes along with modification of In chains which makes a hexagonal shape as shown in the bottom panel. The image is taken from [175].

character to insulating below a temperature of  $T_c \approx 124$  K [80]. This phase transition is reversible and comes along with a structural change where the system transforms into  $8 \times 2$ -In/Si(111) by doubling its periodicity along the chain  $[1\bar{1}0]$  direction.

Fig. 6.1 shows the ideal structural model (taken from [175]) of In/Si(111) system. Top and side views of the  $4 \times 1$ -In/Si(111) reconstruction are shown in the top and middle panels, respectively, while the top view of the  $8 \times 2$ -In/Si(111) reconstruction is shown in the bottom panel.

As can be seen, the  $4 \times 1$ -In/Si(111) system consists of two In atomic rows arranged in a zigzag shape between two similar zigzag shaped chains formed by Si atoms. Below the phase transition temperature  $T_c$ , the In atoms rearrange slightly by breaking and forming In-In bonds, thereby giving a hexagonal shape reflecting the newly formed the  $8 \times 2$ -In/Si(111) periodicity. Investigation of the electronic structure of  $4 \times 1$ -In/Si(111) revealed the presence of three metallic bands (m1, m2, and m3) of 1-D nature [76, 80–84]. These subbands disperse strongly in the direction parallel to the wires ( $\Gamma X$ ) and are shown in Fig. 6.2 taken from [80]. In the direction perpendicular to the wires ( $\Gamma Y$ ), the bands remain rather localized.

Formation of  $8 \times 2$ -In/Si(111) phase is followed by a bandgap opening of  $\Delta E \approx 100 - 200$  meV in the electronic structure [76, 85]. The origin of the metal to insulator transition being linked to simple CDW formation, as proposed in [76, 81] is controversial. It has been recognized that a simple CDW picture cannot fully explain this transition owing to the large bandgap size and different electronic band structures for  $4 \times 1$  and  $8 \times 2$  phases ([80, 176] and references given therein).

Our conducted phase transition study on the In/Si(111) system can be categorized in two parts of (i) thermally driven, and (ii) optically driven.

For the thermally driven phase transition part, temperature-dependent angle-resolved photoelectron spectroscopic (ARPES) measurements were performed

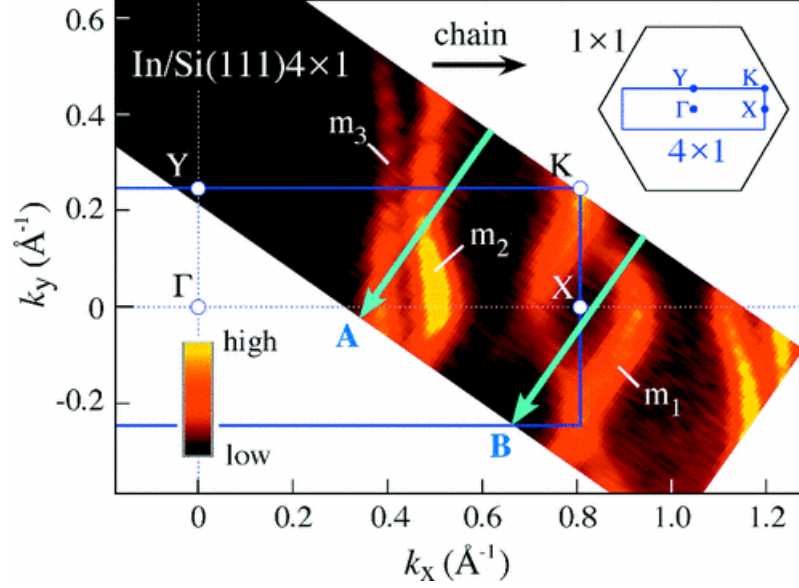


Figure 6.2: Photoemission intensity map of  $4\times 1$ -In/Si(111) surface at  $E_F$  ( $E_F \pm 30$  meV) as a function of two dimensional wave vector, taken from [80]. The subbands  $m_1$ ,  $m_2$ , and  $m_3$  show anisotropic dispersion. In the inset, BZ of Si(111)- $1\times 1$  (black hexagon) and In- $4\times 1$  (blue rectangle) reconstruction are shown.

from the BZ center  $\Gamma$  to the BZ boundary  $k_F$  along the wire  $[1\bar{1}0]$  direction, below and above the phase transition temperature. Near the BZ center  $\Gamma$ , four distinct electronic bands with their specific dispersions were identified. Two bands lying close to the Fermi level  $E_F$  showed slightly different dispersion relation  $E(k_x)$  (where,  $k_x \parallel [1\bar{1}0]$ ) for the  $8\times 2$ -In/Si(111) and  $4\times 2$ -In/Si(111) phases. Additionally, at the BZ boundary  $k_F$  bands  $m_2$  and  $m_3$  were found exhibiting metallic or insulating behavior depending upon the phase of the system, consistent with earlier studies [76, 80, 81, 85].

For the optically driven phase transition part, we conducted time- and angle-resolved pump-probe ARPES measurements at BZ center  $\Gamma$  and the BZ boundary  $k_F$ . It should be noted here that no phase transition was carried out upon optical pumping in our study. However, our investigations serve as the complementary study of time-resolved electron diffraction study in which the phase transition was carried out upon optical pumping. In addition, *ab*

*initio* molecular dynamics simulations were performed to understand the phase transition and results were published in [86]. Optical pumping of electrons in layered bulk CDW material generate transient change in the potential energy landscape that results in the displacive excitation of optical phonon modes that are connected to the periodic lattice distortion of the CDW [177, 178]. This combined study is performed to investigate such a structural transition at the surface. It was found that the excited electrons survived in their excited state for  $\sim 500$  fs and the structural transition, which is the indication of the CDW melting upon the laser excitation, occurred within 350 fs. Therefore, results prove that the electron lives in the excited state for long enough time at which the structural transition can occur.

## 6.2 Experimental Method

Experimental setup and procedures have been discussed in detail in chapter 3, so only relevant details will be briefly discussed here. Thermally driven phase transition was studied using ARPES technique employing laser pulses of energy  $\hbar\omega = 6.2$  eV at various temperatures above and below the phase transition temperature  $T_c$ . The temperature was varied by controlling the flow of  $LN_2$  through the cryostat, which allowed to achieve a minimum temperature of  $T \approx 85$  K at the sample, well below the transition temperature of 124 K.

Angle-resolved data was collected in normal photoemission geometry by changing polar rotation ( $\phi$ ) of the sample. In the experimental configuration, where the position-sensitive time-of flight (pTOF) spectrometer was employed to obtain the measurements, a maximum rotation of  $\phi = 42^\circ$  was achieved. Due to a large opening angle of  $\pm 11^\circ$  of pTOF, momentum region reaching  $k_x = 0.56 \text{ \AA}^{-1}$  becomes accessible, thus enabling the probing of the metallic m2 and m3 bands found at the boundary of the surface Brillouin zone (BZ) [76, 80, 81].

Time- and angle-resolved photoelectron emission spectroscopy (trARPES) was performed utilizing the pump and probe laser pulses of energy  $\hbar\omega_{pump} = 1.55$  eV and  $\hbar\omega_{probe} = 6.2$  eV, respectively. Two crucial momentum region of center and boundary of the surface BZ ( $\Gamma$  and  $k_F$ ), where the impact of the photo-induced phase transition could be pronounced, were chosen for the pump-probe measurements. At the  $\Gamma$  point, the time-of-flight (TOF) spectrometer was used for the measurement, with an opening angle of  $\pm 3.8^\circ$ . Population dynamics curves were obtained in the integrated accessible momentum range. The incident fluence of the pump laser pulse was  $0.25$  mJ/cm<sup>2</sup>. The temporal and spectral resolution of the experiment was 140 fs and 55 meV, respectively.

### 6.2.1 In Nanowires: Preparation and Characterization

N-doped Si(111) wafers with  $2^\circ$  miscut angle along the  $[\bar{1}\bar{1}2]$  direction were used for growing In nanowires on top. The miscut produces steps running along  $[1\bar{1}0]$  direction. These steps break the three-fold symmetry of the Si(111) surface and defines the direction for the growth of single domain In nanowires [179].

Obtaining a clean Si (111)-7x7 surface sample was the first step of preparation and requires a simple process as performed for the Pb/Si(557) and Pb/Si(111) system. The sample was ignited first in the UHV chamber ( $p < 1 \times 10^{-10}$  mbar) by applying a small direct current of 0.1 A parallel to the steps ( $[1\bar{1}0]$ ) direction. In this current limiting mode, Si sample was ignited at  $V \approx 120$  V. After the ignition, the Si substrate is operated in so called current controlled mode that allows a smooth change of temperature by controlling the applied current. Degassing of the Si substrates was performed by heating the sample at  $600^\circ\text{C}$  for 10-12 hours to ensure that there is no more outgassing from the sample and by the end of which, the chamber returns to its base pressure. Removal of native oxides from the surface was performed in flashing steps, where the sample was kept for 5 seconds at  $T = 1200^\circ\text{C}$  and the process

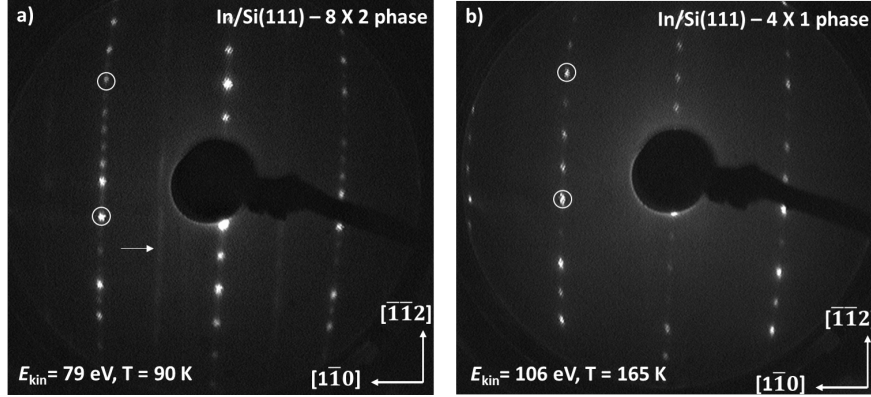


Figure 6.3: LEED pattern of (a) single domain  $8 \times 2$ -In/Si(111) reconstruction, taken at a sample temperature of 90 K and the primary electron energy of 79 eV, and (b) the modified  $4 \times 1$ -In/Si(111) reconstruction taken at 165 K, well above the phase transition temperature of  $T_c \approx 124 \text{ K}$  with a primary electron energy of 106 eV. Main integer spots are encircled in both LEED images. A modification in the number of diffraction spots in between two main integer spots reflects the change of surface symmetry upon phase transition. Elongated two-fold spots in  $8 \times 2$ -In/Si(111) reconstruction are indicated by the arrow.

repeated for 2-3 cycles. In the last step of flashing, the sample was cooled slowly from  $900^\circ\text{C}$  to  $700^\circ\text{C}$ , to obtain an ordered Si(111)- $7 \times 7$  reconstruction. Morphology of the sample was verified using LEED before In deposition.

From an e-beam evaporator, In was deposited for three minutes onto the clean Si(111)- $7 \times 7$  surface kept at a temperature of  $490^\circ\text{C}$ . Absolute amount of In deposition is not very critical for the growth of correct structure. Finally, the morphology of the grown structure is verified through LEED which shows either  $4 \times 1$ -In/Si(111) or  $8 \times 2$ -In/Si(111) reconstruction, depending on the sample temperature.

Fig. 6.3a and 6.3b show the LEED images, obtained for the insulating phase with electrons energy  $E_{kin} = 79 \text{ eV}$  at  $T = 90 \text{ K}$  and metallic phase with  $E_{kin} = 79 \text{ eV}$  at  $T = 165 \text{ K}$ , respectively. Single domain reconstruction of  $8 \times 2$  spots is visible in the left panel which undergoes surface structural change above the phase transition temperature of  $T \approx 124 \text{ K}$  and consequently  $4 \times 1$

reconstruction pattern emerges, as shown in the right panel. Transition from  $4\times 1\text{-In/Si(111)}$  to  $8\times 2\text{-In/Si(111)}$  structures reflects the periodicity doubling perpendicular to the wire direction in the real space. In the LEED image, it appears in the number of diffraction spots doubling between two main integer spot which are encircled in both LEED images. Elongation of the two-fold spots along the chain direction in  $8\times 2\text{-In/Si(111)}$  structure (indicated by arrow) is caused by the disordered registry of the neighboring In atoms [85, 180].

## 6.3 Temperature Driven Phase Transition

### 6.3.1 Phase Transition at Brillouin Zone Boundary

Fig. 6.4a and 6.4b show the photoemission intensity plot in false color representation obtained using laser pulses of energy  $\hbar\omega = 6.2$  eV for the low temperature (LT)  $8\times 2\text{-In/Si(111)}$  and the high temperature (HT)  $4\times 1\text{-In/Si(111)}$  phases, respectively. Horizontal axes in the plot, show the maximum accessible momentum range allowed by our experimental geometry, along the chain ( $k_x$ ) direction obtained for the integrated window of perpendicular momentum direction  $\Delta k_y = 0.04\text{\AA}^{-1}$  across  $\Gamma$ . With this accessible momentum range along the  $k_x$  direction, we already reach the surface Brillouin zone boundary [76, 80].

As can be seen in Fig. 6.4b, for the spectra taken at  $T = 127$  K for the HT  $4\times 1\text{-In/Si(111)}$  phase, at  $k_x \approx 0.55\text{\AA}^{-1}$ , a band crosses the Fermi level  $E_F$  (at the intersection of two lines), indicating the metallic nature of this phase. However, for the spectra taken at  $T = 104$  K (Fig. 6.4a), the electronic feature clearly stays below the Fermi level  $E_F$  at the same  $k_x$  value (at the intersection of two lines), thus indicating the insulating nature of the  $8\times 2\text{-In/Si(111)}$  phase. This experimentally observed band showing metallic and insulating behavior upon phase transition is similar to the Indium m2 and m3 band found at the momentum region of  $\Delta k_x = 0.46\text{\AA}^{-1}$  in earlier

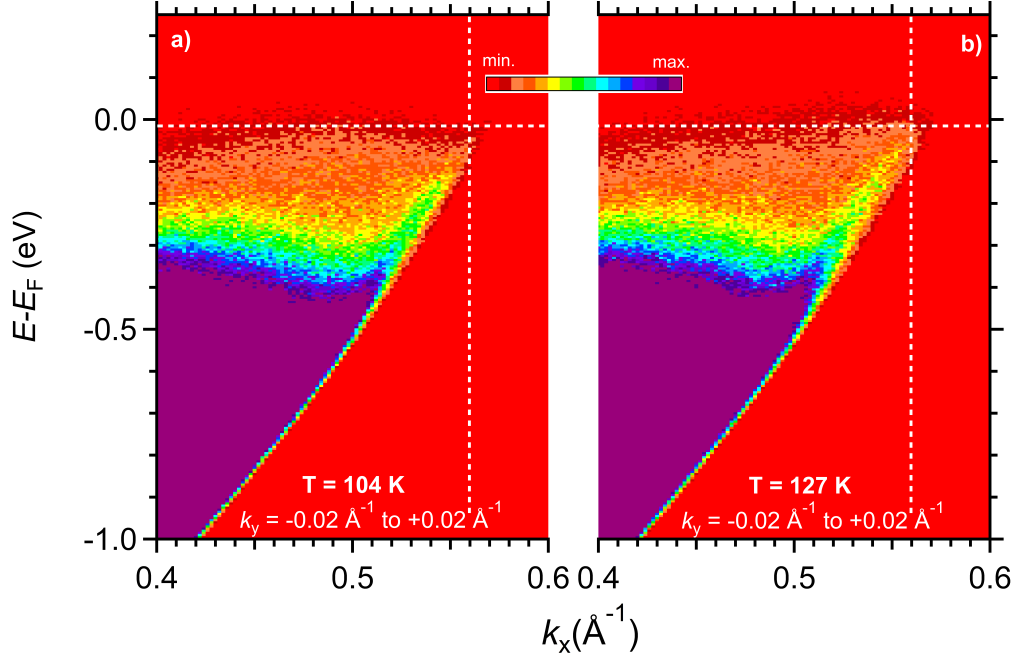


Figure 6.4: False color direct photoemission spectra recorded with  $\hbar\omega = 6.2$  eV laser energy pulse along the chain ( $k_x \parallel [1\bar{1}0]$ ) direction in an integrated  $k_y$  window around  $\Gamma$  ( $\Delta k_y = 0.04 \text{ \AA}^{-1}$ ) from maximum allowed rotation of sample ( $\phi = 42^\circ$ ), for (a) low-temperature ( $T = 104$  K) insulating and (b) high-temperature ( $T = 127$  K) metallic phase. The energy axes show the binding energy with respect to the Fermi level  $E_F$ . Vertical dashed line drawn to indicate the different spectral weight near the Fermi level  $E_F$  for both phases.

experimental temperature-dependent ARPES study [80]. Fig. 6.5 shows the energy distribution curves (EDCs) extracted at various temperatures above and below the phase transition temperature of  $T \approx 124$  K for the integrated momentum region of  $k_x = 0.46 \text{ \AA}^{-1}$  to  $0.6 \text{ \AA}^{-1}$  and  $k_y = -0.1 \text{ \AA}^{-1}$  to  $+0.1 \text{ \AA}^{-1}$ . Larger momentum window for integration provides EDCs with better statistics. As can be seen for the EDCs extracted above and below the phase transition temperature, there is a clear shift of the peak maxima of about  $\Delta E \approx 70$  meV, for the electronic state lying close to the Fermi level. Furthermore, the EDCs extracted for a specific phase, do not show any shift in the peak maximum position. This confirms that the change in the electronic structure is caused by

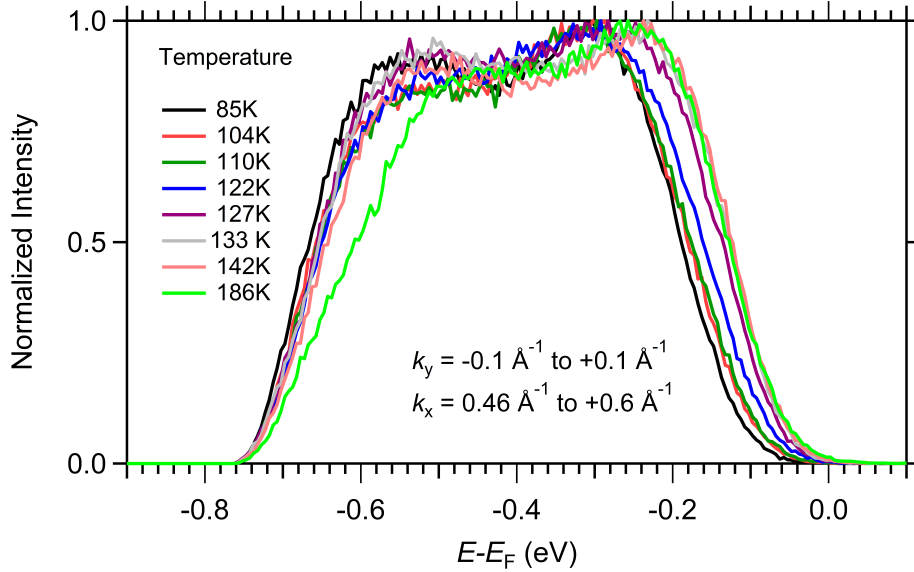


Figure 6.5: Temperature-dependent EDCs extracted for momentum windows  $\Delta k_x = +0.46 - 0.6 \text{ \AA}^{-1}$ ,  $\Delta k_y = \pm 0.1 \text{ \AA}^{-1}$  around  $\Gamma$ . Effect of the phase transition is evident in the peak close to the Fermi level  $E_F$  where a shift of  $\Delta E = 70$  meV in the peak maximum position is observed for the EDCs above and below the phase transition temperature ( $T \approx 124$  K).

the effect of phase transition and not the temperature.

### 6.3.2 Electronic Band Structure of $8 \times 2$ and $4 \times 1$ Phases

Fig. 6.6 shows the direct photoemission intensity plots in false color representation, obtained along  $k_x$  direction for three different polar angles (see Fig. 3.11) by integrating whole accessible  $k_y$  range shown in the top panel, for LT- $8 \times 2$ -In/Si(111) phase. These direct photoemission intensity plots were obtained for the higher momenta and also for the HT-  $8 \times 2$ -In/Si(111) phase (not shown in the figure). In the measured intensity plots, various distinct electronic features are identified showing different dispersion. In order to visualize the bands clearly, EDCs were extracted by integrating the accessible  $k_y$  window ( $\Delta k_y = \pm 0.1 \text{ \AA}^{-1}$ ), for various  $k_x$  values and the result is plotted in the Fig. 6.7 with an artificially induced offset in the vertical direction for clear visibility.

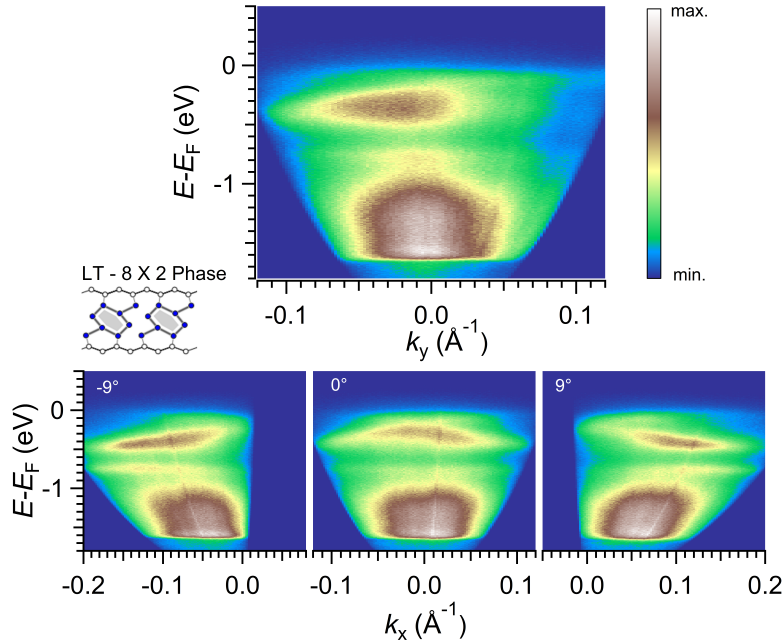


Figure 6.6: False color representation of the angle-resolved photoemission measurement obtained by recording spectra for different polar angles of sample rotation that gives the energy relation with momentum along the chain  $k_x$  direction, while the  $k_y$  window remains fixed. Plots only show the low temperature phase for three different angles while it was collected for various angles to access larger  $k_x$  window also for the HT phase. The line like variations running from low energy to the high energy feature in the lower three color plots are artifacts from the detector potentially caused by inhomogeneity in the detection efficiency and/or the missing signal from a dead channel in the detector.

In both, left and the right panels showing  $8 \times 2$ -In/Si(111) and  $4 \times 1$ -In/Si(111) phases respectively, four distinct electronic peaks are identified at the lower momenta and marked as E1, E2, E3, and E4 in order from higher towards the lower binding energy with respect to the Fermi level  $E_F$ . The identified peak remains distinguishable from each other until  $\Delta k_x = 0.24 \text{\AA}^{-1}$  for both phases, and undergo spectral broadening and merge together at the higher momenta.

Energetic positions of the identified peaks as a function of momentum  $k_x$  i.e. the band dispersion are plotted in Fig. 6.8a and 6.8b, for  $8 \times 2$ -In/Si(111)

### 6.3. TEMPERATURE DRIVEN PHASE TRANSITION

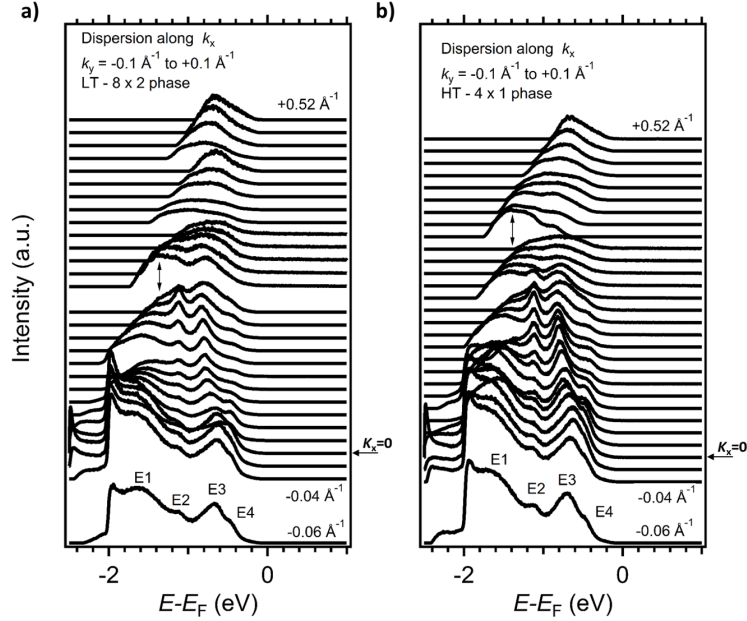


Figure 6.7: Energy distribution curves (EDCs) extracted along  $k_x$  direction for integrated window of  $\Delta k_y = \pm 0.1 \text{ \AA}^{-1}$  are shown for the low-temperature (LT) phase in (a) and high-temperature (HT) phase in (b). Offset was introduced in the vertical direction, which helps to recognize the dispersion of various bands. At momentum close to the  $\Gamma$ , four distinct electronic features E1-E4 are identified at both LT and HT phases. The sudden change between EDCs (indicated by double headed arrow and elsewhere) appears due to measurements obtained at different tilt angles of the sample. At different tilt angle, combine effect of light vector modification with respect to the surface normal and angular dependence of the photoemission signal causes variation in the photoemission yield.

and  $4 \times 1$ -In/Si(111) phases, respectively. For the spectrally broad peaks at the higher momenta of  $k_x > 0.5 \text{ \AA}^{-1}$ , peak positions were extracted by fitting with two Gaussian peaks.

As can be seen, the electronic band E1 shows an upward dispersion while the band E2 remains rather flat for both of the phases. The band E3 shows a downward dispersion for both phases. Upon reaching at higher momenta of  $k_x > 0.24 \text{ \AA}^{-1}$ , identification of the individual bands remains no more possible as they merge together. These bands remain merged in the momentum region

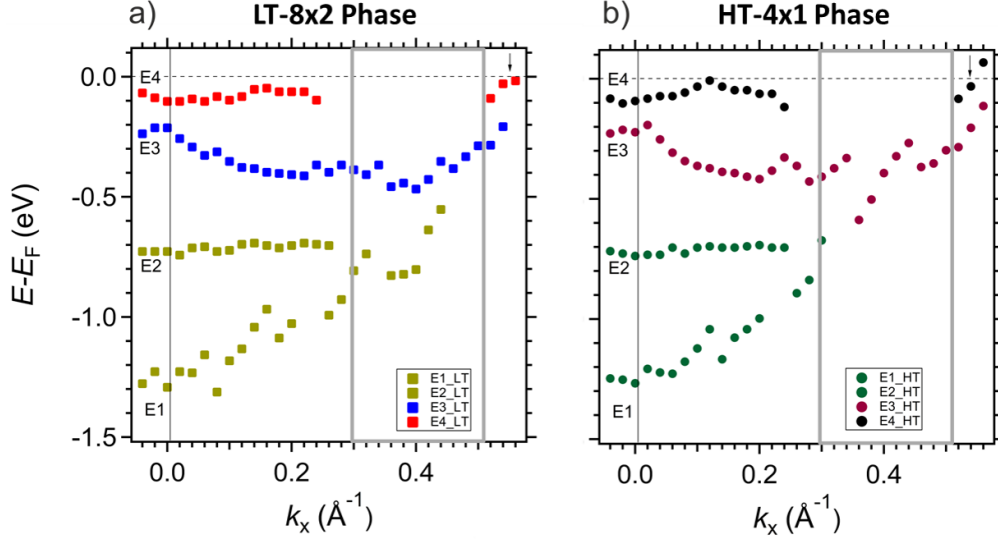


Figure 6.8: From the extracted EDCs, the energy peak positions of E1-E4 electronic bands are plotted against  $k_x$  and shown for LT phase in (a) and for HT phase in (b). The E4 band in (b) seems to cross the Fermi level  $E_F$  at  $k_x \approx 0.12 \text{ \AA}^{-1}$  and in particular at  $k_x \approx 0.54 \text{ \AA}^{-1}$ . The E4 band for the insulating LT phase shown in (a) stays below the Fermi level  $E_F$  in the accessible momentum range. Grey boxes show the momentum window where peaks become spectrally broadened and identification of individual peaks is no more possible.

depicted by the grey box. One remarkable difference is observed at the higher momentum  $k_x > 0.5 \text{ \AA}^{-1}$  where two bands show an upward dispersion for both phases but only for the high temperature  $4 \times 1$ -In/Si(111) phase, they get close (or passes) to the Fermi level  $E_F$ . These bands are similar to the m2 and m3 Indium bands.

In order to observe the effect of phase transition on the bands near the Fermi level, we plotted the E3 and E4 bands for both phases together in a smaller  $k_x$  window, as shown in Fig. 6.9. The difference in the dispersion of E4 band for the two phases is evident close to  $k_x = 0.12 \text{ \AA}^{-1}$ . Until this  $k_x$  value, the E4 band for the metallic phase exhibits an upward dispersion reaching near the Fermi level  $E_F$  followed by a downward dispersion. The insulating E4 band remains rather flat in this momentum region. A maximum difference in the

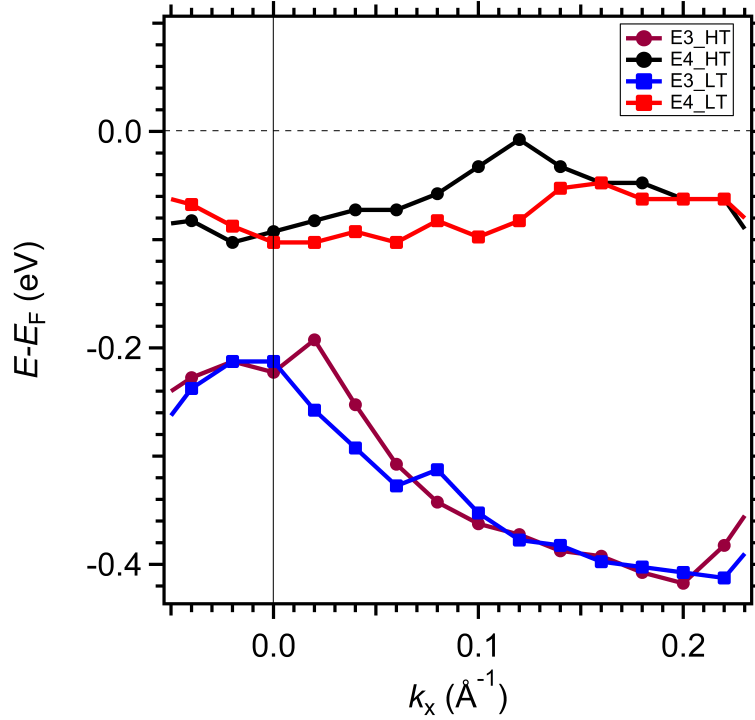


Figure 6.9: E3 and E4 bands for the HT and LT phases. For the E4 band, the dispersion is clearly different near the momentum region  $k_x \approx 0.12 \text{ \AA}^{-1}$ , where the E4 band from LT exhibits a flatter dispersion. E3 bands in both phases are also slightly different near the  $\Gamma$  ( $k_{||}=0$ ).

energy between the E4 band of the two phases was  $\Delta E \approx 90 \text{ meV}$ , as observed at  $k_x = 0.12 \text{ \AA}^{-1}$ . Also, the E3 band of the two phases shows the maximum difference at  $k_x = 0.04 \text{ \AA}^{-1}$  and the dispersion remains almost identical in rest of the momentum region.

### 6.3.3 DFT Calculations

Fig. 6.10 shows the result of the DFT calculations performed for  $8 \times 2$ -In/Si(111) and  $4 \times 1$ -In/Si(111) in the top and bottom panels, respectively. These calculations were performed in the group of Prof. Dr. Wolf Gero Schmidt and have been published in [86].

DFT within the local-density approximation was utilized to determine

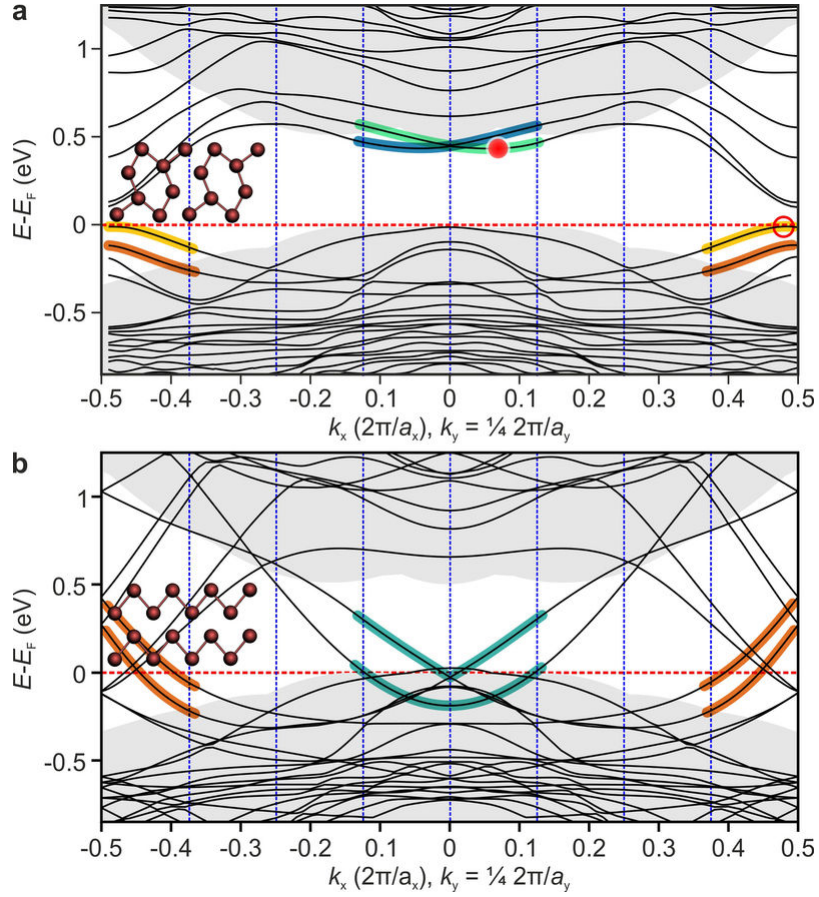


Figure 6.10: a, b, Calculated electronic band structure for  $8 \times 2$ -In/Si(111) (a) and  $4 \times 1$ -In/Si(111) (b) (phases depicted in the insets). The grey shaded areas show the projected Si bulk bands. Excitation with a partially emptied zone-boundary valence state (a, orange and yellow) and partially occupied zone-center conduction state (a, green and blue) are indicated with red open and filled circles. Taken from [86].

ground and excited atomic and electronic structure of the two phases. Modeling of the surface was performed using periodic boundary conditions within a supercell that contains three bilayers of silicon with the bottom layer saturated with hydrogen. For the DFT calculations of  $4\times 1$ -In/Si(111) reconstruction, two important momentum regions near  $\Gamma$  and at the higher momenta  $k_x > 0.4\text{\AA}^{-1}$  were identified, where the band passes through the Fermi level  $E_F$ . These bands are shaded blue and orange in the plot and reflect the metallic nature of this phase. For the  $8\times 2$ -In/Si(111) phase, however, the orange shaded band at the higher momenta  $k_x > 0.4\text{\AA}^{-1}$ , shifts downward and stays below the Fermi level, whereas the blue shaded bands near  $\Gamma$  move above the Fermi level  $E_F$  and become the unoccupied bands.

### 6.3.4 Discussions

Now, we turn to the discussion of temperature induced differences observed in the electronic band structure as a result of the transition between  $8\times 2$ -In/Si(111) and  $4\times 1$ -In/Si(111) phases. Near the BZ boundary along the chain ( $k_x$ ) direction, we identified one electronic feature (Fig. 6.4) that reflects the metallic and insulating behavior upon phase transition.

Energy distribution curves extracted in integrated momentum region  $\Delta k_x = +0.46 - 0.6\text{\AA}^{-1}$  and  $\Delta k_y = -0.1 - +0.1\text{\AA}^{-1}$  indicated a shift in the energy position of the peak maximum of  $\Delta E \approx 70$  meV upon phase transition. This energy shift is only observed for the peak located near the Fermi level  $E_F$  (Fig. 6.5). This shift which indicates the bandgap opening near  $E_F$  upon phase transition which is small compared to reported  $0.1 - 0.3$  eV gap size in the other studies [80, 85]. However, the other studies are performed at the BZ boundary even along the  $k_y$  direction ( $k_y \approx 0.2\text{\AA}^{-1}$ , see Fig. 6.2), while our EDCs are extracted around  $k_y = 0$ . Therefore, we related the difference in bandgap opening size to the momentum cut at which this and other studies are performed. The effect of the phase transition is more pronounced at the

BZ boundaries that manifests itself in larger gap opening of the electronic structure. Experimental constraints do not allow us to reach the BZ boundary along  $k_y$  direction.

In the following discussion, phase transition induced changes in the experimentally observed electronic band structure (Fig. 6.8 and 6.9) is compared with the DFT calculations (Fig. 6.10). Presence of various occupied electronic bands near the  $\Gamma$  region is shown in the DFT calculations. In our experiment, we identified four bands (E1-E4) near  $\Gamma$  with the dispersion that is in agreement with the few bands shown in the calculations. The absence of the various bands in the experimental data compared to the DFT calculations, could possibly be caused by the light polarization used. With the  $p$  polarized 6.2 eV laser pulses, only those bands are probed which possess the even symmetry character with respect to the scattering plane.

E1 and E2 bands with higher binding energies, for both  $4\times 1$ -In/Si(111) and  $8\times 2$ -In/Si(111) phases show identical dispersion that remains unaffected by the phase transition. Therefore, E3 and E4 bands located close to the Fermi level  $E_F$  will be focused in this discussion. The E4 band, in particular for the  $4\times 1$ -In/Si(111) phase, exhibits upward dispersion that continues until close to the Fermi level at  $k_x \approx 0.12\text{\AA}^{-1}$  followed by a downward dispersion (Fig. 6.8b). The DFT calculations (Fig. 6.10b) shows a blue shaded band that disperses upward and crosses the Fermi level  $E_F$ . Another band which is initially exhibiting a flat dispersion and located just above the Fermi level starts to show a strong downward dispersion at  $k_x \approx 0.12\text{\AA}^{-1}$ . These two bands in combination describe the dispersion of experimentally observed E4 band.

Furthermore, at larger momenta  $k_x \approx 0.5\text{\AA}^{-1}$ , the orange shaded bands in the calculation are in agreement with the two experimentally observed bands showing upward dispersion and passing through the Fermi level indicating the metallic phase (Fig. 6.8b). At this higher momentum region, also for the  $8\times 2$ -In/Si(111) phase, experimental and theoretical results are found to be

identical with the bands remaining below the Fermi level  $E_F$ , thereby indicating the insulating behavior of this phase. The situation is, however, different near  $\Gamma$  where the blue shaded bands move above the Fermi level  $E_F$  according to the DFT calculations. The experimental results show the presence of this band with almost identical dispersion which differs from the metallic phase only in the momentum region  $k_x \approx 0.12\text{\AA}^{-1}$  (Fig. 6.9).

## 6.4 Pump-Probe Spectroscopy

### 6.4.1 At Brillouin Zone Center and Boundary

Fig. 6.11 shows a false color representation of trARPES measurements performed in normal emission geometry using TOF spectrometer with  $\hbar\omega_{pump} = 1.55$  eV and  $\hbar\omega_{probe} = 6.2$  eV energy laser pulses. The vertical axis shows the energy scale referenced to the Fermi level  $E_F$  as a function of the time delay in the horizontal axis, introduced between the pump and the probe laser pulses to investigate the transient evolution of interesting energy features. The negative time on the delay axis corresponds to photoemission spectra taken with  $\hbar\omega_{probe} = 6.2$  eV only, whereas the time zero (vertical line) indicates a complete temporal overlap of the pump and the probe laser pulses. The correlated signal, which is the result of the pumping of the In/Si(111) system is shown in the upper panel. The time-resolved measurements also obtained at the higher momenta  $k_x = k_F$  using the pTOF spectrometer. The corresponding accessible momentum range was integrated to extract the population dynamics.

In Fig. 6.12a, population dynamics curves were obtained at various energy cuts above the Fermi level  $E_F$  are shown. The extracted population dynamics curves present the transient evolution of the population buildup and subsequent depopulation or the relaxation of photoexcited electrons. The trailing edges of the curves are fitted with exponential decay function. Lifetime values obtained

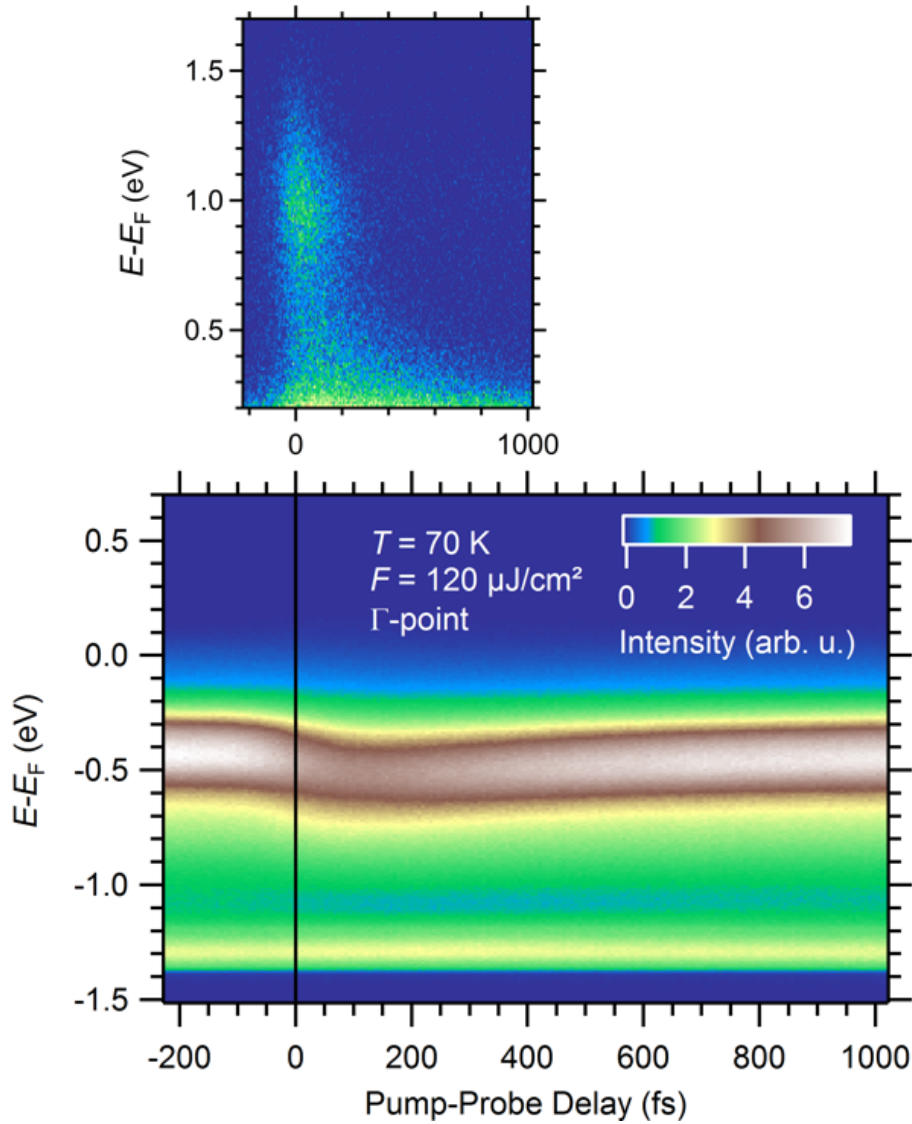


Figure 6.11: The lower panel shows the false color representation of photoemission intensity as a function of pump-probe delay. Pump beam of energy  $\hbar\omega = 1.55$  eV drives the system out of equilibrium and the time-delayed probe pulse of energy  $\hbar\omega = 6.2$  eV generates photoelectrons. The pump-probe measurements shown here are obtained in the vicinity of  $\Gamma$ . In the upper panel, a magnified image of the correlated signal obtained near  $\Delta t = 0$  from the lower panel is shown with enhanced color intensity.

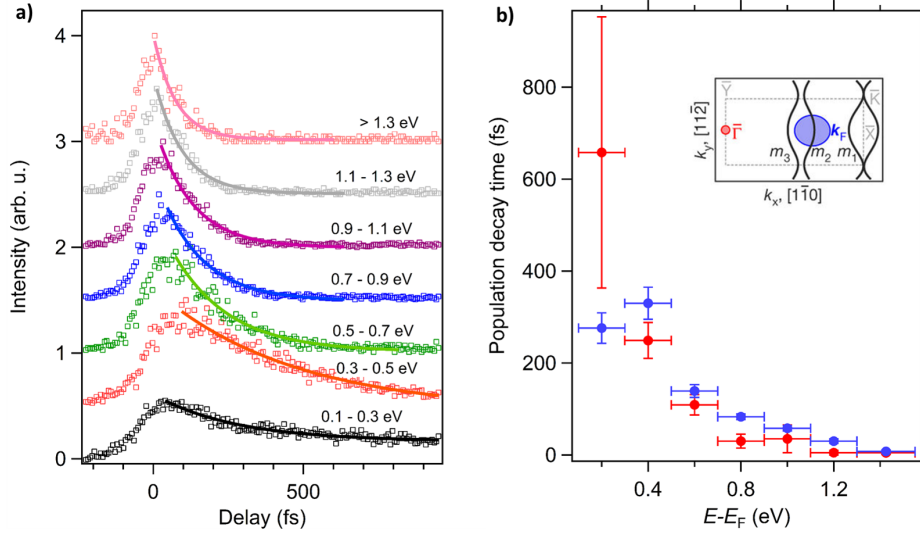


Figure 6.12: (a) Population dynamics curves extracted in selected energy windows  $E - E_F$  above the Fermi energy  $E_F$ , obtained in normal emission geometry for fluence  $\Phi = 0.25 \text{ mJ/cm}^2$ . Curves are offset for clear visibility. (b) Population decay times extracted from exponential fits to the trailing edges in (solid lines in (a)), for  $\Gamma$  (red) and  $k = k_F$  (blue). Error bars along the energy axis indicate the energy windows integrated to obtain the transient population curves, with the centers of the energy intervals shown as circles. Vertical error bars are standard deviation from the fit. Areas for momentum integration and the high-symmetry directions of  $4 \times 1\text{-In/Si}(111)$  are indicated in the inset, which depicts the first surface Brillouin zone along ( $k_x$ ) and perpendicular ( $k_y$ ) to the wire directions.  $m_1$ ,  $m_2$ , and  $m_3$  denote the bands crossing the Fermi level. The graph is taken from [86] and modified with the addition of the exponential fits.

as a result of the fits are plotted in Fig. 6.12b, from the curves obtained near BZ center  $\Gamma$  and BZ boundary  $k_F$  (shown in the inset). The decrease in the lifetimes with an increase of the energy above the  $E_F$  is evident at both  $\Gamma$  and  $k_F$ , as shown by the red and blue symbols, respectively.

## 6.4.2 Discussions

The trARPES results presented here serve as the complementary findings that support the optically induced phase transition observed in the In/Si(111)

system using time-resolved electron diffraction technique and *ab initio* molecular dynamics calculations. These results have been published together in [86]. It has already been discussed that the In/Si(111) system presents a case of CDW system with a metal to insulator phase transition temperature of  $T \approx 124K$ . In temperature-dependent phase transition, the low temperature phase represents a broken symmetry ground state CDW system with  $(8 \times 2)$ -In/Si(111) reconstruction. In this reconstruction, the In atoms form a hexagon. Above the phase transition temperature, CDW melts and In atom transforms into two zigzag chains through soft, shear and rotational phonon modes. The time-resolved electron diffraction experiment conducted with pump laser pulses of 1.55 eV having a pulse width of 120 fs, and the electron pulses of sub-300 fs which probe the transient state of atoms upon electron excitation. It was observed that the femtosecond laser excitation caused pronounced changes in the diffraction pattern, where the  $8 \times 2$  spots quenched and  $4 \times 1$  spots appear within 350 fs. This time is much smaller than 2.2 ps time needed for the energy transfer from the electron to the lattice, that proves the origin of the phase transition is not thermally driven. The *ab initio* molecular dynamics simulation then provides a better insight to the coupling of initial electronic excitation and subsequent nuclear motion. Depopulation of the occupied bands at the BZ boundary and population of the unoccupied band near  $\Gamma$ , destabilizes the CDW. The generated electron-hole pairs modify the potential energy landscape in a way that the energy decreases along  $(8 \times 2)$  to  $(4 \times 1)$  nuclear coordinates. The fact that for CDW melting, the population of zone-center conduction states and depopulation of zone-boundary conduction state is important, is explained below. The unoccupied electronic state close to the  $\Gamma$  corresponds to In-In zigzag chain and their population employ an attractive shear force between the zigzag chain and excitation of the shear phonon. Valence states at the BZ boundaries are related to the indium bonds that form when the hexagon is formed. A depopulation of electron at this momentum region leads

to weakening of these bonds and excites the rotary phonon. The excitation of an electron-hole pair at the  $\Gamma$  and the zone boundary couples to the two phonon modes responsible of transition of insulating CDW phase in the metallic phase. The *ab initio* molecular dynamics simulation were performed in the adiabatic approximation, that assumes that the photoexcited electrons remain in the excited states during the phase transition [86].

In order to verify this, trARPES measurements were conducted whose results are shown in Fig. 6.12a and 6.12b. The lifetime values obtained at the BZ center  $\Gamma$  and BZ boundary  $k_F$  point shows an increase for the energies  $E$  closer to the Fermi level  $E_F$ . The lifetime increases from a few femtoseconds as extracted at  $E - E_F = 1.5$  eV to about 500 fs at  $E - E_F = 0.2$  eV. Therefore, the photoexcited electrons live long enough in the excited state, to drive the structural transition.

## 6.5 Summary

In summary, we investigated the effect of phase transition on the electronic band structure by varying the temperature and obtaining the ARPES data above and below the phase transition temperature of  $T \approx 124$  K. The ARPES results indicate a switching between insulating  $8 \times 2$ -In/Si(111) and metallic  $4 \times 1$ -In/Si(111) character in the electronic structure upon phase transition, with a band gap opening of  $\Delta E \approx 70$  meV. This band gap opening is smaller compared to reported gap size of  $0.1 - 0.3$  eV [76, 80, 81], which is possibly originating from the different momentum regions at which the measurements are performed. Furthermore, the experimental results show the presence of four distinct electronic bands E1, E2, E3, and E4 near the  $\Gamma$  region. These bands with their specific dispersion are also identified in the DFT calculations. The effect of phase transition modifies the dispersion of the identified bands at the BZ boundary along the chain direction and also near  $\Gamma$ . For the metallic

$4\times 1$ -In/Si(111) phase, fine agreement existed between the theoretical and the experimental results. However, for the insulating  $8\times 2$ -In/Si(111) phase, in particular for the E4 band near  $\Gamma$  experimental and theoretical data do not comply well.

Concerning the optically driven phase transition, a time-resolved electron diffraction revealed that the CDW melting of  $8\times 2$ -In/Si(111) phase takes place at an ultrafast timescale of 350 fs by laser pulse excitation. The population of very specific electronic states brings a transient change in the potential energy landscape. This directly couples to the two characteristic vibrational lattice modes that drive the structural transition [86]. Our trARPES measurements, revealed the lifetime at BZ center  $\Gamma$  and BZ boundary  $k_F$  of upto 500 fs for the states located near  $E_F$ . This lifetime value is larger than the 350 fs time at which CDW melting was observed. The extracted lifetime confirms that the electrons survive in the excited state for a timescale sufficient to drive the structural transition.



---

## Conclusion

In this thesis, the unoccupied electronic band structure, and the ultrafast electron dynamics in quasi low-dimensional material systems have been investigated. The metal-semiconductor based quasi 2D and 1D systems are attractive due to intriguing physics that they manifest and their potential application in technology. In these systems, the study of the electronic structure and the ultrafast dynamics are important which give the information about the macroscopic physical properties of the system. We have investigated these quasi low-dimensional systems by means of femtosecond laser based two-photon photoemission (2PPE), angle-resolved direct photoemission (ARPES), time- and angle-resolved two photon photoemission (tr2PPE), and time- and angle-resolved photoemission spectroscopy (trARPES) techniques.

To summarize, for the 4/3-ML of Pb/Si(111) in the vicinity of  $\Gamma$  ( $k_{\parallel}=0$ ), two-photon photoemission investigation revealed three distinct unoccupied electronic states. Their unoccupied nature was confirmed by analyzing the temporal evolution of population dynamics obtained using tr2PPE. A remarkable feature of these identified electronic states was the marked asymmetry character across

---

the  $\Gamma$  point. Their peculiar asymmetries included the presence of the linear dichroism in the angular distribution (LDAD) ( $I(+k) \neq I(-k)$ ) and apparently asymmetric electronic band structure ( $E(+k_x) \neq E(-k_x)$ ). Furthermore, pump polarization-dependent 2PPE measurements revealed a switching of the orbital symmetry character between even and odd at the opposite momentum of  $+k_x \parallel [\bar{1}\bar{1}2]$  and  $-k_x \parallel [11\bar{2}]$ . Our analysis revealed that all the observed asymmetry character can be explained by the phenomenon of the LDAD. In addition to asymmetric intensity distribution, it can result in an asymmetric electronic dispersion, and also gives a false sense of orbital character switching for the electronic states with mixed orbital symmetry at the opposite momentum  $\pm k_x$ . It was further established, that there are various underlying causes of the LDAD including the symmetry breaking of experimental geometry due to off-normal incidence of  $p$  polarized light, involvement of bulk states, final state effects, and spin- dependent asymmetries present in the strong SOC system. The phenomenon of bulk states effects and off-normal light incidence reasonably describe the apparently asymmetric electronic band structure and photoemission intensity distributions observed with  $p$  polarized light but not the asymmetry observed with the  $s$  polarized pump light. However, the other two effects, i.e. the final state effect and strong SOC can induce LDAD irrespective of the polarization of the incident light. The correct determination may require further experimental studies, e.g. spin-resolved photoemission and corresponding detailed theoretical calculations that disentangle the individual contribution of asymmetries.

2PPE investigation on the Pb nanowires arrays grown on stepped Si(557) surface revealed two distinct unoccupied electronic states whose presence were verified by the DFT calculations. Time-resolved measurements provided a rather long lifetime of both states for momentum averaged analysis indicating that these states are energetically located within a window of a reduced electronic density of states of the underlying silicon substrate. In the momentum-resolved

---

analysis a pronounced momentum dependence in perpendicular to the step ( $k_y$ ) direction was observed. It was found out that the population dynamics evolution could not be described under the framework of a simple rate equation model. It is suggested that this non-trivial population dynamics is caused by the momentum dependent dephasing rate associated with the elastic scattering from the step edges. This momentum dependent dephasing also explains the observed difference in the 2PPE yield across  $k_y = 0$ . For further studies, it is suggested that detailed theoretical calculations are carried out to explain the anisotropy of scattering dynamics in order to clearly separate the role of intra-band scattering processes resulting from energetic relaxation and quasi-elastic scattering or dephasing processes induced by the presence of steps.

Temperature-dependent measurements performed on Pb/Si(557) with slightly higher photon energies ( $\hbar\omega_1 = 2.08$  eV,  $\hbar\omega_2 = 4.13$  eV) revealed the presence of two electronic states of unoccupied character. The binding energies of newly identified states with respect to the Fermi level are different compared to the states A and B investigated with  $\hbar\omega_1 = 1.9$  eV and  $\hbar\omega_2 = 3.8$  eV. In addition, the momentum integrated analysis manifested a different temporal evolution of population dynamics compared to the state A and B obtained at a temperature of  $T = 85$  K, suggesting a different nature of newly identified states. Their population dynamics curves contain two different decay components that could not be described under the framework of a simple rate equation. Furthermore, the decay dynamics of both states are dissimilar to each other but none revealed any notable difference associated with the phase transition at  $T = 78$  K. The possible explanation of this indifference of the scattering behavior is the equal impact of the reduction of phase space and enhancement of the scattering between the hot carriers that essentially balances out potential changes associated with the reduction in dimension of electronic structure. In addition, the excited carriers localized in the electronic states with large binding energies ( $E - E_F > 3$  eV) may not feel the small bandgap opening

---

of  $\Delta E = 20$  meV at the Fermi level  $E_F$  caused by the phase transition. This may result in a very small change in lifetimes which is not detectable under a femtosecond time-resolution of our experimental tool.

For In/Si(111) system, we investigated the occupied electronic structure above and below the phase transition temperature of  $T_c \approx 124$  K. The electronic structure showed a transition from the metallic  $4 \times 1$ -In/Si(111) to an insulating  $8 \times 2$ -In/Si(111) phase with a bandgap opening of  $\Delta E \approx 70$  meV. The ARPES measurements revealed the presence of four occupied electronic states whose presence confirmed by the DFT calculations. At the BZ boundary in  $k_x$  (along the chain) direction, only two bands were identified that switched between metallic and insulating character depending on the temperature of the electronic system. Phase transition modified the electronic band structure also near the  $\Gamma$  point, in addition to the BZ boundary.

Our pump-probe trARPES results for this system served as a complementary investigation for an optically driven phase transition study using time-resolved electron diffraction and *ab-initio* calculations. This study revealed that the CDW melting of  $8 \times 2$ -In/Si(111) phase takes place at an ultrafast time scale of 350 fs by laser pulse excitation. It was concluded that the population of very specific electronic states bring a transient change in the potential energy landscape. These changes directly couple to the two characteristic vibrational lattice modes that drive the structural transition. In our trARPES measurements, the extracted lifetime for the electronic state located energetically close to  $E_F$  was found to be  $\sim 500$  fs, both at the BZ center  $\Gamma$  and BZ boundary  $k_F$  which is fairly larger than the CDW melting time of 350 fs observed in the time-resolved electron diffraction study. This finding confirms that the optically excited electrons remain long enough in the excited state at which structural transition can be driven.



---

# Polarization Dependent Linear and Non-Linear Photoemission of Pb/Si(557)

## A.1 Introduction

The results concerning the unoccupied electronic structure and ultrafast dynamics in quasi-one-dimensional reconstructions of Pb atoms on a Si(557) surface have been presented in chapter-5 of this thesis work. In the following, we give an overview of further investigations performed to understand the occupied and the unoccupied electronic structure of this system using polarization dependent linear and two-photon photoemission (2PPE) measurements.

Experimental constraints allow us only to have the scattering plane along  $[1\bar{1}0]$  direction. This implies a geometry in which the mirror plane of the system does not overlap with the scattering plane. For a polarization dependent photoemission measurements, this is not an ideal geometry because dipole selection rules cannot be applied strictly at a generic  $k$  point away from the mirror plane

due to symmetry mixing of the final states. Therefore, the symmetry character of initial or the intermediate states may not be unambiguously determined. Nevertheless, the obtained results provide interesting insights which are unique from a general prospect of polarization dependent photoemission study. In this work, the polarization dependent linear photoemission and the polarization dependent 2PPE results are presented for Pb/Si(557) system.

## A.2 Experimental Setup

The experimental methods have been discussed in detail in previous chapters and remain the same for these measurements conducted on the Pb/Si(557) system. For investigation of the occupied electronic states, laser pulses of  $h\nu = 6.06$  eV were used in combination with a  $\lambda/2$  waveplate. In addition, the polarization dependent two-photon photoemission (2PPE) measurements were conducted using laser pulses of energies  $h\nu_1 = 1.9$  eV and  $h\nu_2 = 3.8$  eV and their polarization were modified using independent  $\lambda/2$  waveplates. During all the measurements, the sample temperature was maintained at  $T \approx 85$  K by cooling with liquid nitrogen. The temperature was monitored using a calibrated infrared pyrometer (IMPAC IGA 140).

The experimental geometry is shown in Fig. 1. Incoming laser lights make an angle of  $45^\circ$  with respect to normal of the surface. Position-sensitive time of flight (pTOF) spectrometer is located normal to the surface and accepts electron emitted normal as well as off-normal to the surface due to its large acceptance angle of  $11^\circ$ . As can be seen, the scattering plane which is defined as a plane containing incoming laser light, outgoing electrons, and the spectrometer, lies perpendicular to the mirror plane of the sample. Within this experimental geometry, the dipole selection rules are not strictly valid.

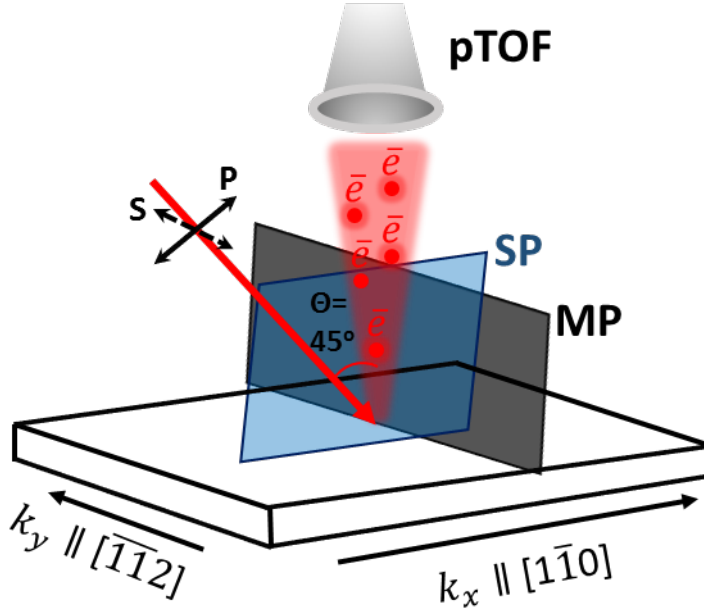


Figure A.1: Sketch of the experimental geometry for linear and 2PPE photoemission. For all laser pulses used in this experiment, the incident angle is  $45^\circ$  with respect to the surface normal. Position-sensitive time of flight spectrometer (pTOF) is also placed normal to the surface which detects the photoelectrons in two mutually perpendicular momentum directions ( $k_x \parallel [1\bar{1}0]$  and  $k_y \parallel [\bar{1}12]$ ) as a function of their energy.

### A.3 Occupied Electronic Structure

Figure A.2 shows the linear photoemission intensity plot in false color representation obtained using  $p$  polarized laser pulses of energy  $h\nu = 6.06$  eV, along two high symmetry, parallel ( $k_x \parallel [1\bar{1}0]$ ) and perpendicular ( $k_y \parallel [\bar{1}12]$ ) to the step directions. Zero in-plane electron momentum refers to normal photoemission  $\Gamma$  from the macroscopic Si(557)-surface, which is  $9.45^\circ$  tilted with respect to the microscopic Si(111) terraces. At normal photoemission, two distinct occupied electronic signatures C and D could be identified at the binding energies 0.45 eV and 0.55 eV below the Fermi level  $E_F$ , respectively, as determined at  $k_x = 0$ . The white closed circles in the left panel represent the dispersion relation  $E(k_x)$  of states C and D. This is obtained by extracting energy distribution

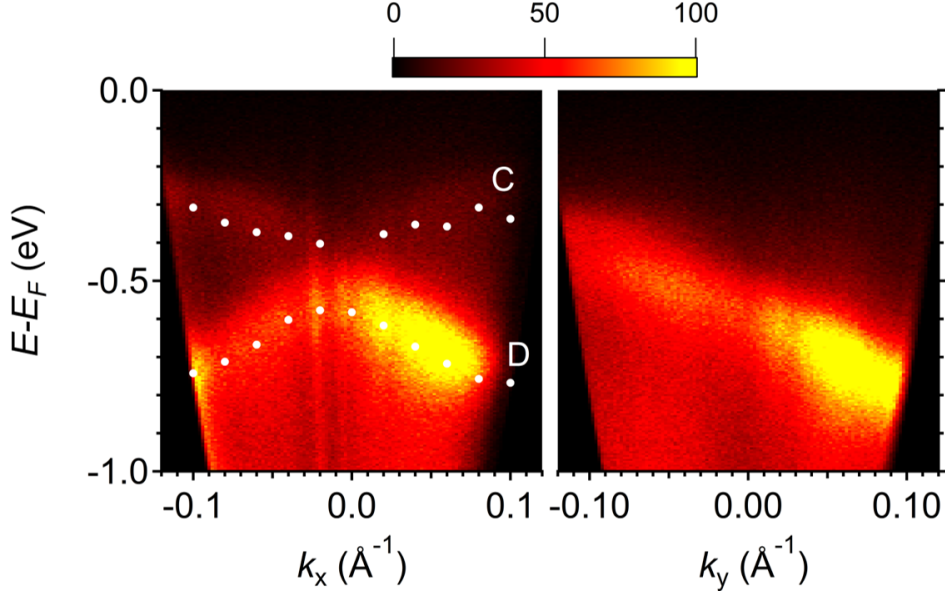


Figure A.2: False color representation of linear photoemission spectra recorded parallel ( $k_x$ ) and perpendicular ( $k_y$ ) to the wire directions using  $h\nu = 6.06$  eV laser pulses. The vertical axes represent the binding energy scale, referenced to the Fermi level  $E_F$ . Closed white circles indicate the dispersion relation of both states along  $k_x$ . An asymmetric electronic dispersion is evident across  $k_y = 0$ . The photoemission intensity of the electronic signatures can be followed from the color legend on top of the panels.

curves (EDCs) at various  $k_x$  values and plotting the intensity maxima of both electronic states. Along this direction, states C and D exhibit a symmetric upward and downward dispersion across  $k_x = 0$ , respectively. However, a clear asymmetry in the photoemission intensity distribution is evident for state D which exhibits a large spectral weight at  $k_x > 0$  compared to  $k_x < 0$ .

In the direction perpendicular to the steps ( $k_y$ ), a clear asymmetric electronic structure is observed where the dispersion relation  $E(k_y) = E(-k_y)$  does not hold. Furthermore, the intensity distribution for this single electronic signature exhibits strong asymmetry across  $k_y = 0$ .

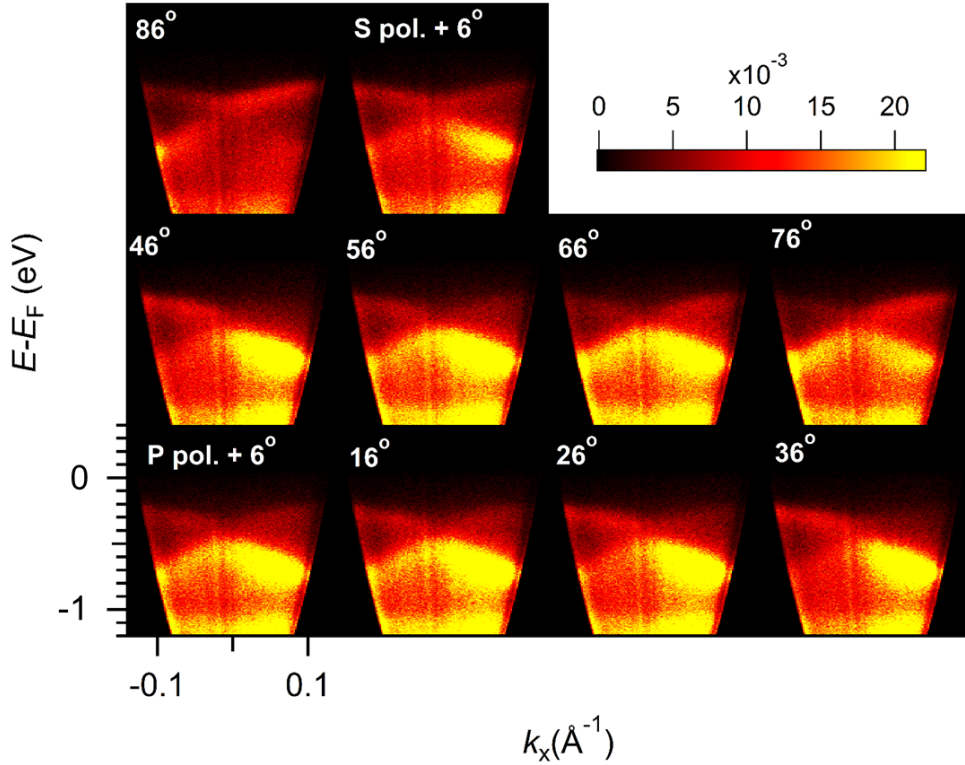


Figure A.3: False color representation of the polarization dependent linear photoemission spectrum recorded along the wire,  $k_x$  direction for each  $10^\circ$  change in the E-field vector of  $h\nu = 6.06$  eV laser pulses. The color legend shows the intensity scale which remains the same for each recorded spectrum to directly visualize the intensity change as a result of modification of laser pulse polarization.

### A.3.1 Polarization Dependent Linear Photoemission

Polarization dependent photoemission provides further knowledge concerning the electronic structure, e.g their symmetry character based on which the orbitals character can be determined. Polarization dependent change occurring in the photoemission intensity distribution of the occupied electronic states is recorded by modifying the E-field vector of the incident laser pulses from nearly  $p$  to  $s$  polarization in steps of  $10^\circ$ . The resulting PE intensity plots in false color representation along  $k_x$  direction are shown in Fig. A.3.

Since these intensity plots contain a rich amount of information, we analyze

### A.3. OCCUPIED ELECTRONIC STRUCTURE

---

them by addressing specific momentum regions of the electronic states in a step-wise manner. Starting from the energetically lower lying state D while looking in the momentum range  $k_x > 0$ , a large spectral weight is observed with nearly  $p$  polarized laser pulses, as can be seen in the lower left panel. At first, a gain in the photoemission intensity is observed as the E-field vector rotates towards  $s$  polarization. However, this initial gain was overtaken by a reduction in the intensity as the E-field vector reaches close to  $s$  polarization, where almost a complete suppression of the photoemission intensity is seen. As the E-field vector rotates further, a drastic gain in the intensity is observed, as can be seen in the top right panel of Fig. A.3. In the momentum region  $k_x < 0$ , initially a decrease in the photoemission intensity is evident in a phase where E-field vector is nearly  $p$  polarized to an angle of  $46^\circ$ . Subsequently, a sudden intensity gain followed by an almost complete suppression occurs just below the  $s$  polarized light. Just above the  $s$  polarized light, a slight gain in the intensity occurs, as can be seen in the top right panel of Fig. A.3. Remarkably, the evolution of the polarization dependent intensity variation is opposite at the momentum regions  $k_x > 0$  and  $k_x < 0$ .

For the energetically higher lying state C, at the momentum region  $k_x > 0$  and  $k_x < 0$ , the polarization dependent photoemission intensity variations occur in a much similar manner as for state D. The gain and losses in photoemission intensity manifest an opposite evolution at the opposite momentum region of  $k_x > 0$  and  $k_x < 0$ .

In order to clearly visualize the observed polarization dependent variations in the photoemission intensity, we quantify these effects. In particular, the peculiar behavior of the opposite evolution of the polarization dependent intensity growth in momentum regions  $k_x > 0$  and  $k_x < 0$  is interesting. Therefore, we focus on the specific equivalent but opposite momentum across  $k_x = 0$  to analyze their differences.

The energy distribution curves (EDCs) extracted at  $k_x = \pm 0.07 \text{ \AA}^{-1}$  in

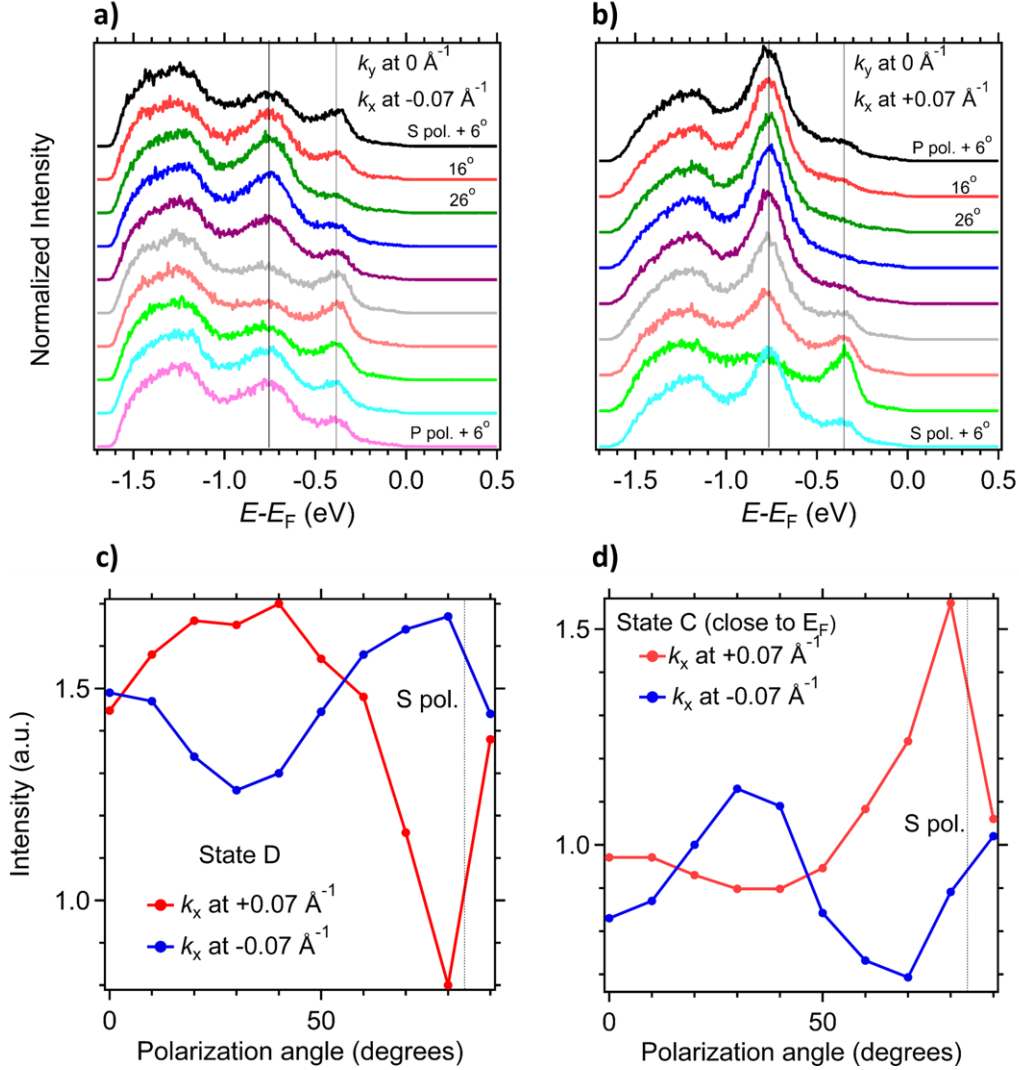


Figure A.4: Energy distribution curves (EDCs) are extracted in a momentum window of width  $\Delta k = 0.02 \text{ \AA}^{-1}$  centered at  $+k_x = 0.07 \text{ \AA}^{-1}$  (a) and  $-k_x = 0.07 \text{ \AA}^{-1}$  (b) from the polarization dependent intensity plots of Fig. A.3. An offset artificially introduced among the EDCs for better visualization. Vertical lines are drawn to follow the position of the electronic signatures C ( $E - E_F = -0.45 \text{ eV}$ ) and D ( $E - E_F = -0.55 \text{ eV}$ ). The intensities of the electronic states from the EDCs are plotted as a function of polarization of 6.06 eV laser pulses for the state D and C in (c) and (d), respectively. Red and blue solid lines with closed circle refer to the momentum  $+k_x$  and  $-k_x$ , respectively, for which the curves are extracted. The occurrence of the *s* polarized laser pulses is marked by a dotted line on both graphs.

### A.3. OCCUPIED ELECTRONIC STRUCTURE

---

an integrated momentum window of  $\Delta k_x = 0.02 \text{ \AA}^{-1}$ , are shown in Fig. A.4a and A.4b, respectively. An offset along the vertical intensity scale was introduced among the EDCs for clear visibility. Solid lines are drawn to track any polarization dependent change in the peak maximum position of electronic states C and D. It can be seen, that the peak energy position remains same at opposite momentum  $k_x = \pm 0.07 \text{ \AA}^{-1}$  for all polarization of incident light. Intensities of states C and D obtained from the above EDCs as a function of light polarization at opposite momenta  $\pm k_x$ , are shown in Fig. A.4c and A.4d, respectively. Solid red and blue curves indicate the polarization dependent intensity variations occurring at  $+k_x$  and  $-k_x$ , respectively. The occurrence of the *s* polarized laser pulses is also marked on the graph plots. At momentum region  $+k_x$  for state D, first a finite PE intensity is observed close to *p* polarized light. This region exhibits a certain gain in the intensity and shows a maximum at a polarization angle of  $\sim 35^\circ$ . A sudden drop at the intensity subsequently takes place and a minimum occurs roughly at the *s* polarization of laser pulse. This followed again by a drastic increase in the intensity. The same electronic state D, at the negative momenta  $-k_x$  exhibits an opposite dependence on the laser pulse polarization. The magnitude of intensity change is smaller compared to the positive momentum  $+k_x$  region. It should be noted that the polarization dependent intensity curve for  $-k_x$  is scaled up to compare directly with the curve obtained for  $+k_x$ . For the energetically higher lying state C, the polarization dependent intensity variation curves exhibit an opposite evolution at the opposite momenta of  $\pm k_x$  similar to state D.

These observations concerning the polarization dependent intensity behavior are remarkable in many ways. First of all, no complete suppression of the intensity was observed at any angle of the E-field vector of the laser pulses. Secondly, the maximum and the minimum of the curves occur within a polarization angle change of  $\sim 50^\circ$  instead of  $90^\circ$ . Finally, the opposite polarization dependent intensity dependence at  $\pm k_x$  is counter intuitive to a simple symmetry picture,

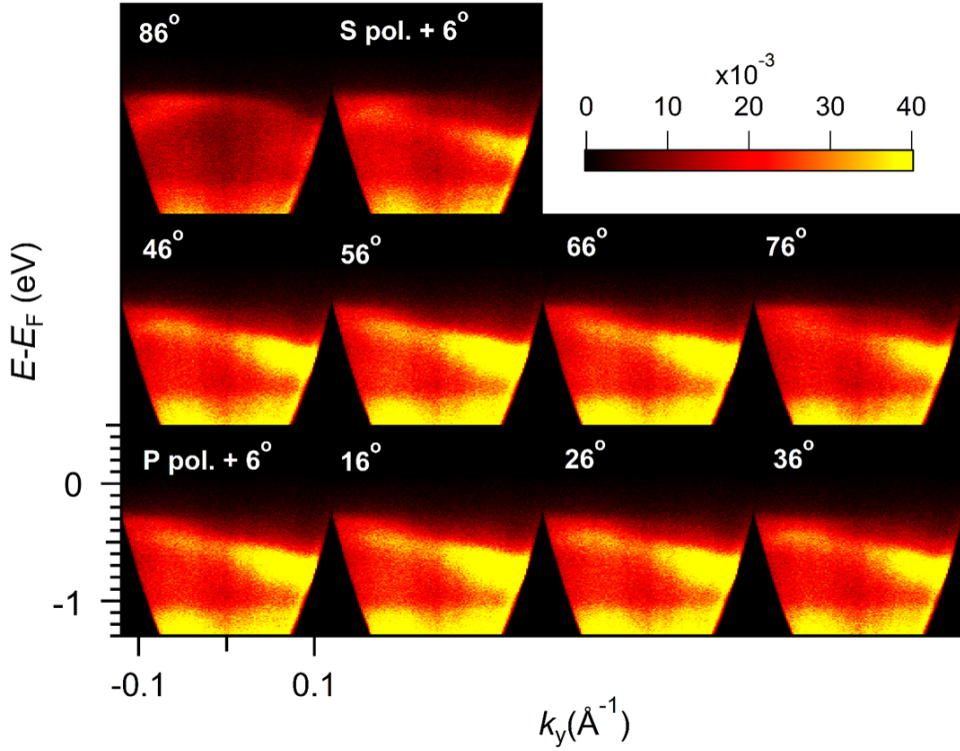


Figure A.5: False color representation of the polarization dependent direct photoemission spectrum recorded perpendicular to the wire ( $k_y$ ) direction for each  $10^\circ$  change in the E-field vector of  $h\nu = 6.06$  eV laser pulses. Color legend shows the intensity scale which remains the same for each recorded spectra to directly visualize the photoemission intensity variation as a result of modification of laser pulses polarization.

which suggests the same orbital character at the opposite momentum. These aspects will be discussed in detail in the next section.

The polarization dependent photoemission intensity plots obtained in the direction perpendicular to steps ( $k_y$ ) are shown in Fig. A.5. Once again, a linear photoemission intensity plot is recorded for each  $10^\circ$  change in the E-field vector of the incident laser pulse. The asymmetric electronic structure across  $k_y = 0$  can be observed for nearly  $p$  polarized laser pulses (bottom left panel). For this single visible electronic signature, the intensity clearly decreases as the E-field vector rotates towards the  $s$  polarization, in the whole momentum

space. Nevertheless, the asymmetry in the electronic structure remains for all polarizations. Due to the absence of the corresponding electronic structure at the opposite momentum region, we restrained ourselves from an in-depth analysis of the polarization dependent data along this direction.

#### A.3.2 Discussions

##### Occupied electronic states

First, we discuss the origin of the asymmetric electronic dispersion relation perpendicular to the step direction, i.e.  $E(+k_y) \neq E(-k_y)$ . This asymmetry was not observed along the step ( $k_x$ ) direction. The angle-resolved photoemission measurements conducted on Si(111)- $7 \times 7$  reconstructed surface [136] revealed the presence of symmetric and asymmetric electronic dispersion along  $\Gamma K \parallel [1\bar{1}0]$  and  $\Gamma M \parallel [\bar{1}\bar{1}2]$  directions, respectively. It was concluded in this study that the asymmetric electronic structure is caused by the break of time-reversal symmetry associated to the bulk state photoemission. In fcc crystals that are cut along the (111) orientation, the atomic stacking results in equivalent  $\Gamma K$  and  $\bar{\Gamma K}$  but nonequivalent  $\Gamma M$  and  $\bar{\Gamma M}$  directions. This leads to a situation in which the perpendicular momentum component  $k_\perp$  of electrons may switch their directions while going from  $\Gamma M$  to  $\bar{\Gamma M}$ . Consequently, certain electronic state may not show up at the opposite momentum. This aspect has been discussed in detail in connection with the asymmetries observed for Pb/Si(111) in chapter 4 of this thesis work.  $\Gamma K$  and  $\Gamma M$  directions correspond to  $k_x$  and  $k_y$  directions in the Pb/Si(557) system. It is therefore concluded, that the observed asymmetric dispersion along  $k_y$  shows up due to the bulk character of investigated occupied states. The asymmetric photoemission intensity distribution observed along both momentum directions  $k_x$  and  $k_y$  is possibly a result of off-normal light incidence of  $p$  polarized light [40], final states effects [45], or spin-effects [47]. These asymmetric effects are very similar to our observation and understanding for the Pb/Si(111) system.

### Polarization dependent photoemission

First of all, the polarization dependent intensity variations are rather small. This is understandable because the experimental geometry suggests that the scattering plane does not overlap with the mirror plane of the system. This leads to the symmetry mixing of the final states and no strict application of the dipole selection rules. A very peculiar observation in the polarization dependent photoemission intensity graph plots (Fig. A.4) is the occurrence of maxima and minima by a  $\sim 50^\circ$  change in the angle of E-field vector instead of  $90^\circ$ . This indicates that there can be no simple explanation of the symmetry character of these states. In fact, the underlying physics may be much more complicated and not explainable in the framework of the dipole selection rules.

## A.4 Unoccupied Electronic Structure

### A.4.1 Pump Polarization Dependence

The 2PPE spectra obtained for the Pb/Si(557) system with  $p$ - $p$  polarization combination of pump (UV,  $h\nu_2 = 3.8$  eV) and probe (VIS,  $h\nu_1 = 1.9$  eV) laser pulses have already been discussed in chapter 5 of this thesis work. The unoccupied nature of electronic states A ( $E - E_F = 3.55$  eV) and B ( $E - E_F = 3.3$  eV) was confirmed by the time-resolved measurements. In the following discussion, polarization dependent photoemission studies performed on the Pb/Si(557) are presented.

Polarization dependent change occurring in the 2PPE intensity of electronic states recorded by modifying the pump laser pulses polarization for fixed  $p$  polarization of probe laser pulses at maximum temporal overlap ( $\Delta t = 0$ ). In Fig. A.6, 2PPE spectra obtained along  $k_x$  direction for every  $10^\circ$  change in the E-field vector of pump laser pulses are shown. Similar to the analysis performed for the occupied electronic states, the opposite momentum regions

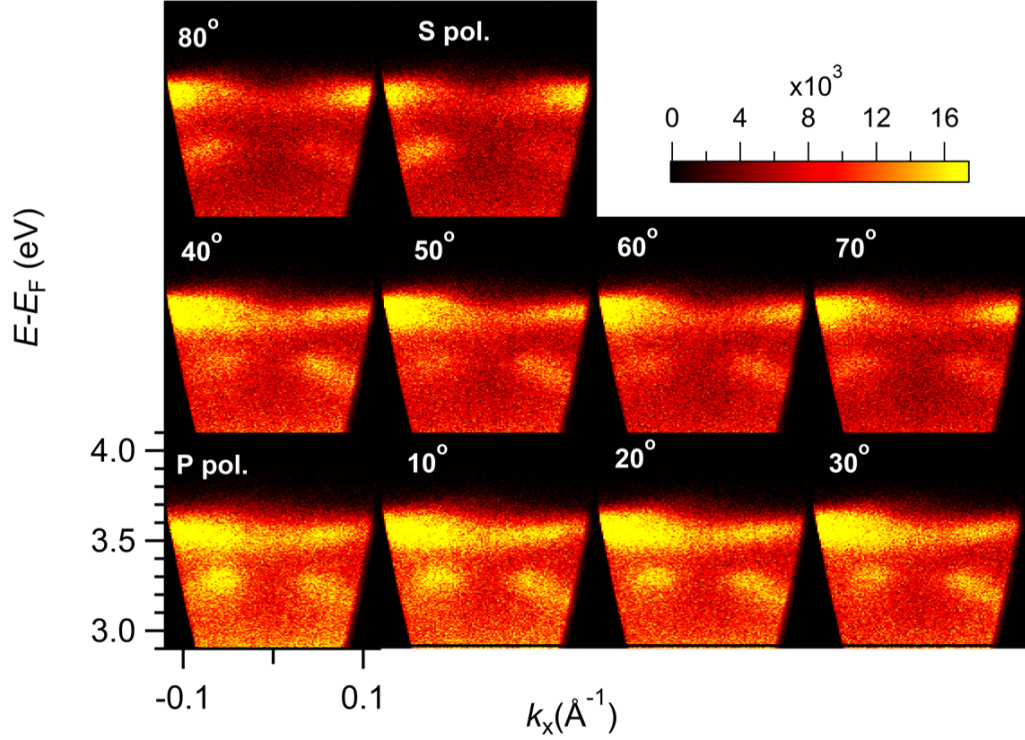


Figure A.6: False color representation of pump laser pulse ( $h\nu_2 = 3.8$  eV) polarization dependent 2PPE spectra recorded along  $k_x$  for each  $10^\circ$  change in the E-field vector. The color legend shows the intensity scale which remains the same for each spectrum, so that a change in the 2PPE intensity as a result of polarization could be visualized. Probe laser pulses ( $h\nu_1 = 1.9$  eV) were kept fixed at  $p$  polarization during the whole measurement.

$\pm k_x$  are focused on investigating the symmetry character of the unoccupied states. The EDCs are extracted at the opposite momentum of  $k_x = \pm 0.07 \text{ \AA}^{-1}$  in an integrated momentum window of  $\Delta k_x = 0.02 \text{ \AA}^{-1}$  and plotted in Fig. A.7. An artificial offset along the intensity scale is introduced among the EDCs for clear visibility. Vertical lines are drawn to track the energy position of peaks maximum of states A and B. As it can be seen, the peak position of state B remains fixed for the EDCs obtained at the opposite momentum  $\pm k_x$  and for all angles of the E-field vector of the pump beam. On the other hand, state A exhibits a shift to lower binding energy with a maximum peak shift of  $< 50$  meV. This might be an indication of two different electronic states located

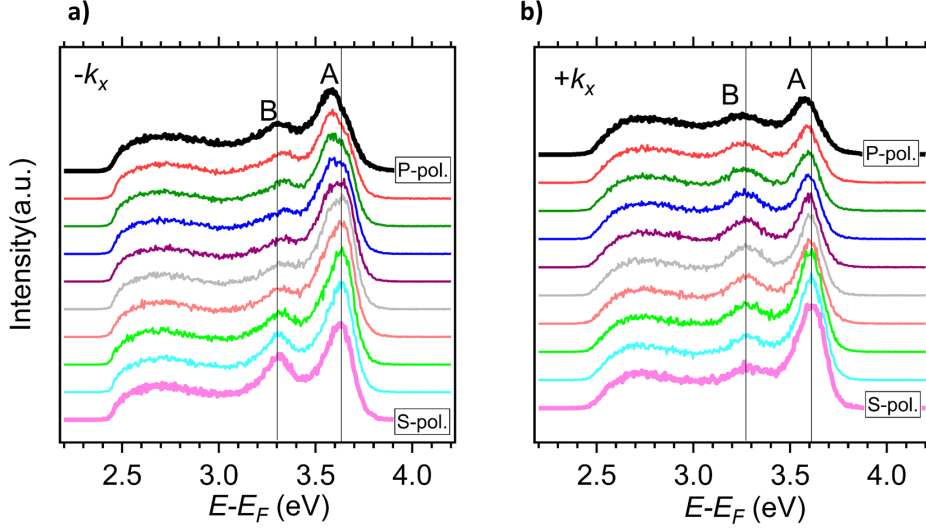


Figure A.7: EDCs are extracted in a momentum window of width  $\Delta k = 0.02 \text{ \AA}^{-1}$  centered at  $-k_x = 0.07 \text{ \AA}^{-1}$  (a) and  $+k_x = 0.07 \text{ \AA}^{-1}$  (b) from the polarization dependent intensity plots of Fig. A.6. An offset artificially induced among the EDCs for better visualization. Vertical lines are drawn to follow the position of the electronic states A ( $E - E_F = 3.55 \text{ eV}$ ) and B ( $E - E_F = 3.3 \text{ eV}$ ).

energetically closed to each other and possess opposite symmetry character. These opposite characters are probed with the opposite  $s$  and  $p$  polarization of pump laser pulses.

Nevertheless, we proceed with plotting the intensities of states A and B as a function of pump laser pulse polarization and the results are shown in Fig. A.8. Electronic state A at the opposite momentum  $\pm k_x$  shows a nearly similar evolution of polarization dependent 2PPE intensity, as can be seen in the left panel. Curves obtained for opposite momentum regions exhibit a clear minimum and maximum at the  $p$  and  $s$  polarization of the pump pulse, respectively. From the minimum of both of the curves, it can be seen that a finite intensity always remains and no complete suppression of the intensity occurs at any polarization. Polarization dependent 2PPE intensity curves obtained at the opposite momentum for state B manifest an opposite evolution

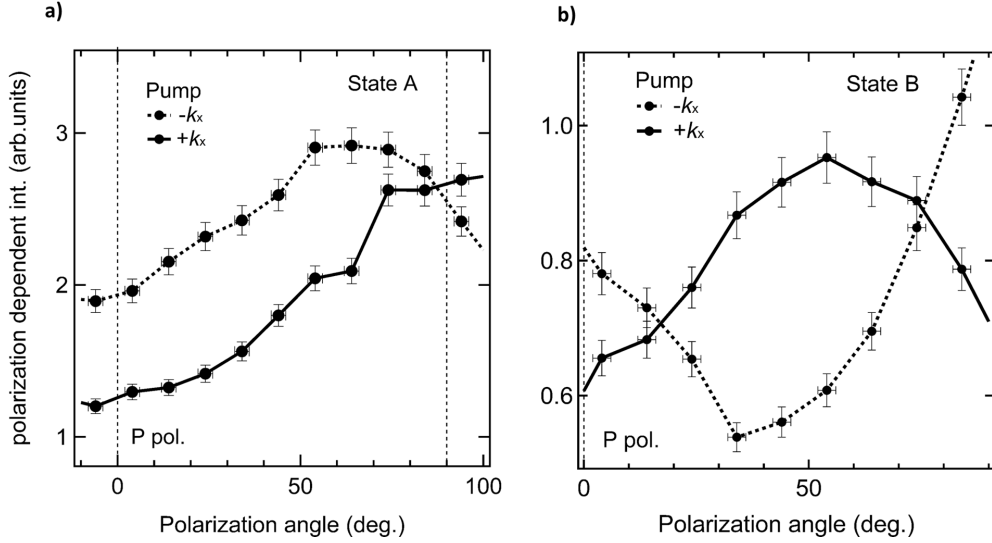


Figure A.8: The intensities of the electronic states from the energy distribution curves (EDCs) in Fig. A.7 is plotted as a function of polarization of pump laser pulses for the state A and B, shown in (a) and (b), respectively. Black solid and dotted lines with closed circles refer to the polarization dependence at the momentum  $+k_x$  and  $-k_x$ , respectively. The occurrence of the  $p$  and  $s$  polarized pump laser pulses is marked by a dashed line on both graphs.

(see Fig. A.8b). More interestingly, the maximum and minimum at these curves do not occur at  $s$  or  $p$  polarization of light. The maximum for the  $+k_x$  curve (solid line) shows up at  $\sim 60^\circ$  and the minimum of the  $-k_x$  curve occurs at  $\sim 40^\circ$  angle of the E-field vector. These findings indicate that no conclusive statements can be made concerning the orbital character of state B with respect to the scattering plane. Nevertheless, a nearly opposite evolution of polarization dependent 2PPE intensity curves indicates opposite orbital characters at the opposite momentum.

#### A.4.2 Probe Polarization Dependence

2PPE measurements were also performed to investigate the effect of probe beam polarization on the 2PPE intensity of unoccupied states while keeping the pump beam polarization fixed at  $p$ . The probe polarization dependent

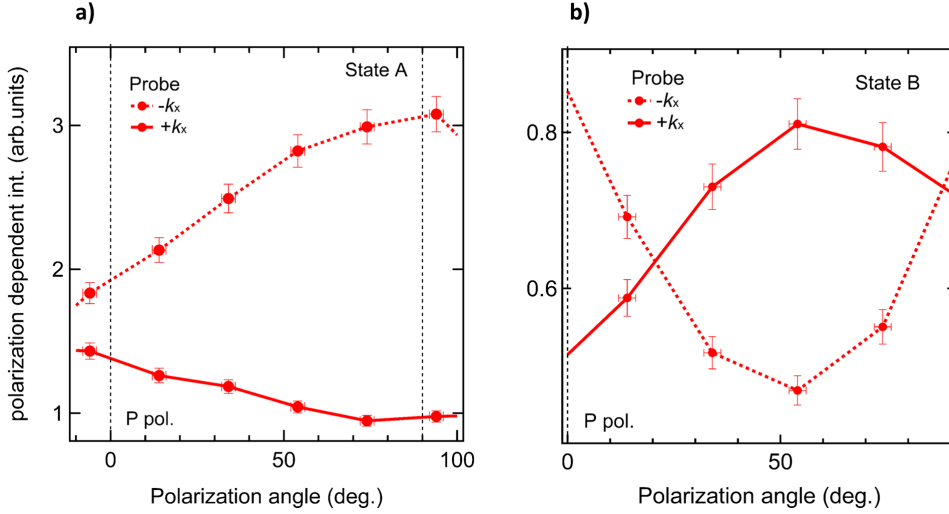


Figure A.9: Plot of intensities of the unoccupied electronic states as a function of polarization of probe laser pulse shown for state A and B in (a) and (b), respectively. The solid and dashed red lines indicate the polarization dependence at  $k_x = +0.07 \text{ \AA}^{-1}$  and  $-k_x = 0.07 \text{ \AA}^{-1}$ , respectively. The polarization of the pump laser pulse was kept fixed at  $p$  polarization during the whole measurement. The occurrence of  $p$  and  $s$  polarized probe laser pulses is marked on the graphs.

2PPE intensity evolution for both states A and B is investigated at the opposite momentum of  $\pm k_x$ . The results of the quantitative analysis are shown in Fig. A.9.

Probe polarization dependent 2PPE intensity curves obtained for state A at the opposite momentum of  $\pm k_x$  show an opposite evolution, as can be seen in the left panel. The maximum and minimum of  $+k_x$  curve shows up at  $p$  and  $s$  polarized probe light, respectively. The situation completely reverses for  $-k_x$  curve. Although no complete suppression of intensity is observed for any of the two curves, their opposite evolution indicates opposite symmetry character at the opposite momentum.

For state B, the polarization dependent intensity curves do not show a maximum or minimum at either  $p$  or  $s$  polarization of the probe laser pulses. Instead, the maximum and the minimum occurred at  $\sim 60^\circ$  of E-field vector for both  $+k_x$  and  $-k_x$  curves. Nevertheless, the evolution of the 2PPE intensity

at the opposite momentum of  $\pm k_x$  is once again opposite.

### A.4.3 Discussions

Pump and probe beam polarization dependent studies performed on Pb/Si(111) manifest interesting results. The major findings of these studies are summarized as follows.

- Polarization dependent 2PPE intensity modification is very small, in particular for state A and no complete suppression of the 2PPE intensity is observed for any polarization angle of the pump and probe laser pulses.
- Maximum and minimum of the polarization-dependent 2PPE curves for state B occur at laser pulse polarization other than  $s$  and  $p$ .
- Polarization dependent 2PPE curves obtained at the opposite momentum exhibit an opposite evolution indicating different symmetry of orbitals.

The small polarization dependent change brought about by the variation of E-field vector is rather easy to understand. From the experimental geometry, it is clear that the scattering and mirror plane in this experimental geometry does not overlap. For this case, the dipole selection rules are not strictly applicable, in particular at generic  $k$  points where the electronic states are not of even or odd symmetry but a linear combination of both the symmetries. This suggests the presence of finite 2PPE intensity at all angle of polarization.

The observation of a maximum and minimum of polarization dependent 2PPE curve occurring at a polarization angle other than  $s$  and  $p$  refers to an orbital symmetry which is not even or odd with respect to the scattering plane. This rather suggests a dipole vector belonging to the involved orbitals located at a finite angle from the scattering plane. Since the adsorbate Pb forms a  $30^\circ$  rotated  $\sqrt{3} \times \sqrt{3}$  structure on top of Si substrate, the electronic states belonging to pure Si or Pb may have the dipole which are not aligned.

Therefore, the observed difference in the polarization dependence for states A and B, likely referring to the fact that they are Pb and Si driven states.

Finally, the different symmetry character at the opposite momentum  $\pm k_x$  is similar to the case of Pb/Si(111). It was concluded for this asymmetry associated with the unoccupied electronic states of Pb/Si(111) that they possess mixed symmetry character due to strong spin-orbit coupling. A specific light polarization combined with the effect of linear dichroism may excite the electron from a specific momentum region. The other polarization excites the electron from the opposite momentum region only. This results in a false appearance of opposite symmetry character at the opposite momentum. Due to the similarity of both systems, the above interpretation may also be valid for Pb/Si(557).

However, most of the above qualitative description demands further verification from the detailed theoretical studies for this complex metal-semiconductor structure.



---

---

## Bibliography

- <sup>1</sup>M. J. Duff, *The world in eleven dimensions: supergravity, supermembranes and M theory* (Taylor & Francis, 1999).
- <sup>2</sup>J. M. Carpinelli, H. H. Weitering, E. W. Plummer, and R. Stumpf, “Direct observation of a surface charge density wave”, *Nature* **381**, 398 (1996).
- <sup>3</sup>T. Hirahara, T. Komorida, Y. Gu, F. Nakamura, H. Idzuchi, H. Morikawa, and S. Hasegawa, “Insulating conduction in Sn/Si(111): Possibility of a Mott insulating ground state and metallization/localization induced by carrier doping”, *Physical Review B* **80**, 235419 (2009).
- <sup>4</sup>T. Zhang, P. Cheng, W.-J. Li, Y.-J. Sun, G. Wang, X.-G. Zhu, K. He, L. Wang, X. Ma, X. Chen, Y. Wang, Y. Liu, H.-Q. Lin, J.-F. Jia, and Q.-K. Xue, “Superconductivity in one-atomic-layer metal films grown on Si(111)”, *Nature Physics* **6**, 104 (2010).
- <sup>5</sup>K. Yaji, S. Hatta, T. Aruga, and H. Okuyama, “Structural and electronic properties of the Pb/Ge(111)- $\beta(\sqrt{3} \times \sqrt{3})R30^\circ$  surface studied by photoelectron spectroscopy and first-principles calculations”, *Physical Review B* **86**, 235317 (2012).
- <sup>6</sup>K. Yaji, Y. Ohtsubo, S. Hatta, H. Okuyama, K. Miyamoto, T. Okuda, A. Kimura, H. Namatame, M. Taniguchi, and T. Aruga, “Large Rashba spin splitting of a metallic surface-state band on a semiconductor surface”, *Nature Communications* **1**, 17 (2010).
- <sup>7</sup>R. E. Peierls, *Quantum Theory of Solids* (Oxford University Press, 2001).

## BIBLIOGRAPHY

---

- <sup>8</sup>G. Grüner, “The dynamics of charge-density waves”, *Reviews of Modern Physics* **60**, 1129 (1988).
- <sup>9</sup>J. M. Luttinger, “Analytic properties of single-particle propagators for many-Fermion systems”, *Physical Review Journal Archive* **121**, 942 (1961).
- <sup>10</sup>G. E. Moore, “Cramming more components onto integrated circuits”, *Electronics* **38**, 114 (1965).
- <sup>11</sup>G. E. Moore, “Progress in digital integrated electronics”, *IEEE Solid-State Circuits Society Newsletter* **11**, 36 (2006).
- <sup>12</sup>W. H. Choi, K. S. Kim, and H. W. Yeom, “High-resolution core-level photoemission study of dense Pb overlayers on Si(111)”, *Physical Review B* **78**, 195425 (2008).
- <sup>13</sup>J. A. Carlisle, T. Miller, and T.-C. Chiang, “Photoemission study of the growth, desorption, Schottky-barrier formation, and atomic structure of Pb on Si(111)”, *Physical Review B* **45**, 3400 (1992).
- <sup>14</sup>D. R. Heslinga, H. H. Weitering, D. P. van der Werf, T. M. Klapwijk, and T. Hibma, “Atomic-structure-dependent schottky barrier at epitaxial Pb/Si(111) interfaces”, *Physical Review Letters* **64**, 1589 (1990).
- <sup>15</sup>M. Hupalo, J. Schmalian, and M. C. Tringides, ““Devil’s Staircase” in Pb/Si(111) ordered phases”, *Physical Review Letters* **90**, 216106 (2003).
- <sup>16</sup>E. Ganz, H. Ing-Shouh, X. Fulin, S. K. Theiss, and J. Golovchenko, “Growth and morphology of Pb on Si(111)”, *Surface Science* **257**, 259 (1991).
- <sup>17</sup>K. Sakamoto, H. Kakuta, K. Sugawara, K. Miyamoto, A. Kimura, T. Kuzumaki, N. Ueno, E. Annese, J. Fujii, A. Kodama, T. Shishidou, H. Namatame, M. Taniguchi, T. Sato, T. Takahashi, and T. Oguchi, “Peculiar Rashba splitting originating from the two-dimensional symmetry of the surface”, *Physical Review Letters* **103**, 156801 (2009).

- <sup>18</sup>K. Nakajin and S. Murakami, “Theory of unconventional spin states in surfaces with non-Rashba spin-orbit interaction”, *Physical Review B* **91**, 245428 (2015).
- <sup>19</sup>I. Gierz, T. Suzuki, E. Frantzeskakis, S. Pons, S. Ostanin, A. Ernst, J. Henk, M. Grioni, K. Kern, and C. R. Ast, “Silicon surface with giant spin splitting”, *Physical Review Letters* **103**, 046803 (2009).
- <sup>20</sup>E. Frantzeskakis, S. Pons, and M. Grioni, “Band structure scenario for the giant spin-orbit splitting observed at the Bi/Si(111) interface”, *Physical Review B* **82**, 085440 (2010).
- <sup>21</sup>Y. Ohtsubo, S. Hatta, K. Yaji, H. Okuyama, K. Miyamoto, T. Okuda, A. Kimura, H. Namatame, M. Taniguchi, and T. Aruga, “Spin-polarized semiconductor surface states localized in subsurface layers”, *Physical Review B* **82**, 201307 (2010).
- <sup>22</sup>S. Hatta, T. Aruga, Y. Ohtsubo, and H. Okuyama, “Large Rashba spin splitting of surface resonance bands on semiconductor surface”, *Physical Review B* **80**, 113309 (2009).
- <sup>23</sup>S. D. Stolwijk, K. Sakamoto, A. B. Schmidt, P. Krüger, and M. Donath, “Spin texture with a twist in momentum space for Tl/Si(111)”, *Physical Review B* **91**, 245420 (2015).
- <sup>24</sup>J. Ibañez-Azpiroz, A. Eiguren, and A. Bergara, “Relativistic effects and fully spin-polarized Fermi surface at the Tl/Si(111) surface”, *Physical Review B* **84**, 125435 (2011).
- <sup>25</sup>S. D. Stolwijk, A. B. Schmidt, M. Donath, K. Sakamoto, and P. Krüger, “Rotating spin and giant splitting: Unoccupied surface electronic structure of Tl/Si(111)”, *Physical Review Letters* **111**, 176402 (2013).
- <sup>26</sup>S. D. Stolwijk, K. Sakamoto, A. B. Schmidt, P. Krüger, and M. Donath, “Thin line of a Rashba-type spin texture: unoccupied surface resonance of Tl/Si(111) along  $\overline{\Gamma m}$ ”, *Physical Review B* **90**, 161109 (2014).

## BIBLIOGRAPHY

---

- <sup>27</sup>P. Eickholt, P. Krüger, S. D. Stolwijk, A. B. Schmidt, and M. Donath, “Effects of orbital composition in a pair of spin-orbit-split surface bands at Tl/Ge(111)”, *Physical Review B* **93**, 085412 (2016).
- <sup>28</sup>U. Bovensiepen and P. Kirchmann, “Elementary relaxation processes investigated by femtosecond photoelectron spectroscopy of two-dimensional materials”, *Laser & Photonics Reviews* **6**, 589 (2012).
- <sup>29</sup>E. Pop and K. Goodson, “Thermal phenomena in nanoscale transistors”, *Journal of Electronic Packaging* **128**, 102 (2006).
- <sup>30</sup>W. Shockley and H. J. Queisser, “Detailed balance limit of efficiency of p n junction solar cells”, *Journal of Applied Physics* **32**, 510 (1961).
- <sup>31</sup>T.-L. Chan, C. Z. Wang, M. Hupalo, M. C. Tringides, Z.-Y. Lu, and K. M. Ho, “First-principles studies of structures and stabilities of Pb/Si(111)”, *Physical Review B* **68**, 045410 (2003).
- <sup>32</sup>M. Hupalo, T. L. Chan, C. Z. Wang, K. M. Ho, and M. C. Tringides, “Atomic models, domain-wall arrangement, and electronic structure of the dense Pb/Si(111)– $\sqrt{3} \times \sqrt{3}$  phase”, *Physical Review B* **66**, 161410 (2002).
- <sup>33</sup>S. Stepanovsky, M. Yakes, V. Yeh, M. Hupalo, and M. C. Tringides, “The dense  $\alpha - \sqrt{3} \times \sqrt{3}$  Pb/Si(111) phase: A comprehensive STM and SPA-LEED study of ordering, phase transitions and interactions”, *Surface Science* **600**, 1417 (2006).
- <sup>34</sup>V. Yeh, M. Yakes, M. Hupalo, and M. C. Tringides, “Low temperature formation of numerous phases in Pb/Si(111)”, *Surface Science* **562**, L238 (2004).
- <sup>35</sup>X.-Y. Ren, H.-J. Kim, S. Yi, Y. Jia, and J.-H. Cho, “Spin-orbit coupling effects on the stability of two competing structures in Pb/Si(111) and Pb/Ge(111)”, *Physical Review B* **94**, 075436 (2016).

- <sup>36</sup>C. Brand, S. Muff, M. Fanciulli, H. Pfnür, M. C. Tringides, J. H. Dil, and C. Tegenkamp, “Spin-resolved band structure of a densely packed Pb monolayer on Si(111)”, *Physical Review B* **96**, 035432 (2017).
- <sup>37</sup>M. Bauer, S. Pawlik, R. Burgermeister, and M. Aeschlimann, “Symmetry properties of an electronic alkali excitation at a noble metal surface as investigated by two-photon photoemission”, *Surface Science* **402**, 62 (1998).
- <sup>38</sup>T. K. Rügheimer, T. Fauster, and F. J. Himpsel, “Unoccupied electronic states in atomic chains on Si(557)-Au: Time-resolved two-photon photoemission investigation”, *Physical Review B* **75**, 121401 (2007).
- <sup>39</sup>M. Wolf, A. Hotzel, E. Knoesel, and D. Velic, “Direct and indirect excitation mechanisms in two-photon photoemission spectroscopy of Cu(111) and CO/Cu(111)”, *Physical Review B* **59**, 5926 (1999).
- <sup>40</sup>H. Bentmann, H. Maaß, E. E. Krasovskii, T. R. F. Peixoto, C. Seibel, M. Leandersson, T. Balasubramanian, and F. Reinert, “Strong linear dichroism in spin-polarized photoemission from spin-orbit-coupled surface states”, *Physical Review Letters* **119**, 106401 (2017).
- <sup>41</sup>H. Maaß, H. Bentmann, C. Seibel, C. Tusche, S. V. Eremeev, T. R. Peixoto, O. E. Tereshchenko, K. A. Kokh, E. V. Chulkov, J. Kirschner, and F. Reinert, “Spin-texture inversion in the giant Rashba semiconductor BiTeI”, *Nature Communications* **7**, 11621 (2016).
- <sup>42</sup>K. Biedermann, S. Regensburger, T. Fauster, F. J. Himpsel, and S. C. Erwin, “Spin-split silicon states at step edges of Si(553)-Au”, *Physical Review B* **85**, 245413 (2012).
- <sup>43</sup>S. Bouzidi, F. Coletti, J. M. Debever, P. A. Thiry, P. Dumas, and Y. J. Chabal, “Inverse-photoemission spectroscopy of the unreconstructed, ideally H-terminated Si(111) surface”, *Physical Review B* **45**, 1187 (1992).

- <sup>44</sup>S. Bouzidi, J.-L. Guyaux, V. Langlais, H. Belkhir, J.-M. Debever, and P. Thiry, “Inverse photoemission study of non-reconstructed Si(111) surfaces: a comparison between H-Si(111)  $1 \times 1$  and As:Si(111)  $1 \times 1$ ”, *Surface Science* **331-333**, 1244 (1995).
- <sup>45</sup>M. Mulazzi, G. Rossi, J. Braun, J. Minár, H. Ebert, G. Panaccione, I. Vobornik, and J. Fujii, “Understanding intensities of angle-resolved photoemission with circularly polarized radiation from a Cu(111) surface state”, *Physical Review B* **79**, 165421 (2009).
- <sup>46</sup>L. Bawden, J. M. Riley, C. H. Kim, R. Sankar, E. J. Monkman, D. E. Shai, H. I. Wei, E. B. Lochocki, J. W. Wells, W. Meevasana, T. K. Kim, M. Hoesch, Y. Ohtsubo, P. Le Fèvre, C. J. Fennie, K. M. Shen, F. Chou, and P. D. C. King, “Hierarchical spin-orbital polarization of a giant Rashba system”, *Science Advances* **1**, e1500495 (2015).
- <sup>47</sup>G. Bian, L. Zhang, Y. Liu, T. Miller, and T.-C. Chiang, “Illuminating the surface spin texture of the giant-rashba quantum-well system Bi/Ag(111) by circularly polarized photoemission”, *Physical Review Letters* **108**, 186403 (2012).
- <sup>48</sup>K. Ishizaka, M. S. Bahramy, H. Murakawa, M. Sakano, T. Shimojima, T. Sonobe, K. Koizumi, S. Shin, H. Miyahara, A. Kimura, K. Miyamoto, T. Okuda, H. Namatame, M. Taniguchi, R. Arita, N. Nagaosa, K. Kobayashi, Y. Murakami, R. Kumai, Y. Kaneko, Y. Onose, and Y. Tokura, “Giant Rashba-type spin splitting in bulk BiTeI”, *Nature Materials* **10**, 521 (2011).
- <sup>49</sup>S. Jakobs, A. Ruffing, M. Cinchetti, S. Mathias, and M. Aeschlimann, “Orbital angular momentum structure of an unoccupied spin-split quantum-well state in Pb/Cu(111)”, *Physical Review B* **87**, 235438 (2013).
- <sup>50</sup>C. Jozwiak, C. H. Park, K. Gotlieb, C. Hwang, D. H. Lee, S. G. Louie, J. D. Denlinger, C. R. Rotundu, R. J. Birgeneau, Z. Hussain, and A. Lan-

- zara, “Photoelectron spin-flipping and texture manipulation in a topological insulator”, *Nature Physics* **9**, 293 (2013).
- <sup>51</sup>A. Kimura, E. E. Krasovskii, R. Nishimura, K. Miyamoto, T. Kadono, K. Kanomaru, E. V. Chulkov, G. Bihlmayer, K. Shimada, H. Namatame, and M. Taniguchi, “Strong Rashba-type spin polarization of the photocurrent from bulk continuum states: Experiment and theory for Bi(111)”, *Physical Review Letters* **105**, 076804 (2010).
- <sup>52</sup>H. Mirhosseini, J. Henk, A. Ernst, S. Ostanin, C.-T. Chiang, P. Yu, A. Winkelmann, and J. Kirschner, “Unconventional spin topology in surface alloys with Rashba-type spin splitting”, *Physical Review B* **79**, 245428 (2009).
- <sup>53</sup>A. Ruffing, S. Vollmar, S. Jakobs, S. Kaltenborn, A. Baral, M. Cinchetti, S. Mathias, H. C. Schneider, and M. Aeschlimann, “Ultrafast electron dynamics in a metallic quantum well nanofilm with spin splitting”, *Physical Review B* **88**, 075148 (2013).
- <sup>54</sup>S. N. P. Wissing, A. B. Schmidt, H. Mirhosseini, J. Henk, C. R. Ast, and M. Donath, “Ambiguity of experimental spin information from states with mixed orbital symmetries”, *Physical Review Letters* **113**, 116402 (2014).
- <sup>55</sup>K. Yaji, K. Kuroda, S. Toyohisa, A. Harasawa, Y. Ishida, S. Watanabe, C. Chen, K. Kobayashi, F. Komori, and S. Shin, “Spin-dependent quantum interference in photoemission process from spin-orbit coupled states”, *Nature Communications* **8**, 14588 (2017).
- <sup>56</sup>M. Ärrälä, H. Hafiz, D. Mou, Y. Wu, R. Jiang, T. Riedemann, T. A. Lograsso, B. Barbiellini, A. Kaminski, A. Bansil, and M. Lindroos, “Laser angle-resolved photoemission as a probe of initial state  $k_z$  dispersion, final-state band gaps, and spin texture of Dirac states in the  $\text{Bi}_2\text{Te}_3$  topological insulator”, *Physical Review B* **94**, 155144 (2016).

- <sup>57</sup>S. Moser, “An experimentalist’s guide to the matrix element in angle resolved photoemission”, *Journal of Electron Spectroscopy and Related Phenomena* **214**, 29 (2017).
- <sup>58</sup>J. Reimann, J. Gdde, K. Kuroda, E. V. Chulkov, and U. Hfer, “Spectroscopy and dynamics of unoccupied electronic states of the topological insulators  $\text{Sb}_2\text{Te}_3$  and  $\text{Sb}_2\text{Te}_2\text{S}$ ”, *Physical Review B* **90**, 081106 (2014).
- <sup>59</sup>A. Sterzi, G. Manzoni, A. Crepaldi, F. Cilento, M. Zacchigna, M. Leclerc, P. Bugnon, A. Magrez, H. Berger, L. Petaccia, and F. Parmigiani, “Probing band parity inversion in the topological insulator  $\text{GeBi}_2\text{Te}_4$  by linear dichroism in ARPES”, *Journal of Electron Spectroscopy and Related Phenomena* **225**, 23 (2018).
- <sup>60</sup>J. A. Waugh, T. Nummy, S. Parham, Q. Liu, X. Zhang, A. Zunger, and D. S. Dessau, “Minimal ingredients for orbital-texture switches at Dirac points in strong spin – orbit coupled materials”, *Npj Quantum Materials* **1**, 16025 (2016).
- <sup>61</sup>M. J. Xia, Z. R. W. J. Ye, Y. H. Zhang, Y. Chen, S. D. Niu, X. H. Xu, D. F. Chen, F. Chen, X. H. Xie, B. P. Zhang, and D. L. T. Feng, “Angle resolved photoemission spectroscopy study on the surface states of the correlated topological insulator  $\text{YbB}_6$ ”, *Scientific Reports* **4**, 5999 (2014).
- <sup>62</sup>Z. Xie, S. He, C. Chen, Y. Feng, H. Yi, A. Liang, L. Zhao, D. Mou, J. He, Y. Peng, X. Liu, Y. Liu, G. Liu, X. Dong, L. Yu, J. Zhang, S. Zhang, Z. Wang, F. Zhang, F. Yang, Q. Peng, X. Wang, C. Chen, Z. Xu, and X. J. Zhou, “Orbital-selective spin texture and its manipulation in a topological insulator”, *Nature Communications* **5**, 3382 (2014).
- <sup>63</sup>A. Yang, J. Schneeloch, G. D. Gu, M. Brahlek, N. Bansal, S. Oh, A. Zunger, and D. S. Dessau, “States in three-dimensional topological insulators”, *Nature Physics* **9**, 499 (2013).

- <sup>64</sup>Z. H. Zhu, C. N. Veenstra, G. Levy, A. Ubaldini, P. Syers, N. P. Butch, J. Paglione, M. W. Haverkort, I. S. Elfimov, and A. Damascelli, “Layer-by-layer entangled spin-orbital texture of the topological surface state in  $\text{Bi}_2\text{Se}_3$ ”, *Physical Review Letters* **110**, 216401 (2013).
- <sup>65</sup>Z.-H. Zhu, C. N. Veenstra, S. Zhdanovich, M. P. Schneider, T. Okuda, K. Miyamoto, S.-Y. Zhu, H. Namatame, M. Taniguchi, M. W. Haverkort, I. S. Elfimov, and A. Damascelli, “Photoelectron spin-polarization control in the topological insulator  $\text{Bi}_2\text{Se}_3$ ”, *Physical Review Letters* **112**, 076802 (2014).
- <sup>66</sup>W. Berthold, J. Gdde, P. Feulner, and U. Hfer, “Resonant interband scattering of image-potential states”, *Applied Physics B* **73**, 865 (2001).
- <sup>67</sup>T. Fauster, M. Weinelt, and U. Hfer, “Quasi-elastic scattering of electrons in image-potential states”, *Progress in Surface Science* **82**, Dynamics of Electron Transfer Processes at Surfaces, 224 (2007).
- <sup>68</sup>M. Roth, T. Fauster, and M. Weinelt, “Scattering of electrons in image-potential states by steps”, *Applied Physics A* **88**, 497 (2007).
- <sup>69</sup>M. Roth, M. Weinelt, T. Fauster, P. Wahl, M. Schneider, L. Diekhner, and K. Kern, “Scattering of image-potential-state electrons by steps on  $\text{Cu}(001)$ ”, *Applied Physics A* **78**, 155 (2004).
- <sup>70</sup>M. Roth, M. Pickel, M. Weinelt, and T. Fauster, “Dynamics of image-potential states on stepped  $\text{Cu}(001)$  surfaces”, *Applied Physics A* **78**, 149 (2004).
- <sup>71</sup>M. Roth, M. Pickel, W. Jinxiong, M. Weinelt, and T. Fauster, “Electron scattering at steps: Image-potential states on  $\text{Cu}(119)$ ”, *Physical Review Letters* **88**, 096802 (2002).
- <sup>72</sup>C. Tegenkamp, Z. Kallassy, H. Pfnr, H.-L. Gnter, V. Zielasek, and M. Henzler, “Switching between one and two dimensions: conductivity of Pb-induced chain structures on  $\text{Si}(557)$ ”, *Physical Review Letters* **95**, 176804 (2005).

## BIBLIOGRAPHY

---

- <sup>73</sup>C. Tegenkamp, T. Ohta, J. L. McChesney, H. Dil, E. Rotenberg, H. Pfnür, and K. Horn, “Coupled Pb chains on Si(557): Origin of one-dimensional conductance”, *Physical Review Letters* **100**, 076802 (2008).
- <sup>74</sup>P. S. Kirchmann, L. Rettig, X. Zubizarreta, V. M. Silkin, E. V. Chulkov, and U. Bovensiepen, “Quasiparticle lifetimes in metallic quantum-well nanostructures”, *Nature Physics* **6**, 782 (2010).
- <sup>75</sup>A. S. Syed, V. M. Trontl, M. Ligges, S. Sakong, P. Kratzer, D. Lükermann, P. Zhou, I. Avigo, H. Pfnür, C. Tegenkamp, and U. Bovensiepen, “Unoccupied electronic structure and momentum-dependent scattering dynamics in Pb/Si(557) nanowire arrays”, *Physical Review B* **92**, 134301 (2015).
- <sup>76</sup>H. W. Yeom, S. Takeda, E. Rotenberg, I. Matsuda, K. Horikoshi, J. Schaefer, C. M. Lee, S. D. Kevan, T. Ohta, T. Nagao, and S. Hasegawa, “Instability and charge density wave of metallic quantum chains on a silicon surface”, *Physical Review Letters* **82**, 4898 (1999).
- <sup>77</sup>O. Bunk, G. Falkenberg, J. H. Zeysing, L. Lottermoser, R. L. Johnson, M. Nielsen, F. Berg-Rasmussen, J. Baker, and R. Feidenhans'l, “Structure determination of the indium-induced Si(111)–(4 × 1) reconstruction by surface x-ray diffraction”, *Physical Review B* **59**, 12228 (1999).
- <sup>78</sup>H. Morikawa, I. Matsuda, and S. Hasegawa, “Direct observation of soliton dynamics in charge-density waves on a quasi-one-dimensional metallic surface”, *Physical Review B* **70**, 085412 (2004).
- <sup>79</sup>S. J. Park, H. W. Yeom, S. H. Min, D. H. Park, and I. W. Lyo, “Direct evidence of the charge ordered phase transition of indium nanowires on Si(111)”, *Physical Review Letters* **93**, 106402 (2004).
- <sup>80</sup>Y. J. Sun, S. Agario, S. Souma, K. Sugawara, Y. Tago, T. Sato, and T. Takahashi, “Cooperative structural and Peierls transition of indium chains on Si(111)”, *Physical Review B* **77**, 125115 (2008).

- <sup>81</sup>H. W. Yeom, K. Horikoshi, H. M. Zhang, K. Ono, and R. I. G. Uhrberg, “Nature of the broken-symmetry phase of the one-dimensional metallic In/Si(111) surface”, *Physical Review B* **65**, 241307 (2002).
- <sup>82</sup>J. R. Ahn, J. H. Byun, H. Koh, E. Rotenberg, S. D. Kevan, and H. W. Yeom, “Mechanism of gap opening in a triple-band peierls system: In atomic wires on Si”, *Physical Review Letters* **93**, 106401 (2004).
- <sup>83</sup>I. G. Hill and A. B. McLean, “Detection of a Fermi level crossing in three-domain Si(111)-In( $4 \times 1$ )”, *Physical Review B* **59**, 9791 (1999).
- <sup>84</sup>I. G. Hill and A. B. McLean, “Metallicity of In chains on Si(111)”, *Physical Review B* **56**, 15725 (1997).
- <sup>85</sup>O. Gallus, T. Pillo, M. Hengsberger, P. Segovia, and Y. Baer, “A system with a complex phase transition: Indium chains on Si(111)”, *The European Physical Journal B - Condensed Matter and Complex Systems* **20**, 313 (2001).
- <sup>86</sup>T. Frigge, B. Hafke, T. Witte, B. Krenzer, C. Streubühr, A. Samad Syed, V. Mikšić Trontl, I. Avigo, P. Zhou, M. Ligges, D. Von Der Linde, U. Bovensiepen, M. Horn-von Hoegen, S. Wippermann, A. Lücke, S. Sanna, U. Gerstmann, and W. G. Schmidt, “Optically excited structural transition in atomic wires on surfaces at the quantum limit”, *Nature* **544**, 207 (2017).
- <sup>87</sup>H. Hertz, “Ueber einen einfluss des ultravioletten lichtes auf die electriche entladung”, *Annalen der Physik* **267**, 983 (1887).
- <sup>88</sup>A. Einstein, “On a heuristic point of view concerning the production and transformation of light (english translation)”, *Annalen der Physics* **17**, 132 (1905).
- <sup>89</sup>J. D. Koralek, J. F. Douglas, N. C. Plumb, J. D. Griffith, S. T. Cundiff, H. C. Kapteyn, M. M. Murnane, and D. S. Dessau, “Experimental setup for low-energy laser-based angle resolved photoemission spectroscopy”, *Review of Scientific Instruments* **78**, 053905 (2007).

## BIBLIOGRAPHY

---

- <sup>90</sup>M. P. Seah and W. A. Dench, “Quantitative electron spectroscopy of surfaces: A standard data base for electron inelastic mean free paths in solids”, *Surface and Interface Analysis* **1**, 2 (1979).
- <sup>91</sup>W. Kuch and C. M. Schneider, “Magnetic dichroism in valence band photoemission”, *Reports on Progress in Physics* **64**, 147 (2001).
- <sup>92</sup>C. N. Berglund and W. E. Spicer, “Photoemission studies of Copper and Silver: Theory”, *Physical Reviews Journals Archive* **136**, A1030 (1964).
- <sup>93</sup>S. Hüfner, *Photoelectron spectroscopy : principles and applications*, edited by S. Hüfner (Stephan Hüfner, 2003).
- <sup>94</sup>J. Pendry, “Theory of photoemission”, *Surface Science* **57**, 679 (1976).
- <sup>95</sup>N. Smith, “Inverse photoemission and related techniques”, *Vacuum* **33**, 803 (1983).
- <sup>96</sup>T. Fauster and W. Steinmann, *Photonic Probes of Surfaces*, edited by P. Halevi (Elsevier, 1995).
- <sup>97</sup>H. Ueba and B. Gumhalter, “Theory of two-photon photoemission spectroscopy of surfaces”, *Progress in Surface Science* **82**, 193 (2007).
- <sup>98</sup>P. S. Kirchmann, “Ultrafast electron dynamics in low-dimensional materials”, PhD thesis (Freie University Berlin, 2008).
- <sup>99</sup>B. Rethfeld, A. Kaiser, M. Vicanek, and G. Simon, “Ultrafast dynamics of nonequilibrium electrons in metals under femtosecond laser irradiation”, *Physical Review B* **65**, 214303 (2002).
- <sup>100</sup>M. Lisowski, P. Loukakos, U. Bovensiepen, and M. Wolf, “Femtosecond dynamics and transport of optically excited electrons in epitaxial Cu films on Si(111)-7 × 7”, *Applied Physics A* **79**, 739 (2004).
- <sup>101</sup>W. S. Fann, R. Storz, H. W. K. Tom, and J. Bokor, “Direct measurement of nonequilibrium electron-energy distributions in subpicosecond laser-heated gold films”, *Physical Review Letters* **68**, 2834 (1992).

- <sup>102</sup>L. Rettig, “Ultrafast Dynamics of Correlated Electrons”, PhD thesis (Free University of Berlin, 2012).
- <sup>103</sup>R. Haight, “Electron dynamics at surfaces”, *Surface Science Reports* **21**, 275 (1995).
- <sup>104</sup>T. Fauster, “Electron dynamics in image potential states at metal surfaces”, in *Dynamics at solid state surfaces and interfaces* (Wiley-VCH Verlag GmbH & Co. KGaA, 2010).
- <sup>105</sup>J. J. Quinn and R. A. Ferrell, “Electron self-energy approach to correlation in a degenerate electron gas”, *Physical Review Journals Archive* **112**, 812 (1958).
- <sup>106</sup>P. Coleman, *Introduction to many-body physics*, edited by P. Coleman (Cambridge University Press, 2015).
- <sup>107</sup>T. Hertel, E. Knoesel, M. Wolf, and G. Ertl, “Ultrafast electron dynamics at Cu(111): Response of an electron gas to optical excitation”, *Physical Review Letters* **76**, 535 (1996).
- <sup>108</sup>E. Knoesel, A. Hotzel, and M. Wolf, “Temperature dependence of surface state lifetimes, dephasing rates and binding energies on Cu(111) studied with time-resolved photoemission”, *Journal of Electron Spectroscopy and Related Phenomena* **88-91**, 577 (1998).
- <sup>109</sup>A. J. Stähler, “Electron Transfer and Solvation Dynamics at D<sub>2</sub>O and NH<sub>3</sub> – Metal Interfaces”, PhD thesis (Free University of Berlin, 2007).
- <sup>110</sup>C. L. Group, *Verdi V-18 Diode-Pumped Lasers*, Coherent Inc. (Santa Clara, 2007).
- <sup>111</sup>C. L. Group, *Rega 9050 System*, Preliminary Version 2.1, Coherent Inc. (Santa Clara, 1997).
- <sup>112</sup>C. L. Group, *The Coherent Modell 9800 Optical Parametric Amplifier*. Coherent Inc. (Santa Clara, 1994).

## BIBLIOGRAPHY

---

- <sup>113</sup>C. L. Group, *The Coherent Mira 900-B Laser*, Coherent Inc. (Santa Clara, 1993).
- <sup>114</sup>I. Agarwal, “Electron Transfer Dynamics in Halobenzenes at Ice and Metal Interfaces”, PhD thesis (University of Duisburg-Essen, 2017).
- <sup>115</sup>C. Rullière, *Femtosecond Laser Pulses : Principles and Experiments*, edited by C. Rullière (Springer, Berlin, Heidelberg, 1998).
- <sup>116</sup>A. Zangwill, *Physics at Surfaces*, edited by A. Zangwill (Cambridge University Press, 1988).
- <sup>117</sup>P. S. Kirchmann, L. Rettig, D. Nandi, U. Lipowski, M. Wolf, and U. Bovensiepen, “A time-of-flight spectrometer for angle-resolved detection of low energy electrons in two dimensions”, *Applied Physics A* **91**, 211 (2008).
- <sup>118</sup>O. Jagutzki, A. Cerezo, A. Czasch, R. Dorner, M. Hattas, M. Huang, V. Mergel, U. Spillmann, K. Ullmann-Pfleger, T. Weber, H. Schmidt-Bocking, and G. D. W. Smith, “Multiple hit readout of a microchannel plate detector with a three-layer delay-line anode”, *IEEE Transactions on Nuclear Science* **49**, 2477 (2002).
- <sup>119</sup>K. Takayanagi, Y. Tanishiro, S. Takahashi, and M. Takahashi, “Structure analysis of Si(111)- $7 \times 7$  reconstructed surface by transmission electron diffraction”, *Surface Science* **164**, 367 (1985).
- <sup>120</sup>M. Czubanowski, A. Schuster, S. Akbari, H. Pfnür, and C. Tegenkamp, “Adsorbate induced refacetting: Pb chains on Si(557)”, *New Journal of Physics* **9**, 338 (2007).
- <sup>121</sup>A. Kirakosian, R. Bennewitz, J. N. Crain, T. Fauster, J.-L. Lin, D. Y. Petrovykh, and F. J. Himpsel, “Atomically accurate Si grating with 5.73 nm period”, *Applied Physics Letters* **79**, 1608 (2001).

- <sup>122</sup>M. Yakes, V. Yeh, M. Hupalo, and M. C. Tringides, “Self-organization at finite temperatures of the devil’s staircase in Pb/Si(111)”, *Physical Review B* **69**, 224103 (2004).
- <sup>123</sup>I. Brihuega, O. Custance, M. M. Ugeda, and J. M. Gómez-Rodríguez, “Defects in the  $(\sqrt{3} \times \sqrt{3}) \Leftrightarrow (3 \times 3)$  phase transition in the Pb/Si(111) system”, *Physical Review B* **75**, 155411 (2007).
- <sup>124</sup>W.-Y. Chan, H.-S. Huang, W.-B. Su, S.-M. Lu, G. Hoffmann, and C.-S. Chnag, “Energy spacing between electronic resonances: A physical quantity correlating to diverse phases of the dense Pb overlayers on Si(111)”, *Journal of Vacuum Science & Technology B* **32**, 011801 (2013).
- <sup>125</sup>J. Henk, M. Hoesch, J. Osterwalder, A. Ernst, and P. Bruno, “Spin-orbit coupling in the L-gap surface states of Au(111): spin-resolved photoemission experiments and first-principles calculations”, *Journal of Physics: Condensed Matter* **16**, 7581 (2004).
- <sup>126</sup>Y. Ohtsubo, S. Hatta, H. Okuyama, and T. Aruga, “A metallic surface state with uniaxial spin polarization on Tl/Ge(111)  $(1 \times 1)$ ”, *Journal of Physics: Condensed Matter* **24**, 092001 (2012).
- <sup>127</sup>C. Tegenkamp, D. Lükermann, H. Pfnür, B. Slomski, G. Landolt, and J. H. Dil, “Fermi nesting between atomic wires with strong spin-orbit coupling”, *Physical Review Letters* **109**, 266401 (2012).
- <sup>128</sup>J. H. Dil, F. Meier, J. Lobo-Checa, L. Patthey, G. Bihlmayer, and J. Osterwalder, “Rashba-type spin-orbit splitting of quantum well states in ultrathin Pb films”, *Physical Review Letters* **101**, 266802 (2008).
- <sup>129</sup>J. H. Dil, “Spin and angle resolved photoemission on non-magnetic low-dimensional systems”, *Journal of Physics: Condensed Matter* **21**, 403001 (2009).

## BIBLIOGRAPHY

---

- <sup>130</sup>T. Okuda and A. Kimura, “Spin- and angle-resolved photoemission of strongly spin-orbit coupled systems”, *Journal of the Physical Society of Japan* **82**, 021002 (2013).
- <sup>131</sup>S. LaShell, B. A. McDougall, and E. Jensen, “Spin splitting of an Au(111) surface state band observed with angle resolved photoelectron spectroscopy”, *Physical Review Letters* **77**, 3419 (1996).
- <sup>132</sup>K. Gotlieb, Z. Li, C.-Y. Lin, C. Jozwiak, J. H. Ryoo, C.-H. Park, Z. Hussain, S. G. Louie, and A. Lanzara, “Symmetry rules shaping spin-orbital textures in surface states”, *Physical Review B* **95**, 245142 (2017).
- <sup>133</sup>K. N. Altmann, J. N. Crain, A. Kirakosian, J.-L. Lin, D. Y. Petrovykh, F. J. Himpsel, and R. Losio, “Electronic structure of atomic chains on vicinal Si(111)-Au”, *Physical Review B* **64**, 035406 (2001).
- <sup>134</sup>T. Matsushita, S. Imada, H. Daimon, T. Okuda, K. Yamaguchi, H. Miyagi, and S. Suga, “Linear and circular dichroism in photoemission angular distribution from the valence band of  $1T$ -TaS<sub>2</sub>”, *Physical Review B* **56**, 7687 (1997).
- <sup>135</sup>A. Winkelmann, V. Sametoglu, J. Zhao, A. Kubo, and H. Petek, “Angle-dependent study of a direct optical transition in the *sp* bands of Ag(111) by one- and two-photon photoemission”, *Physical Review B* **76**, 195428 (2007).
- <sup>136</sup>J. Kanasaki, H. Tanimura, K. Tanimura, P. Ries, W. Heckel, K. Biedermann, and T. Fauster, “Ultrafast dynamics in photoexcited valence-band states of Si studied by time- and angle-resolved photoemission spectroscopy of bulk direct transitions”, *Physical Review B* **97**, 035201 (2018).
- <sup>137</sup>Q. Liu, X. Zhang, J. A. Waugh, D. S. Dessau, and A. Zunger, “Orbital mapping of energy bands and the truncated spin polarization in three-dimensional Rashba semiconductors”, *Physical Review B* **94**, 125207 (2016).
- <sup>138</sup>T. Fauster and W. Steinmann, *Electromagnetic waves: Recent developments in research*, edited by P. Halevi (Elsevier, 1995).

- <sup>139</sup>H. Petek and S. Ogawa, “Femtosecond time-resolved two-photon photoemission studies of electron dynamics in metals”, *Progress in Surface Science* **56**, 239 (1997).
- <sup>140</sup>M. Weinelt, “Time-resolved two-photon photoemission from metal surfaces”, *Journal of Physics: Condensed Matter* **14**, R1099 (2002).
- <sup>141</sup>U. Bovensiepen, H. Petek, and M. Wolf, *Dynamics at Solid State Surfaces and Interfaces* (Wiley, 2010).
- <sup>142</sup>P. Echenique, R. Berndt, E. Chulkov, T. Fauster, A. Goldmann, and U. Höfer, “Decay of electronic excitations at metal surfaces”, *Surface Science Reports* **52**, 219 (2004).
- <sup>143</sup>R. Knorren, K. H. Bennemann, R. Burgermeister, and M. Aeschlimann, “Dynamics of excited electrons in copper and ferromagnetic transition metals: Theory and experiment”, *Physical Review B* **61**, 9427 (2000).
- <sup>144</sup>X. Cui, C. Wang, A. Argondizzo, S. Garrett-Roe, B. Gumhalter, and H. Petek, “Transient excitons at metal surfaces”, *Nature Physics* **10**, 505 (2014).
- <sup>145</sup>S. Neppl, R. Ernstorfer, A. L. Cavalieri, C. Lemell, G. Wachter, E. Magerl, E. M. Bothschafter, M. Jobst, M. Hofstetter, U. Kleineberg, J. V. Barth, D. Menzel, J. Burgdörfer, P. Feulner, F. Krausz, and R. Kienberger, “Direct observation of electron propagation and dielectric screening on the atomic length scale”, *Nature* **517**, 342 (2015).
- <sup>146</sup>W. Berthold, U. Höfer, P. Feulner, E. V. Chulkov, V. M. Silkin, and P. M. Echenique, “Momentum-resolved lifetimes of image-potential states on Cu(100)”, *Physical Review Letters* **88**, 056805 (2002).
- <sup>147</sup>K. Boger, M. Weinelt, and T. Fauster, “Scattering of hot electrons by adatoms at metal surfaces”, *Physical Review Letters* **92**, 126803 (2004).

## BIBLIOGRAPHY

---

- <sup>148</sup>H. Petek, H. Nagano, M. J. Weida, and S. Ogawa, “Surface femtochemistry frustrated desorption of alkali atoms from noble metals”, *The Journal of Physical Chemistry B* **105**, 6767 (2001).
- <sup>149</sup>M. Bauer, S. Pawlik, and M. Aeschlimann, “Decay dynamics of photoexcited alkali chemisorbates: Real-time investigations in the femtosecond regime”, *Physical Review B* **60**, 5016 (1999).
- <sup>150</sup>J. Gauyacq, A. Borisov, and M. Bauer, “Excited states in the alkali/noble metal surface systems: A model system for the study of charge transfer dynamics at surfaces”, *Progress in Surface Science* **82**, 244 (2007).
- <sup>151</sup>S. Ogawa, H. Nagano, and H. Petek, “Optical intersubband transitions and femtosecond dynamics in Ag/Fe(100) quantum wells”, *Physical Review Letters* **88**, 116801 (2002).
- <sup>152</sup>S. Mathias, A. Ruffing, F. Deicke, M. Wiesenmayer, M. Aeschlimann, and M. Bauer, “Band structure dependence of hot-electron lifetimes in a Pb/Cu(111) quantum-well system”, *Physical Review B* **81**, 155429 (2010).
- <sup>153</sup>P. C. Snijders and H. H. Weitering, “Colloquium: Electronic instabilities in self-assembled atom wires”, *Reviews of Modern Physics* **82**, 307 (2010).
- <sup>154</sup>R. V. Yusupov, T. Mertelj, J.-H. Chu, I. R. Fisher, and D. Mihailovic, “Single-particle and collective mode couplings associated with 1- and 2-directional electronic ordering in metallic RTe<sub>3</sub> (R=Ho,Dy,Tb)”, *Physical Review Letters* **101**, 246402 (2008).
- <sup>155</sup>F. Schmitt, P. S. Kirchmann, U. Bovensiepen, R. G. Moore, L. Rettig, M. Krenz, J.-H. Chu, N. Ru, L. Perfetti, D. H. Lu, M. Wolf, I. R. Fisher, and Z.-X. Shen, “Transient electronic structure and melting of a charge density wave in TbTe<sub>3</sub>”, *Science* **321**, 1649 (2008).

- <sup>156</sup>T. Rohwer, S. Hellmann, M. Wiesenmayer, C. Sohrt, A. Stange, B. Slomski, A. Carr, Y. Liu, L. M. Avila, M. Källäsingne, S. Mathias, L. Kipp, K. Rosnagel, and M. Bauer, “Collapse of long-range charge order tracked by time-resolved photoemission at high momenta”, *Nature* **471**, 490 (2011).
- <sup>157</sup>M. Eichberger, H. Schäfer, M. Krumova, M. Beyer, J. Demsar, H. Berger, G. Moriena, G. Sciaini, and R. J. Miller, “Snapshots of cooperative atomic motions in the optical suppression of charge density waves”, *Nature* **468**, 799 (2010).
- <sup>158</sup>T.-R. T. Han, Z. Tao, S. D. Mahanti, K. Chang, C.-Y. Ruan, C. D. Malliakas, and M. G. Kanatzidis, “Structural dynamics of two-dimensional charge-density waves in CeTe<sub>3</sub> investigated by ultrafast electron crystallography”, *Physical Review B* **86**, 075145 (2012).
- <sup>159</sup>S. Wall, B. Krenzer, S. Wippermann, S. Sanna, F. Klasing, A. Hanisch-Blicharski, M. Kammler, W. G. Schmidt, and M. Horn-von Hoegen, “Atomistic picture of charge density wave formation at surfaces”, *Physical Review Letters* **109**, 186101 (2012).
- <sup>160</sup>K. S. Kim, W. H. Choi, and H. W. Yeom, “Photoemission study of the anisotropic phase formation of Pb on Si(557)”, *Physical Review B* **75**, 195324 (2007).
- <sup>161</sup>K. S. Kim, H. Morikawa, W. H. Choi, and H. W. Yeom, “Strong lateral electron coupling of Pb nanowires on stepped Si(111): Angle-resolved photoemission studies”, *Physical Review Letters* **99**, 196804 (2007).
- <sup>162</sup>C. Tegenkamp, “Vicinal surfaces for functional nanostructures”, *Journal of Physics: Condensed Matter* **21**, 013002 (2009).
- <sup>163</sup>W. B. M Rohleder, K. Duncker, and U. H. J. Gütde, “Momentum-resolved dynamics of Ar/Cu(100) interface states probed by time-resolved two-photon photoemission”, *New Journal of Physics* **7**, 103 (2005).

## BIBLIOGRAPHY

---

- <sup>164</sup>S. Sakong, P. Kratzer, S. Wall, A. Kalus, and M. Horn-von Hoegen, “Mode conversion and long-lived vibrational modes in lead monolayers on silicon (111) after femtosecond laser excitation: A molecular dynamics simulation”, *Physical Review B* **88**, 115419 (2013).
- <sup>165</sup>G. Kresse and J. Furthmüller, “Efficient iterative schemes for ab initio total-energy calculations using a plane-wave basis set”, *Physical Review B* **54**, 11169 (1996).
- <sup>166</sup>J. P. Perdew, K. Burke, and M. Ernzerhof, “Generalized gradient approximation made simple”, *Physical Review Letters* **77**, 3865 (1996).
- <sup>167</sup>P. M. Echenique and J. B. Pendry, “The existence and detection of Rydberg states at surfaces”, *Journal of Physics C: Solid State Physics* **11**, 2065 (1978).
- <sup>168</sup>P. S. Kirchmann and U. Bovensiepen, “Ultrafast electron dynamics in Pb/Si(111) investigated by two-photon photoemission”, *Physical Review B* **78**, 035437 (2008).
- <sup>169</sup>M. Aeschlimann, M. Bauer, S. Pawlik, R. Knorren, G. Bouzerar, and K. H. Bennemann, “Transport and dynamics of optically excited electrons in metals”, *Applied Physics A* **71**, 485 (2000).
- <sup>170</sup>R. Loudon, *The quantum theory of light*, Oxford science publications (Clarendon Press, 1983).
- <sup>171</sup>W.-L. Chan, J. Tritsch, A. Dolocan, M. Ligges, L. Miaja-Avila, and X.-Y. Zhu, “Communication: Momentum-resolved quantum interference in optically excited surface states”, *The Journal of Chemical Physics* **135**, 031101 (2011).
- <sup>172</sup>C. Tegenkamp and H. Pfnür, “Switching between one- and two-dimensional conductance: Coupled chains in the monolayer of Pb on Si(557)”, *Surface Science* **601**, 2641 (2007).

- <sup>173</sup>H. Hirayama, S. Baba, and A. Kinbara, “Summary abstract: the work function of In/Si(111) superstructures”, *Journal of Vacuum Science and Technology A: Vacuum, Surfaces and Films* **4**, 1416 (1986).
- <sup>174</sup>T. Aiyama and S. Ino, “RHEED observation of the Si(111)(31 × 31)R ± 9°-In structure”, *Surface Science* **82**, L585 (1979).
- <sup>175</sup>U. Gerstmann, N. J. Vollmers, A. Lücke, M. Babilon, and W. G. Schmidt, “Rashba splitting and relativistic energy shifts in In/Si(111) nanowires”, *Physical Review B* **89**, 165431 (2014).
- <sup>176</sup>C. González, J. Ortega, and F. Flores, “Metal–insulator transition in one-dimensional In-chains on Si(111): combination of a soft shear distortion and a double-band Peierls instability”, *New Journal of Physics* **7**, 100 (2005).
- <sup>177</sup>H. Schäfer, V. V. Kabanov, M. Beyer, K. Biljakovic, and J. Demsar, “Disentanglement of the electronic and lattice parts of the order parameter in a 1D charge density wave system probed by femtosecond spectroscopy”, *Physical Review Letters* **105**, 066402 (2010).
- <sup>178</sup>L. Perfetti, P. A. Loukakos, M. Lisowski, U. Bovensiepen, H. Berger, S. Biermann, P. S. Cornaglia, A. Georges, and M. Wolf, “Time evolution of the electronic structure of 1T–TaS<sub>2</sub> through the insulator-metal transition”, *Physical Review Letters* **97**, 067402 (2006).
- <sup>179</sup>T. Abukawa, M. Sasaki, F. Hisamatsu, T. Goto, T. Kinoshita, A. Kakizaki, and S. Kono, “Surface electronic structure of a single-domain Si(111)4 × 1-In surface: a synchrotron radiation photoemission study”, *Surface Science* **325**, 33 (1995).
- <sup>180</sup>A. Hanisch-Blicharski, A. Janzen, B. Krenzer, S. Wall, F. Klasing, A. Kalus, T. Frigge, M. Kammler, and M. Horn-von Hoegen, “Ultra-fast electron diffraction at surfaces: From nanoscale heat transport to driven phase transitions”, *Ultramicroscopy* **127**, 2 (2013).



# List of Publications

1. A. Samad Syed, V. M. Trontl, M. Ligges, S. Sakong, P. Kratzer, D. Lükermann, P. Zhou, H. Pfnür, C. Tegenkamp, and U. Bovensiepen "Unoccupied electronic structure and momentum-dependent scattering dynamics in Pb/Si(557) nanowire arrays"  
Phys. Rev. B **92**, 134301 (2015)
2. T. Frigge, B. Hafke, T. Witte, B. Krenzer, C. Streubühr, A. Samad Syed, V. M. Trontl, I. Avigo, P. Zhou, M. Ligges, D. Von Der Linde, U. Bovensiepen, M. Horn-Von Hoegen, S. Wippermann, A. Lücke, S. Sanna, U. Gerstmann, W.G. Schmidt "Optically excited structural transition in atomic wires on surfaces at the quantum limit"  
Nature **544**, 207 (2017)

